Rotation Invariant Classification of 3D Surface Texture Using Photometric Stereo

Jiahua Wu B.Eng

Thesis submitted

for the

Degree of Doctor of Philosophy

Department of Computer Science

School of Mathematical and Computer Sciences

Heriot-Watt University

Edinburgh

2003

To Dad and Mum

&

Carrie

Table of Contents

List of Figures

List of Tables

Abstract

This thesis presented a new three-dimensional surface texture classification scheme which was invariant to surface-rotation using photometric stereo. Many texture classification approaches had been presented in the past that were image-rotation invariant, however, *image* rotation was not necessarily the same as *surface* rotation. A classifier therefore had been developed that used invariants that were derived from surface properties rather than image properties.

Firstly, various surface models were considered and a classification scheme was developed that used magnitude spectra of the partial derivatives of the surface obtained using photometric stereo. A simple frequency domain method of removing the directional artefacts of partial derivatives was presented, and a *1D* feature set of polar spectrum was also extracted from resulting spectrum. Classification was performed by comparing training and classification polar spectra over a range of rotations. Secondly, a new feature generator albedo spectrum was introduced to provide more information on surface texture properties, and an additional *1D* feature set of the radial spectrum was employed too. In addition, by examining the effect of shadowing, a four-image photometric stereo method was developed to provide more accurate three-dimensional surface properties. Finally, a verification step was included in the classification where the *2D* spectrum features were compared instead of *1D* spectrum features.

The classification results using new-developed photometric stereo real texture database shown that combining *2D* gradient and albedo data improves the classification's performance to provide a successful classification rate of *99%*.

Acknowledgements

Initially, I would especially like to thank my supervisor, Dr. Mike Chantler who give me an opportunity to do this research in which I am really interested, and make this thesis possible in the Department of Computing and Electrical Engineering at Heriot-Watt University, Edinburgh. I sincerely can not help expressing how I should credit this thesis to his support and guidance whenever I dropped in his office, his encouragement and stimulation throughout the duration of my writing up.

I am also very grateful to Dr. Gerald McGunnigle in the texture laboratory for his warm and selfless advice, help and patience. In addition, many thanks also to my other colleagues in the texture laboratory, particularly Miss. Cristina Gullon, Miss. Jennifer Pfeiffer, Mr. Andy Spence and Mr. Junyu Dong, for providing such a stimulating and relaxed research environment, entertainment and fun stuffs in Edinburgh.

Great many thanks I would like to give to lab manager Mr. Alistair Houston and computer officer Mr. Iain McCrone for their kindly smiles and instant response whenever and wherever I asked for supporting my research in the department.

Finally, very special thanks are also due to my dad and mum in Beijing and my girlfriend, Carrie in Brighton, and all of my friends in the U.K. for their great support and encouragement in whole remarkable days.

Many thanks to everybody who ever gave me help and support.

CHAPTER 1

Introduction

1.1. Motivation and Background

Many texture classification scheme have been presented that are invariant to image rotation [Cohen91] [Mao92] [Haley96] [Porter97] [Pietikainen00]. They normally derive their features directly from a single image and are tested using rotated images. If the image texture results solely from albedo variation rather that surface relief or if the illumination is not directional or immediately overhead, then these schemes are surface-rotation invariant as well. However, *3D* surface textures are often illuminated from one side when they are photographed in order to enhance their image texture, e.g. [Brodatz66]. Such imaging acts as a directional filter of the *3D* surface texture [Chantler94]. This phenomena is illustrated below. *Figure 1. 1* shows the same sample of *3D* surface texture imaged using two different illumination conditions.

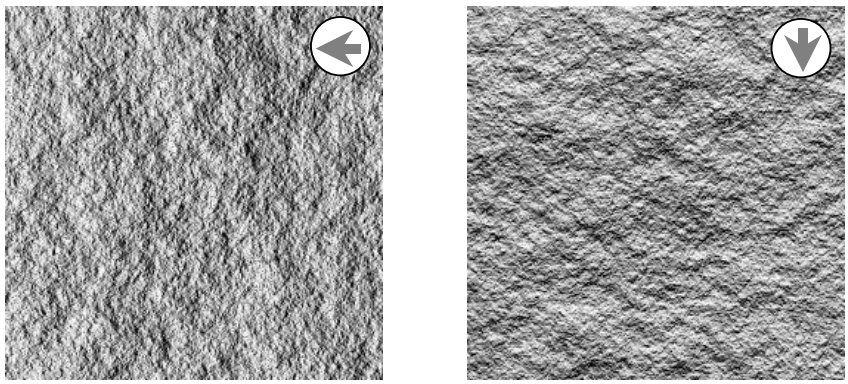

$\tau = 0°$ $\tau = 90°$

Figure 1. 1 Images of the same 3D surface texture imaged at two different illuminant tilt (τ) directions shown by the top-right arrows.

The directional filtering effect is more obvious in the frequency domain. *Figure 1. 2* shows the Fourier transforms of the two image textures shown above. This shows more clearly that side-lighting accentuates texture components in the illuminant tilt direction *(τ)* and attenuates those at right angles.

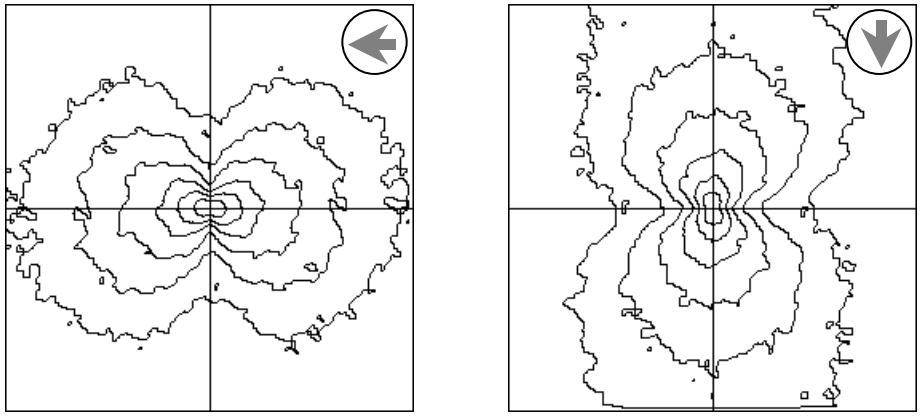

Figure 1. 2 FFTs of the image shown in Figure 1. 1.

In many cases rotation of a textured surface produces images that differ radically from those provided by pure image rotation (see *Figure 1. 3*). These images show that rotation of a *3D* surface texture does not result in a simple rotation of the image texture. Rotation of the physical texture surface under fixed illumination conditions can also cause significant changes to its appearance. This is mainly due to the directional filtering effect of imaging using side-lighting [Chantler94a, Chantler94b]. It also causes failure of classifiers designed to cope with image rotation [McGunigle98].

We have shown that rotation of a rough surface is not equivalent to rotation of its image, and that conventional rotation-invariant algorithms may fail under these conditions. The aim of this thesis is therefore to develop a new classification scheme that uses surface information derived from photometric stereo to provide a surface rotation invariant classifier.

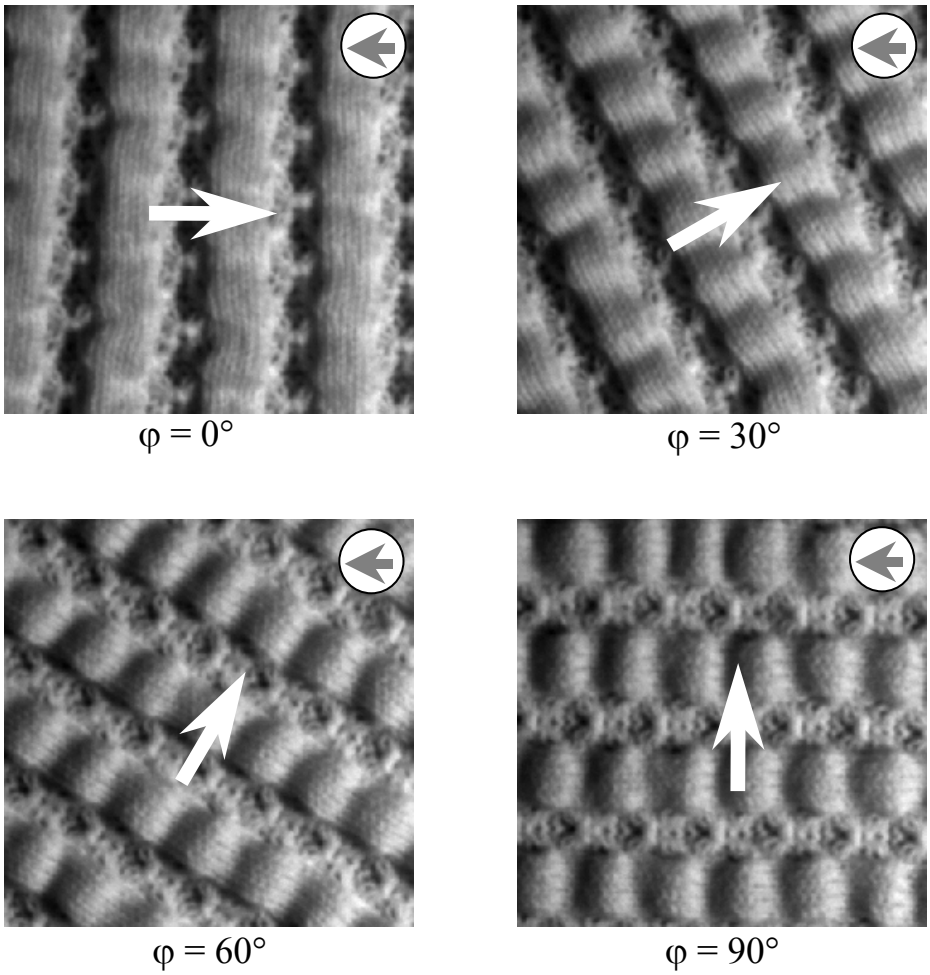

Figure 1. 3 Four images of a directional 3D surface texture rotated at angles of φ=0°, 30°, 60° and 90° (indicated by the center white arrows). The illuminant tilt is kept constant at τ=0° (indicated by the top-right black arrows in white circles).

1.2. Scope of Research

The surface is considered to lie in the *x-y* plane. Furthermore, this work uses a linear reflection model based on Kube and Pentland's linear model [Kube88]. The surface reflectance is therefore considered to be diffuse, and uniform throughout the surface. The light incident on the surface is considered to be parallel and of equal intensity across the imaged region. The imaging device is assumed to be a monochrome CCD camera located directly overhead the surface texture sample. Finally, we assume the topography of the surface is small relative to the distance between the camera and the surface, and that the projection of the surface onto the CCD array is orthographic. In

general, the imaging geometry is illustrated in *Figure 1. 4*. The test surface is mounted in the *x-y* plane and is perpendicular to the camera axis *(z-axis)*, and the surface is illuminated by a point source located at infinity. The surface rotation is measured in the *x-y* plane.

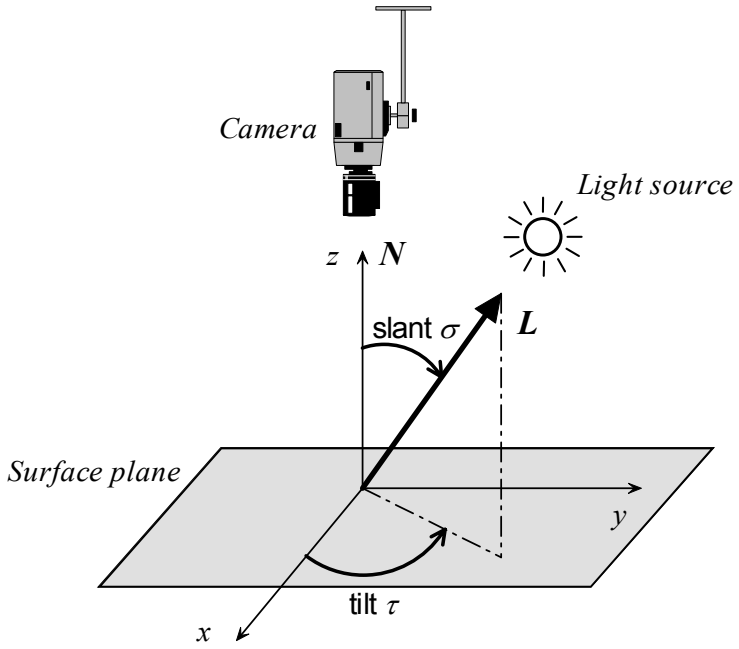

Figure 1. 4 Imaging geometry.

All of the classifiers considered in this thesis ignore phase information and discriminate on a sampling of the power spectrum of either surface derivatives or surface albedo.

1.3. Original Work

It is believed that this thesis represents three main original contributions to the field of rotation-invariant texture classification:

- Regarding the texture database, we note that currently existing and publicly available ones [Brodatz66] [Dana99a] [Ohanian92] [Ojala96] are not suitable for

our research, as they can not provide registered photometric stereo data set for surface textures. The texture due to surface roughness has complex dependencies on orientation, viewing and illumination direction. These dependencies can not be studied using those texture databases that include few images of each sample. We therefore develop our novel ***photometric stereo 3D surface texture database***, which is not only concerned with surface rotation, but also with the different and controlled illuminant conditions. It covers a diverse collection of *4* synthetic and *30* natural surfaces, and it is intended to provide photometric data for the study of rotation-invariant surface texture classification.

Note that our texture database is similar to *PhoTex* database [McGunnigle01]. However, the main variables in *PhoTex* database are azimuth and zenith of the illumination. Although some surface sample are rotated, it does not provide full surface rotation samples so that it can not be used in this work.

- The recovery of an intrinsic description of a surface (e.g. surface orientation) by photometric stereo is, without any doubt, a necessary step for our surface texture classification. The *1D* feature spaces ***polar spectrum*** and ***radial spectrum*** by means of surface derivative fields in the frequency domain has been added to the benefit of accounting for surface properties. The surface orientation can also be estimated via polar spectra. Furthermore, an efficient classifier could be based directly on the new-developed feature generators ***gradient spectrum*** and ***albedo spectrum*** as they hold sufficient information on the surface topology and orientation.

- An important contribution of this thesis is the development of a complete classification scheme to reduce the effect of surface orientation changes and the effect of surface shadow on classifier accuracy. A simple strategy of ***photometric stereo using four light sources*** is therefore developed. With regarding to the classification design, a new classification scheme using ***2D feature space comparison*** is finally developed to achieve the better classification results.

1.4. Organisation of This Thesis

Chapter 2 provides a survey of research into the rotation invariant texture classification, which includes texture feature measurement, image rotation invariant features and surface rotation invariant features. We note that there are few methods in which the effect of changing illumination conditions are taken into account. In *Chapter 3* we present a short review of reflection and illumination models from surface to image. Thereafter, Kube and Pentland's surface model [Kube88], a linear Lambertian model, is identified and investigated in terms of its frequency domain response, directional filtering effect, non-linear terms and shadowing. We also demonstrate that surface rotation classification is not equivalent to image rotation classification. Photometric stereo is introduced in *Chapter 4*. It enables us to estimate surface properties rather than image properties using several images of a surface taken from the same viewpoint but under illumination from different directions. The surface derivatives obtained by photometric stereo are also examined in *Chapter 5*.

Chapter 6 proposes an algorithm for rotation invariant texture classification using polar spectra and gradient spectra obtained using photometric stereo. The surface partial derivatives obtained by a simple solution of three-image photometric stereo are combined in the frequency domain in such a way as to remove the directional artefacts. The results from both synthetic and real textures show that a rotation of the surface produces a corresponding rotation of its gradient spectrum. We note that the nature of gradient spectrum provides very useful information relating to the type of surface structure and the predominant orientation of the surface texture. Thus the surface orientation can be estimated via their polar spectra. In *Chapter 7*, we design and carry out the experimental work using *4* synthetic textures and *30* real textures to test the efficiency of the proposed classification scheme. Since currently existing and publicly available texture databases are not suitable for our tasks, we develop our photometric stereo texture database. After investigating the misclassifications described in *Chapter 7*, we introduce a new classification feature space in *Chapter 8.* The radial spectrum and a new feature generator, albedo spectra are added in order to provide more information on surface texture properties and improve the

classification performance. The problem of shadowing using three-image photometric stereo is considered in *Chapter 9*. We develop a four-image photometric stereo to provide more accurate *3D* surface texture properties in the presence of shadows. At the final stage, the classifications perform on comparison of 2D spectrum.

Finally, in *Chapter 10*, the work of the previous chapters is summarised, and we present the conclusions of the thesis.

CHAPTER 2

Rotation Invariant Texture Classification

The objective of the method presented in this thesis is surface rotation invariant classification of texture. This chapter survey work relevant to this goal. Definition of image texture and surface texture are reviewed, and rotation invariant classification techniques are surveyed.

2.1. What is Texture?

Texture can be seen in many images from multi-spectral remote sensed data to microscopic photography. The term of *texture* is a somewhat misleading term in computer vision, which is not the normal meaning of the word. We recognise texture when we see it but it is very difficult to describe. Despite its importance, there is no unique and precise definition of *texture* in [Pratt78], Cross and Jain [Cross83]. Each texture analysis method characterises image texture in terms of the features it extracts from the image. Therefore, it depends not only on studying the images but also on the goal for which the image texture is used and the features that are extracted from the image.

Despite the lack of a universally agreed definition, all researchers agree on two points [Jain96].

1. There is significant variation in intensity levels between nearby pixels; that is, at the limit of resolution, there is non-homogeneity.

2. Texture has a homogeneous property at some spatial scale larger than the resolution of the image.

2.1.1. Some Definitions of Texture

Texture is an important surface characteristic we use to identify and recognise objects. The texture of an image may be thought as something which describes the characteristic of the intensity surface of the image. Intensity can be measured at resolution of a single pixel, whereas texture can only be perceived from an image region which is large enough. Compared with intensity, texture is more of a *global* property.

- The Longman Dictionary
  something composed of closely interwoven elements or an organisation of constituent particles of a body or substance; and the visual or tactile surface characteristics and appearance of something (e.g. fabric).

- Haralick [Haralick79]
  The image texture we consider is non-figurative and cellular… An image texture is described by the number and types of its (tonal) primitives and the spatial organisation or layout of its (tonal) primitives…

- Faugeras and Pratt [Faugeras80]
  The basic pattern and repetition frequency of a texture sample could be perceptually invisible, although quantitatively present … In the deterministic formulation texture is considered as a basic local pattern that is periodically or quasi-periodically repeated over some area.

- Bovik, Clarke and Geisler [Bovik90]
  an image texture may be defined as a local arrangement of image irradiances projected from a surface patch of perceptually homogeneous irradiances.

- Jain and Karu [Jain96]

  Texture is characterized not only by the grey value at a given pixel, but also by the grey value `pattern' in a neighbourhood surrounding the pixel.

For detailed discussions on what is and what is not texture, see Karu and Jain [Karu96]. For more definitions of texture, see Coggins [Coggins82], Tuceryan and Jain [Tuceryan93].

2.1.2. Texture in Visual Perception

Texture is the visual cue due to the repetition of image patterns, which may be perceived as being directional or non-directional, smooth or rough, coarse or fine, regular or irregular, etc. The following images in *Figure 2. 1* illustrate this. The objective of the problem of texture representation is to reduce the amount of raw data presented by the image, while preserving the information needed for the task.

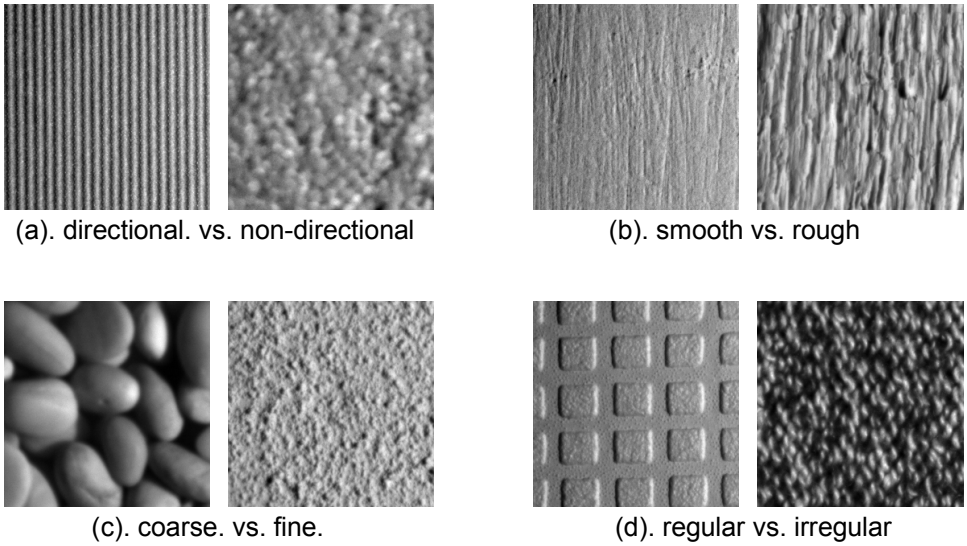

Figure 2. 1 Perception of textures. (a). directional vs. non-directional; (b). smooth vs. rough; (c). coarse vs. fine; and (d). regular vs. irregular.

2.1.3. 3D Surface Relief and Albedo

The term of *image texture*, or simply texture, usually refers to the image of a textured surface. Image texture can arise not only from surface albedo variations (2D) but also from surface height variations (3D). The distinction between 2D texture and 3D texture is explored in recent work by Dana and Nayar *et al* [Dana97], Stavridi and Koenderink [Stavridi97], Leung and Malik [Leung97]. However, there remains an absence of a clear distinction between surface relief (geometry) and surface albedo (reflectance).

Surface relief and albedo information are two important visual cues that provide a relatively large amount of information from surfaces in the scene. Although historically, they share a common role in the scenes, they have been studied separately in computer vision due to the difficulty that both properties present. To avoid any possible confusion, where applicable:

- *Surface relief* is used only to refer to the topology of a 3D physical surface in which only the surface height varies; in contrast,
- the term *surface albedo* refers to surface markings or surface reflectance.

The term *image texture* in this thesis consists of intensity variations in the image plane that are due either to surface relief or to surface albedo variation or a combination of both. An example of extracting surface relief and albedo from a 3D surface is illustrated in *Figure 2. 2*.

(a). 3D Surface

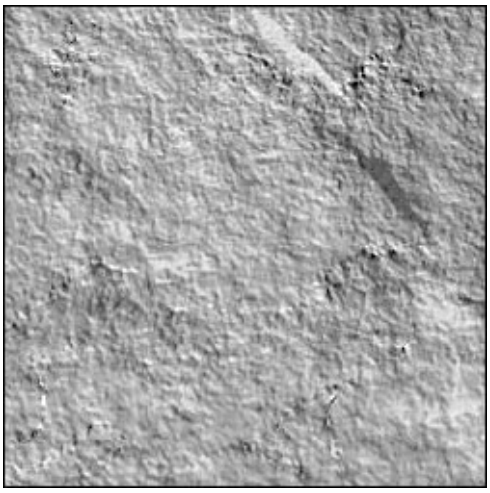

(b). Surface relief

(c). Albedo

Figure 2. 2 Extracting surface relief and albedo from 3D surface

2.2. Texture Features

Texture feature extraction is the procedure of generating descriptions of a textured surface in terms of measurable parameters. The extracted features represent the relevant properties of the surface, and may be sued with a classifier. It is commonly agreed that textural features play a fundamental role in classifying textured surface and texture segmentation.

2.2.1. Three Stages of Texture Classification System

A general texture classification system can be summarised in *Figure 2. 3*.

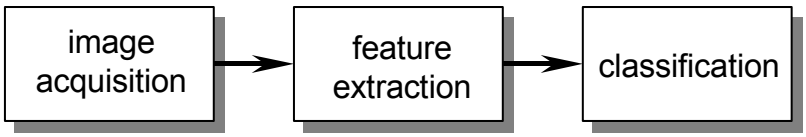

Figure 2. 3 Texture classification system

- ***Image acquisition***

The first and arguably most important stage is that of image acquisition. The application of suitable physical constraints to the observed scene may be used to significantly reduce the complexity of subsequent stage. Careful structuring of the lighting arrangement and camera position may be used to enhance the particular features of interest.

- ***Feature extraction***

Feature extraction is concerned with the quantification of texture characteristics in terms of a collection of descriptors or quantitative feature measurements, often referred to as a feature vector. The choice of appropriate descriptive parameters will radically influence the reliability and effectiveness of subsequent feature qualification through classification [Awcock95].

Texture features and texture analysis methods can be loosely divided into two categories – *statistical* and *structural* [Haralick79].

1. *Statistical* methods define texture in terms of local grey-level statistics which are constant or slowly varying over a textured region. Different textures can be discriminated by comparing the statistics computed over different sub-regions.
2. *Structural* texture models try to determine the primitives which compose the texture. The extracted primitives and their placement rules can be utilised not only to recognise texture but also to synthesise new images with a similar texture.

- ***Texture classification***

Most natural surfaces and naturally occurring patterns exhibit texture. A texture classification system will therefore be a natural part of many computer vision systems. The problem is that, given a texture region, to decide which of a finite number of classes that it belong to?

If the classes have not been defined a priori, the task is referred to as *unsupervised texture classification*. On the other hand, if the classes have already been defined through the use of training textures, then the process is referred to as *supervised texture classification*. In this thesis, only *supervised texture classification* will be considered, and classification accuracy can refer to the percentage of correctly classified texture samples.

2.2.2. Surveys

There are several methods for defining textural features. Each method has its own way to define the features that are used in the classification problem. Many textural features proposed by researchers have been reported in the literature and are widely used in texture analysis. Haralick [Haralick79], Wechsler [Wechsler80], van Gool, Dewaele and Oosterlinck [VanGool85], Tuceryan and Jain [Tuceryan93], Reed and du Buf [Reed93] surveyed the state of the art in texture analysis.

2.2.3. Texture Feature Methods

A wide variety of methods for describing texture features have been proposed. Tuceryan and Jain [Tuceryan93] divided texture analysis methods into four major categories: *statistical*, *geometrical*, *model-based* and *signal processing* methods. The following discussion provides brief introduction to each of the four categories.

- ***Statistical method***

Statistical methods analyse the spatial distribution of grey values, by computing local features at each point in the image, and deriving a set of statistics from the distributions of the local features. With this method, the textures are described by statistical measures. Depending on the number of pixels defining the local feature, the statistical methods can be further classified into first-order (one pixel), second-order (two pixels) and higher-order (three or more pixels) statistics. The performance of these method have been evaluated by Conner and Harlow [Conners80].

One commonly applied and referenced method is the co-occurrence method, introduced by Haralick [Haralick73]. In this method, the relative frequencies of grey level pairs of pixels separated by a distance *d* in the direction θ combined to form a relative displacement vector *(d, θ)*, which is computed and stored in a matrix, referred to as *grey level co-occurrence matrix* (GLCM) **P**. This matrix is used to extract second-order statistical texture features. Haralick suggests *14* features describing the two dimensional probability density function p_{ij}. Four of the most popular commonly used are listed in [Haralick73] [Strand94]. They are *ASM* (Angular Second Moment), *Con* (Contrast), *Cor* (Correlation) and *Ent* (Entropy):

$$ASM = \sum_{i=0}^{N-1}\sum_{j=0}^{N-1} {p_{ij}}^2 \qquad (2.1)$$

$$Con = \sum_{i=0}^{N-1}\sum_{j=0}^{N-1} (i-j)^2 p_{ij} \qquad (2.2)$$

$$Cor = \frac{1}{\sigma_x \sigma_y}\sum_{i=0}^{N-1}\sum_{j=0}^{N-1}\left[(ij)p_{ij} - \mu_x \mu_y\right] \qquad (2.3)$$

$$Ent = \sum_{i=0}^{N-1}\sum_{j=0}^{N-1} p_{ij} \log p_{ij} \qquad (2.4)$$

where μ_x, μ_y, σ_x, and σ_y are the means and the standard deviations of the corresponding distributions; and N is the number of grey levels.

The another most widely used statistical method is the grey level differences method (GLDM) introduced by Weszka et al. [Weszka76]. It estimates the probability density function for differences taken between picture function values.

Other statistical approaches include an autocorrelation function, which has been used for analysing the regularity and coarseness of texture by Kaizer [Kaizer55]. This function evaluates the linear spatial relationships between primitives. The set of autocorrelation coefficients shown below are used as texture features:

$$C(p,q)=\frac{MN}{(M-p)(N-q)}\frac{\sum_{i=1}^{M-p}\sum_{j=1}^{N-q}f(i,j)f(i+p,j+q)}{\sum_{i=1}^{M}\sum_{j=1}^{N}f^2(i,j)} \qquad (2.5)$$

where *p, q* is the positional difference in the *i, j* direction, and *M, N* are image dimensions.

Alternatively, the autocorrelation function can be determined in the frequency domain from the power spectrum method (PSM) of the Fourier transform [Castleman96]. Average values of energy of wedges or rings of Fourier spectrum can be used as features, shown in . Ring features measure coarseness or fineness, whereas wedge features measures directionality.

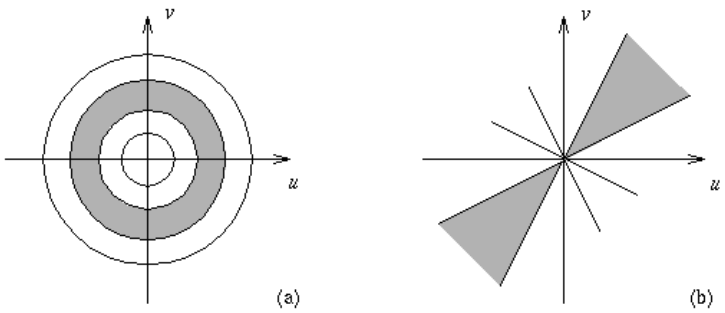

Figure 2. 4 Partitioning of Fourier Spectrum. (a). ring Filter; (b). wedgy filter.

Grey level run length features were introduced by Galloway [Galloway75], they estimate the length of identical runs where an identical run is defined as a set of connected pixels having the same grey level. The element *r(I, j|θ)* of the grey level

run length matrix specifies the number of times a picture contains a run of length j for grey level i in the angle θ direction. Tang [Tang98] demonstrated that textural features extracted from a new run-length matrix can produce improved classification results over traditional run-length techniques.

- ***Geometrical model***

The geometrical models of texture are based on the view that textures are made up of primitives with geometrical properties, In these models, it is common either to compute statistical features, or to identify the placement rules that describe the texture. These structural methods model textures as consisting of primitives that appear in certain patterns. A texture is then defined by these primitives and some displacement rules [Rosenfeld70]. In general, it is difficult to extract these elements from a real textures. Structural methods may also be used for texture synthesis.

The primitives may be extracted by edge detection with a Laplacian-of-Gaussian or difference-of-Gaussian filter [Tuceryan90], by adaptive region extraction [Tomita90], or by mathematical morphology [Matheron75] [Serra73]. Once the primitives have been identified, the analysis is completed either by computing statistics of the primitives (e.g. intensity, area, elongation, and orientation) or by deciphering the placement rule of the elements [Fu82].

The structure and organisation of the primitives can also be presented using Voronoi tessellations [Tuceryan90]. Image edges are an often used primitive element. Davis et al. [Davis81] defined generalised cooccurrence matrices, which describe second-order statistics of edges. Dyer et al. [Dyer80] extended this approach by including the grey levels of the pixels near the edges into the analysis. An alternative to generalised cooccurrence matrices is to look for pairs of edge pixels, which fulfil certain conditions regarding edge magnitude and direction. Hong, Dyer and Rosenfeld [Hong80] assumed that edge pixels form a closed contour, and thus extracted primitives by searching for edge pixels with opposite directions (i.e. they

are assumed to be on the opposite sides of the primitive), followed with a region growing operation. Properties of the primitives (e.g. area and average intensity) were used as texture features.

- ***Model-base methods***

Model-based texture methods try to capture the process that generated the texture. With model-based features, some image model is assumed, its parameters estimated for a subimages, and the model parameters or attributes derived from them , are used as features. There are currently three major model based methods: Markov Random Fields (MRF) by Dubes and Jain [Dubes89], fractals by Pentland [Pentland84], and The multi-resolution autoregressive (AR) features introduced by Mao and Jain [Mao92]. For detailed discussions of image models see Kashyap [Kashyap86], and Chellappa et al. [Chellappa93].

Features extracted from Markov random fields are both descriptive and generative. Thus they have been found to be very useful for texture classification, image segmentation, and other applications by Khotanzad and Kashyap [Khotanzad87]. Random field models analyze spatial variations in two dimensions. Global random field models treat the entire image as a realization of a random field, whereas local random field models assume relationships of intensities in small neighbourhoods. A widely used class of local random field models type are Markov random field models .The Markov Random Fields model for texture assumes that the texture field is stochastic and stationary and satisfied a conditional independence assumption.

The auto-regression model provides a way to use linear estimates of a pixel's grey level, given the grey levels in the neighbourhood containing it. For coarse textures, the coefficients will all be similar. For fine textures, the coefficients will vary widely. Various types of models can be obtained with different neighbourhood system. One-dimensional time-series models, autoregressive (AR), moving-average (MA), and autoregressive-moving-average (ARMA), model statistical relationships by

McCormick & Jayaramamurthy [McCormick74], and Box [Box76]. General class of 2D autoregressive models has been applied for describing textures and subsequent recognition and classification by [Sarkar97]. The power of the auto-regression linear estimator approach is that it is easy to use the estimator in a mode that synthesises texture from any initially given linear estimator. Its weakness it that the textures it can characterise are likely to consist mostly of micro textures.

Mandelbrot [Mandelbrot83] proposed describing images with fractals, a set of self-similar functions characterized by so-called fractal dimension, which is correlated to the perceived roughness of image texture [Pentland84]. In contrast to autoregressive and Markov models, fractals have high power in low frequencies, which enables them to model processes with long periodicities. An interesting property of this model is that fractal dimension is scale invariant. Several methods have been proposed for estimating the fractal dimension of an image [Keller89] [DuBuf90]. Fractal models of surfaces have been employed in image analysis where the objects are rough, irregular, and multi-scale such as cloud, trees and natural textures [Huang90] [Peli90].

- ***Signal processing***

Signal processing methods perform frequency analysis of the textures. This is achieved by using spatial filters or through filtering in the frequency domain. Randen [Randen99] presented a comparative study of filtering for texture classification. Some well known signal processing method are based on Law's Filter [Law80], Gabor filters [Bovik90] [Jain91], and pseudo-Wigner distribution [Jacobson82].

Laws [Law80] observed that certain gradient operators such as Laplacian and Sobel operators accentuated the underlying microstructure of texture within an image. This was the basis for a feature extraction scheme based on a series of pixel impulse response arrays obtained from combinations of 1-D vectors shown in *Figure 2. 5*.

Level	L5 =	[1 4 6 4 1]
Edge	E5 =	[-1 –2 0 2 1]
Spot	S5 =	[-1 0 2 0 –1]
Wave	W5 =	[-1 2 0 –2 1]
Ripple	R5 =	[1 –4 6 –4 1]

Figure 2. 5 Five 1-D arrays identifed by Laws.

For each mask, a texture feature is extracted using the following steps:

- convolve the image with the mask (i.e., position the mask at each pixel, compute the sum of products of mask elements and corresponding pixel values, and then assign the sum to the central pixel).
- compute the average of the squared values at all pixels in the convolved image (except border pixels)
- the average value is saved as the texture feature.

Law's energy filters are tested in texture classification by Pietikainen [Pietikainen82], Greenhill and Davis [Greenhill93], DuBuf [DuBuf90], et al.

Another class of spatial filters are moments, which correspond to filtering the image with a set of spatial masks. The resulting images are then used as texture features. Tuceryan [Tuceryan92] used moment-based features successfully in texture segmentation. Multi-resolution analysis, the so-called wavelet transform, is achieved by using a window function, whose width changes as the frequency. If the window function is Gaussian, the obtained transform is called the Gabor transform [Bovik87].

A two-dimensional Gabor filter is sensitive to a particular frequency and orientation. An example of a Gabor filter in spatial domains is given in *Figure 2. 6.*

Other spatial/spatial-frequency method includes the pseudo-Wigner distribution introduced by Jacobson and Wechsler [Jacobson82]. Texture description with these methods is performed by filtering the image with a bank of filters, each filter having a specific frequency (and orientation). Texture features are then extracted from the

filtered images. For a detailed discussion on spatial/spatial-frequency methods see Reed and Wechsler [Reed90].

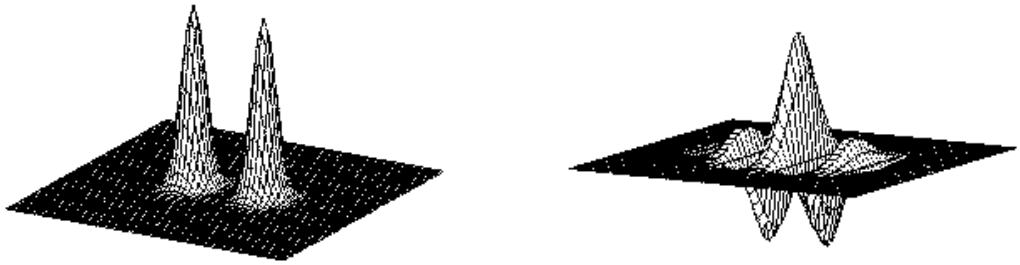

Figure 2. 6 A directional Gabor filter in the frequency (left) and spatial(right) domains

2.3. Image Rotation Invariant Features

2.3.1. Introduction

Our problem associated with texture classification is the task of identifying an isotropic or directional texture at different surface orientations. Unfortunately most techniques assume that the textures are captured from the same viewpoint. This is an unrealistic assumption in the real world. Robust rotation invariant features are the need of the day [Tan95]. In many applications, it is very difficult and impossible to ensure that surfaces captured have the same rotations between each other and such an assumption is rather restrictive in many practical applications. Therefore we consider rotation invariant texture features.

Numerous approaches have been developed that use rotation invariant texture features. A review of invariant texture features can be found on [Porter97] [Fountain98] [Zhang2002a] [Chantler94a]. As it is very difficult to include all the work in such a review of rotation invariant features. Major representative work can be divided into two categories:

- statistical methods;
- model based method and

2.3.2. Statistical Methods

With statistical methods, the stochastic properties of the spatial distribution of grey levels in an image are characterised. Many of the methods are based on the fact that the human visual system uses statistic features for texture discrimination, which are broadly classified into first-order statistics, second-order statistics, and higher-order statistics.

The simplest rotation invariant image statistics are the mean value, variance of the pixel intensities and intensity histogram. However they are very poor in performance, as there is a limited amount of textural information contained within them. More reliable rotation invariant image statistics are moment invariant firstly introduced by Hu [Hu62]. In addition, it is demonstrated by Wang and Healey [Wang98] that Zernike moments perform well in practice to obtain geometric invariance. In their method, Zernike moments of multispectral correlation functions characterise the texture. The classification accuracy rate is reported to be up to 100% for their database which contained seven textures.

The approach was adopted by Haralick [Haralick73] who suggested that the values of grey-level co-occurrence matrix features should be averaged over all directions. The problem with this approach lies that directionality, an important characteristic of the texture, is lost when an isotropic feature is considered. Some work had also been made to extract rotation invariant features from different textures. A better technique would be one which would enable a characterisation of the directionality of the texture, whilst avoiding a dependence upon the texture orientation.

Polarogram introduced by Davis [Davis81] is a polar plot of texture features as a function of orientation. When the image is rotated, the corresponding polarogram is translated by that angle. However the shape and moment features of the polarogram are invariant to rotation. A flat polarogram indicates a texture which is isotropic with

respect to the underlying texture feature. In his experiment by using image rotation, the correct classification rate is obtained up to *90%*. Unfortunately Davis does not however consider the effects of illumination or physical surface rotation in his experiment.

Rotation invariant texture classification is achieved by Alapati and Sanderson [Alapati85] by filtering input images with a set of 2D complex filters which are rotation invariant. Such filters have been known as circular harmonic function filters. The response profile of each circular harmonic filter is polar separable. The algorithm is tested on only four textures from the Brodatz database [Brodatz66] and achieves a classification accuracy of *90%*.

You and Cohen [You93] extend Laws' scheme for rotated and scaled textured images. The method uses standard deviation of pixel grey scale within a specified window computed after convolution with a texture "tuned" mask. Texture energy is a useful measure of texture features, but varies with orientation of the image. A tuned mask on samples overcomes this problem over a range of ration changes to produce a high clustering texture energy term. Although the classification accuracy achieved is *91%* using the Brodatz textures [Brodatz66], the amount of training to tune the masks is significant.

2.3.3. Model Based Methods

In addition to statistical rotation invariant methods, another approach to the problem is to apply a model to the texture image and then to derive a classification algorithm from the model. In most statistically oriented techniques, the image is modelled as a Markov Random Field (MRF) of pixels. In these approaches, the relationships between the intensities of neighbouring pixels are statistically characterised. These are computationally intensive compared to feature based approaches. The challenge is how to achieve rotation invariant schemes. Rotation invariance can be achieved in one of two ways, either by extracting rotation-invariant features or by the appropriate

training of the classifier to make it learn invariant properties. Since general MRF models are inherently dependant on rotation, several methods were introduced to obtain rotation invariance. To identify the class of an arbitrarily rotated sample, the likelihood function associated with the Fourier transform of the image data is maximised with respect to the rotation parameters. This determines the class of the sample as well as the rotation angle the test sample has undergone.

Cohen, Fan and Patel [Cohen91] modelled textures as Gaussian Markov random fields (GMRF) and used the maximum likelihood method to estimate the rotation and scale parameter. Their model essentially parameterises a planar texture model based on second order statistics with three-dimensional spatial parameters. Wu and Wei [Wu96] have use a classical dyadic wavelet decomposition on spiral resampling lattice, the phase and therefore the rotation of the spiral is removed in the decomposition thus enabling rotationally invariant measures to be produced from the resulting subbands, where rotation invariance was achieved by translation invariance. The correct classification rate of *95.1%* is obtained. They explicitly do not consider topological texture or illuminant effects. In addition, the problem of these approaches to rotation invariant texture analysis is their computational complexity (e.g. in [Cohen91] [Chen95]), which may render them impractical. Finally, using a large number of features to describe each texture can lead to an unmanageable size of feature space [Chen95].

Kashyap and Shotanzad [Kashyap86] proposed a circular symmetric auto-regressive (CSAR) model for extraction of rotation invariant texture features. Spatial interaction models such as this represent the grey level values at a pixel as a linear combination of its neighbours plus a noise component. This method is tested on differently oriented textures and a *80- 90%* classification accuracy was achieved. However, this method is computationally inefficient. On the basis of this model Mao and Jain [Mao92] developed a multivariate rotation invariant simultaneous autoregressive (RISAR) model and extended it to a multi-resolution (MR-RISAR) model. However, the training sets in those experiments contain samples of different orientations. The

performance of those features, when applied to samples with different scaling and orientation than those in the training set, is not clear.

A multi-channel filtering technique based on Gabor filters in the frequency domain is used to acquire rotation invariant texture features. Haley and Manjunath [Haley96] propose an isotropic form of the 2D Gabor function. Here the Gabor function is extended in a 2D form in the frequency domain, it is the product of a set of 1D analytic function of radial frequency and a Gaussian function of orientation θ provide a set of filter. Using these features the classification performance is tested on a set of *13* Brodatz textures, and achieved a *96.4%* correct classification rate. In other techniques, features based on Gabor filters are extracted, that allow the formulation of a rotation invariant model [Leung92]. The central step of their approach is to identify the rotation angle of the test sample with respect to a reference orientation, and then transforming the test sample to the reference orientation before classification.

Greenspan et al [Greenspan94] employed a set of oriented filters which are complex exponential functions modulated by Gaussian filter acting on the Laplacian pyramid. Feature vectors are formed from the outputs of the oriented filters, describing the local characteristics of the original images. A DFT of the feature vector in orientation dimension is insensitive to this circular shift of points. This provides the rotation invariant features used in the study. A set of thirty textures from Brodatz is used for validation and the best classification accuracy is *91.5%* for *K*-nearest classifier.

In the earlier studies, the testing was done in such a way that rotated samples of the textures were included in both the training and the classification stage. Recently, Pietikainen et al. [Pietikainen00] suggest that the rotation-invariant algorithm should be able to classify the texture classes even if the training procedure is to run on the texture samples for only one rotation. Ojala et al. [Ojala00] showed that such an approach is much more challenging. We have therefore followed the second principle in this thesis. Recently, Pietikainen and Ojala [Pietikainen00] introduced a set of related measures, including two local centre-symmetric auto-correlation

measures, with linear (SAC) and rank-order versions (SRAC), together with a related covariance measure (SCOV). A distribution-base classification approach is applied to rotation invariant texture classification. A difficult classification problem of fifteen different Brodatz textures and seven rotation angles is used in experiments. It was reported that the best results were achieved with distributions of joint pairs of features.

Note that the accuracy of classification presented in this section are not comparable each other, since they use different texture data as test and training set.

However, it should be noted that the above classifications are performed using image rotations rather actual physical surface rotation. The objective of this thesis is to analysis surface rotation invariant texture classification. We will discuss surface rotation invariant features in the next section.

2.4. Surface Rotation Invariant Features

Leung and Malik present a classification system which is trained on textures that are each imaged under 20 different illumination and orientation conditions [Leung99]. Their textures were obtained from the Columbia-Utrecht Reflectance and Texture Database [Dana99b]. Such natural textures arise from spatial variation of two surface attributes: (1) reflectance and (2) surface normal. The main idea is to construct a vocabulary of prototype tiny surface patches with associated local geometric and photometric properties. They call these 3D *textons*. This generalises the classifier but does not use explicit 3D surface texture information directly.

Dana and Nayar describe a correlation model for 3D surface texture and suggest how this might be used to provide a 3D surface texture feature, correlation length. They present a model which uses surface statistical parameters to predict the change in the correlation length with illumination directions. They do not, however, use this for texture classification purposes [Dana99a].

Varma and Zisserman [Varma02] [Varma02a] present a classification method which is based on the statistical distribution of filter responses in a low dimensional space. They perform their texture classification from a single image acquired with both unknown viewpoint and illumination directions. Therefore, the classification results achieved via clustering are comparable to the results achieved by using the PDF and that representing a texture by its distribution of texture elements (*textons*) is not detrimental to classification. They also demonstrate that it is possible to reliably measure a rotationally invariant co-occurrence orientation statistic.

Smith also uses 3D surface texture information directly [Smith99a]. He uses photometric stereo to acquire surface gradient information and suggests the use of features derived from the gradient space (including attitude, principal orientation, shape factor, and shape distribution) for the "quantitative analysis of repetitive surface textures". He does not go as far as applying this approach to the task of classification of rough surfaces using a conventional classifier - although it would be very interesting to see the results on the detection of surface faults. His method is summarised below in *Figure 2. 7*. We note, however, this still includes a directional filtering effect and suppression of a significant amount of surface information.

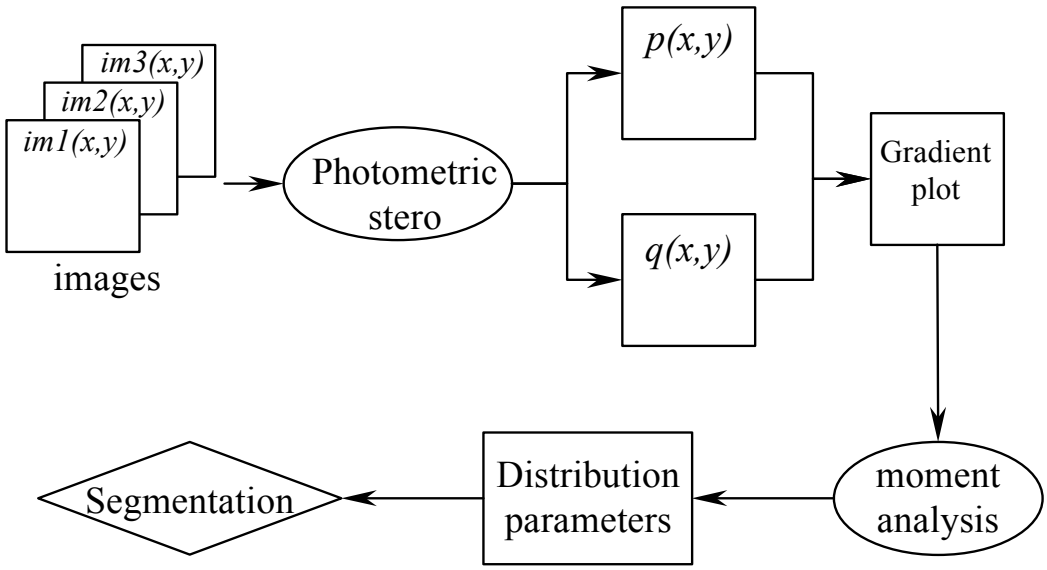

Figure 2. 7 Smith's surface rotation invariant segmentation scheme

McGunnigle and Chantler [McGunnigle97] [McGunnigle98] have developed a novel approach to classification. It uses photometric stereo to determine the surface gradients. Their work is very important as it separately verified that simple three-point photometric methods are effective at separating albedo patterns from surface gradient information. This will enable classification to be performed by comparing texture features computed directly from surface properties rather than image intensity values. Thus they can for instance compare surface relief against surface relief rather than pixel patterns against image data. The scheme was not rotation invariant. Later they proposed another photometric-based system, however, this time the gradient information was directly filtered using isotropic Gabor filters to provide a rotation insensitive scheme [McGunnigle99a].

2.5. Summary

In this chapter, the survey of rotation invariant texture classification is presented. Before we discuss the texture analysis and rotation invariant texture feature, some definitions of texture, surface relief and albedo are given.

Our problem associated with texture classification is the task of identifying an texture at its different surface orientations. Therefore, a general survey of texture feature analysis and particular rotation invariant feature analysis are given respectively. We note that most of rotation invariant feature methods are based on image rotation rather than physically surface rotation, where our main interest exists. Furthermore, most of approaches discussed above assume that images are captured in a frontal-parallel setup so that rotation only occurs around the optical axis, and there are few methods in which the effect of changing illumination conditions are taken into account.

In *Chapter 3*, the process form surface to image is presented, which enables us to estimate surface properties but image properties using photometric stereo in *Chapter 4*. Furthermore the gradient space is introduced in *Chapter 5*. Therefore we may

propose a rotation invariant texture classification scheme based on the features of polar spectra on gradient spectra in *Chapter 6*.

CHAPTER 3

From Surface to Image

3.1. Introduction

Given a light source, a surface, and an observer, a reflectance model describes the intensity and spectral composition of the reflected light reaching the observer. The intensity of the reflected light is determined by the intensity and size of the light source and by the reflecting ability and surface properties of the surface. In this chapter, we will discuss the modelling techniques from 3D surface to 2D image.

First all, we introduce surface roughness models, including height distribution model and slope distribution model, and then the illumination geometry used in this thesis is illustrated. Secondly, various reflection and illumination modelling is under the review. Therefore a simple Lambertian illumination model is presented to describe diffuse reflection. Thirdly, We present the Kube-Pentland's surface model, a linear Lambertian model used in this thesis. A deep investigation about this model is given, with regard to its frequency domain responses, directional filter, effect of non-linear and shadowing. Fourthly, four models of rough synthetic surfaces are given for the purpose of simulation process. Finally, we demonstrate that surface rotation classification is not equivalent to image rotation classification.

3.1.1. Surface Roughness

The manner in which light is reflected by a surface is dependent on the shape characteristics of the surface. In order to analyse the reflection of incident light, we must know the shape of the reflecting surface. In another words, we need a mathematical model of the surface. There are two ways to describe the model of surface and its roughness: the height distribution model and the slope distribution model [Nayar91]. A brief discussion of existing surface roughness models is given below, in order to identify significant limitations in currently applied methods.

- ***Height distribution model***

In height distribution model, the height coordinate of the surface may be expressed as a random function and then the shape of the surface is determined by the probability distribution of the height coordinates. The usual general measures of surface roughness are the standard deviation of the surface heights σ_s (root-mean-square roughness) and average roughness R_{cla} (Centre Line Average CLA), which can be obtained as follows:

$$\sigma_s = \sqrt{\frac{1}{n}\sum_{x=1}^{n}\left[s(x) - \overline{s(x)}\right]^2} \tag{3. 1}$$

$$R_{cla} = \frac{1}{n}\sum_{x=1}^{n}\left|s(x)\right| \tag{3. 2}$$

where $s(x)$ presents the height of a surface at a point x along the profile, $\overline{s(x)}$ is the expectation of $s(x)$ and n is the number of pixels. Hence, they provide measures of the average localised surface deviation about a nominal path. The shape or form of the textural surface cannot be implied from these measures. Indeed textures with differing physical characteristics may result in similar values [Smith99a]. We also have to note that the surface roughness cannot be defined by one of these parameters, either σ_s or R_{cla}, since two surfaces with the same height distribution function may not resemble each other in many cases [Nayar91]. Hence using such a model, it is difficult to derive a reflectance model for arbitrary source and viewer directions.

- ***Slope distribution model***

The slope distribution model is commonly utilised in the analysis of surface reflection as the scattering of light rays has been shown to be dependent on the local slope of the surface and not the local height of the surface. The slope model is therefore more suitable for investigation of the problem of surface reflection. It is useful to think of a surface as a collection of planar micro-facets, as illustrated in *Figure 3. 1*.

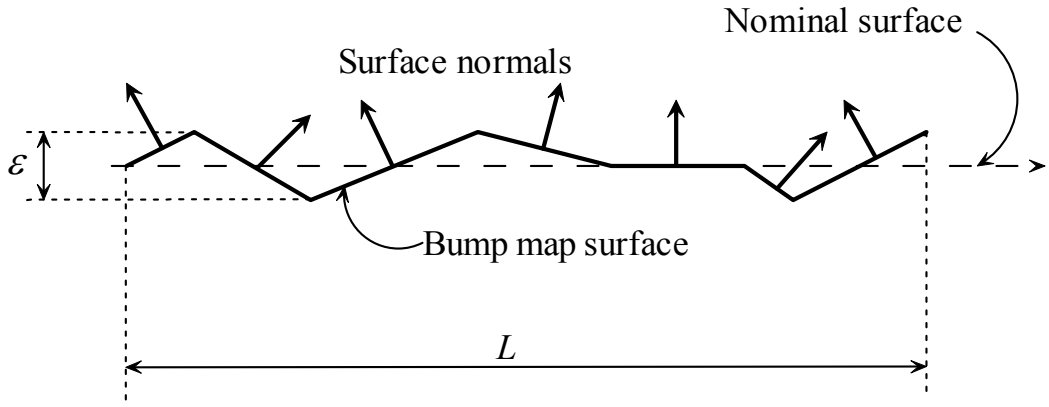

Figure 3. 1 A surface as a collection of planar micro-facets

If a surface is mathematically smooth and each facet area ε is small compared to the area L of the surface patch $(L >> \varepsilon)$, we may use two slope parameters, p_{rms} and q_{rms}, as a measure of roughness. They correspond to the standard deviation of the surface partial derivatives p and q.

$$p_{rms} = \sqrt{\frac{1}{n}\sum_{x=1}^{n}\left(\frac{\partial s(x,y)}{\partial x} - \overline{\frac{\partial s(x,y)}{\partial x}}\right)^2} \tag{3. 3}$$

$$q_{rms} = \sqrt{\frac{1}{n}\sum_{x=1}^{n}\left(\frac{\partial s(x,y)}{\partial y} - \overline{\frac{\partial s(x,y)}{\partial y}}\right)^2} \tag{3. 4}$$

where $\frac{\partial s(x,y)}{\partial x}$ and $\frac{\partial s(x,y)}{\partial y}$ are surface partial derivatives measured along the x and y axes respectively. Hence p_{rms} and q_{rms} can be used to describe surfaces with both isotropic and directional roughness.

3.1.2. Illumination Geometry

Before we consider the reflectance model which defines the relationship between a surface and the corresponding image intensities, we first give the definition of illumination angles related to the light source in *Figure 3. 2*. These definitions are used throughout this thesis. The imaging geometry assumptions are as follows:

- *the test surface* is mounted in the *x-y* plane and is perpendicular to the camera axis (the *z*-axis).
- the test surface is illuminated by *a point source* located at infinity, i.e. the incident vector field is uniform in magnitude and direction over the test area.
- *the tilt angle* τ of illumination is the angle that the projection of the illuminant vector incident onto the test surface plane makes with an axis in that plane.
- *the slant angle* σ is the angle that the illuminant vector makes with a normal to the test surface plane.
- *surface rotation* is measured in the *x-y* plane.
- *orthographic camera* model assumed.

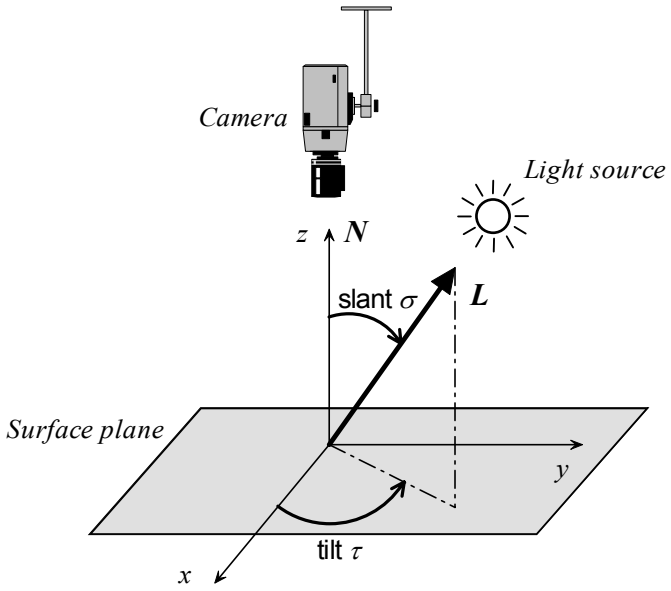

Figure 3. 2 Illumination geometry: the definitions of the tilt angle τ *and the slant angle* σ.

3.1.3. Diffuse and Specular

Reflection from smooth surfaces such as mirrors or a still body of water results in a type of reflection known *specular reflection*. Reflection from rough surfaces such as clothing, paper and an asphalt roadway produces a type of reflection known as *diffuse reflection*. In practice the reflection process may well be a combination of both diffuse and specular components. An example of this is a *spread reflection*, which has a dominant directional component that is partially diffused by surface irregularities. Whether the surface is microscopically rough or smooth has a tremendous impact upon the subsequent reflection of a beam of light. *Figure 3. 3* depicts a beam of light incident upon a surface and the resultant reflection for different types of surfaces. An example of diffuse and specular reflectance for a sphere is shown in *Figure 3. 4*.

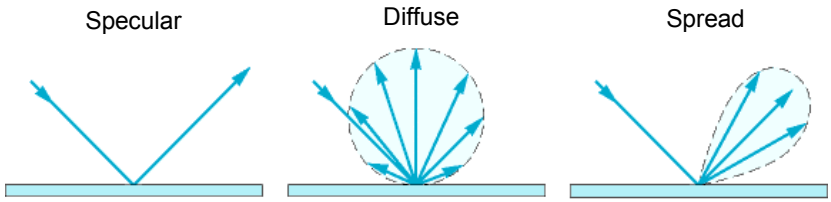

Figure 3. 3 Specular, diffuse and spread reflection from a surface.

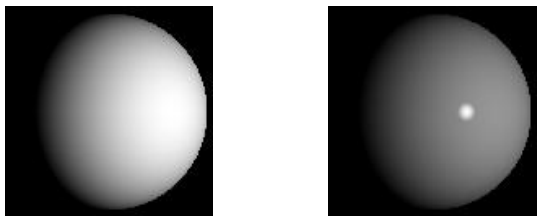

Figure 3. 4 An example of diffuse and specular reflectance.

Several models for the specular component have been proposed. Phong [Phong75] models a reflection lobe which was spread out around the specular direction by using a cosine function raised to a power. Blinn [Blinn77] proposed a model which accounts for off-specular peaks that occur when the incident light is at a grazing

angle. These models are relatively simple with regard to calculation and give reasonably realistic results.

In this thesis, we have to analyse both synthetic and real images, but only the diffuse reflection is taken into account in general. The specular reflection is simply disregarded as noise in most cases except for the method proposed in *Chapter 9*, where a method based on photometric stereo is developed which is similar to the approach by Coleman and Jain [Coleman82].

3.2. Reflection and Illumination modelling

The purpose of reflection models in computer vision is to enable the rendering of a 3D surface in 2D space, such that reality is mimicked to a reasonable level. An image of the surface results from light source reflected from the surface in the direction of the sensor. The intensity at any given point in the image is closely related to the reflectance properties of the corresponding point on the surface. Therefore the prediction or the interpretation of image intensities requires a sound understanding of the various mechanisms involved in the reflection process.

3.2.1. Review of Related Work

Various reflectance models have been developed in the field of computer vision. In general they can be classified into two categories: *the physical models and the geometrical models* in [Nayar91]. The physicals model use electromagnetic wave theory to analyse the reflection of incident light. This is more general than the models based on geometrical optics in that it can describe reflection from smooth to rough surfaces. However, physical models are often inappropriate for use in machine vision as they have functional forms which are difficult to manipulate. On the other hand, geometrical models are derived by analysing the surface and illumination geometry and have simpler functional forms.

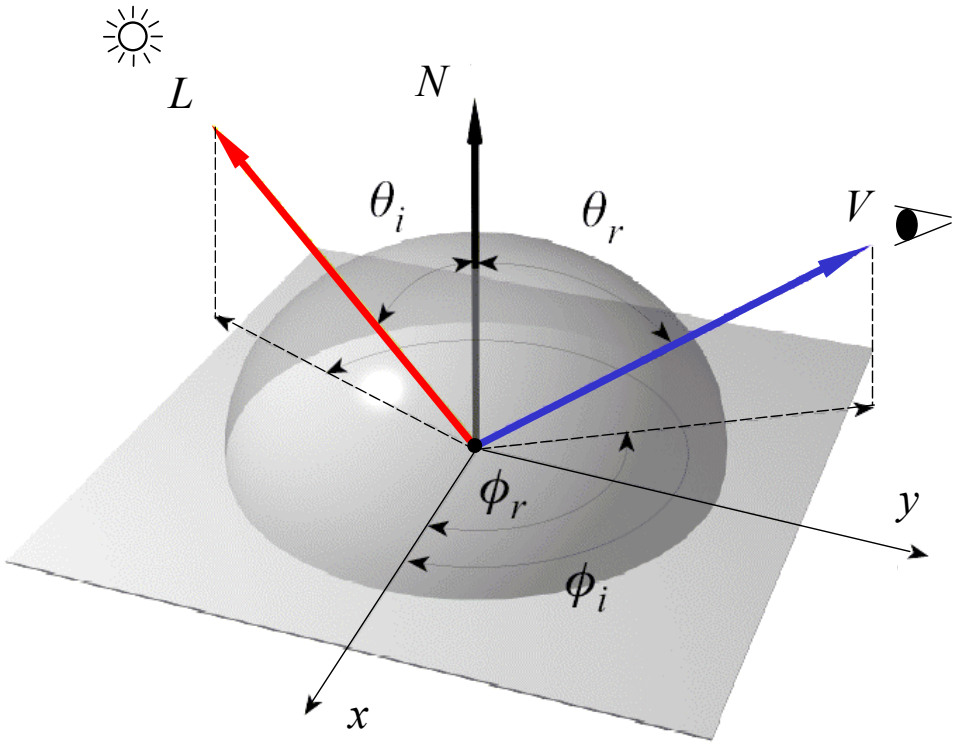

Figure 3. 5 The geometry of light reflection.

The geometry of light reflection at a surface is illustrated in *Figure 3. 5*. Reflection models are generally presented in terms of a *Bidirectional Reflectance Distribution Function (BRDF)*. The BRDF is a general model that relates the energy arriving at a surface from the direction of illumination, to the reflected intensity in the direction of the viewer:

$$BRDF\left(\lambda, \theta_i, \phi_{i,} \theta_{r,} \phi_r\right) \tag{3. 5}$$

Where λ is the wavelength of the incident light, $(\theta_I\ ,\ \phi_i)$ is the direction of the incoming light and $(\theta_r\ ,\ \phi_r)$ is the direction of the reflected light shown in *Figure 3. 5*. The BRDF can be divided into three components: (a) *specular* component, (b) *directional diffuse* component and (c) *uniform diffuse* component demonstrated in *Figure 3. 6*.

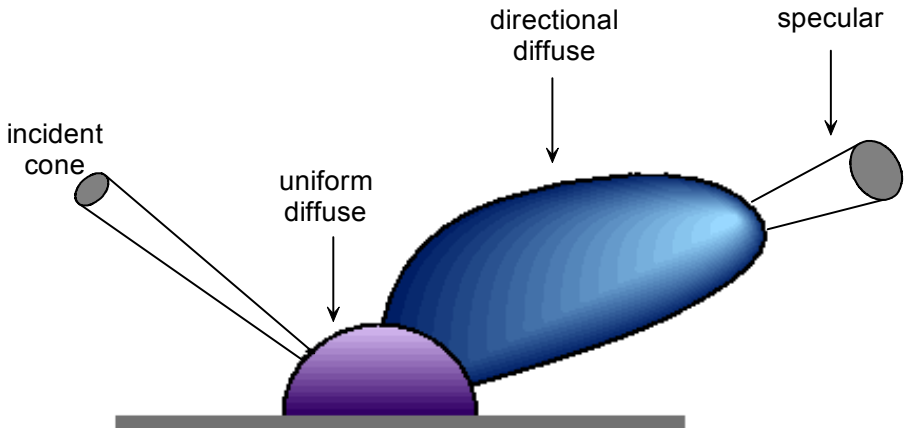

Figure 3. 6 Three components of BRDF: (1). uniform diffuse component; (2). directional diffuse component and (3). specular component.

Over the past twenty years, a variety of BRDF models of increasing sophistication have been proposed. He [He91] proposed a general light reflection model that assumes Gaussian, isotropic rough surface. The model is based on wave optics and accounts for diffraction and scattering effects. The model provides closed-form analytical expressions for the specular, directional diffuse and uniform diffuse components of the BRDF. One paper that does present a method for acquiring BRDFs is [Ward92]. Ward built an imaging reflectometer that uses the two degrees of freedom inherent in a camera imaging system to measure BRDFs and presented an "elliptical Gaussian" model that is capable of modelling certain kinds of anisotropy.

The Lambertian BRDF has enjoyed widespread use for modelling smooth matte surfaces. The Torrance-Sparrow model [Torrance67] for describing surface reflection from rough surfaces has been used extensively in computer vision and graphics. They have appended the Lambertian model to their reflectance model to account for the internal scattering mechanism. The surface is modelled as a collection of planar micro facets and the facet slopes are assumed to be normally distributed. Oren and Nayar [Oren95] derived a reflectance model for matte surfaces which includes local occlusions, shadowing and interreflections. Work by Wolff [Wolff96] developed a simple modification of Lambert's law which accurately accounts for all illumination and viewing directions. Koenderink and van Doorn [Koenderink96] have measured the BRDFs for a variety of surfaces. Their measurements indicate they are fairly well

behaved and can be represented using a relatively small (*50* or less) number of basis BRDFs.

The most commonly used model in computer vision is the Phong reflection model [Phong75], which is a linear combination of specular and diffuse reflection. The specular component is a lobe which spreads out around the specular direction and is modelled by using a cosine function raised to a power. Phong's model is usually given in terms of unit vectors associated with the geometry of the point under consideration:

$$I(n,\Phi) = I_a k_a + I_i k_d (\boldsymbol{L}\cdot\boldsymbol{N}) + I_i k_s (\boldsymbol{R}\cdot\boldsymbol{V})^n \qquad (3.6)$$

where, I_a is the constant intensity of the ambient light;

k_a is the coefficient of ambient reflection of the surface;

I_i is the intensity of the incident light;

k_d is the coefficient of diffuse reflection for the material;

k_s is the coefficient of specular reflection;

Φ is the angle between the mirror vector $\boldsymbol{R}$ and the viewing vector $\boldsymbol{V}$ highlight shown in *Figure 3. 7*, and

n is an index that controls the tightness of the specular lobe.

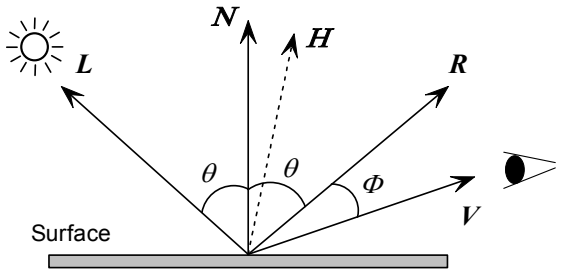

Figure 3. 7 Vectors used in the Phong reflection model.

In Phong's model, the light sources are usually considered as point sources situated infinitely far away. Hence the angle θ between the incident light and the normal to a planar surface is constant over the surface. The viewer is assumed to be positioned at infinity and hence the angle Φ is constant over a planar surface as well. The diffuse and specular terms are modelled as local components only. Shadows are not

considered. The colour of the specular term is assumed to be that of the light source. Empirical results are used to model the distribution of the specular term around the reflection vector. It is also important to note that, unlike Lambert's law, this model has no physical interpretation; it follows nature in an empirical way only.

Estimating the specular component involves the computation of the reflected vector ***R***. This is somewhat computationally expensive and hence this is often replaced by the computation of ***H***, a vector half-way between ***L*** and ***V***. This is often called Blinn's method [Blinn77]. Therefore ***H*** is defined by

$$\boldsymbol{H} = \frac{\boldsymbol{L} + \boldsymbol{V}}{2} \tag{3. 7}$$

The specular term in Phong's model then becomes

$$I_{specular} = I_i k_s \left(\boldsymbol{N} \cdot \boldsymbol{H}\right)^n \tag{3. 8}$$

Cook and Torrance [Cook82] extended this model to account for the spectral composition of highlights – their dependency on material type and the angle of incidence of the light. These advances have a subtle effect on the size and colour of a highlight compared to that obtained from the Phong's model. This model is most successful in rendering shiny metallic-like surfaces

In the next section, we will discuss the Lambertian illumination model which is used in this thesis. The Lambertian illumination model is the simplest type of reflection. It does reasonably well in approximating reflection for a matte surface that looks the same from all directions. It is widely used in the field of computer vision as a simple model.

3.2.2. Lambertian Illumination Model

First of all, consider diffuse – optically rough – surfaces reflecting a portion of the incoming light with radiant intensity uniformly distributed in all directions. A Lambertian surface will look equally bright from any direction for any illumination

direction. In other words, the reflected intensity is independent of the viewing direction. Examples of such surfaces include cotton cloth, many carpets, matte paper and matte paints.

However, the intensity does depend on the light source's orientation relative to the surface. Mathematically, this is represented as the dot product of the surface derivative vector with the illuminant vector, and this forms Lambert's Law.

$$i(x,y) = \rho\lambda(\boldsymbol{N}\cdot\boldsymbol{L}) = \rho\lambda\frac{-p\cos\tau\sin\sigma - q\sin\tau\sin\sigma + \cos\sigma}{\sqrt{p^2+q^2+1}} \tag{3. 9}$$

where

- *i(x,y)* is the image intensity;
- $\boldsymbol{N} = \left(\frac{-p}{\sqrt{p^2+q^2+1}}, \frac{-q}{\sqrt{p^2+q^2+1}}, \frac{1}{\sqrt{p^2+q^2+1}}\right)$ is the unit vector normal to the surface *s(x,y)* at the point *(x,y)*;
- $p = \frac{\partial s(x,y)}{\partial x}$ and $q = \frac{\partial s(x,y)}{\partial y}$ are surface partial derivatives measured along the *x* and *y* axes, respectively;
- $\boldsymbol{L} = (\cos\tau\cdot\sin\sigma,\ \sin\sigma\cdot\sin\tau,\ \cos\sigma)$ is the unit vector towards the light source;
- σ and τ are the illuminant vector's slant and tilt angles defined in *Figure 3. 2*;
- ρ is surface albedo, a material dependent coefficient;
- and λ is the strength of the light source.

To use Lambertian law we have to make the following assumptions:

1) The surface is *ideally diffuse*, where the incident light is equally re-distributed in all directions, and its reflectance function is uniform. The situation where the surface is non-uniform can be dealt with using ρ and λ.
2) The viewer is far away form the surface relative to the size of test surface, so that orthographic projection in the image system can be assumed.
3) Light sources are supposed to be infinity from the surface, such that the light source energy does not depend on the position of the surface. In other words, it assumes that illumination is constant over the whole surface.

4) For a perfect Lambertian model, both *self* and *cast shadows* are ignored, as well as *inter-reflections*.
5) We only consider the angle of incidence θ from *0* to *90* degrees. Greater angles (where the $\boldsymbol{N \cdot L}$ is negative) are blocked by the surface and the reflected energy is *0*. The light is incident on the back of the surface, meaning it is blocked by the object.
6) It is obvious that the Lambertian model cannot describe *specular* reflections, or *highlights*, which occur at places where the direction of direct reflection equals the viewing direction.

The Lambertian model has been shown to describe diffuse reflection reasonably well. It was used by Woodham [Woodham80] to determine surface shape by using the photometric stereo. Coleman and Jain [Coleman82] extend photometric stereo to four light sources, where specular reflections are discarded and estimation of surface shape can be performed by means of diffuse reflections and the Lambertian model. Nayar, Ikeuchi and Kanade [Nayar90] developed the photometric approach which uses a linear combination of Lambertian and an impulse specular component to obtain the shape and reflectance information for a surface.

3.3. Kube-Pentland Surface Model

Kube and Pentland [Kube88] present a spectral model for the formation of the image from an illuminated fractal surface. It is shown that the power spectral density is a function of the illumination angles and therefore extrinsic in nature, while the fractal dimension on the other hand is purely a function of the original surface and is therefore an intrinsic texture measure. Therefore, Kube and Pentland's surface model will be used in this thesis.

3.3.1. Theory

- ***Assumptions***

This theory assumes the following:

1) The surface reflectance is Lambertian;
2) An orthographic camera model;
3) A viewer-centred co-ordinate system, in which the reference plane of the surface is perpendicular to the viewing direction;
4) Surface albedo is constant.
5) A constant illumination vector over the surface;
6) The illumination vector is not close to the viewing direction;
7) Shadows and specularities are two aspects of real illumination not predicted by the model;
8) Inter-reflection is not predicted too.
9) The surface slope angles are small and the surface is smoothed sufficiently for it to be differentiable.

- ***Kube's linear reflectance model***

Kube and Pentland's model predicts that the intensity will approximate a linear combination of the surface derivatives. Now we recall the Lambertian reflectance model in equation *(3. 9)*, where the image *i(x,y)* can then be expressed as a function of the illuminant orientation (τ,σ) and the surface derivative fields, *p(x,y)* and *q(x,y)* where $\rho\lambda=1$. This results in a non-linear operation at each facet. Taking the MacLaurin expansion of $1/\sqrt{p^2+q^2+1}$ in the equation *(3. 9)* and yields

$$i(x,y)=\left(-p\cos\tau\sin\sigma-q\sin\tau\sin\sigma+\cos\sigma\right)\left[1-\frac{p^2+q^2}{2!}+\frac{9\left(p^2+q^2\right)^2}{4!}...\right] \qquad (3.\ 10)$$

Using the first three terms forms a linear estimate

$$i(x,y)=-p\cos\tau\sin\sigma-q\sin\tau\sin\sigma+\cos\sigma \qquad (3.\ 11)$$

or

$$I = \begin{bmatrix} -\cos\tau\sin\sigma & -\sin\tau\sin\sigma & \cos\sigma \end{bmatrix} \begin{bmatrix} p \\ q \\ 1 \end{bmatrix} \quad (3.\ 12)$$

where the approximation is reasonable at $p>>p^2$ and $q>>q^2$ (i.e. p and q are small) so that the quadratic and higher order terms can be neglected. The form of Kube's model is optimal in the least squares sense [McGunnigle98]. Chantler reported that the error introduced by this approximation for a slant angle of $15°$ is 3.5% in [Chantler94a]. It is also noted that if the slant angle σ becomes small, $\sin\sigma \approx 0$ and this means that the quadratic terms in equation *(3. 10)* cannot be neglected. Kube therefore further assumes $\sin\sigma > 0.1$, i.e. the illuminant vector $\boldsymbol{L}$ is not within $6°$ of the z axis [Kube88].

3.3.2. Frequency Domain Responses

More specifically, an expression for the spectrum of the image is developed in terms of the surface texture's spectrum and illuminant vectors. We note that since differentiation is a linear operation, equation *(3. 11)* can be transformed into the frequency domain and expressed as a function of the surface magnitude spectrum while discarding the constant term [Chantler94a] [McGunnigle98]:

$$I_m(\omega,\theta) = i.\omega.\sin\sigma.\cos(\theta-\tau).S_m(\omega,\theta) \quad (3.\ 13)$$

where

- $I_m(\omega,\theta)$ is the image magnitude spectrum;
- $S_m(\omega,\theta)$ is the surface magnitude spectrum;
- ω is the angular frequency of the Fourier component;
- θ is its direction with respect to the x-axis;
- i represents a $90°$ phase shift; and
- σ and τ are the illuminant vector's slant and tilt angles

This equation can be divided into three components:

1. the surface response $I_{ms}(\omega,\theta) = [i \cdot \omega \cdot S_m(\omega,\theta)]$;

2. the tilt response $I_{m\tau}(\omega,\theta)=[cos(\theta-\tau)]$; and
3. the slant response $I_{m\sigma}(\omega,\theta)=[sin\sigma]$.

For the purposes of this thesis it is more helpful to express equation *(3. 13)* in terms of the power spectrum:

$$I(\omega,\theta) = \omega^2 \left|\sin\ \sigma\right|^2 \left|\cos(\ \theta - \tau)\right|^2 S_{\varphi}(\omega,\theta) \qquad (3.\ 14)$$

where

- (ω,θ) is the polar form of spatial frequency with $\theta=0°$ being the direction of the *x*-axis;
- $I(\omega,\theta)$ is the image power spectrum, and
- $S_{\varphi}(\omega,\theta)$ is the surface power spectrum of a surface orientated at φ. Note that surface orientation φ and direction of spectrum θ are on the same plane *x*-*y* with respect to the *x*-axis.

This equation contains simple trigonometric terms, which enable the directional effect of illumination to be more easily understood. Since we are interested in surface rotation, we only deal with the effects of the $\left|\cos(\theta-\tau)\right|^2$ term, which is a directional filter and is independent of radial frequency ω.

3.3.3. Directional Filter

- ***Surface rotation vs. image rotation.***

If we consider only the directional aspects of equation *(3. 14)* we can see that the image directionality is a product of the illuminant tilt angle τ and the surface directionality. In this way a surface rotation may not be equivalent to image rotation if the illuminant is not also rotated. The directionality in the image of a directional surface is the product of both the surface and illuminant directionalities.

If the surface is an isotopic one, then the surface rotation will have no significant effect on the image directionality as long as the illuminant direction is held constant.

On the other hand, if the surface is a directional one, the surface rotation will alter the imaged texture beyond simple rotation. This means that a rotated directional surface is distinctly different in appearance compared to the unrotated surface. Both of these effects can be seen in *Figure 3. 9*.

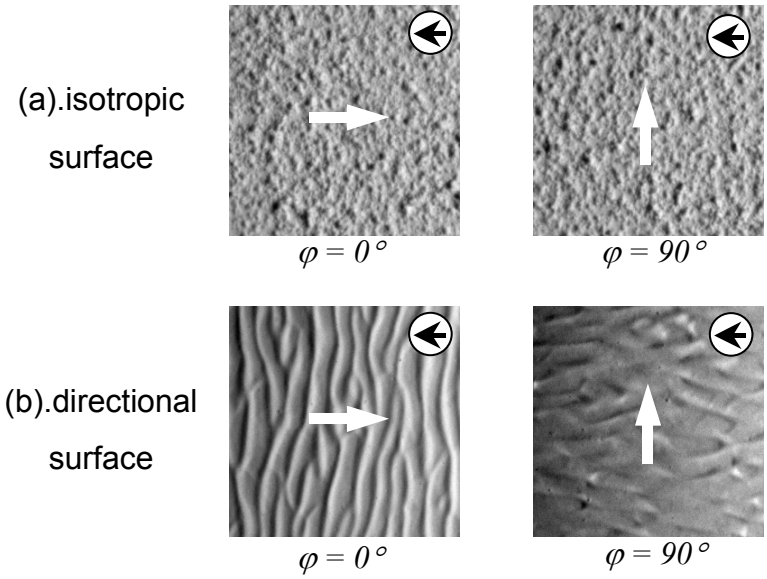

Figure 3. 8 Isotropic surface and directional surface with rotation φ=0° and 90° (indicated by the white arrows in the centre). The illuminant tilt is kept constant at τ=0° (indicated by the black arrows in white circles).

- ***Illumination directional filter.***

In equation *(3. 13)*, the most important feature of Kube's model is the term $I_{m\tau}(\omega,\theta)=[cos(\theta-\tau)]$, which predicts the effect of illumination directional filter in Kube's model. This can be understood by considering *Figure 3. 8.* We may see that, for an isotropic surface, image directionality is only due to the directional effect of the illuminant. Therefore, changing the illuminant directions causes a change in the direction of energy in the corresponding power spectral density (PSD). Furthermore, the highest texture energy lies in the direction of the illuminant tilt angle τ.

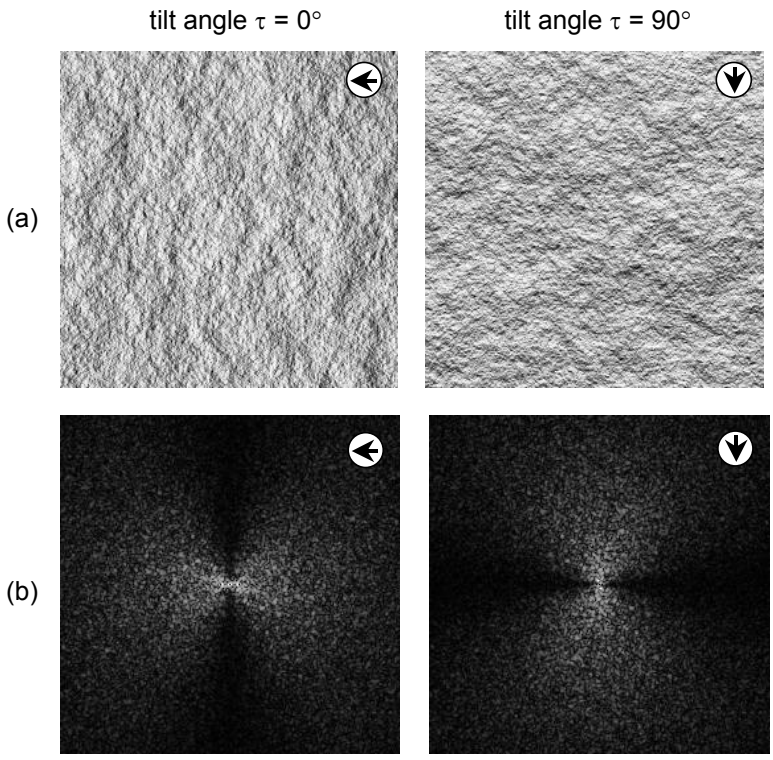

Figure 3. 9 A fractal surface of "rock" rendered by Kube's model (a). Surfaces at two different illumination directions (tilt angle of τ=0° and τ=90°, indicated by the black arrows in white circles); (b). the corresponding power spectral density.

- ***Image variance is not a surface rotation invariant feature for directional surfaces***

There is a problem in the case of directional surfaces, where the image variance will vary with the rotation of the directional surface. Depending on the degree of directionality, the variation in image variance may cause the classifier to fail. In this case, the image variance is not a surface rotation invariant feature for directional surfaces [Chantler94b] [McGunnigle99a].

With regard to the equation *(3. 14)*, the image variance is the integral of the image power spectrum, assuming the mean component to be equal to zero. The following can therefore be obtained:

$$\sigma^2(\varphi) = \int_0^{\infty} \omega^3 \sin^2(\sigma) \cdot 2 \int_0^{\pi} \cos^2(\theta - \tau) \cdot S_{\varphi}(\omega, \theta)\, d\theta\, d\omega \qquad (3.\ 15)$$

If we consider a new axis with the direction of the unidirectional surface texture where $\theta^* = \theta - \varphi$, and then equation *(3. 15)* becomes:

$$\sigma^2(\varphi) = \int_0^{\infty} \omega^3 \sin^2(\sigma) \cdot 2 \int_{-\varphi}^{\pi-\varphi} \cos^2(\theta^* + \varphi - \tau) \cdot S_\varphi(\omega, \theta^*)\, d\theta^*\, d\omega \tag{3. 16}$$

Now if the inner integral part of the equation *(3. 16)* is taken into account:

$$\begin{aligned}
&2 \int_{-\varphi}^{\pi-\varphi} \cos^2(\theta^* + \varphi - \tau) \cdot S_\varphi(\omega, \theta^*)\, d\theta^* \\
&= \int_0^{\pi} \left[1 + \cos(2\theta^* + 2\varphi - 2\tau)\right] \cdot S_\varphi(\omega, \theta^*)\, d\theta^* \\
&= \int_0^{\pi} S_\varphi(\omega, \theta^*)\, d\theta^* + \int_0^{\pi} \cos(2\theta^* + 2\varphi - 2\tau) \cdot S_\varphi(\omega, \theta^*)\, d\theta^* \\
&= \int_0^{\pi} S_\varphi(\omega, \theta)\, d\theta \\
&\quad + \int_0^{\pi} \left[\cos 2\theta \cdot \cos(2\tau - 2\varphi) + \sin 2\theta \cdot \sin(2\tau - 2\varphi)\right] \cdot S_\varphi(\omega, \theta)\, d\theta
\end{aligned} \tag{3. 17}$$

Therefore equation *(3. 15)* can be simply expressed in the form of

$$\begin{aligned}
\sigma^2(\varphi) &= A + \left[B \cos(2\tau - 2\varphi)\right] + \left[C \sin(2\tau - 2\varphi)\right] \\
&= A + \left[D \cos(2\tau + \phi)\right]
\end{aligned} \tag{3. 18}$$

where

$$A = \sin^2(\sigma) \int_0^{\infty} \omega^3 \int_0^{\pi} S_\varphi(\omega, \theta)\, d\theta\, d\omega$$

$$B = \sin^2(\sigma) \int_0^{\infty} \omega^3 \int_0^{\pi} \cos 2\theta \cdot S_\varphi(\omega, \theta)\, d\theta\, d\omega$$

$$C = \sin^2(\sigma) \int_0^{\infty} \omega^3 \int_0^{\pi} \sin 2\theta \cdot S_\varphi(\omega, \theta)\, d\theta\, d\omega$$

$$D = \sqrt{B^2 + C^2}$$

$$\phi = \left[\arctan(C / B)\right] + 2\varphi$$

From equation *(3. 18)*, we may note that

- for an *isotropic surface*, the term D will be equal to zero, and then the image variance $\sigma^2(\varphi)$ will be kept constant;
- on the other hand, for a *directional surface*, the term B will not be equal to zero and therefore image variance $\sigma^2(\varphi)$ will be a raised cosine function of surface orientation.

Figure 3. 10 illustrates the variation of image intensity variance with surface rotation for an isotropic surface *"gr2"* and a directional surface *"wv2"* (shown in *Figure 3. 8* with the constant illumination tilt angle $\tau=0°$). We may note that the variance of image intensity for the directional surface *"wv2"* is certainly not invariant to surface rotation and indeed it is following the cosine term predicted in the model. It is this directional filter effect that makes the outputs of texture features vary with the orientation of a directional surface.

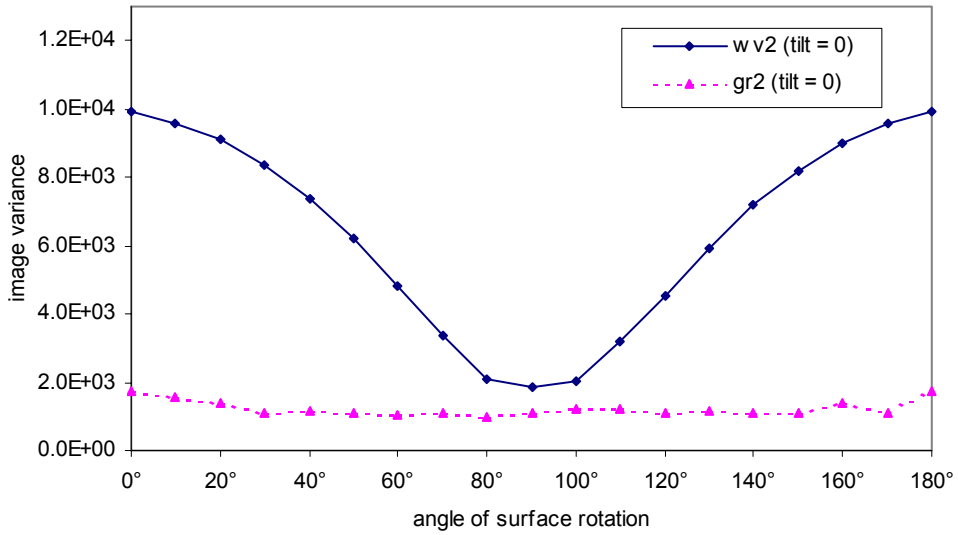

Figure 3. 10 The variation of image intensity variance with surface rotation for an isotropic surface "gr2" and a directional surface "wv2" (illumination tilt angle $\tau=0°$).

3.3.4. Non-linear Effects

In this section, we investigate the non-linear effects occurring in Kube's image model through the use of simulation. One of the reasons for this effect, is that the

quadratic and higher order terms in equation *(3. 10)* are neglected in developing the linear image model in equation *(3. 11)*. Furthermore, the linear image model is based on the assumption that surface height variance is low (i.e. surface slope is less than *15* degrees) and that the slant angle does not approach *0* degrees. These assumptions are necessary to allow the Lambertian model to be linearised [Chantler94].

- ***Surface amplitude variance***

The linear image model assumes a linear relationship between the image variance and surface variance (equation *(3. 13)*). *Figure 3. 11* and *Figure 3. 12* show the effect of increasing the amplitude of a simple sinusoidal surface on images modelled with perfect Lambertian reflection (equation *(3. 9)*) and linear Lambertian reflection given by Kube's model in equation *(3. 11)*. In order to investigate the effect of the non-linear components, we set the illumination slant angle $\sigma=45°$. This angle was chosen because the reflection model assumes a cos^2 relationship between slant angle σ and the reflected intensity, and the model seems to be most linear for a slant angle of around $45°$.

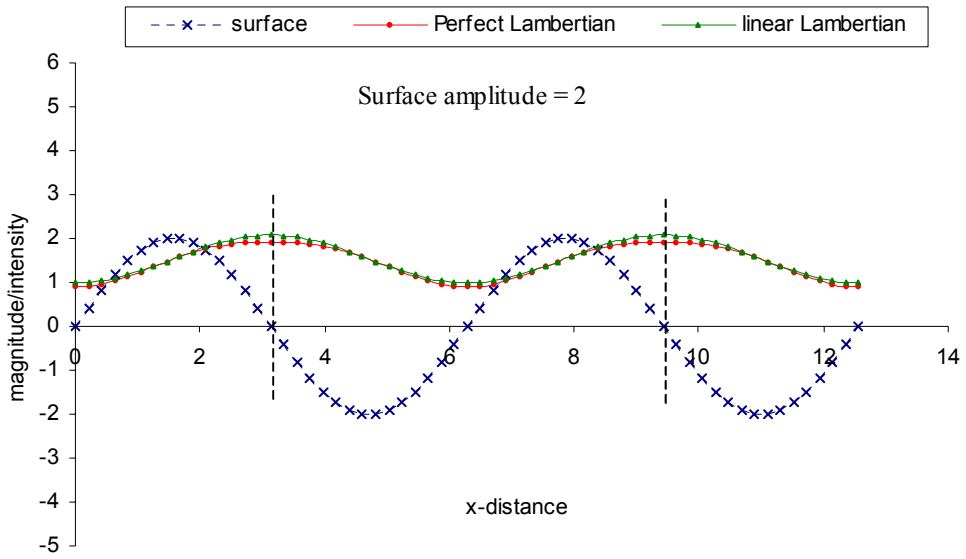

Figure 3. 11 The non-linear effects of a sinusoidal corrugated surface intensity with amplitude=2, predicted by perfect Lambertian model and linear Lambertian model (σ=45°).

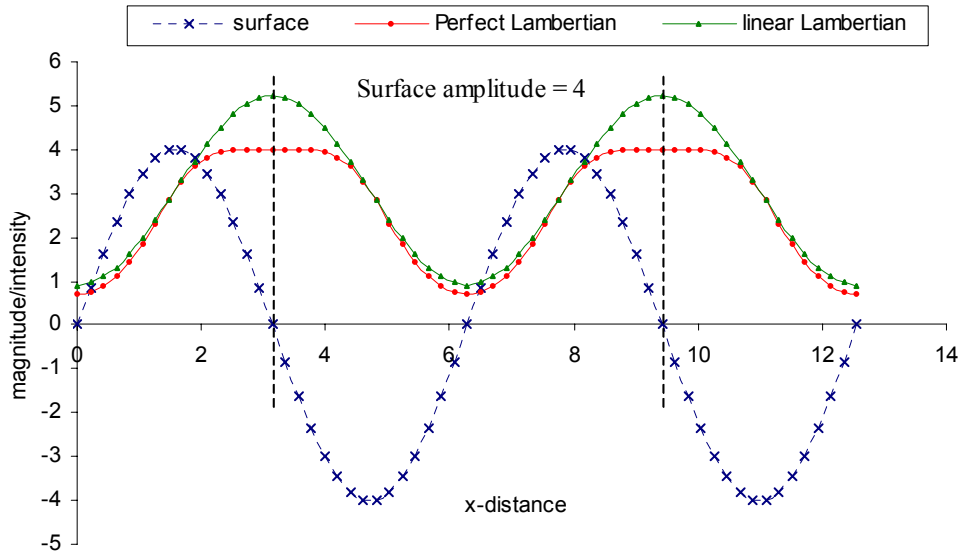

Figure 3. 12 The non-linear effects of a sinusoidal corrugated surface intensity with amplitude=4, predicted by perfect Lambertian model and linear Lambertian model (σ=45°).

In both *Figure 3. 11* and *Figure 3. 12,* it can be seen that the difference or distortion between perfect Lambertian surface and a linear Lambertian surface occurs at the position where the non-linear effects are significant, i.e. where the surface slope

angles approach their maximum values. In addition, increasing the surface amplitude from *2* to *4* accentuates these differences.

Next, we consider the situation where the illumination slant angle σ approaches the extremes i.e. *0°* and *90°*, such that the non-linear effect can be investigated further.

- ***Frequency doubling***

For an illumination slant angle close to *0°*, where the source of illumination is vertically above the surface, the equation *(3. 10)* becomes:

$$i(x,y)=\cos\sigma\left[1-\frac{p^2+q^2}{2!}+\frac{9\left(p^2+q^2\right)^2}{4!}...\right] \tag{3. 19}$$

This shows that the effect of the linear term is reduced and the higher order and quadratic terms now have a greater influence on the image intensity. An example of the frequency doubling effect of a sinusoidal corrugated surface $f(x,y)=\sin\omega x$ is shown in *Figure 3. 13*. It is illuminated at slant angle $\sigma=0°$, therefore the intensity becomes dominated by the "*q*" term while the "*p*" term equals zero. This removes some of the important linear terms and leaves the intensity dependent on the non-linear term in equation *(3. 20)*

$$2\cos^2\omega=1+\cos 2\omega \tag{3. 20}$$

This shows the frequency doubling effect caused by increased distortion from the saturation of the reflection law in the testing at a sinusoidal surface in *Figure 3. 13*.

- ***Clipping***

On the other hand, if the slant angle σ is increased, the reflected intensity of the surface becomes further saturated by distortion as it approaches *90°*. This effect can be seen in *Figure 3. 14* where the surface is illuminated with the slant angles σ of from *40°* to *80°*, respectively. We may see that the *clipping* effects apparently become more severe with increasing the slant angle σ, demonstrating the non-linearity in that region.

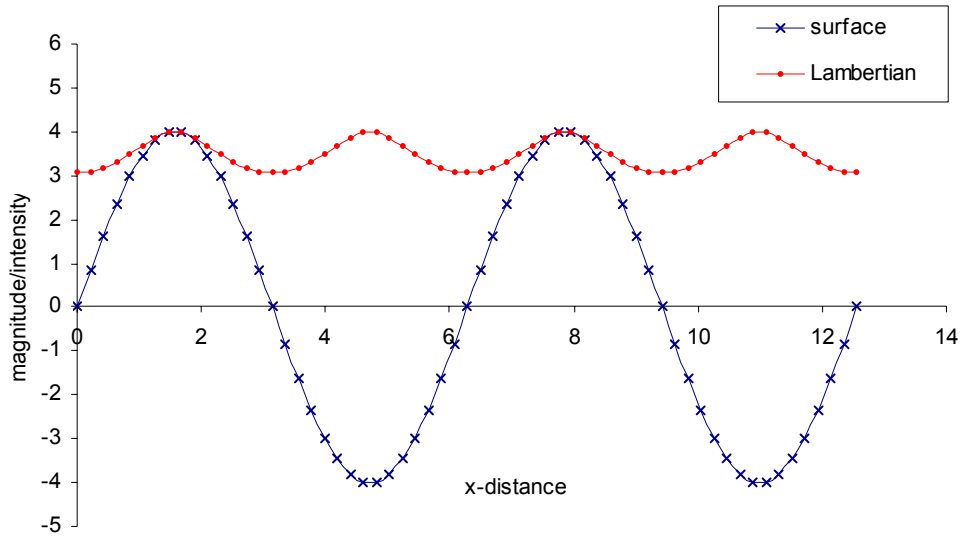

Figure 3. 13 Frequency doubling effect of a sinusoidal corrugated surface illuminated at slant angle σ=0°.

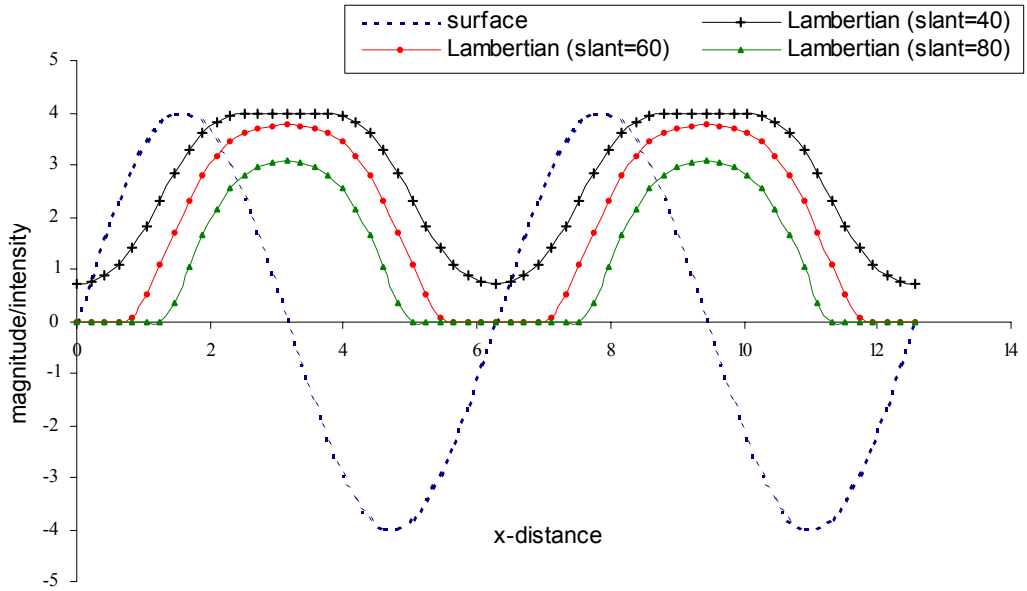

Figure 3. 14 Clipping effect of a sinusoidal corrugated surface illuminated at slant angle σ=40°, 60° and 80°.

3.3.5. Effect of Shadowing

Another non-linear contribution to the model is shadowing. One assumption used in our mathematical equation is Lambertian reflection where shadowing is ignored. Unfortunately in the real world shadows occur. They account for strong disagreement with the Lambertian model when real textures are used. This model is, however, a reasonable approximation of real smooth diffuse reflection given certain constraints. For a rough surface, it is acknowledged that there are significant departures from Lambert's law. Moreover, the departures are most marked for specific viewer and light source directions. The Lambertian model breaks down substantially when the angle between the view vector and the surface normal exceeds *60* degrees [Wollf98]. In this section, we will discuss the effect of shadowing on our model.

- ***Self shadow and cast shadow***

Shadows occur either at places where the path from the light source is blocked or at surfaces which are oriented away from the light source. These effect known as *cast shadow* and *self shadow*, respectively, and illustrated in *Figure 3. 15*. The two kinds of shadows also have quite different properties.

1. The *self shadow* depends on the relation between the surface normal and the lighting direction, and it is observed where the surface does not face the lighting direction.
2. On the other hand, the *cast shadow* depends on the whole 3D shape of the surface, and it is observed where the light is occluded by other objects.

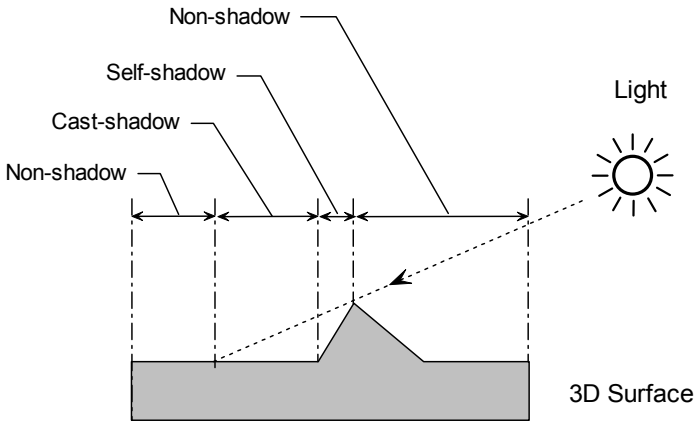

Figure 3. 15 Illustrations of cast shadow and self shadow on a 3D surface.

- ***Kube's model rendered by the effect of shadow***

In *Figure 3. 16*, we simulate sinusoidal surfaces rendered by Kube's model with the effect of shadow. An approximation to shadowing can be simply modelled in the following way: where the shadow occurs the reflected intensity is clipped and set to *0*. We may clearly see that the distortions caused by the shadowing (either self or cast shadow) become more distinctive compared to that without the shadowing effect.

- ***Directional filtering effect reduces with a decrease in the slant angle σ in the case of shadow.***

As discussed in *section 3.3.3* where we considered the directional filtering effect on Kube's model and equation *(3. 19)*, we may note that for a slant angle σ decreasing to near $0°$, the effect of the linear term is reduced compared with that of the square or higher terms. Furthermore the directional filtering effect will be attenuated. *Figure 3. 17* shows the effect of decreasing the slant angle σ from $70°$ to $10°$. It is apparent that the directional filtering effect reduces as the slant angle σ approaches $0°$. In addition, if the surface is rendered with the effect of *shadow* in *Figure 3. 18*, the directional filtering effect with the highest slant angle (i.e. $\sigma = 70°$) is also be attenuated. In this case, the heavy shadow effects the linear approximation of Kube's model, and the majority of the reflected intensity is clipped to *0*.

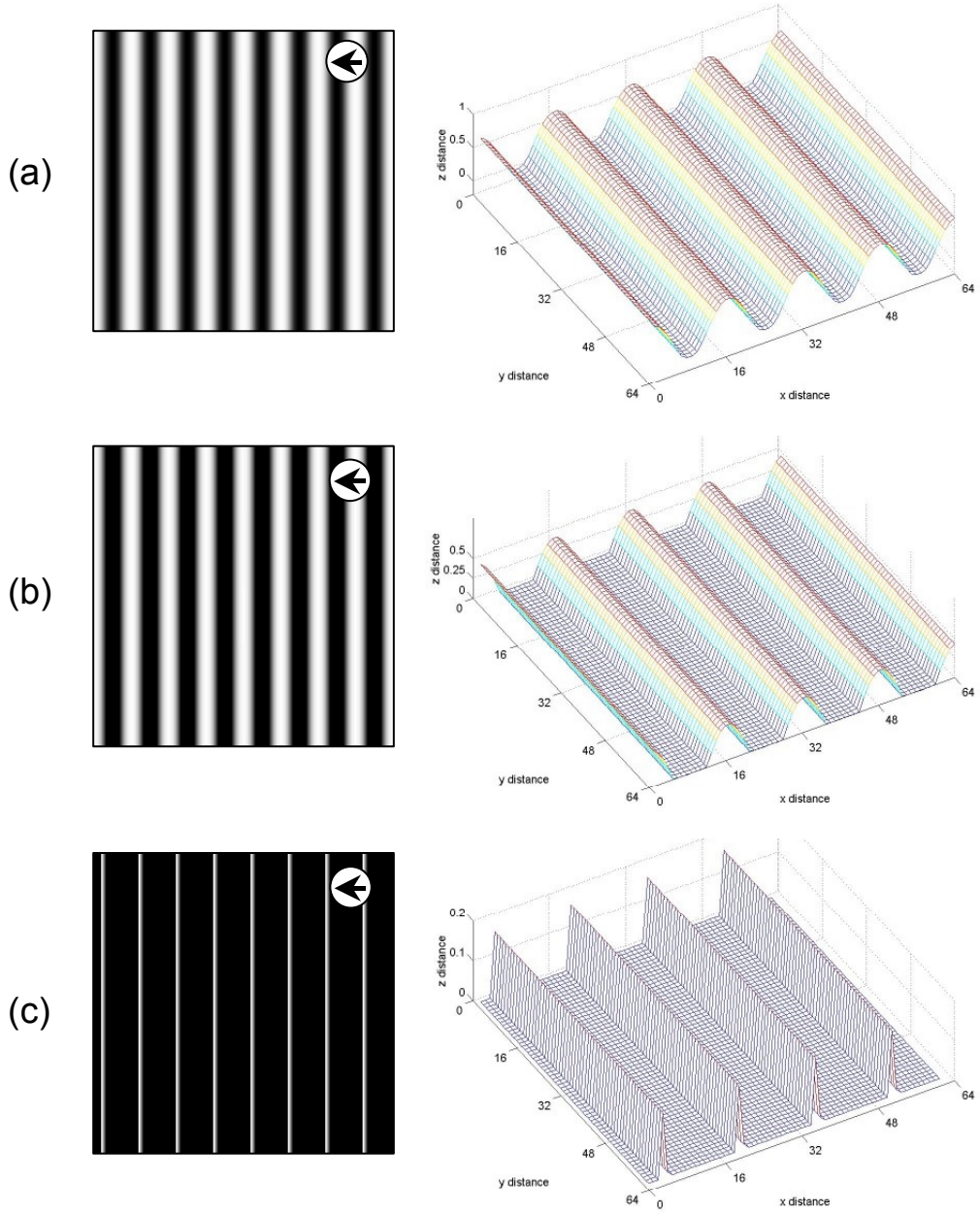

Figure 3. 16 Sinusoidal surfaces rendered by Kube's model (tilt angle τ=0° and slant angle σ=70°) with the effect of shadow. (a). without any shadow; (b). with self shadow only; (c). with both self and cast shadow.

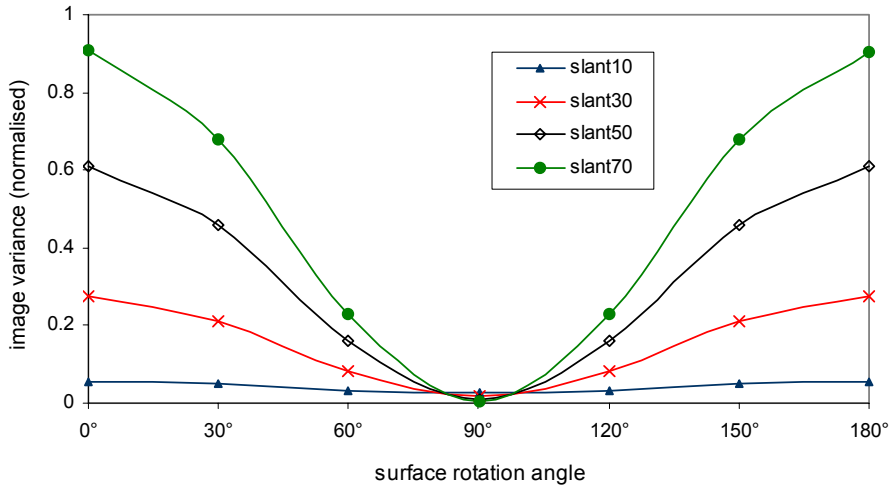

Figure 3. 17 The varation of image intensity variance with surface rotation rendered over a range of illuminant slant angels and without any shadow effect (the surface is sinusoidal one rendered by tilt angle τ=0°).

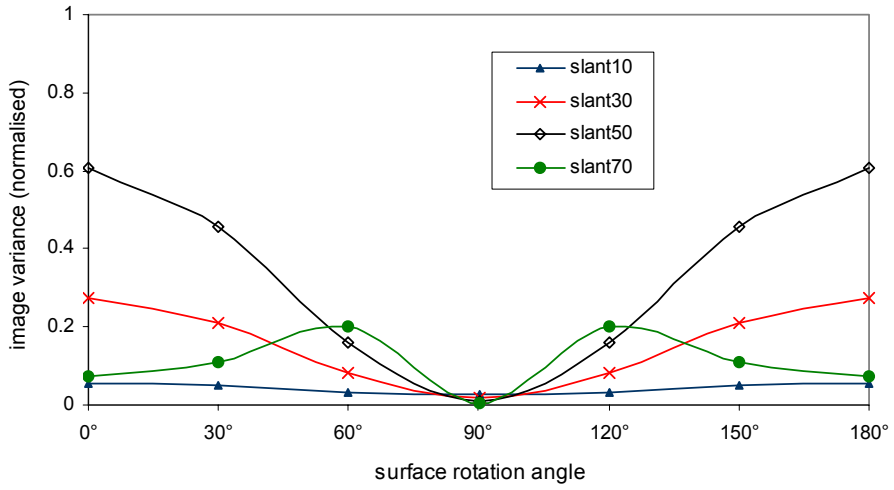

Figure 3. 18 The varation of image intensity variance with surface rotation rendered over a range of illuminant slant angels and with shadow effect (the surface is sinusoidal one rendered by tilt angle τ=0°).

3.3.6. Summary of Kube-Pentland Model

In this section, we presented Kube and Pentland's model which predicts that the intensity approximates a linear combination of the surface derivatives. Furthermore a frequency-domain model of the image of an illuminated three-dimensional texture is

developed in terms of the surface texture's spectrum and illuminant vectors. Both its assumptions and theory are summarised. The linear approximation is reasonable at low surface slope angle.

Firstly, from this theory, the image directionality is a product of the illuminant direction and surface directionality. As a result, a surface rotation is not equivalent to an image rotation if the illuminant is not rotated. It also can be seen that the directional filter characteristics of an image for an isotropic surface are described by the term of $cos(\theta - \tau)$. This predicts that the directionality of an image can be described by a cosine function. In addition, for an isotropic surface, the image variance will be kept constant; while for a directional surface, the image variance is a raised power cosine function of surface rotation. Hence we note that image variance is not a surface rotation invariant feature for a directional surface, which leads to surface-based classification rather than image-based classification.

Secondly, the non-linear effects neglected by the Kube's model are considered. Their effect on surface amplitude variance, frequency doubling and intensity clipping is investigated through the use of simulation. This confirms Kube's linear model must be used on the basis that surface height variance is low and that the slant angle does not approach *0* degrees.

Lastly, the shadowing contribution to the model is shown, as shadowing can not be ignored in the real world.

3.4. Descriptions of Synthetic Surface

In this section, we briefly introduce four models of rough synthetic surfaces, which are used in the whole of this thesis for the purpose of simulation.

If we consider a texture to be a realisation of a two dimensional random process the texture can be described by its mean and its phase. For a *structured surface*, there is

important information in its phase spectrum. However for *unstructured surfaces* the phase spectrum is assumed to be equally distributed. In this thesis, we only deal with unstructured synthetic surfaces so that the phase spectrum is neglected.

In texture analysis, the fractal model is one of the most commonly used: the texture is viewed as the realisation of a random process. To characterise the texture, the fractal dimension has to be estimated. A fractal function is good for modelling 3D real surfaces because many physical processes produce a fractal surface shape. Indeed fractals are widely used as a graphics tool for generating natural-looking shapes. A survey of natural imagery has shown that the 3D fractal surface model furnishes an accurate description of both texture and shaded image regions [Pentland88].

Four surface models have been proposed that are defined in terms of the power spectrum. They are the 2D forms of the fractal [Pentland88], Mulvanney [Mulvanney89], Ogilvey [Sayles78] and sand ripple [Linnett91], where the fractal and Mulvanney surface are isotropic, while the Ogilvey and sand ripple are directional ones. They are defined as follow:

- ***Fractal***

$$S_{Fractal}(\omega) = \frac{k_{rock}}{\omega^3} \tag{3. 21}$$

where $S(\omega)$ is two dimensional power spectrum; ω is the radial frequency and k_{rock} is a constant.

- ***Mulvanney***

$$S_{Mulvanney}(\omega) = k_{malv}\left(\frac{\omega^2}{\omega_c^2}+1\right)^{-3/2} \tag{3. 22}$$

where ω_c is the cut-off frequency and k_{malv} is a constant.

- ***Ogilvey***

$$S_{Ogilvey}(u,v) = \frac{k_{ogil}}{\left(u_c^2+u^2\right)\left(v_c^2+v^2\right)} \tag{3. 23}$$

where u and v are Cartesian frequency coordinates; u_c and v_c are cut-off frequencies in the x and y directions and k_{ogil} is a constant.

- ***Sand ripple*** $$S_{sand}(u,v)=\frac{k_{sand}}{\left[\sqrt{(u-\omega_c)^2+(v-\omega_d)^2}\right]^3} \quad (3.\ 24)$$

where u and v are Cartesian frequency coordinates; ω_c and ω_d are cut-off frequencies in the x and y directions and k_{sand} is a constant.

Images of these surfaces rendered with the Lambertian model are shown in *Figure 3. 19*. Note that in the rest of this thesis, we denote fractal surface as "*rock*", Mulvanney surface as "*malv*", Ogilvey surface as "*ogil*" and sand ripple as "*sand*".

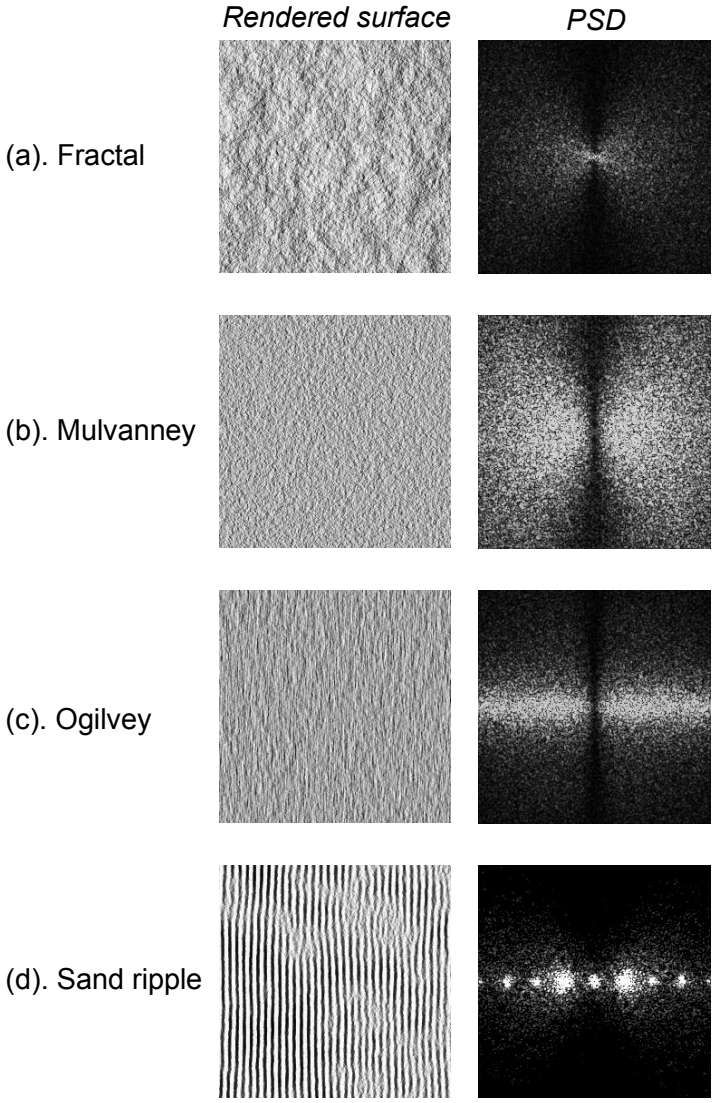

Figure 3. 19 Four synthetic textures rendered with a Lambertian model and their corresponding surface height PSD.

3.5. Image-based Classification vs. Surface-based Classification

Many texture classification schemes have been presented that are invariant to image rotation [Port97a] [Cohen91] [Mao92]. They normally derive their features directly from a single image and are tested using rotated images. If the image texture results solely from albedo variation rather that surface relief or if the illumination is not directional or immediately overhead, then these schemes are surface-rotation invariant as well. However, in many cases *rotation of a textured surface produces images that differ radically* from those provided by pure image rotation (an example can be seen in *Figure 3. 8*). This is mainly due to the directional filtering effect of imaging using side-lighting, described by Kube's frequency model in equation *(3. 13)*. Therefore, a distinction between classifying a surface using measured pixel intensities and classifying on the basis of the reflectance function is apparent.

Kube and Pentland [Kube84] identified and verified a frequency domain model of the image formation process for 3D surface texture. This has shown that the imaging process acts as a directional filter of texture and that changes in illuminant direction can cause catastrophic failure of classifiers [Chantler94b] [McGunnigle98]. Chantler [Chantler94] has used Kube's model to remove the directional effect associated with illumination in his scheme which estimates a quantity that is independent of the orientation of the surface and relative to the illuminant. However, there are two main weaknesses that stem from the linearization of Kube's model. The scheme is firstly unable to deal with the situation where the surface normal is perpendicular to illuminant direction. Secondly, only some classes of surfaces are suitable to the use of a linear model. Based on these reasons, this theme is not sufficiently robust with regard to the rotation of texture. However a new methodology [McGunnigle00] was developed for texture classification based on the direct use of surface gradient and surface reflectance information which used photometric stereo to extract and separate surface relief and albedo information. This enables classification to be performed by comparing texture features computed directly from surface properties rather than image intensity values.

An example of classification accuracy for image rotation and surface rotation is given in *Figure 3. 20.* The statistical classifier is used on a set of isotropic Gabor filters where the features contain no information about the directionality of the texture so that they are rotation insensitive features. The detailed structure of the rotation insensitive classifier can be found in [McGunnigle99a]. The four synthetic test textures used in this experiment are described in the previous section of this chapter. First of all, the image is rotated and then the conventional rotation invariant algorithms are tested. Secondly, the surface is rotated and rendered by Kube's model under the same illuminant condition. From the classification accuracy in *Figure 3. 20*, we may see that the conventional rotation invariant algorithms are not able to deal with the surface rotation compared to those utilising image rotation. In our experiments with data sets at surface rotation $\varphi=0°$, the prominent directionality of the surface is perpendicular to the illuminant direction. Therefore at surface rotation $\varphi=90°$, surface directionality and illuminant direction are the same. This effect makes the discrimination more difficult and the classification accuracy was found to decrease significantly. This again demonstrates that surface rotation is not equivalent to image rotation for 3D surfaces.

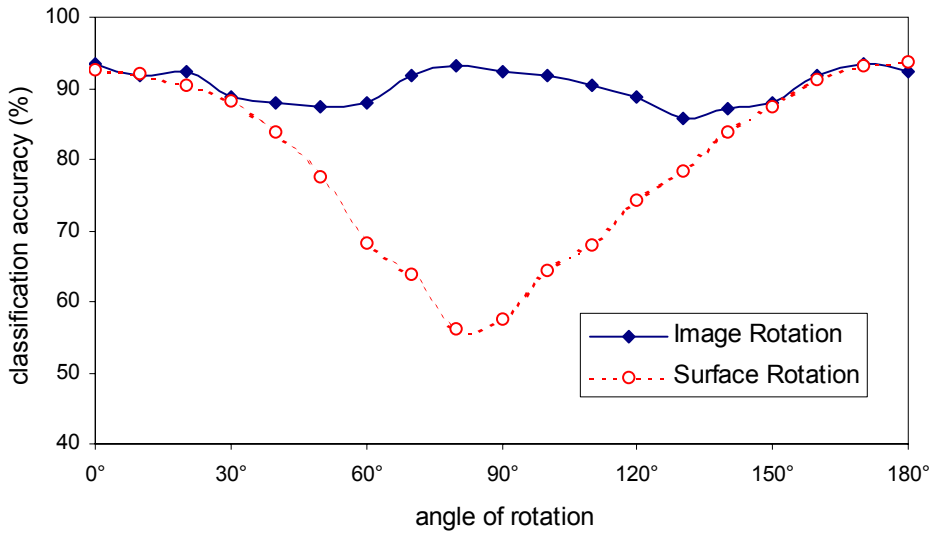

Figure 3. 20 Classification accuracy for image rotation and surface rotation.

3.6. Summary

In this chapter, the process from surface to image is reviewed. First of all, the surface roughness models were discussed, illumination geometry defined and diffuse and specular reflectance were considered. A review of related work on reflection and illumination modelling was given. Afterwards, a simple Lambertian illumination model was selected. It is proven to describe diffuse reflection reasonably well.

We presented Kube's model, a linear Lambertian model, which assumes fixed illumination and viewing geometry and expresses observed intensity as a linear function of surface partial derivatives. We model all the surfaces as Lambertian. Most of the surfaces have moderate slopes and can be accurately rendered using a linear approximation. From this model, one characteristic of rough surface textures is that the appearance of the surface is a function of the illuminant direction as well as of the surface topography. Furthermore, Kube's model functions as a directional filter. In addition, the non-linear effects neglected by the model were investigated. With regard to surface amplitude variance, they are frequency doubling and intensity clipping. Finally the shadowing contribution to the model was also shown.

We briefly introduced four models of rough synthetic surfaces, which are used in the throughout this thesis for the purpose of simulation. They are the 2D forms of the fractal, Mulvanney, Ogilvey and sand ripple.

We demonstrated that the rotation of a directional surface is not equivalent to the rotation of its image. Therefore a surface rotation invariant classifier must take this effect into account. One approach is to classify using the properties of the surface rather than those of the image. If the properties of the surface can be estimated, it may be possible to improve the performance of the classifier. We will introduce the *photometric stereo* technique in the next chapter, which will enable us to directly estimate surface properties from several images illuminated under different lighting sources.

CHAPTER 4

Photometric Stereo

The appearance of a surface in an image results from the effects of illumination, shape and reflectance. Reflectance models have been developed to characterise image radiance with respect to the illumination environment, viewing angles and material properties described in *Chapter 3*. These models provide a local description of reflection mechanisms that can serve as a foundation for appearance representations. *Photometric stereo* approaches utilise reflection models for estimating surface properties from transformations of image intensities that arise from illumination changes [Woodham80]. Furthermore, photometric stereo methods are simple and elegant for Lambertian diffuse models.

4.1. Candidate Surface Recovering Methods

4.1.1. Motivation

The effect of variation in illumination direction on the appearance of textures has already been discussed in previous chapters. As most texture classification schemes depend on the texture's appearance instead of topology, they are more likely to suffer from tilt induced classification error [Chantlter94a]. In the case of rough surface classification, it is therefore better to use surface properties rather than image properties as the basis for our rotation invariant texture classification. In order to do so, an intrinsic characteristic of a surface has to be recovered prior to the classification process.

Given that we are assuming a Lambertian reflectance model, the image intensity of a surface facet at a point *(x, y)* can be determined from the orientation [*p(x,y), q(x,y)*]. On the other hand, a unique surface orientation can not be determined from a single image intensity or radiance value, because there is an infinite number of surface orientations that can give rise to the same value of image intensity. Furthermore, the image intensity has only one degree of freedom and the surface orientation *(p, q)* has two. Therefore, to determine local surface orientation we need additional information. One technique that uses additional information from multiple images is called *photometric stereo*.

As we stated before, classification of surfaces should ideally be carried out on the basis of the texture's surface *s(x, y)* rather than its image *i(x,y)*. Several candidate approaches exist for the recovery of surface topography, including binocular stereo, shape from shading, and photometric stereo.

4.1.2. Binocular Stereo

Binocular stereo is a means of recovering depth by identifying corresponding points in two images taken from different viewpoints. Although binocular stereo has been used successfully in cartography to generate topographic maps of the surface of the Earth, several drawbacks make it unsuitable for this thesis.

1) Additional hardware is necessary, as this method required two cameras.
2) The difficulty in applying binocular stereo arises from reliably determining the corresponding features between two separate images. It is essential that the view position remains fixed during the image acquisition phase, in order to prevent the so called correspondence problem. Implementing the matching algorithm also results in additional computation.
3) The depth of surface is recovered rather than the surface orientation, as illustrated in *Figure 4. 1*. This will introduce noise and artefacts.

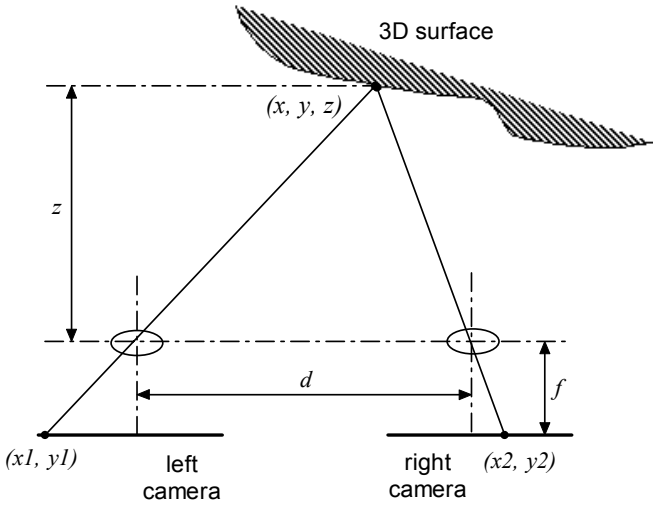

Figure 4. 1 The depth of surface is recovered by binocular stereo.

Given that camera focal length f and camera spacing d. Then the surface depth z can be obtained as follow:

$$z = \frac{d \cdot f}{x1 - x2} \tag{4. 1}$$

4) It is conversely best performed using objects containing discontinuities and shape features, easily corresponded between views. On the other hand, photometric stereo is suited to the objects with uniform surfaces and smooth varying topography [Horn86].

4.1.3. Shape from shading from a single image

The topic of shape from shading (SFS) is concerned with determining the shape of an object solely from the intensity variation in the image plane. Unfortunately, measurements of brightness at a single point in the image only provide one constraint whereas describing surface orientation requires two variables. The problem is ill-posed unless further assumptions are made. It was one of the first areas of study in computer vision and the initial work was carried out by Horn [Horn75] [Horn86] [Horn89].

Assuming a surface with no discontinuities [Horn75], we need knowledge concerning the reflectance properties of the surface that we are trying to describe. In addition the method must have knowledge of the reflectance properties of the surface. In other words, the shading of a surface depends on both how it is illuminated and its reflectance properties. Horn's method relies on a 2-D representation called gradient space [Horn89].

Here is the problem. We have an intensity function *I(x, y)*, the image, and an assumed reflectance function *R(p, q)*. We have:

$$I(x,y) = R(p,q) \tag{4. 2}$$

This is an equation with two unknowns. All we know is that the surface orientation that has produced *I(x, y)* must lie somewhere on a contour of *R(p, q)*. As an infinite number of surface orientations can lie on a single contour, we need further constraints. Horn's method of solving this problem relies on growing a solution by starting at a single point in the image plane $I(x_0, y_0)$ where the surface orientation is known. The method then grows a solution by moving a small amount in the image plane along the contour.

The single-image shape from shading algorithm is still limited even if the exact lighting condition and surface reflectivity are known. One extreme case is that the 3D surface information may be totally lost under certain lighting conditions, and so there is no way to recovery the surface orientation. The problems with extracting shape from shading with a single image are that:

1) It is an approach that relies on having a known reflectance function for a surface.
2) One constraint exists in terms of the mathematical solution for this method. The method relies on *I(x, y)* being continuous. This means there are no discontinuities on the surface, and is therefore unsuitable for 3D texture surface estimation.
3) Another problem is that we really need a starting point to grow a solution. Because the equations that are solved are not over-constrained the method is extremely susceptible to noise in the image.

4.1.4. Photometric stereo

- ***What is photometric stereeo?***

Photometric stereo gives us ability to estimate local surface orientation by using several images of the same surface taken from the same viewpoint but under illumination from different directions (*Figure 4. 2* and *Figure 4. 3*). It was first introduced by Woodham [Woodham80]. The light sources are ideally point sources some distance away in different directions, so that in each case there is a well-defined light source direction from which to measure surface orientation. Therefore, the change of the intensities in the images depends on both local surface orientation and illumination direction.

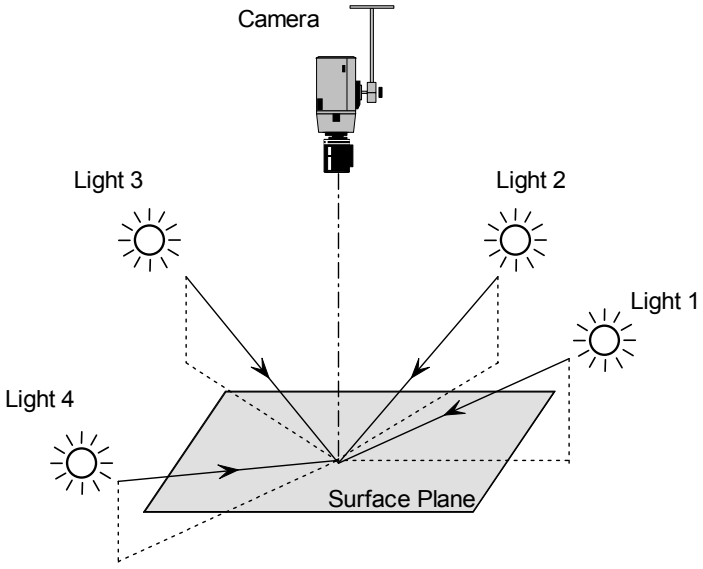

Figure 4. 2 Illustration of photometrc stereo geometry.

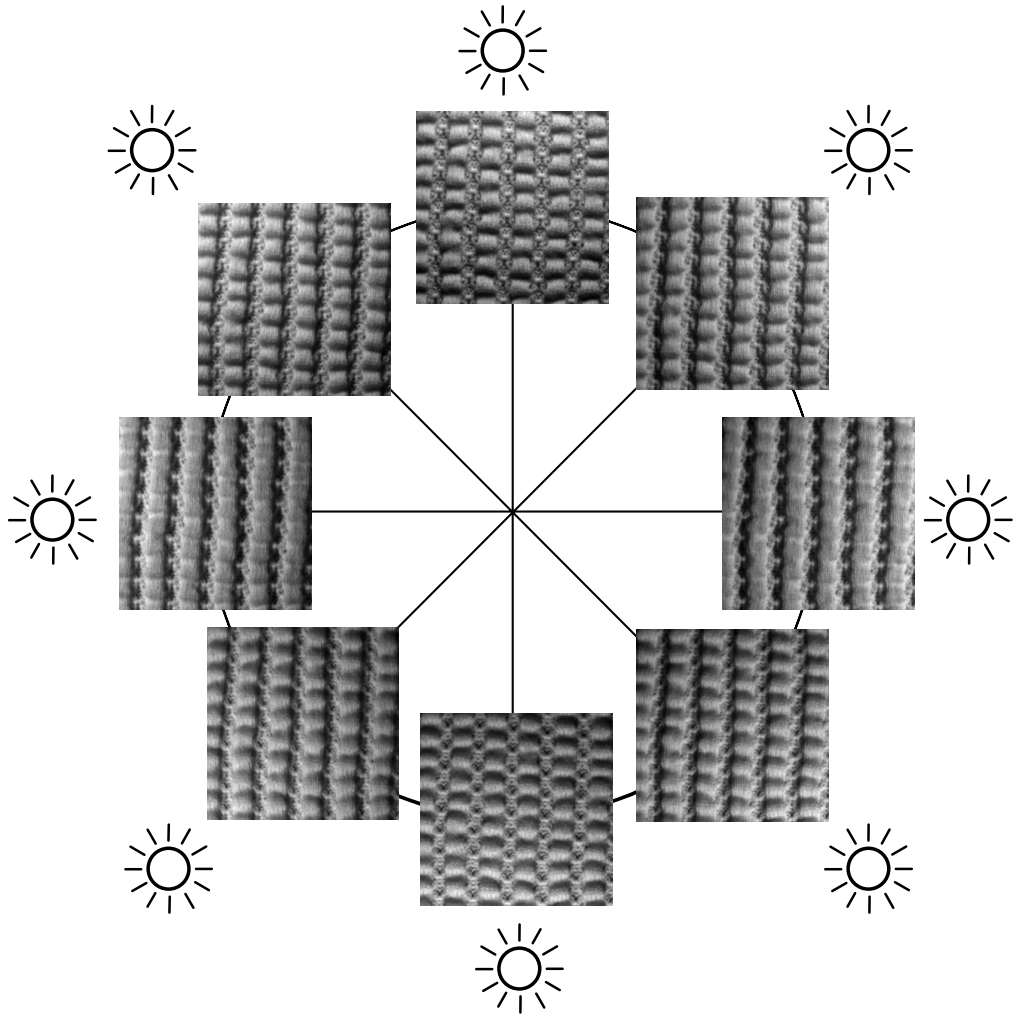

Figure 4. 3 Example of photometric images illuminated by different lighting sources.

- ***Why choose photometric stereo?***

Photometric stereo is a way in which the ill-posed problems in shading from shading can be resolved. It uses several images of the same surface under different illumination directions. The advantages of photometric stereo are:

1) Unlike single image shape from shading algorithms, photometric stereo makes no assumption of the smoothness of the surface (p and q vary continuously over the surface).
2) Furthermore, it requires only additional lighting and can be easily implemented at a reasonable computational cost.
3) Each image brings along its own unique reflectance map, therefore each image will define a unique set of possible orientations for each point.

4) Photometric stereo can recover not only surface orientation *(p, q)*, but also surface albedo ρ [Woodham80].

All of above points make photometric stereo the most suitable candidate relevant to this thesis.

4.2. A General Review of the Development of Photometric Stereo

Woodham [Woodham80] was the first to introduce photometric stereo. He proposed a method which was simple and efficient, but only dealt with Lambertian surfaces and was sensitive to noise. In his method, surface gradient can be solved by using two photometric images, assuming that the surface albedo is already known for each point on surface.

To determine local surface orientation, we need additional information. The simplest approach is to take two images which are of the same surface scene but with different light sources. Therefore we obtain two values of image intensity, $I_1(x, y)$ and $I_2(x, y)$ at each point *(x, y)*. In general, the image intensity values of each light source correspond to two points on the reflectance map, as follow

$$I_1(x,y) = R_1(p,q) \quad \text{and} \quad I_2(x,y) = R_2(p,q) \tag{4. 3}$$

Thus we can determine the surface normal parameters from two images. Defining the two light source vectors as $[p_1, q_1, -1]$ and $[p_2, q_2, -1]$, and equations *(4. 3)* as linear and independent, there will be a unique solution for p and q [Horn86] shown as follow:

$$p = \frac{\left(I_1^2 r_1 - 1\right)q_2 - \left(I_2^2 r_2 - 1\right)q_1}{p_1 q_2 - q_1 p_2} \tag{4. 4}$$

$$q = \frac{\left(I_2^2 r_2 - 1\right)p_1 - \left(I_1^2 r_1 - 1\right)p_2}{p_1 q_2 - q_1 p_2} \tag{4. 5}$$

where provided $p_1 / q_1 \neq p_2 / q_2$; $r_1 = \sqrt{1 + p_1^2 + q_1^2}$ and $r_2 = \sqrt{1 + p_2^2 + q_2^2}$. This gives a unique solution for surface orientation at all points in the image.

If the equations *(4. 3)* are non-linear, there are either no solutions or several solutions. In the case of a Lambertian reflectance function, we have to introduce another image to remove such ambiguities. This image enables us to estimate another surface parameter, *albedo*. It is especially useful in some cases where a surface is not uniform in its reflectance properties.

Lee and Kou [Lee93] were the first ones to introduce parallel and cascade photometric stereo for more accurate surface reconstruction. Parallel photometric stereo combined all of the photometric images together in order to produce the best estimation of the surface. Cascade would take the images, one after another, in a cascading manner. Compared with the conventional photometric stereo method, their iterative method has two major advantages. Firstly, this method determines surface heights directly but surface orientation as the conventional photometric stereo, therefore the integrability problem does not arise in this method. Second, this method is a global method that minimises the intensity errors over all points so that it is insensitive to noise. However, our task is to estimate the surface orientation rather than surface heights.

Cho and Minamitani [Cho93] have applied photometric stereo with three point light sources to recover textured and/or specular surfaces in closed environments like the gastric tract. Their concern was to reduce three-dimensional reconstruction errors due to specularities. Specular reflection produces incorrect surface normal by elevating the image intensity. Facets with estimated reflectivities greater than two standard deviations above the distribution mean are classified as being specular. Therefore they readjusted the pixel with greatest intensity by re-scaling with a modified reflectivity. In that way, the 3-D reconstruction errors may be reduced.

Iwahori and Woodham [Iwahori95] used principal components analysis (PCA) to extract a reduced dimensionality subspace from many more than the theoretical

minimum number of images required. It applied two neural networks that were trained on a calibration sphere. The first one maps image irradiance to surface normal and estimates the surface derivatives, whereas the second one takes these estimates and forms an estimate of the intensity for the facet. The comparison yields a confidence estimate.

Kay and Caelli [Kay95] not only use photometric stereo to estimate the surface normal but also the roughness parameters associated with the Torrance-Sparrow (TS) reflectance model. They assume the reflectance map is a simplified Torrance-Sparrow map with additional Lambertian and mirror-like specular terms. No smoothness or regularization assumptions need be made. The basic approach they use is to apply non-linear regression techniques to photometric stereo. It is noted that in this thesis we only take account into diffuse Lambertian reflectance model, and both glossy specular and mirror specular factors are ignored.

McGunnigle [McGunnigle98] introduces a simple photometric stereo scheme which only considers a Lambertian reflectance model, where the self and cast shadow as well as inter-reflections are ignored. Three images at tilt angle of $90°$ increments are captured and the linear functions mapping surface partial derivatives to image intensity are required. Furthermore his approach does not require albedo information. He suggests using his scheme to provide a first estimate for an iterative procedure. This is in fact a simplified version of Woodham's scheme in which the illumination directions are chosen in order to simplify the mathematics.

Another more difficult problem is that of estimating a surface with an unknown reflectance map. Nayar [Nayar90] used a linear combination of Lambertian and an impulse specular component. He used distributed light sources for photometric stereo of surfaces whose reflection is a sum of specular and Lambertian components.

A technique that separates the effects of geometry and surface coloration/texture in "*tri-luminal*" environment is developed by Angelopoulou and Williams [Angelopoulou99]. Precision calibration of the illumination is not required. They

demonstrate that the tri-luminal environment supports a broad range of analysis techniques: Differential geometric properties of smooth surfaces can be calculated directly from photometric data, albedo can be isolated and geometry-based recognition can be performed without recovering surfaces. Avoiding the recovery step increases both speed and robustness.

Belhumeur *et al* show that the set of images produced by arbitrary illumination of an object is the same as the set of images produced by what they call a "generalized bas-relief transformation" of the object [Belhumeur99]. A generalized bas-relief transformation is a transformation of both the surface shape and the surface albedo for an arbitrary Lambertian surface. While it has been thought that photometric stereo with unknown light source direction could be solved by first estimating the light source directions and then estimating the surface structure, they have shown that these estimates are coupled through an unsolvable generalized bas-relief transformation.

Other robust methods using photometric stereo with more images are reviewed in the latter *section 4.4*.

4.3. Three Image Based Photometric Stereo

In this section, we propose a simple three-image-based photometric stereo solution.

4.3.1. Three Photometric Images

We use three photometric images to recover the local surface orientation and albedo information for a Lambertian surface where the shadow effect is absent. The geometry of the camera / lighting setup can be seen in *Figure 4. 4*. Note that, during image capture, we keep the slant angle constant (σ=*50°*). Furthermore, we apply the same assumptions described in *section 3.3.1*, that is that the surface is parallel to the

image plane of the camera and approximately flat; the light source and camera are located far away from the test sample; and the illumination direction and viewing direction are uniform at each point on the surface.

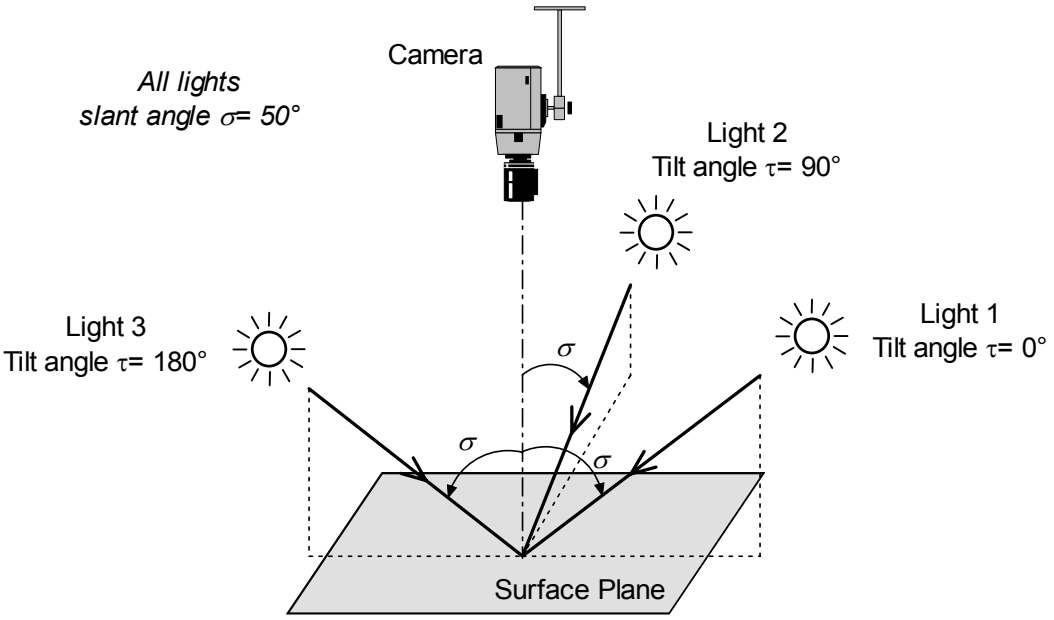

Figure 4. 4 Geometry of three-image based photometric stereo.

4.3.2. Equations of Photometric Stereo

We transfer the Lambertian surface model denoted in *section 3.2.2* into matrix format. Therefore the intensity of pixel in an image can be expressed as follow

$$i_I(x,y) = \rho\left(\mathbf{L_1} \cdot \mathbf{N}\right) \tag{4. 6}$$

where

- $i_I(x, y)$ is image intensity at the point (x, y);
- $\boldsymbol{N} = \dfrac{(p,q,-1)^T}{\sqrt{p^2+q^2+1}} = \left(\dfrac{-p}{\sqrt{p^2+q^2+1}}, \dfrac{-q}{\sqrt{p^2+q^2+1}}, \dfrac{1}{\sqrt{p^2+q^2+1}}\right)^T$ is a surface normal unit vector to the surface $s(x, y)$ at the point (x, y), and $p = \dfrac{\partial s(x,y)}{\partial x}$ and

$q = \dfrac{\partial s(x,y)}{\partial y}$ are surface partial derivatives measured in the x and y directions, respectively;

- $\mathbf{L_1} = [\ l_{x1}, l_{y1,} l_{z1}\ ]^T$ is a unit illumination vector, which is pointing from the surface towards to the light source;
- ρ is surface albedo at the given point *(x, y)*.

Now we consider three light sources with illumination vectors $\mathbf{L_1}$, $\mathbf{L_2}$ and $\mathbf{L_3}$. The equation *(4. 6)* can be rewritten in matrix form

$$\mathbf{I} = \rho \cdot \mathbf{L} \cdot \mathbf{N} \tag{4. 7}$$

where

- $\mathbf{I} = [\ i_1, i_2, i_3\ ]^T$ is image intensity vector;
- $\mathbf{L} = [\ \mathbf{L_1}, \mathbf{L_2}, \mathbf{L_3}\ ]^T$ is photometric illumination matrix which incorporates the light intensity for each light source.

Provided that all of three illumination vectors $\mathbf{L_1}$, $\mathbf{L_2}$ and $\mathbf{L_3}$ are not lying in the same plane (non-coplanar), then the photometric illumination matrix $\mathbf{L}$ is non-singular and its inverse matrix, $\mathbf{L^{-1}}$ exists and

$$\mathbf{M} = \mathbf{L^{-1}} \cdot \mathbf{I} = \rho \cdot \mathbf{N} \tag{4. 8}$$

where $\mathbf{M} = [\ m_1, m_2, m_3\ ]^T$

Therefore the three image based photometric stereo method can be summarised as follow:

1) For each given point *(x, y)* on the surface, the image intensity vector $\mathbf{I}$ is firstly formed by capturing three images under different illumination directions $\mathbf{L_1}$, $\mathbf{L_2}$ and $\mathbf{L_3}$.
2) The vector $\mathbf{M} = [\ m_1, m_2, m_3\ ]^T$ is obtained by the production of $\mathbf{I}$ and $\mathbf{L^{-1}}$.
3) The *surface gradient components* can be calculated via

$$p = -\frac{m_1}{m_3} \quad \text{and} \quad q = -\frac{m_2}{m_3} \tag{4. 9}$$

4) Finally, the *surface albedo* is recovered by finding the length of vector **M**.

$$\rho = \sqrt{m_1^2 + m_2^2 + m_3^2} \tag{4. 10}$$

Those computation is straightforward in this case, and a unique result is assured.

4.3.3. Separating Gradient and Albedo using Photometric Stereo

An example of the results that can be obtained using this approach is shown below in *Figure 4. 5*.

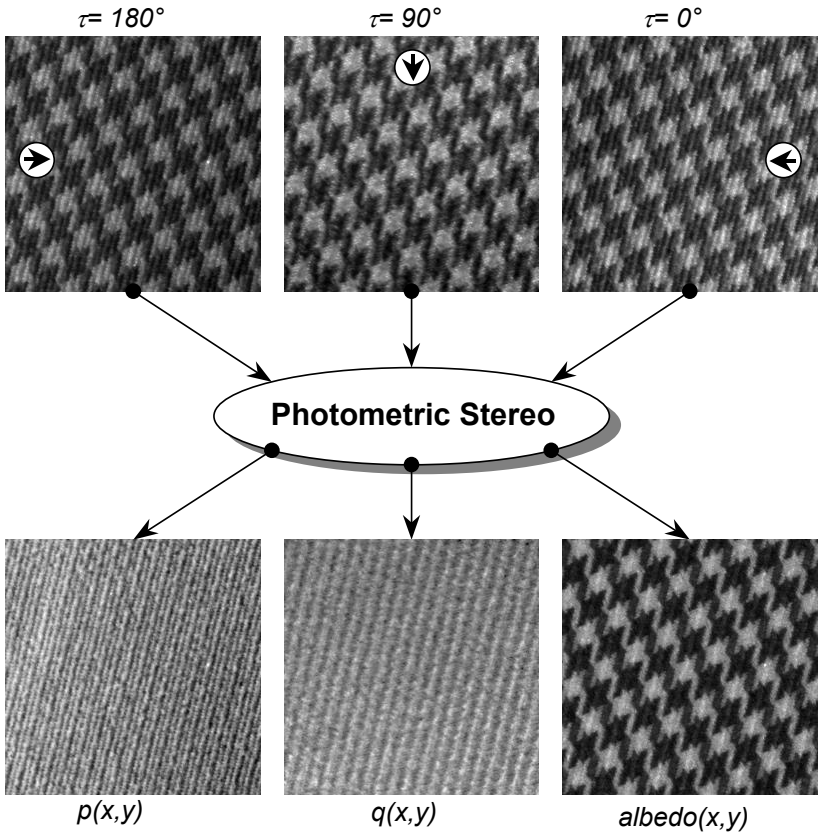

Figure 4. 5 Separating gradient and albedo information using photometric stereo.

4.4. Improvement on Three Image Based Photometric Stereo

There are two well-known problems with the traditional photometric stereo methods:

1) Surfaces are not ideally Lambertian and can contain a *specular* component; and
2) There will be some points that will be in *shadow* for one or more of the images. Therefore, there will not always be the three non-zero values of **I** to use in solving equation *(4. 8)*.

There are many approaches to deal with these problems documented in the computer vision literature.

As stated before, while three photometric images are used to estimate surface orientation and surface albedo, if four or more images are captured using further illumination sources, more information can be obtained. While the concept of photometric stereo is fairly simple, great difficulties arise when considering a realistic illumination model, in particular, a model that can represent diffuse and specular reflection. Only by considering such a model can an accurate representation of a wide range of material properties be achieved.

Ikeuchi [Ikeuchi81] first applied the photometric stereo method to specular surfaces, by using three extended light sources and the reflectance maps for each source in the form of lookup tables. In his research, he used a distributed light source obtained by uneven illumination of a diffusely reflecting planar surface and three input images. This method assumed a known object position and required accurate measurement of reflected brightness.

Coleman and Jain [Coleman82] extended the method and used four-light-source photometric stereo to determine the shape of surfaces that are non-Lambertian. It was based on the assumption that specular highlight areas between images do not overlap; therefore, they used relative deviation to determine the specular source. They proposed to calculate four albedo values based on the four possible combinations of three light sources. For a perfectly Lambertian surface, the four albedo would be identical. However, for surfaces that exhibit some specularities, this

is not the case. Their method reduces the problem to Woodham's photometric stereo solution for three sources. However, they do not recover any specular parameters, only geometric and Lambertian ones.

Compared to Coleman and Jain's method, Tagare and deFigueriredo [Tagare90] do consider Lambertian and glossy specular objects. They show the uniqueness and the completeness of photometric stereo using their m-lobed reflectance maps. They give some results for a synthetic sphere using the reflectance maps of the Torrance-Sparrow model. They used eight light sources to recover the shape of real objects. Their work was continued by Kay and Caelly [Kay95] who investigated the problem of simultaneous estimation of surface normals and surface reflectance parameters from a practical point of view.

Solomon and Ikeuchi [Solomon92] extended Coleman and Jain's method by using four light sources. The shape information is produced directly by three light and four light photometric stereo methods. After they have shape information, statistical segmentation techniques can be applied to determine which pixels are specular and which are non-specular. Then, they can use the specular pixels and shape information, in conjugation with a simplified Torrance-Sparrow reflectance model to determine the surface roughness.

Nayar, Ikeuchi and Kanade [Nayar90] also developed a theory which accounted for specularities. They developed another reflectance model, called a *hybrid reflectance model*, which is the weighted sum of a diffuse lobe represented by a cosine function, and a specular spike, modelled as a delta-function. The relative strength of the specular and diffuse models was not known, and the proposed method could recover not only the local gradient but also the parameters of the reflectance model.

Rushmeier and Taubin [Rushmeier97] designed a system for obtaining bump maps from small sets of images captured under controlled lighting conditions. The bump map capture system complements inexpensive techniques for obtaining complex input data for rendering. The resulting maps can be used to re-render objects without

reconstructing the original geometry. The map can also represent fine scale and self-shadowing geometry that would be difficult to recover from traditional photometric stereo.

Drbohlav and Leonardis [Drbohlav98] presented a global approach to the problem of removing shadows and highlights which is based on photometric image sets. The method exploits the basic properties of Lambertian surfaces and treats shadows and specularities as outliers. They showed that when three images exist in which the brightness value of a given pixel behaves Lambertian, it is enough to predict the brightness of this pixel in any image taken under arbitrary illumination. They also demonstrated that the performance of the principal component analysis can not improve even while increasing the amount of the input image data.

We note that there is no analysis of these above techniques with regard to the techniques of removing the artefacts of shadow and specularity. In *Chapter 8*, we propose a simple but efficient method to reduce effect of artefacts, which is similar to Rushmeier's method [Rushmeier97].

4.5. Summary

In this chapter, we introduce the technique of photometric stereo which gives us the ability to estimate surface properties using several images of a surface taken from the same viewpoint but under illuminations from different directions.

Firstly, some of candidate techniques are compared with photometric stereo. Binocular stereo is not suitable for us mainly due to correspondence problem. Shape from shading is based on smoothness and continuity, although it only needs one image. Photometric stereo technique does not have this problem. It allows us to obtain a surface description from several images of the same texture surface under various illumination directions. It is also a useful means that is suitable to recovery of

the surface characteristics and matches our needs due to the problem caused by variation in illuminant direction.

Furthermore, a general review of development on photometric stereo is presented. It is followed by a solution to photometric stereo, where three photometric images are used to recover both the local surface orientation and albedo information given the assumption that Lambertian surface and both shadow and specular factors are absent. The equations of photometric stereo are expressed in the format of matrix equations.

Finally, some of techniques used to improve photometric stereo by considering shadow and specular effects are reviewed.

CHAPTER 5

Gradient Space

5.1. Introduction

Once the surface properties (p and q) have been captured using photometric stereo, it is useful to initially represent these data in an alternative form, in order to isolate the significant textural feature of interest, especially some rotation invariant features. This may readily be achieved by performing a transformation of those data from surface to the Extended Gaussian Image, further more to the gradient space in spatial domain. In this chapter, we will mainly discuss gradient space domain.

5.2. Extended Gaussian Image

The Gaussian image of a three dimensional object is obtained by mapping surface points to a unit sphere, called the Gaussian sphere, such that points on both the sphere and original object have a corresponding surface normal direction. Hence for curved convex objects, each surface point will map to a unique location on the Gaussian sphere, while objects containing, for example planar regions, will result in object areas represented by a single point on the Gaussian sphere. An alternative representation, known as *the Extended Gaussian Image (EGI)* [Horn79] additionally associated each point on the Gaussian sphere with the inverse of the Gaussian curvature at the corresponding object point. This causes flat planar areas to appear as impulses upon the EGI, where a weight is assigned to each point on the Gaussian

sphere equal to the area of the surface having the given normal. An example of such an extended Gaussian image is shown in *Figure 5. 1*.

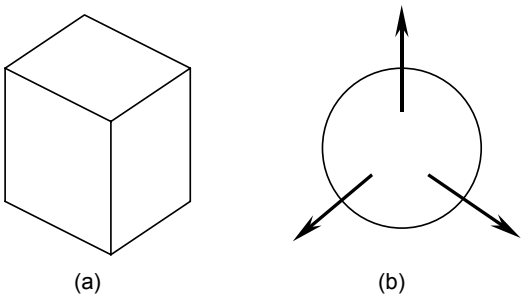

Figure 5. 1 The example of the EGI. (a) an object. (b) The EGI representation of the object in (a).

The extended Gaussian image representation is local since every surface patch on an object corresponds to a point on the sphere. Thus it has the advantage of direct computation from image data, especially when surface normal is easily available. On the other hand, the extended Gaussian image has two disadvantages:

1. The mapping to the Gaussian sphere is unique for convex objects.
2. An infinite number of non-convex objects can possess the same extended Gaussian image. For example in *Figure 5. 1*, those two objects have the same extended Gaussian image.

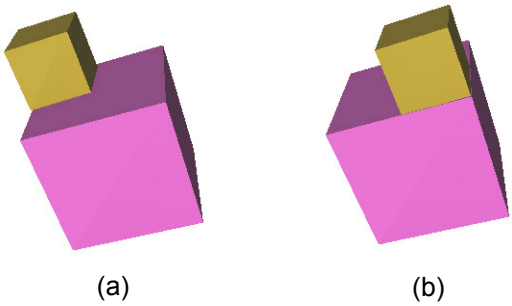

Figure 5. 2 Examples of objects with the same EGL.

Although the mapping of EGI may be extended to non-convex objects, extended Gaussian image is itself inconvenient to use because of its three dimensional curved surface. However, given that points on the Gaussian sphere specify directions in space, and because orientations has only two degrees of freedom, an alternative representation can be obtained by projecting the visible half of the Gaussian sphere

onto an infinite plane, called the *gradient space*. In the next section, we will discuss the gradient space, and in this manner a surface can therefore be represented as a distribution of points in gradient space.

5.3. From Surface Normal to Gradient Space

Gradient space is a two-space representation of the orientation of every point on a surface. It is a scatter plot between surface partial derivatives p and q. We consider that the surface that we are viewing has been projected into a two-space or image plane representation. In addition, we take the projection direction along the $-z$ axis and consider only orthographic projections. Our surface is:

$$z = f(x, y) \tag{5. 1}$$

Every visible point on the surface is projected into the image plane. Each of these points has a world space surface normal and we can represent the orientation of the surface normal of each by a single point in the two-space. This space is called the *gradient space*. *Figure 5. 3* shows the relationship between gradient space and a surface normal.

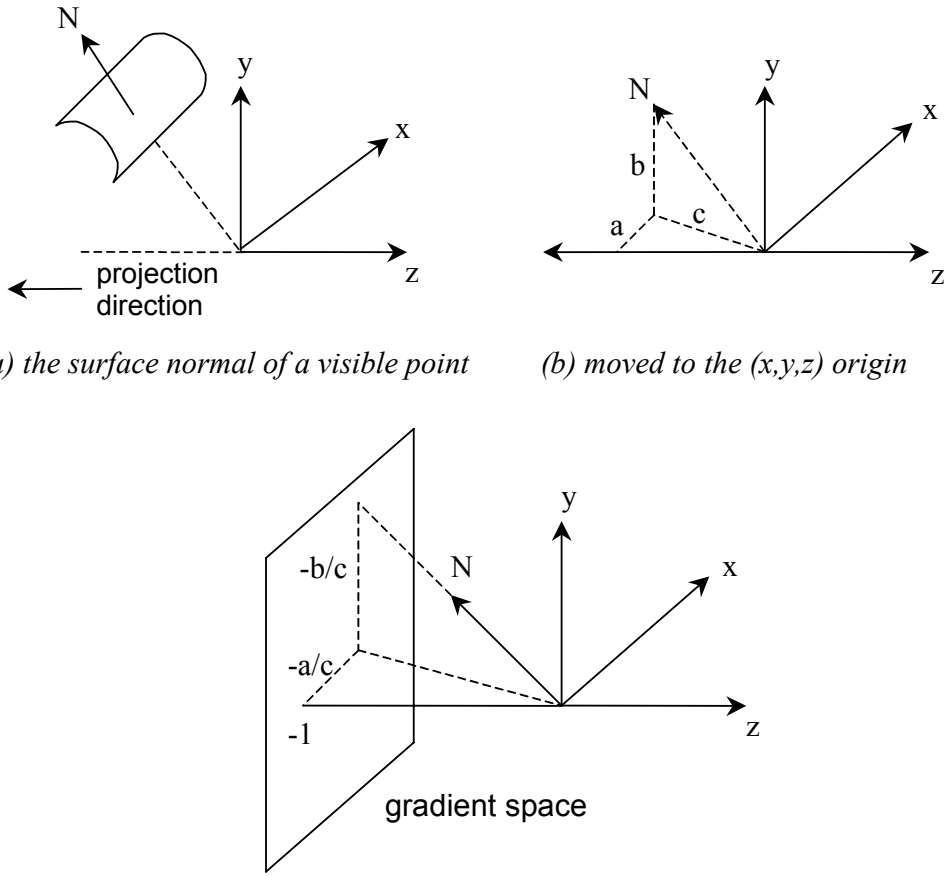

(a) the surface normal of a visible point *(b) moved to the (x,y,z) origin*

(c) extended to intersect the plane z=-1

Figure 5. 3 The mapping of surface normal data to the gradient space domain.

This shows a surface normal *N* at a point on a surface. All visible points on this surface will have surface normals with negative *z* components. To represent such normals in two-space we first extend the vector back to the *(x, y, z)* origin and assign coordinates *(a, b, c)* to it (*Figure 5. 3(b)*). If we consider a plane normal to the *z* axis positioned at *z=-1* then vector intersects this plane at coordinates *(p, q)*, where

$$\begin{aligned} p &= -a / c \\ q &= -b / c \end{aligned} \tag{5. 2}$$

Now the direction of the normal to surface *z=f(x, y)* is $(\partial f / \partial x, \partial f / \partial y, -1)$ and we get

$$p = \partial f / \partial x$$
$$q = \partial f / \partial y \tag{5. 3}$$

Therefore the surface orientation can be presented in gradient space *G(p, q)* [Horn79] [Smith99a].

5.4. Surface Orientation in Gradient Space

5.4.1. Surface Distribution of Gradient Space

In essence, as already described, the concept of gradient space *G(p, q)* facilitates the mapping of an array of surface normals to a series of co-ordinate points, *(p, q)* within the two dimensional gradient space domain, where *p* and *q* describe the surface partial derivatives (the local surface slope). By mapping such an array of surface normals into the gradient space domain, an indication of the global surface normal distribution, and hence global surface shape, can readily be obtained [Smith99a]. Horn has described such a concept for the recognition and attitude determination [Horn79].

Figure 5. 4 shows the distribution of gradient space *G(p, q)* for four synthetic textures and *Figure 5. 5* shows their corresponding 3D frequency distribution.

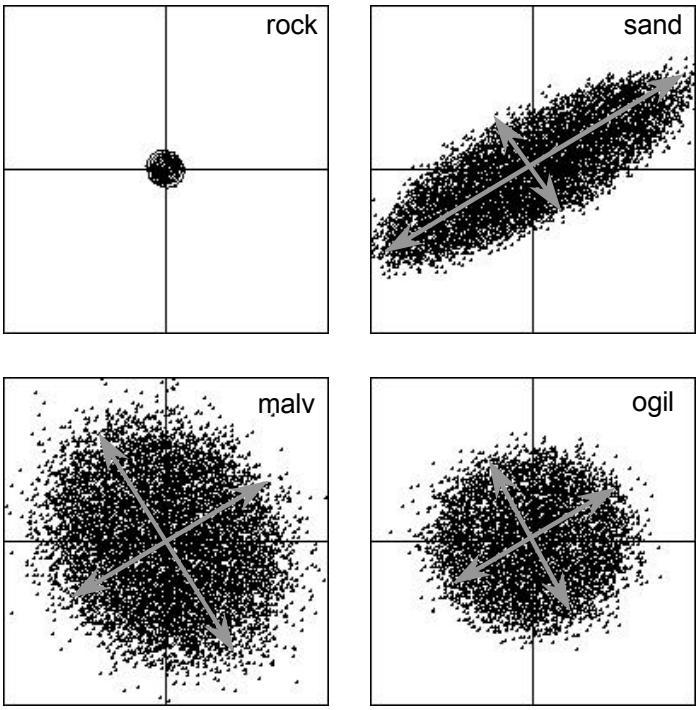

Figure 5. 4 Distribution of gradient space G(p, q) for four synthetic textures.

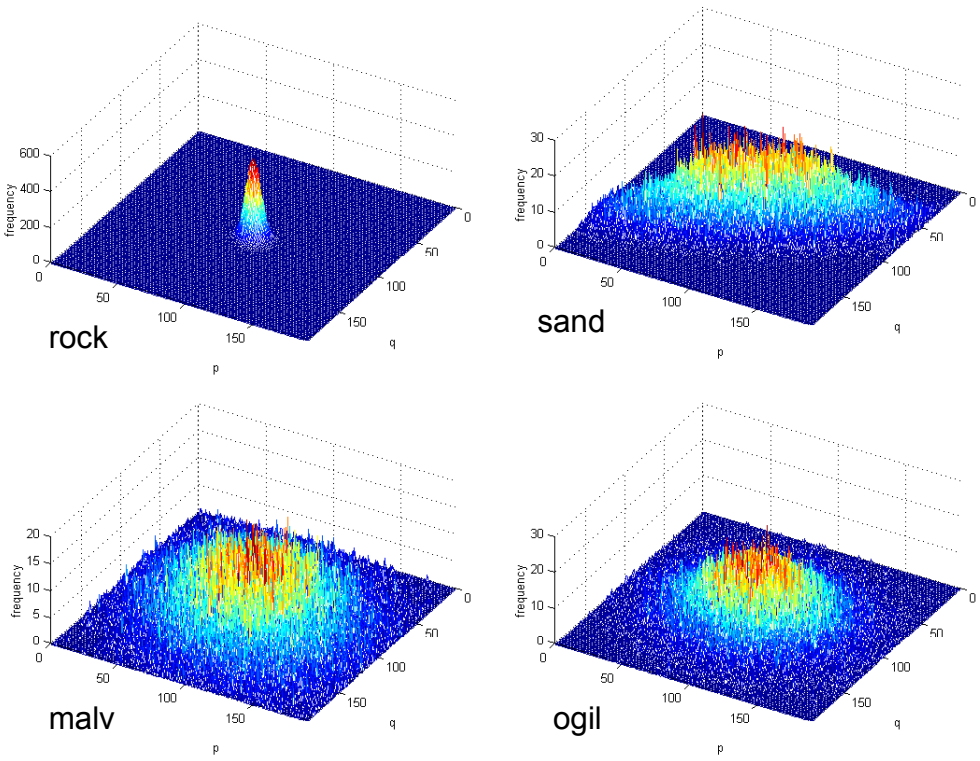

Figure 5. 5 3D Distribution of gradient space g(p, q) for four synthetic textures.

5.4.2. Presentation of Surface Orientation in Gradient Space

The mapping of surface normals data to the gradient space domain would seem to offer a useful mechanism for the representation of surface shape. It will be shown here that the distribution of a given gradient space may in fact be considered to represent an invariant description of the entire observed surface. Examples of gradient space for four synthetic textures at different surface orientations are shown in *Figure 5. 6*.

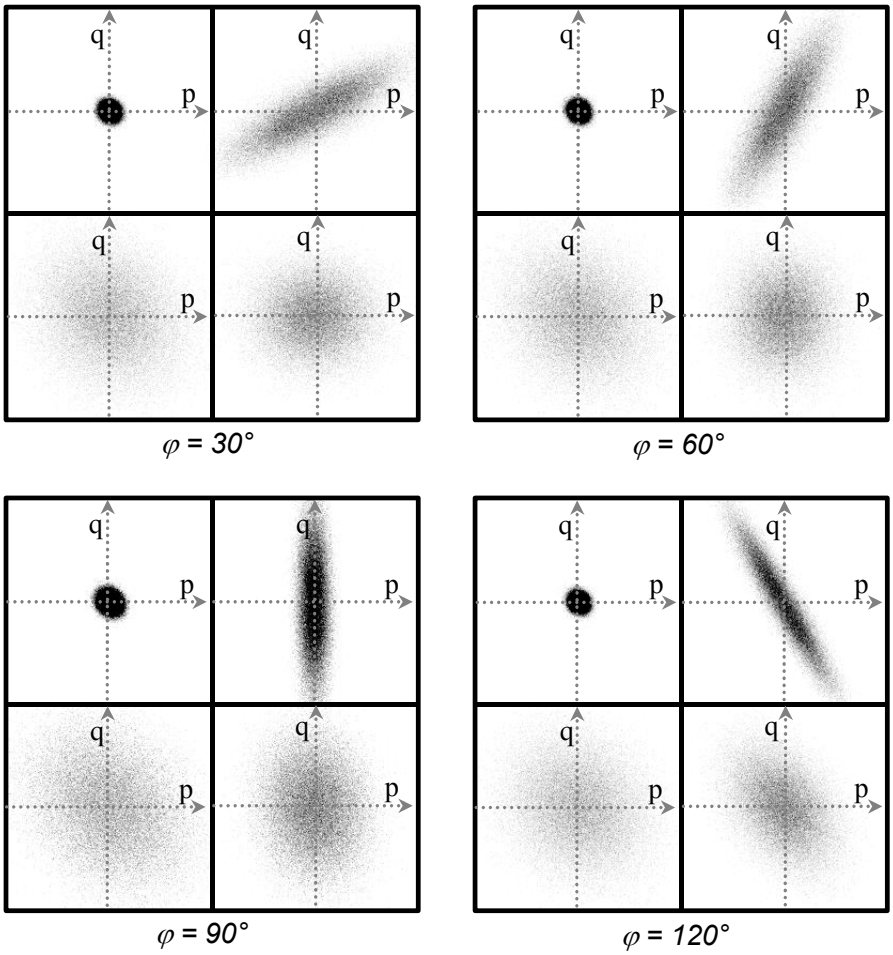

Figure 5. 6 Gradient space G(p, q) for four synthetic textures at different surface orientations φ=30°, 60°, 90° and 120°, shown in montage format. The textures are rock(left-top), sand(right-top), malv(left-bottom) and ogil(right-bottom).

As shown in *Figure 5. 6*, the presence of a texture will be manifest as a spreading of impulsive distribution within the gradient space domain. In order to describe the

distribution of gradient space, it is useful to compare the rotation invariant moments among those textures. For example, consider the following two main texture feature parameters calculated by moments:

- *Eccentricity (shape factor)* E_m. Obtained from the ratio principal second order moments.

$$E_m = \frac{E_1}{E_2} \tag{5. 4}$$

Where the principal second order moments are given by:

$$E_1 = \frac{(M_{20} + M_{02})}{2} + \sqrt{\left[\frac{(M_{20} - M_{02})}{2}\right]^2 + M_{11}^2} \tag{5. 5}$$

$$E_2 = \frac{(M_{20} + M_{02})}{2} - \sqrt{\left[\frac{(M_{20} - M_{02})}{2}\right]^2 + M_{11}^2} \tag{5. 6}$$

where M_{ij}'s are second order moments of the gradient space image $G(p, q)$ given in the following:

$$M_{11} = \sum_p \sum_q (pq) G(p,q) \tag{5. 7}$$

$$M_{20} = \sum_p \sum_q (p^2) G(p,q) \tag{5. 8}$$

$$M_{02} = \sum_p \sum_q (q^2) G(p,q) \tag{5. 9}$$

- *Polar moment* P_m.

$$P_m = \sum_p \sum_q (p^2 + q^2) G\ (p,q) \tag{5. 10}$$

Table 5. 1 and *Table 5. 2* show the eccentricity E_m and polar moment P_m of the gradient space for two example synthetic texture *sand* and *malv* in various surface orientations from *0°* to *150°*. We note that both eccentricity E_m and polar moment P_m are rotation invariant moments.

Orientation	*0°*	*30°*	*60°*	*90°*	*120°*	*150°*
sand	4.18E-02	9.69E-02	9.59E-02	4.17E-02	2.84E-02	2.79E-02
malv	6.40E-01	7.15E-01	7.17E-01	6.46E-01	7.13E-01	7.07E-01

Table 5. 1 Eccentricity of gradient space (E_m) for synthetic texture sand and malv in various surface orientations.

Orientation	*0°*	*30°*	*60°*	*90°*	*120°*	*150°*
sand	1.09E+08	1.38E+08	1.30E+08	1.11E+08	1.36E+08	1.26E+08
malv	2.01E+08	1.69E+08	1.65E+08	2.02E+08	1.64E+08	1.66E+08

Table 5. 2 Polar moment of gradient space (P_m) for synthetic texture sand and malv in various surface orientations.

Classification feature space among textures (*rock, sand, malv and ogil*) with respect to various surface orientations (from *0°* to *180°*) can be seen in *Figure 5. 7*. We also note that they are not discriminative enough to enable the classifier to be robust to surface rotation for various texture surfaces. The clusters between texture class *sand* and *ogil* are too close, where the classification may be failed so that we have to seek other more feature spaces being robust to surface orientation and being more discriminative to various texture classes in the next chapter.

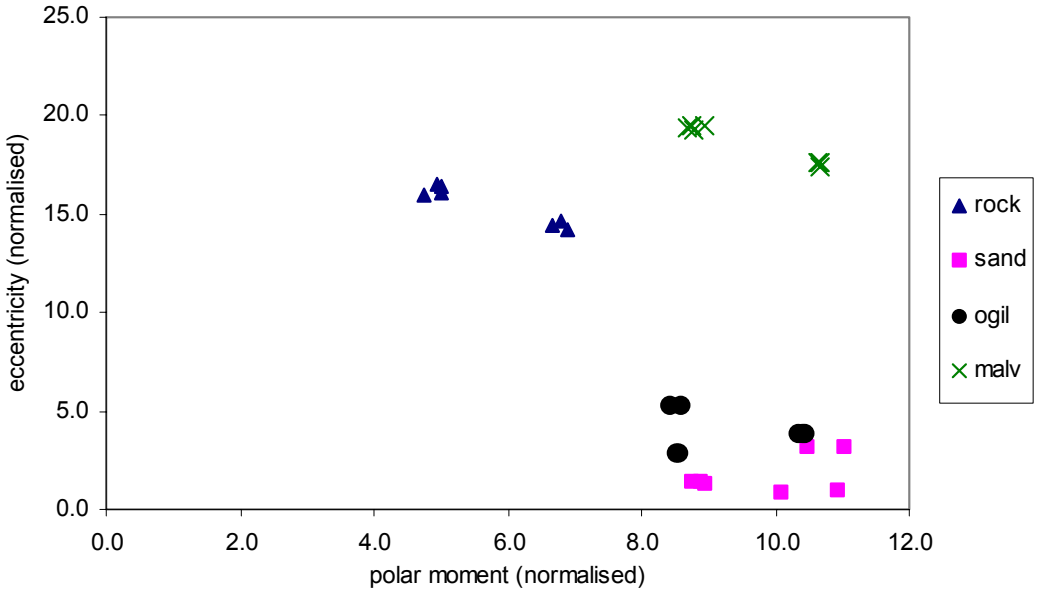

Figure 5. 7 Classification feature space among textures (rock, sand, malv and ogil) with respect to various surface orientations (from 0° to 180°).

5.4.3. Estimate Surface Orientation by Moment

From the *Figure 5. 6*, we can see that the principal axes of gradient space image (especially for texture *sand*) presents the surface orientation. Therefore we may estimate surface orientation by analysing the moment in gradient space. The publication results by Hu [Hu62], Teh and Chin [Teh86] show directly or indirectly that only moments invariants based on the moments of order two are actually almost invariant to rotation. The moments of higher order are so sensitive to digitalisation errors, minor shape deformations, etc., that the corresponding moment invariants can be hardly used for shape identification. In order to illustrate the estimation and to make the step clear, we show as a very easy and well-known example the derivation of the second order central moments invariant to rotation.

We regard the gradient space image as a function of two variables, $G(p, q)$. Therefore the principal orientation (θ) of surface is obtained from the principal axis of the gradient distribution.

$$\tan 2\theta = \frac{2M_{11}}{M_{20} - M_{02}} \tag{5. 11}$$

where the origins of the coordinate have been centred at the centroid of each gradient space image.

In order to test the estimation of surface orientation by moment, we carry out an experiment by using four synthetic texture (rock, sand, ogil and malv). Their surface partial derivatives p and q at surface orientation angle of $0°$ are firstly estimated by photometric stereo, and then their corresponding gradient space $G(p, q)$ are built as references (training set at surface orientation $\varphi=0°$). Secondly, the test sets of gradient space at surface rotation angles of $30°$, $60°$, $90°$, $120°$, $150°$ and $180°$ are estimated by rotating their surface, respectively. Finally the surface orientation angles θ on both test and training sets are calculated by the moments of their gradient space through above equation.

Figure 5. 8 shows the estimated surface orientation angles (θ) for above four synthetic textures obtained from their corresponding gradient space $G(p, q)$. It can be readily seen that only for the directional texture *"sand"*, the estimation processing is achieved a good result, while it fails with the rest of three textures (*rock*, *malv* and *ogil*). This is because the distribution of the gradient space for these three textures (non-directional) does not relate well to the surface orientations and leads to the failures.

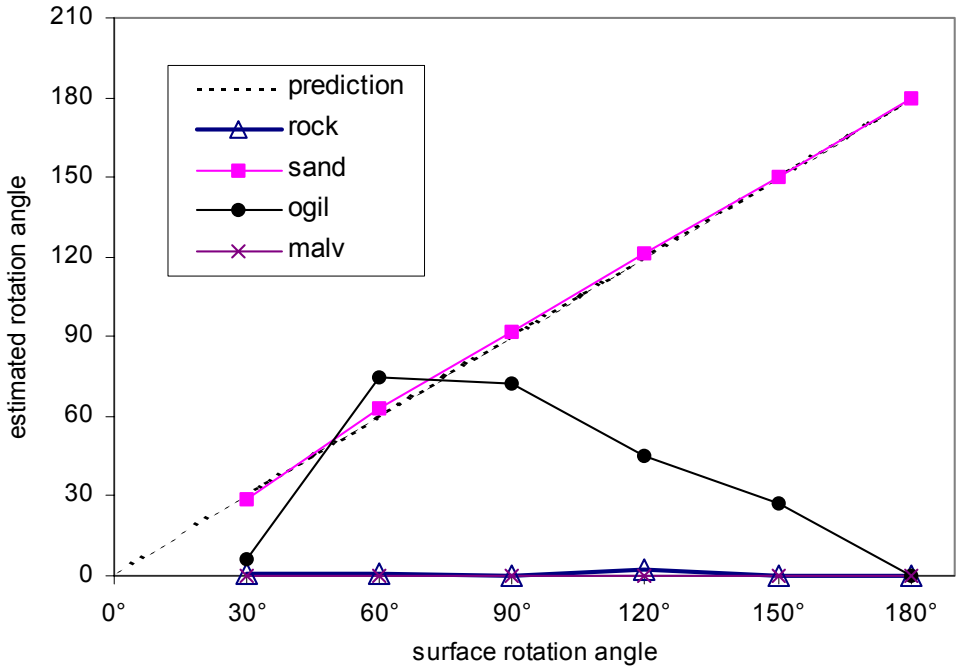

Figure 5. 8 Estimation of the surface orientation angles for four synthetic textures (rock, sand, malv and ogil) obtained from gradient space G(p, q).

We note that the angle θ obtained with equation *(5. 11)* may be with respect to either the major principal axis or the minor principal axis. The correct rotation angle will be $\theta + n\pi/2$ where n is chosen to satisfy the constraints. Problems may occur when a gradient space image is *n-fold* symmetric since there are multiple possible sets of principal axes, such as gradient spaces for texture *rock* and *malv* in *Figure 5. 6*.

We therefore present our new algorithm in next chapter, which is rotation invariant texture classification using gradient space in *frequency domain* rather than the above in *spatial domain*.

5.5. Summary

In this chapter, following by discussing the disadvantages from the Extended Gaussian Image (EGI), which is that the Gaussian sphere is unique for convex

objects and an infinite number of non-convex objects can processed the same extended Gaussian image, we therefore introduce gradient space.

In general, the concept of gradient space *G(p, q)* facilitates the mapping of an array of surface normal to a series of coordinate points *(p, q)* within the two-dimensional gradient domain, where *p* and *q* describe the surface gradient in two orthogonal degrees of freedom at a given location. By mapping such an array of surface normals into gradient space, the global surface normal distribution can readily be obtained. The utilisation of gradient space mapping offers an advantage in terms of surface orientation dependence. Further, the distribution shape of gradient space about the plot centroid will remain constant, and the magnitude and directional distribution of surface gradient within the space becomes clearly visible. Hence the character of the distribution can be used to classify the texture.

We analysis the gradient space using various moments. The eccentricity moment and polar moment are considered to provide the indication of gradient space distribution. Both of them are rotation invariant features with respect to surface orientations, however, they are not robust to the various surface texture classes. In addition, we also estimate surface orientation using second order moments of principal axes in gradient space. However the estimation process on non-directional texture surfaces has been failed, because the problems may occur when a gradient space image is *n-fold* symmetric where there are multiple possible sets of principal axes.

With regard to the surface rotation invariant classification, there are some difficulties associated with the surface derivatives in gradient space *G(p, q)* as feature spaces. The first is that the surface derivatives *p* and *q* are vectors rather than scalar quantities. We will have to use these two surface derivatives together in classifier, rather than one scalar quantity. Recovery of the surface height map by integrating the surface derivatives may yield a scalar field which can be directly incorporated into an existing classifier. However the integration error may be well increase via accumulation. The other difficulty is that there is a direction-related factor, which is an artefact of the partial derivative operator. In this case, this directionality

component should be removed before classification. In general, the gradient space $G(p, q)$ will not subsequently use in our classification scheme. Those matters are discussed in the next chapter.

In next chapter, we proposes a method by which the partial derivatives may be combined in the frequency domain in such a way as to remove these directional artefacts. Note that the gradient space $G(p, q)$ is a scatter plot of surface partial derivatives p and q presenting in the spatial domain, it is not the inverse Fourier transform of the measure gradient spectrum $M(\omega, \theta)$ presented in the next chapter.

CHAPTER 6

An Algorithm of Rotation Invariant Texture Classification

6.1. Introduction

Many texture classification schemes have been presented that are invariant to image rotation so far. The major existing approaches include image rotation invariant statistical features, moment invariants, polarogram features, Hough transform features, iso-energy directional signatures in 2D Fourier spectra, autoregressive models, Gaussian Markov random field models, multi-channel filtering and wavelet transforms. Details can be found in *Chapter 2*.

Image rotation invariant classifiers normally derive their features directly from a single image and are tested using rotated images. If the image texture results solely from albedo variation rather that surface relief or if the illumination is not directional or immediately overhead, then these schemes are surface-rotation invariant as well. However, in many cases rotation of a textured surface produces images that differ radically from those provided by pure image rotation (see *Figure 6. 1*). These images show that rotation of a 3D surface texture does not result in a simple rotation of the image texture. This is mainly due to the directional filtering effect of imaging using side-lighting [Chantler94a, Chantler94b]. Such changes in appearance can cause significant failures in image-base texture classifiers. For instance a rotation of *90°* of the illuminant tilt angle can cause the mis-classification rate of a texture classifier to change from *4-5%* to nearly *100%* [Chantler94a]. In another way, rotation of the

physical texture surface under fixed illumination conditions can also cause significant changes to its appearance. It causes failure of classifiers designed to cope with image rotation as well [McGunigle98].

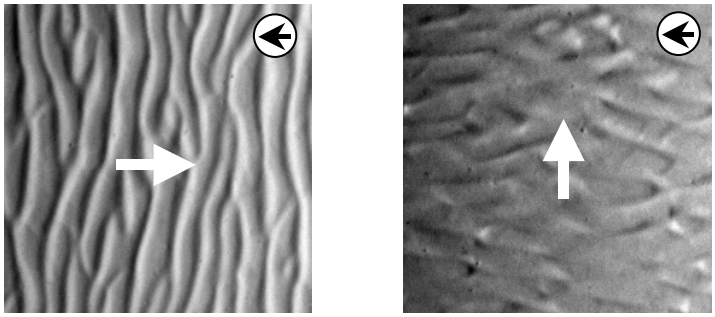

φ = 0° φ = 90°

Figure 6. 1 Two images of the same directional 3D rotated surface texture with identical illuminant. The surface has been rotated through of 0° and 90° (indicated by the white arrows in the centre). The illuminant tilt is kept constant at τ=0° (indicated by the black arrows in white circles).

In this chapter, we present a novel *surface rotation invariant* approach to texture classification. Our approach uses polarograms [Davis81] derived from surface derivative spectra. We use photometric stereo to obtain the required partial derivative fields. They are Fourier transformed and combined to provide a frequency domain function that does not contain the directional artefacts associated with partial derivatives. Polarograms of this function are compared with those of training classes using a goodness-of-fit measure to provide rotation invariant texture classification.

6.2. Surface Rotation-Invariant Texture Features

In previous chapters, we have discussed that we can successfully obtain surface properties using photometric stereo and we will use these 3D surface properties in image properties for classification. The next step is to derive surface rotation-invariant texture features from 3D surface properties that have the ability to provide discrimination between texture classes.

6.2.1 Related Work

As previously stated in *Chapter 2* many texture classification schemes have been presented that are invariant to image rotation [Port97] [Cohen91] [Mao92]. Few take into account the problems caused by illumination described in *Figure 6. 1*. Exceptions include Leung and Malik's classification system which is trained on textures that are each imaged under 20 different illumination and orientation conditions [Leung99]. This generalises the classifier but does not use explicit 3D surface texture information directly; Dana and Nayer describe histogram and correlation model for 3D surface texture and suggest how this might be used to provide a 3D surface texture feature, correlation length [Dana99a]; McGunnigle and Chantler proposed a model-based scheme that used photometric stereo to obtain gradient information [McGunnigle97]. Smith also uses 3D surface texture information directly [Smith99a]. He uses photometric stereo to acquire surface gradient information and suggests the use of features derived from the gradient space. More details about above methods can be recalled in *Chapter 2*.

6.2.2 Development of Features in Frequency Domain

Chantler [Chantler94a] notes that both the directional characteristics and the variance of images of three-dimensional textures can be affected by changing the illumination vector. A frequency domain model based on Kube and Pentland's illumination model is presented and the results of simulations and laboratory experiments allow it to be evaluated. Moreover the model is further developed using empirical data and the resulting model used to design a set of tilt-compensation filters. These filters are used to pre-process images to reduce the effects of changes in the angle of tilt of the illumination (see *Figure 6. 2*).

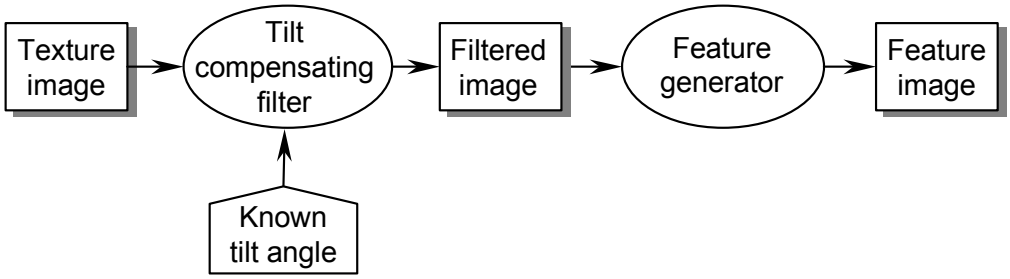

Figure 6. 2 Chantler's frequency domain compensation model for illuminant tilt variation

The classifier is trained under a set of illumination conditions but it is used with arbitrary tilt angles. Application of the filters to the test image set reduced the classification tilt-related errors associated with directional textures only. His method is a simple implementation and avoids high training requirements; however, the illuminant tilt angle has to be known during both the training and classification process. In addition, we have to consider two aspects of illumination conditions: not only tilt angle but also slant angle variations, but he did not give a frequency domain slant compensation scheme. Finally, this single image scheme is not able to estimate signal components perpendicular to the illuminant direction due to the linearization inherent in Kube and Pentland's model.

McGunnigle [McGunnigle98] states that a technique which uses a representation of the physical surface as the basis for the generation of appropriate training data is appropriate. The surface derivative fields of the training surface are estimated using photometric techniques. This allows him to recover surface intrinsic characteristics from several images of the same surface taken at different illumination conditions. A rendering algorithm uses these estimates to simulate the appearance of the training surface when it is illuminated form an arbitrary direction. It is shown that where illuminant direction is varied this system is able to perform significantly better than a naive classifier, and in some cases approaches the level of accuracy obtained from training the classifier under the conditions at which classification is performed.

The scheme was not rotation invariant. Later he proposed another photometric-based system, which is outlined in *Figure 6. 3*. This time, however, the gradient information was directly filtered using isotropic Gabor filters to provide a rotation

insensitive scheme [McGunnigle99a]. The filtered derivative fields $p_g(x,y)$ and $q_g(x,y)$ still contain the artefacts of directionality due to the differentiation. As they are only interested in the amount of energy contained in each frequency band, the post-processing stage of the norm function can be non-linear. The resulting quantity is free of the directional filtering effect. A filter approach is adopted to estimate the magnitude and followed by a low-pass filter. Finally, his classification is performed by the statistical discriminated maximum likelihood method.

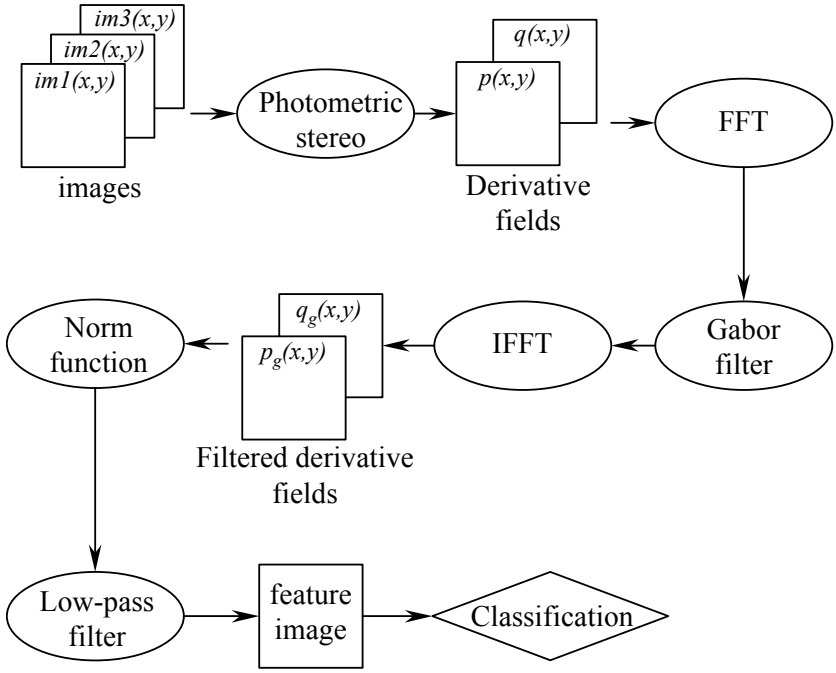

Figure 6. 3 McGunnigle's surface rotation invariant classification scheme

In his scheme, firstly we note that he only use three images to estimate surface derivatives and ignores the shadowing effect. However, in general the shadowing will play an important role in the photometric stereo techniques. Secondly, he assumes that the surface is of approximately Lambertian reflectance and uniform albedo. He does not use any albedo information in his classifier, although albedo information can be isolated from the training data sets. Thirdly, his classification is only performed on the variations in illuminant tilt and the slant angle is kept constant. The effect of slant variation will also have a significant effect on photometric stereo techniques applied to 3D rough surface.

Quivy [Quivy98] presents a look-up table for CFFT based texture classification (see *Figure 6. 4*). The non-linear mapping between image irradiance and surface orientation is represented in a look-up table. He used a calibration object of known shape to generate data mapping the measured brightness values to the corresponding gradient. He then obtained the spectra of the texture gradient by applying a Complex Fast Fourier Transformation (CFFT) to the complex gradient combination $p(x.y)+\boldsymbol{j}\bullet q(x,y)$. Finally, the classification is performed on the maximum of the normalised correlation coefficient between the featured test images and training images. He has to estimate the surface orientation angle by rotating one of the spectra images before comparing the data for classification purposes. Hence this scheme is computationally expensive. On the other hand, the classification accuracy is heavily dependent on the accuracy of the estimated rotation angle. In this circumstance, he reports that an isotropic texture could lead to potential misclassification due to failure of the angle estimation processing.

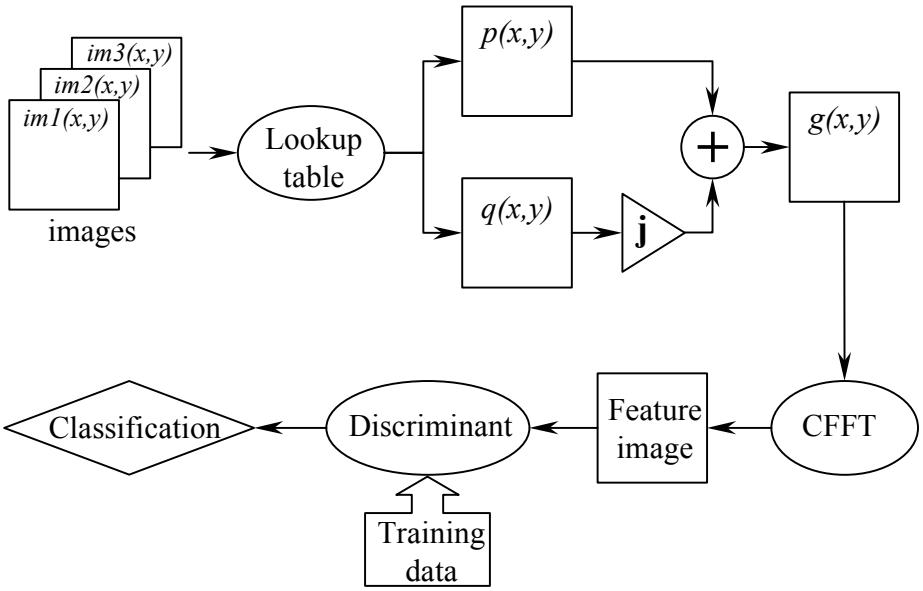

Figure 6. 4 Quivy's lookup table and CFFT based texture classification

Damoiseau [Damoiseau97] developed a correlation method based on polar spectra. She investigated its performance using a set of twenty Brodatz textures (see *Figure 6. 5*). Using multiple frequency ranges on the polar spectra enabled estimation of surface orientation angles more accurately. The overlapping range defined on the

frequency range also improves the accuracy of the classifier, although they are all based on the same classification principal. The classification is based on features defined to be the maximum value of the cross-correlation between the polar spectra of the test sample and that of each training sample. We note that Damoiseau's method is based on image data rather than on surface data and the location of the frequency ranges appears to be a very sensitive parameter.

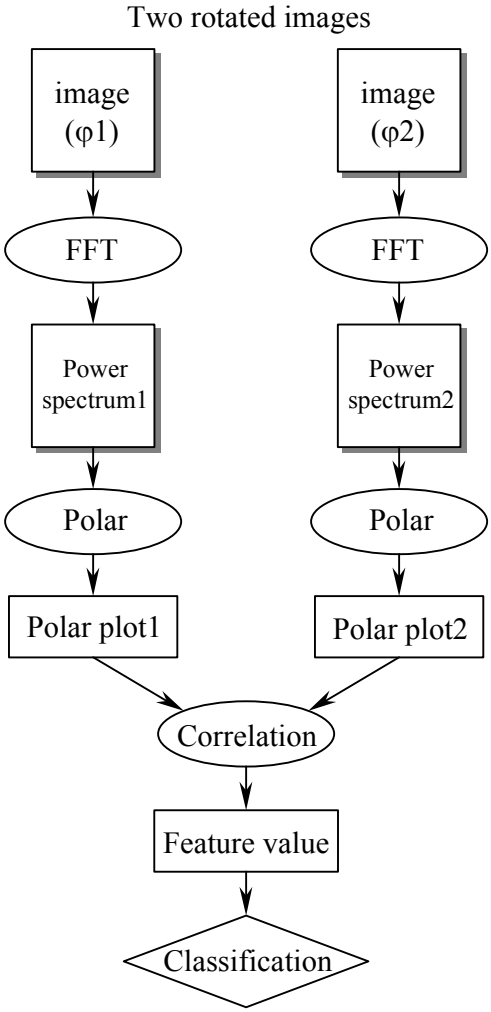

Figure 6. 5 Damoiseau's classification scheme using polar plot and correlation

In general, Chantler's single image scheme [Chantler94a] only gave a frequency domain tilt compensation but slant compensation, and it also share the significant weakness that stems from the linearisation inherent in Kube's model [McGunnigle98]. In McGunnigle's method [McGunnigle98], he ignored the effect of shadowing and kept the surface albedo and slant angle constant in his experiments.

Quivy's method [Quivy98] is computationally expensive and heavily dependent on the accuracy of the estimated rotation angle, which results in the potential misclassification for an isotropic texture. Although the computation in Damoiseau's method [Damoiseau97] is not expensive, it is based on image data but surface data. Therefore, we develop our surface rotation invariant texture classification scheme using photometric stereo.

6.3. Photometric Stereo in Frequency Domain Dual

The aim of this chapter is to develop an algorithm of rotation invariant texture classification for 3D surfaces, so the directional effects which come from the illuminant conditions must be removed before the classification. In this section, we will discuss two of the difficulties in photometric stereo and how we remove the directional artefacts in the frequency domain. Finally we evaluate our algorithm on four synthetic textures and four real textures.

6.3.1 Difficulties in Photometric Stereo

As discussed earlier, we have to use the basic surface properties of the surface rather than the image intensity properties in order to eliminate the effects of illumination and enable the classifier to be robust to the surface rotation. We obtain the partial derivatives of the surface height function using photometric stereo, in which several images of the same surface are taken under different illumination conditions. The photometric stereo method enables us to estimate surface shape. It requires only one camera with a movable light source and can be easily implemented without extra cost in computation. In addition, there is no assumption of smoothness of the 3D surface as required in most single image shape from shading algorithms. We note, however, that there are two main difficulties associated with the surface derivatives:

1. The first is that the surface derivatives are vectors rather than scalar quantities. We will have to use these two surface derivatives together in classifier, rather than one scalar quantity. Recovery of the surface height map by integrating the surface derivatives may yield a scalar field which can be directly incorporated into an existing classifier. However the integration error may be well increase via accumulation.

2. The other difficulty is that there is a direction-related factor, which is an artefact of the partial derivative operator. In this case, this directionality component should be removed before classification.

These two difficulties mean that the partial derivatives of the surface cannot be used directly in a rotation invariant classifier; they must be processed first.

6.3.2 Frequency Domain Dual

This section proposes a method by which the partial derivatives may be combined in the frequency domain in such a way as to remove these directional artefacts. The surface gradient estimations provided by photometric stereo are normally in the form of the partial derivative fields *p(x,y)* and *q(x,y)*.

$$p(x,y) = \partial z(x,y)/\partial x \qquad (6.1)$$

$$q(x,y) = \partial z(x,y)/\partial y \qquad (6.2)$$

where *z(x, y)* is the surface height function of a texture in the *x*-*y* plane,

and *p(x,y)* and *q(x,y)* are surface partial derivative fields along the *x* direction and *y* direction respectively.

The Fourier transforms of equation (6. 1) and (6. 2) are:

$$P(u,v) = iuS(u,v) = i\omega(\cos\theta)\, S(\omega,\theta) \qquad (6.3)$$

$$Q(u,v) = ivS(u,v) = i\omega(\sin\theta)\, S(\omega,\theta) \qquad (6.4)$$

where $S(u,v)$ and $S(\omega,\theta)$ are the surface magnitude spectrum in its Cartesian and polar forms,

u,v are spatial frequency variables,

and ω,θ are their polar equivalents.

$P(u,v)$ and $Q(u,v)$ are the Fourier transforms of *p(x,y)* and *q(x,y)* respectively.

Now equation (6. 3) and (6. 4) show that both derivatives act as directional filters due to the $\cos\theta$ and $\sin\theta$ terms. In particular the partial derivative of a surface rotated by φ is not simply a rotation of the original partial derivative, i.e.

$$P_{\varphi}(\omega,\theta) = i\omega(\cos\theta)S(\omega,\theta+\varphi) \neq P(\omega,\theta+\varphi) \qquad (6.5)$$

However, we may combine the partial derivatives to provide a function free of directional artefacts:

$$M(u,v) = |P(u,v)|^2 + |Q(u,v)|^2 = [\ \omega|S(u,v)|\ ]^2 \qquad (6.6)$$

where *M(u, v)* is the corresponding gradient spectra. *M(u, v)* is the mathematic non-linear combination between the surface partial derivatives *P(u, v)* and *Q(u, v)* in the frequency main, in which the surface directional artefact apart from those directly inherent from the surface spectrum has been removed. In the other words, the directionalities of *M(u, v)* present the surface orientations only, which give us the ability to design the surface rotation invariant classification scheme.

We can readily see that the orientation of gradient spectra *M(u, v)* only depends on the orientation of surface spectra $S(u,v)$ since ω is a rotation invariant scalar. Note that gradient spectra *M(u, v)* is not equivalent to the Fourier transform of gradient space *G(p, q)* presented in Chapter *5* where its directionality component is not removed.

From equation (6. 3), (6. 4) and (6. 6), we note that the spectra of the derivative fields $P(u,v)$ and $Q(u,v)$ have the directionality of the derivative fields. While the gradient spectra *M(u, v)* is a combination of $P(u,v)$ and $Q(u,v)$ they do not have any directional component apart from those directly inherent from the surface spectrum $S(u,v)$. Note that

$$M(\omega,\theta+\phi)=\left[\omega\left|S(\omega,\theta+\phi)\right|\right]^2=M_{\phi}(\omega,\theta) \qquad (6.7)$$

hence rotation of the surface should produce a pure rotation of the corresponding *M(ω, θ)* spectrum, shown in *Figure 6. 7*.

Finally, it is interesting to note that the measures of *M(u, v)* spectrum presented in equation (6. 6) is obviously non-linear, and the following chapters no longer rely on the linearization presented in Chapter *3* and Chapter *4*.

6.3.3 Directional Characteristic of M(ω, θ)

In this section, we will test the gradient spectrum *M(ω, θ)* on both synthetic textures and real textures in terms of its ability to discriminate and determine directionality for different kinds of textures.

- ***Synthetic textures***

Firstly, we examine the gradient spectra *M(ω, θ)* of four synthetic textures, which have already been introduced and defined in chapter 3. The four textures in montage format (see *Figure 6. 6*) are *rock* (left-top), *sand*(right-top), *malv*(left-bottom) and *ogil*(right-bottom).

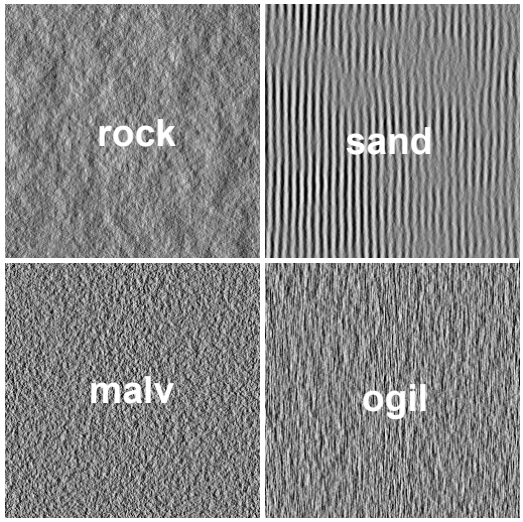

Figure 6. 6 Four synthetic textures in montage format at surface rotation $\varphi = 0°$ with constant illumination tilt angle $\tau = 0°$ and slant angle $\sigma = 50°$

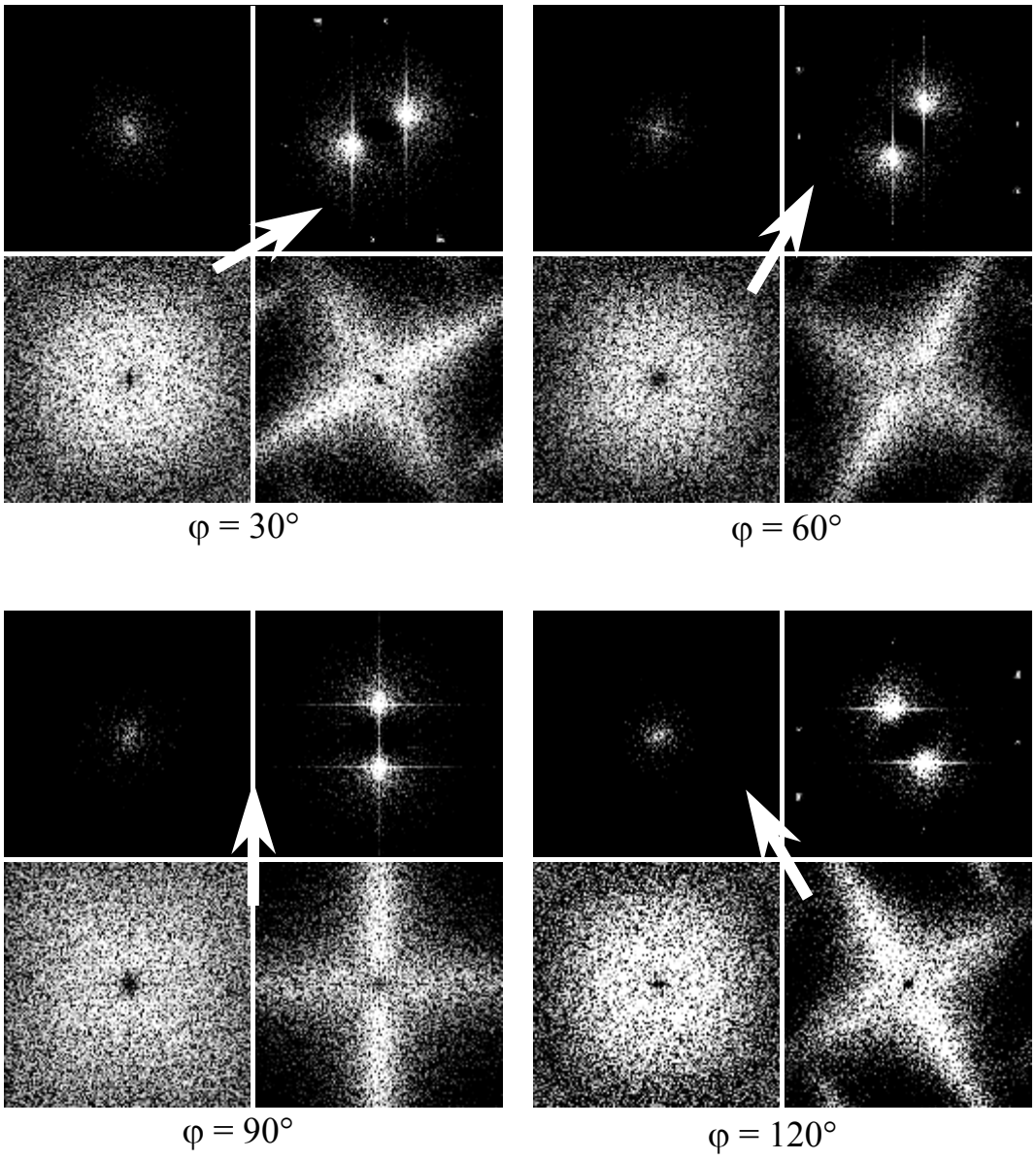

Figure 6. 7 Gradient spectra $M(\omega, \theta)$ of 4 synthetic textures shown in montage format for 4 surface rotations ($\varphi = 30°, 60°, 90°$ and $120°$). The textures are rock (left-top), sand(right-top), malv(left-bottom) and ogil(right-bottom).

From *Figure 6. 7* , which shows the $M(\omega, \theta)$ gradient spectra of four synthetic textures, it can be seen that rotation of each of the surface *($\varphi = 30°, 60°, 90°$ and 120°)* produces a corresponding rotation of their gradient spectra $M(\omega, \theta)$. On the other hand, the directionality in the directional (*sand*) or bi-directional (*ogil*) texture

surfaces results in the directionality of the distribution of gradient spectra $M(\omega, \theta)$. This rotation variant property, $M_{\varphi}(\omega, \theta) = M(\omega, \theta + \varphi)$, is very important to our surface rotation invariant texture classification scheme, because the directionality of a surface is an important cue to its identification.

Also, it is very interesting to note that whether the textures are isotropic ones or directional ones, the nature or shape of distributions in the gradient spectra $M(\omega, \theta)$ is insensitive to the variation of surface rotations. We note that, theoretically, the shape of the gradient distribution will be unique and unchanged for a certain texture, although it may be rotated due to surface rotation.

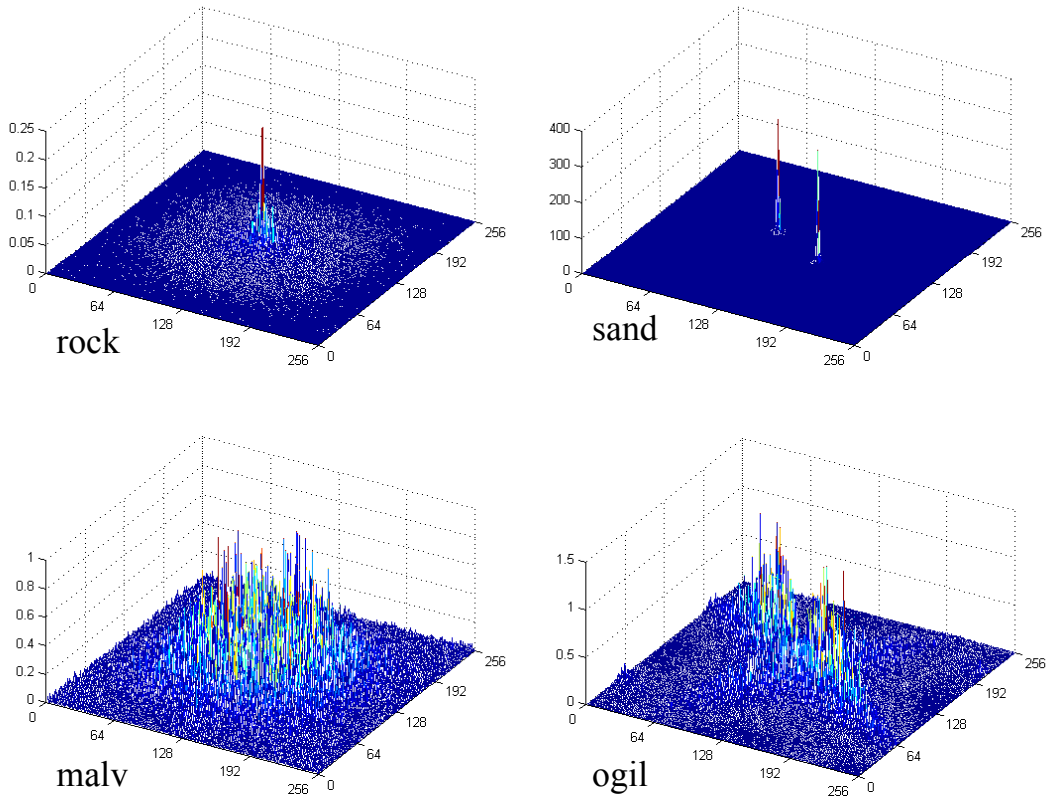

Figure 6. 8 $M(\omega, \theta)$ as a frequency distribution within a 3D gradient spectra domain for 4 synthetic textures (surface orientation $\varphi = 30°$).

By plotting gradient spectra $M(\omega, \theta)$ as a frequency distribution within a 3D gradient spectra domain, a distinctive representation of the distribution can readily be obtained as shown in *Figure 6. 8*.

We consider some of the useful information for texture description which can be interpreted from the gradient spectra $M(\omega, \theta)$:

(1) the prominent peaks in the gradient spectra give the principal direction of the texture surface;
(2) the location of the peaks gives the fundamental spatial period of the texture; and
(3) the gradient spectra are symmetric about the origin, so that only half of the frequency plane needs to be calculated.

It is the nature of the observed distributions in the gradient spectra domain that gives us very useful descriptive signatures for the observed surface textures. Considering the different textures, each texture produces a distinctive gradient spectra. For example, *rock* produces a distribution of circular pattern with an impulse in the centre, while *sand* produces two impulses linear pattern. In this case, the form and parameter of the distribution may be analysed later on and we may apply and identify these characters of distribution in gradient spectra domain and incorporate them into our surface rotation invariant texture classification scheme.

Note that in this thesis we only consider the magnitude information in gradient spectrum $M(\omega, \theta)$, while the phase information is ignored.

- ***Real textures***

Here we examine the gradient spectra $M(\omega,\theta)$ of real textures for their discrimination abilities and directionality. *Figure 6. 9* shows the gradient spectra M(ω, θ) of four real textures *(gr2, wv2, grd1, an4)* at three surface rotations $\varphi = 30°, 90°$ *and* $150°$, with the surface orientations $\varphi = 0°$. In addition, in order to show that the $M(\omega, \theta)$ functions of the rotated textures are simply a rotation of the original $(\varphi = 0°)$ $M(\omega, \theta)$ function as predicted, we plot gradient spectra $M(\omega, \theta)$ as a frequency distribution within a 3D gradient spectra domain for real textures *wv2* at surface orientations $\varphi = 0°, 30°, 60°, 90°$ (*Figure 6. 10*). This shows that the $M(\omega, \theta)$ function simply rotates by the angle of surface rotation.

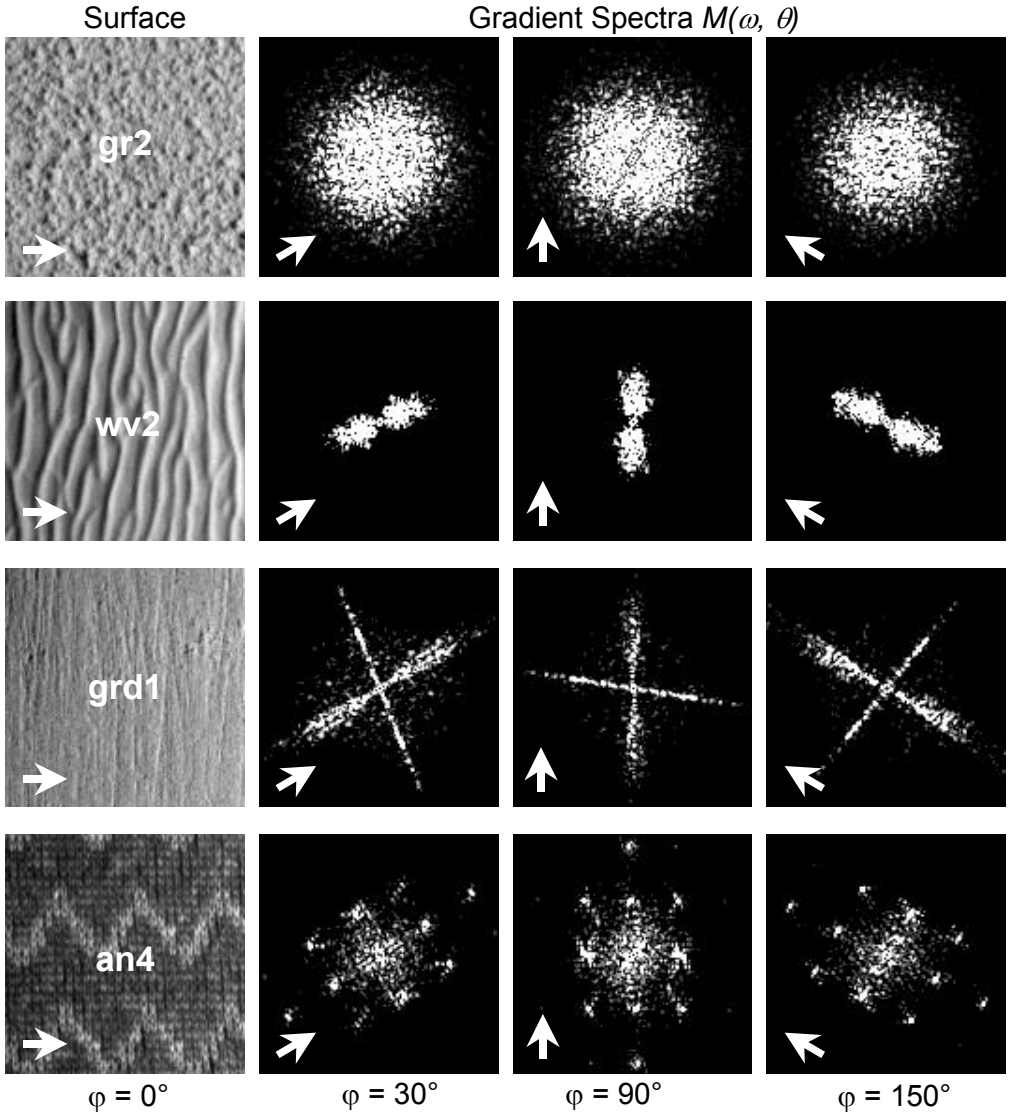

Figure 6. 9 Gradient spectra M(ω, θ) of 4 real textures (gr2, wv2, grd1, an4) at 3 surface rotations (φ = 30°, 90° and 150°). The white arrows indicate the surface corresponding orientations.

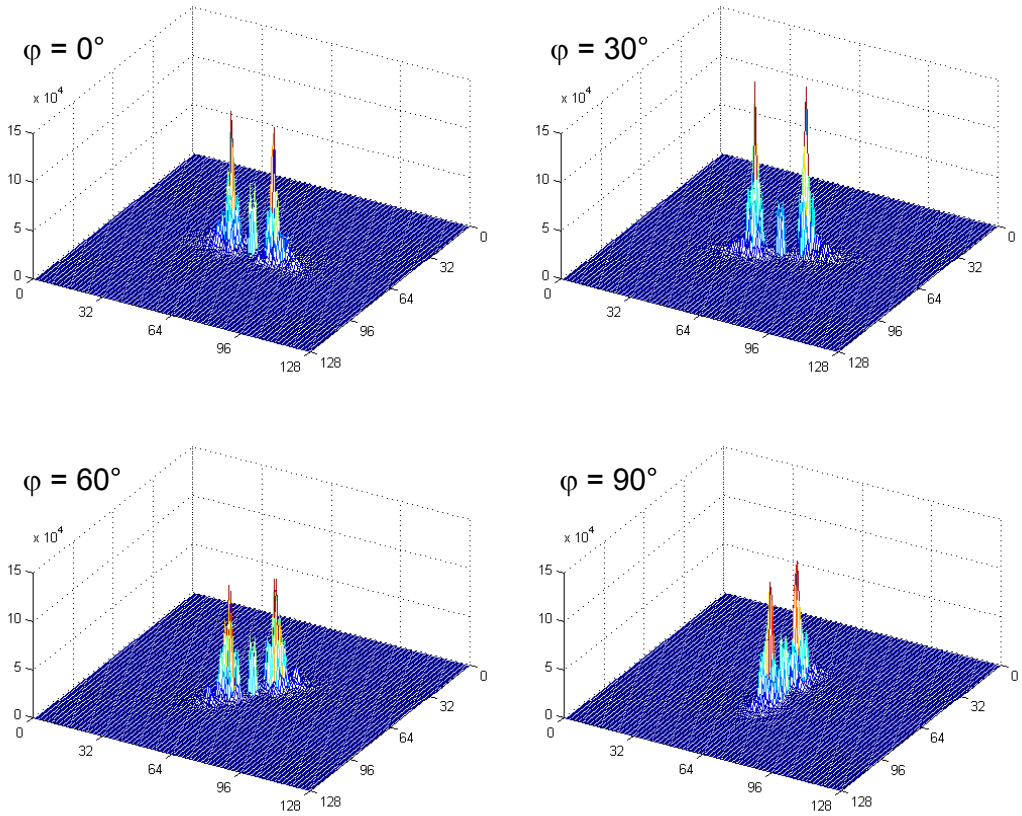

Figure 6. 10 M(ω, θ) as a frequency distribution within a 3D gradient spectra domain for real textures wv2 at surface orientation φ = 0°, 30°, 60°, 90°.

6.3.4 Summary

In the previous sections we note that in our surface rotation invariant texture classification scheme, we will directly use surface relief characteristics rather than image intensity characteristics so that the classifier will be robust to surface rotation. Therefore the surface partial derivatives are estimated using photometric stereo. It uses multiple images of the same scene obtained under different illumination orientations. However, the surface partial derivatives are not surface rotation invariant features. Moreover they represent a two dimensional vector quantity rather than a scalar field and contain directional artefacts.

Firstly, we therefore transfer the surface partial derivatives into the frequency domain and form the gradient spectra function $M(\omega, \theta)$ which is free of directional

artefacts. Secondly, we assess the discrimination ability and directionality of gradient spectra $M(\omega, \theta)$ on both synthetic textures and real textures. The results show that a rotation of the surface produces a corresponding rotation of its gradient spectrum $M(\omega, \theta)$. Also it is not surprising to note that the nature of gradient spectrum $M(\omega, \theta)$ provides very useful information relating to the type of surface structure (isotropic, directional or bi-directional) and the predominant orientation of the surface textures. Hence we may use this distinctive information in our surface rotation invariant texture classification scheme.

For classification we need to match the spectra of test and training textures in a rotation invariant manner. Comparing the gradient spectra of a test texture with those of the training classes over a complete range of rotations is computationally prohibitive. For example, for each rotated test texture sample, we have to perform *180* rotations on its gradient spectra $M(\omega, \theta)$ image in order to estimate its orientation angle between the test sample and training sample.

In the next section, we therefore use a function to compress the data but maintain their major characteristics of directionality: the *polar spectrum*. The main motivation for using polar spectrum is that we reduce the number of feature measures compared with the gradient spectrum $M(\omega, \theta)$. Polar spectrum also gives us the ability to estimate the surface orientation with less computation than those directly calculated from gradient spectra $M(\omega, \theta)$.

6.4. Polar Spectrum

6.4.1 Introduction

In this section, regarding classification we must first decide which characteristics of the texture should be measured to produce descriptive parameters. The particular resulting parameter values comprise the feature vector for each texture object. Proper selection of the features is important since only these will be used to identify the

textures. Therefore, we will initially extract useful features from gradient spectra $M(\omega, \theta)$ using the polar spectrum.

The polar spectrum can be used to generate the rotation invariant features which are sensitive to texture directionality and capture the directionality of textures at different orientations. Davis [Davis81] introduces this new tool, known as a *polarogram* and uses it to achieve invariant texture features.

We have to assess the discrimination ability of the polar spectrum, in which the features should be significantly different for the textures belonging to different classes. Regarding the surface rotation, the polar spectrum should have the ability of reliability in order to enable the classifier to be robust to variance of the surface orientations and also have the ability to estimate the surface orientation angle. The advantages and drawbacks of the polar spectrum are hence considered.

Finally, we test the polar spectrum which is derived from gradient spectra $M(\omega, \theta)$ on both synthetic textures and real textures.

6.4.2 Definition of Polar Spectrum

The polar spectrum is calculated by integration of all the contributions (or values) along a line of orientation θ passing through the origin in the image of gradient spectra $M(\omega, \theta)$. We can then calculate the function of polar spectrum $\Pi(\theta)$ as:

$$\Pi(\theta) = \int_0^{\infty} M(\omega, \theta)\, d\omega \qquad (6.8)$$

That means the polar spectrum adds the magnitudes of all frequencies in one certain direction θ to produce a measure for the intensity in this direction. All these frequencies are lying in a radial line. The output of the polar spectrum is the variance as a function of the angle θ. This plot is used for illustrating directionality in the image. We illustrate the definition of polar spectrum in *Figure 6. 11* by demonstrating two textures (isotropic texture *gr2* and directional texture *grd1*).

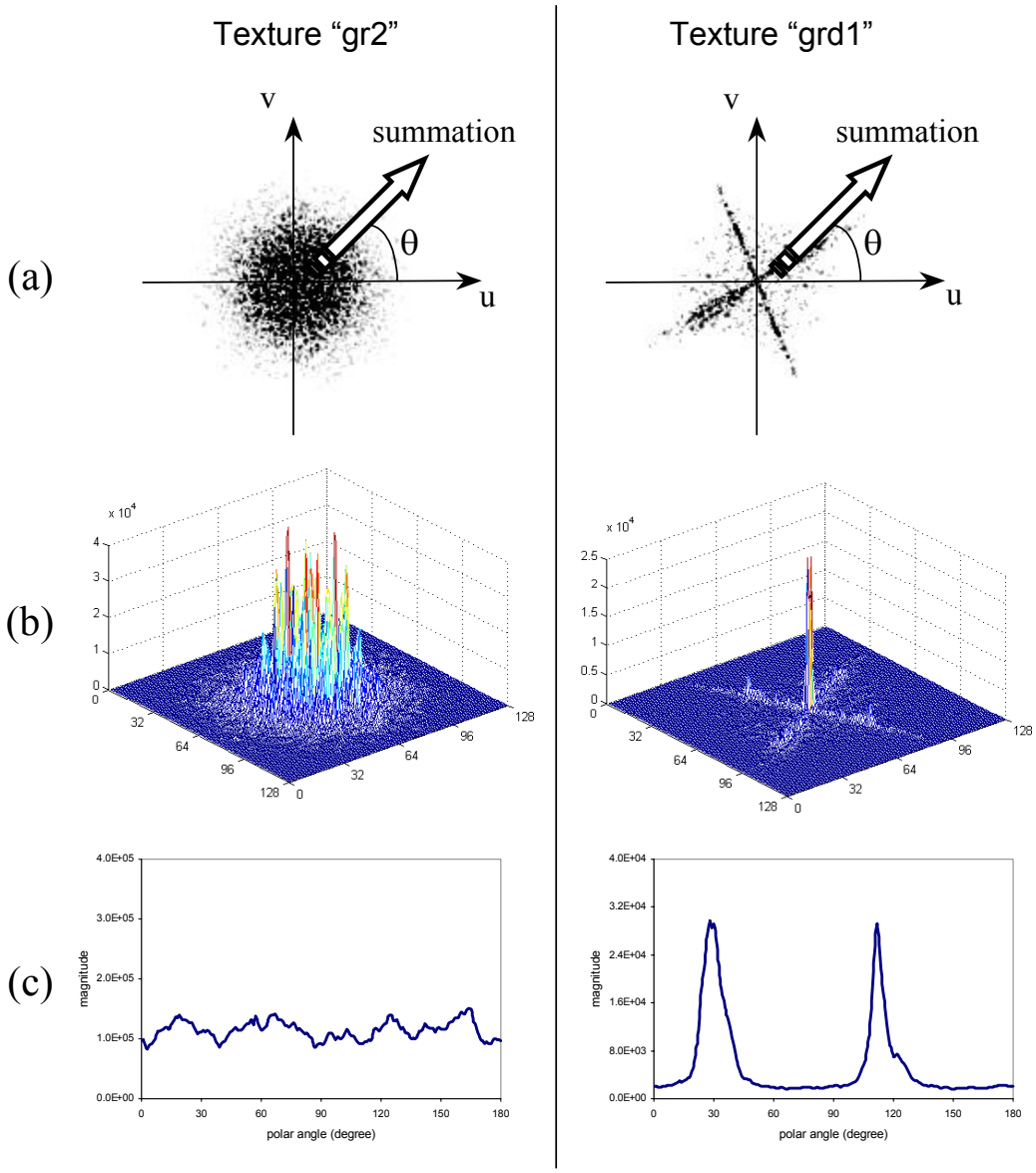

Figure 6. 11 Definition of polar spectrum Π(θ) on gradient spectra M(ω, θ) by demonstrating two textures, gr2(left column) and grd1 (right column). (a). graphical representation of polar spectrum on gradient spectra M(ω, θ); (b). M(ω, θ); (c). Polar spectra.

Note that

$$\Pi_{\phi}(\theta) = \int_{0}^{\infty} M_{\phi}(\omega,\theta)\,d\omega = \int_{0}^{\infty} M(\omega,\theta+\phi)\,d\omega = \Pi(\theta+\phi) \qquad (6.9)$$

thus a rotation of φ of a surface produces a translation of φ in the polar spectrum.

The polar spectrum $\Pi(\theta)$ is derived from the gradient spectrum $M(\omega, \theta)$ simply by expressing the spectrum in polar coordinates. It is obvious that the texture's gradient spectra are rotation dependent and it is a periodic function of θ with a period of π.

Recalling the *Figure 6. 11*, we may note that the polar spectrum of directional texture *grd1* shows prominent peaks at intervals of $90°$, which clearly correspond to the periodicity in the gradient spectra. Moreover, in the gradient spectra $M(\omega, \theta)$ of texture *grd1* is directional and so the polar spectrum $\Pi(\theta)$ tends to be a peak (at $\theta=30°, 120°$). On the other hand, there are no peaks or marked directionality in the polar spectrum of isotropic texture *gr2*. This observation indicates the usefulness of the polar spectrum $\Pi(\theta)$ in summarising the directional properties of a texture.

6.4.3 Drawbacks and Solutions

Prior to discussing the properties of the polar spectrum in terms of directionality and the effects of surface rotation, we have to consider some of its drawbacks.

- **Interpolation**

The gradient spectra are calculated by using a discrete FFT. Hence the polar spectrum $\Pi(\theta)$ (equation *(6. 8)*) is obtained by summing discrete coefficient values:

$$\Pi(\theta) = \sum_{\omega=1}^{R} M(\omega, \theta) \qquad (6.10)$$

where R is the radius high frequency range of a circle centred at the origin. For an $N \times N$ gradient spectra $M(\omega, \theta)$, R is typically chosen as $N/2$.

Therefore, while calculating the value of $\Pi(\theta)$, noises will be introduced since the gradient data is produced in a Cartesian described from $M(\omega, \theta)$ and has a finite resolution. In *Figure 6. 12(a)*, we note that some of the points on the calculating line of *R2* at the polar angle θ do not correspond to any points of the $M(\omega, \theta)$ spectra,

compared to those points along the line of *R1*. An interpolation algorithm was implemented in order to estimate the new point values on the line of *R2*. Depending on the amount of detail present in the spectrum along with the final requirements of the images, an appropriate interpolation scheme may be employed. In our circumstance, since a pixel falling between locations will always be somewhere in between four valid pixel locations, four pixels (*pt.1, pt.2, pt.3 and pt.4*) surrounding the calculated pixel location (*desired pt.*) will be used to contribute to the estimation of the desired coefficient, shown in *Figure 6. 12 (b)*.

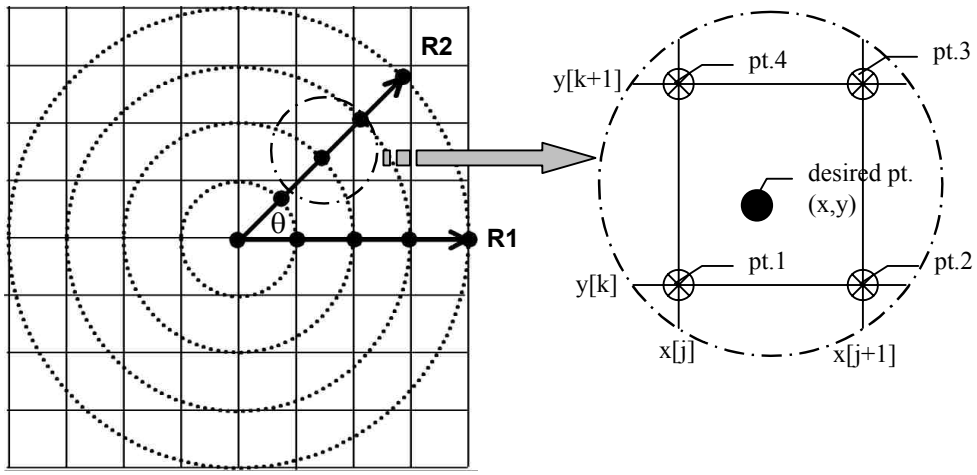

Figure 6. 12 Illustrating effect of interpolation while calculating polar spectrum Π(θ) from discrete Cartesian M(u,v) spectra. (a). Effect on a grid square. (b). Definition of the grid square.

The simplest interpolation is *bilinear* interpolation in the grid square [Press92]. The aim of this interpolation is to estimate the function *f(x,y)* at some untabulated point (x_i, y_i). This can be performed using the values of the function at the four tabulated points that surround the desired interior point. This is illustrated in *Figure 6. 12(b)*. This figure defines j and k as:

$$\begin{aligned} x[j] \le x_i \le x[j+1] \\ y[k] \le y_i \le y[k+1] \end{aligned} \qquad (6.11)$$

and then

$$
\begin{aligned}
f_1 &= \mathrm{f}\,(\,x[j], y[k]\,) \\
f_2 &= \mathrm{f}\,(\,x[j+1], y[k]\,) \\
f_3 &= \mathrm{f}\,(\,x[j+1], y[k+1]\,) \\
f_4 &= \mathrm{f}\,(\,x[j], y[k+1]\,)
\end{aligned}
\qquad (\,6.\,12\,)
$$

The formulae of the interpolation is then given by :

$$
\begin{aligned}
t &\equiv \frac{x_i - x[j]}{x[j+1] - x[j]} \\
u &\equiv \frac{y_i - y[k]}{y[k+1] - y[k]}
\end{aligned}
\qquad (\,6.\,13\,)
$$

$$
y(x_i, y_i) = f_1 \times (1-t) \times (1-u) + f_2 \times t \times (1-u) + f_3 \times (1-u) \times t + f_4 \times t \times u \qquad (\,6.\,14\,)
$$

- **Frequency range selection : low frequency f_{low}**

One of the problems with the interpolation algorithm is that the estimated point values near the centre frequency ($\omega=1$) provide poor angular resolution. Therefore, we modify the definition of polar spectrum $\Pi(\theta)$ in equation *(6. 10)* to a band-pass filter:

$$
\Pi\ (\theta) = \sum_{\omega=f_{low}}^{f_{high}} M(\omega, \theta) \qquad (\,6.\,15\,)
$$

where f_{low} and f_{high} are used in the band-pass filter, which is illustrated in *Figure 6. 13*.

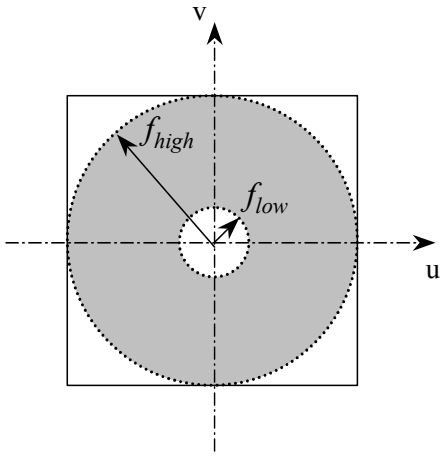

Figure 6. 13 Frequency range selection of band-pass filter while calculating polar spectrum.

This effect can readily been seen in *Figure 6. 14*, which plots the polar spectrums of texture "*grd1*" derived from calculations in different low frequency ranges *(ω = 1, ω = 2, and ω = 8)*. For the size of $N \times N$ gradient spectra $M(\omega, \theta)$, f_{high} is set to $N/2$ as default, while we change the f_{low} to the value of *1*, *2* and *8* respectively. It is clear to see that the peaks of *A1* and *A2* in the polar spectrum with $f_{low} = 1$ are the correct ones derived from the dominant directionalities in gradient spectra $M(\omega, \theta)$. However, the peaks of *B1* and *B2* come from the interpolation noise at certain polar angles θ of about $45°$ and $135°$ respectively and do not correspond to the directionality in the gradient spectra $M(\omega, \theta)$. On the other hand, increasing the low frequency range f_{low} to the value of *8*, the noise disappears due to the increased angular resolution at this frequency.

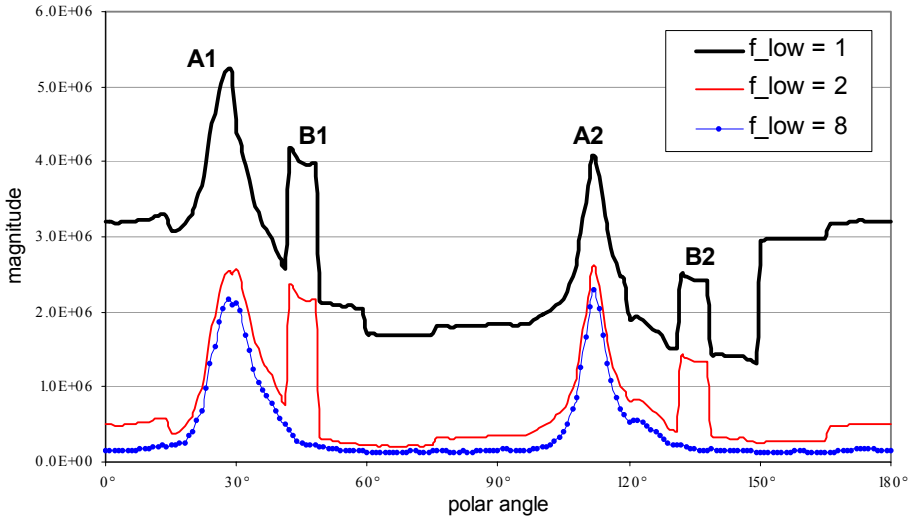

Figure 6. 14 Polar spectrums of texture "grd1" derived from calculating in different low frequency ranges ($\omega = 1$, $\omega = 2$, and $\omega = 8$).

It is worth noticing that increasing the low frequency range results in decreasing the polar spectra magnitude or energy. This is illustrated in *Figure 6. 15*.

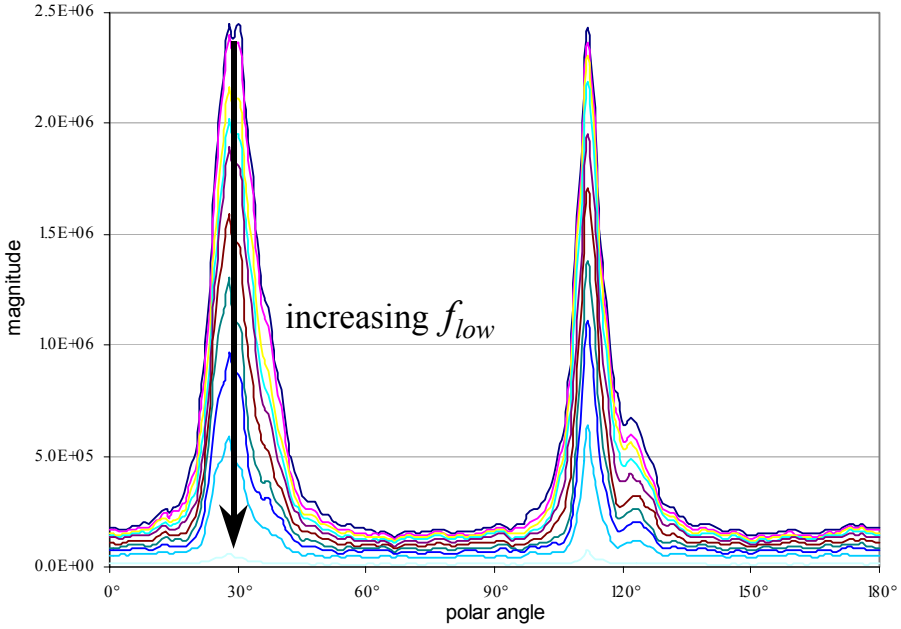

Figure 6. 15 Increasing the low frequency range results in decreasing the polar spectra magnitude or energy as more and more components of M(u, v) are neglected (low frequency value f_{low} starts from 4 to 64) for texture grd1.

In general, the estimated point values near the centre frequency ($\omega=1$) provide poor angular resolution (*Figure 6. 14*). On the other hand, increasing the low frequency range results in decreasing the polar spectra magnitude (*Figure 6. 15*). We decide to set the low frequency range starting at the value of 8.

- **Frequency range selection : high frequency f_{high}**

Regarding equation *(6. 15)*, the band-pass filter is applied to the gradient spectra. In this case we will also lose some of the information in high frequency range. However, most of the image power is concentrated in the low frequency components. This is highlighted by circles superimposed at different radii on the gradient spectra. We calculate the proportion of the total sum of gradient spectra $M(\omega, \theta)$ over the entire domain contained within each circle, then we find the relationship shown in the *Table 6. 1* ($f_{low}= 1$). We note that with the high frequency f_{high} set to *64*, the image width of gradient spectra will be *128* and we still have most of the power *(99.35%)* of the image. Therefore, we will set gradient spectra size to *128 × 128* pixels as the default setting in further investigations, since it will give us enough information for the post-processing.

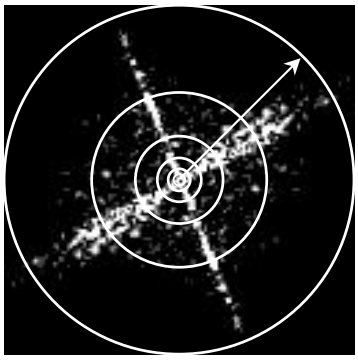

$2 \times f_{high}$ (cycles/image-width)	% image power
2	71.80%
4	81.95%
8	84.71%
16	89.92%
32	96.33%
64	99.35%
128	99.98%

Table 6. 1 The percentage of gradient spectra power $M(\omega, \theta)$ with increasing high frequency f_{high} for texture grd1 ($f_{low}= 1$).

6.4.4 Polar Spectrum is a Function of Texture Directionality

In this section, we will test the polar spectrum as a function of texture directionality using four synthetic textures and four real textures.

- ***Synthetic textures***

Polar spectra of the four selective synthetic textures *(rock, sand, ogil and malv)* defined in chapter 3 on gradient spectra $M(\omega, \theta)$ at surface rotation of $\varphi = 30°$ are shown in *Figure 6. 16*. It is interesting to note that there are no marked peaks on the polar spectrum for isotropic texture *rock* and *malv*, while there is a sharp peak *A* at the polar angle $\theta = 30°$ on the polar spectrum of the directional texture *sand*. There are two peaks, *B1* at the polar angle $\theta = 30°$ and *B2* at the polar angle $\theta = 120°$, on the polar spectrum of the bi-directional texture *ogil*, although *B2* is not the dominant direction having viewed the original surface. In general, all of the peaks appearing on the polar spectrum do correspond to the directionality of the original textures.

- ***Real textures***

We repeat this process on four selective real textures *(gr2, wv2, grd1* and *an4)*. The results are shown below in *Figure 6. 17*. The same conclusions can also be made: the polar spectrum is a function of texture directionality. It is obvious that for a given texture surface, the texture directionality varies with change of orientation. These changes in directionality can be captured by the polar spectrum. For example, the directionality of texture *wv2* can be characterised by peak *A*, on the other hand, the directionalities of texture *an4* may be presented as peaks *D*, *E* and *F* in its corresponding polar spectrum $\Pi(\theta)$.

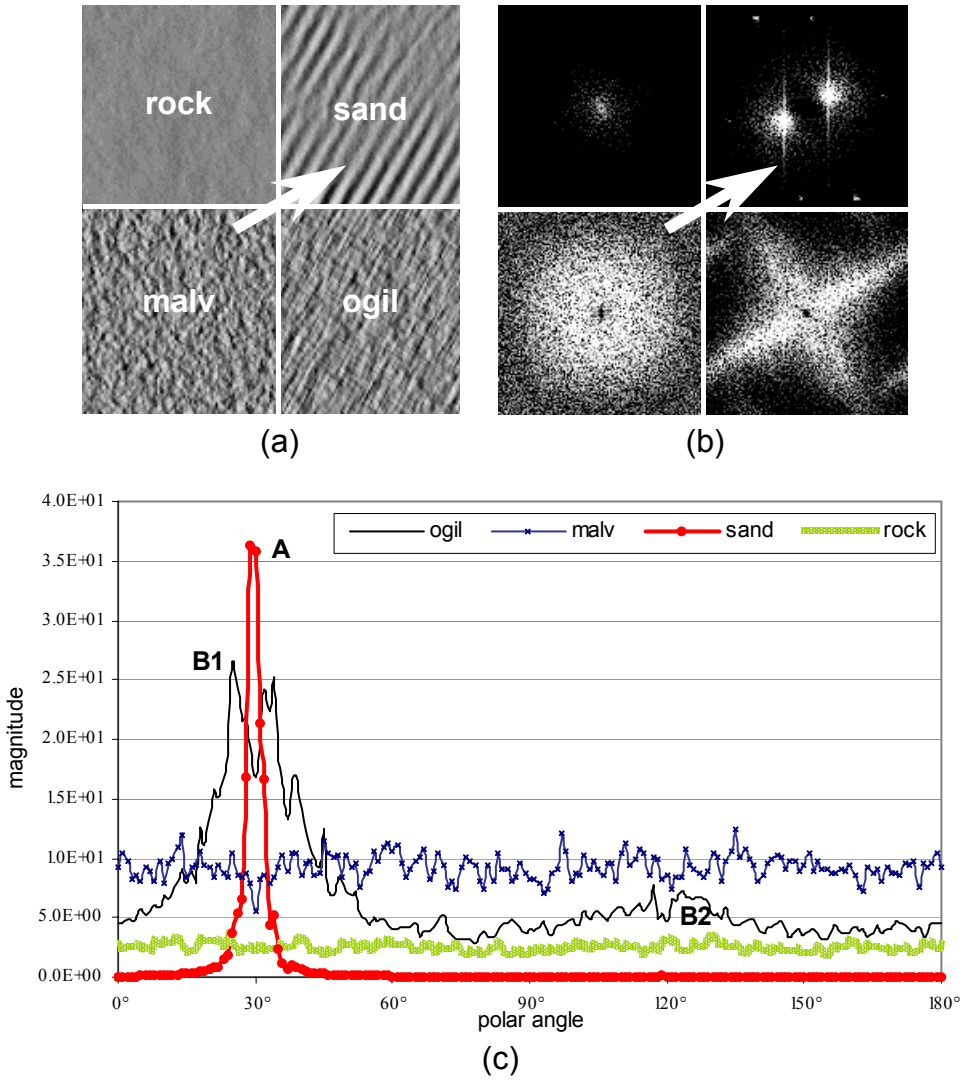

Figure 6. 16 Polar spectrums of four selective synthetic textures (rock, sand, ogil and malv) on gradient spectra M(ω, θ) at surface rotation of φ = 30°. (a). surface at constant tilt angle τ = 0°; (b) gradient spectra; (c) polar spectrum.

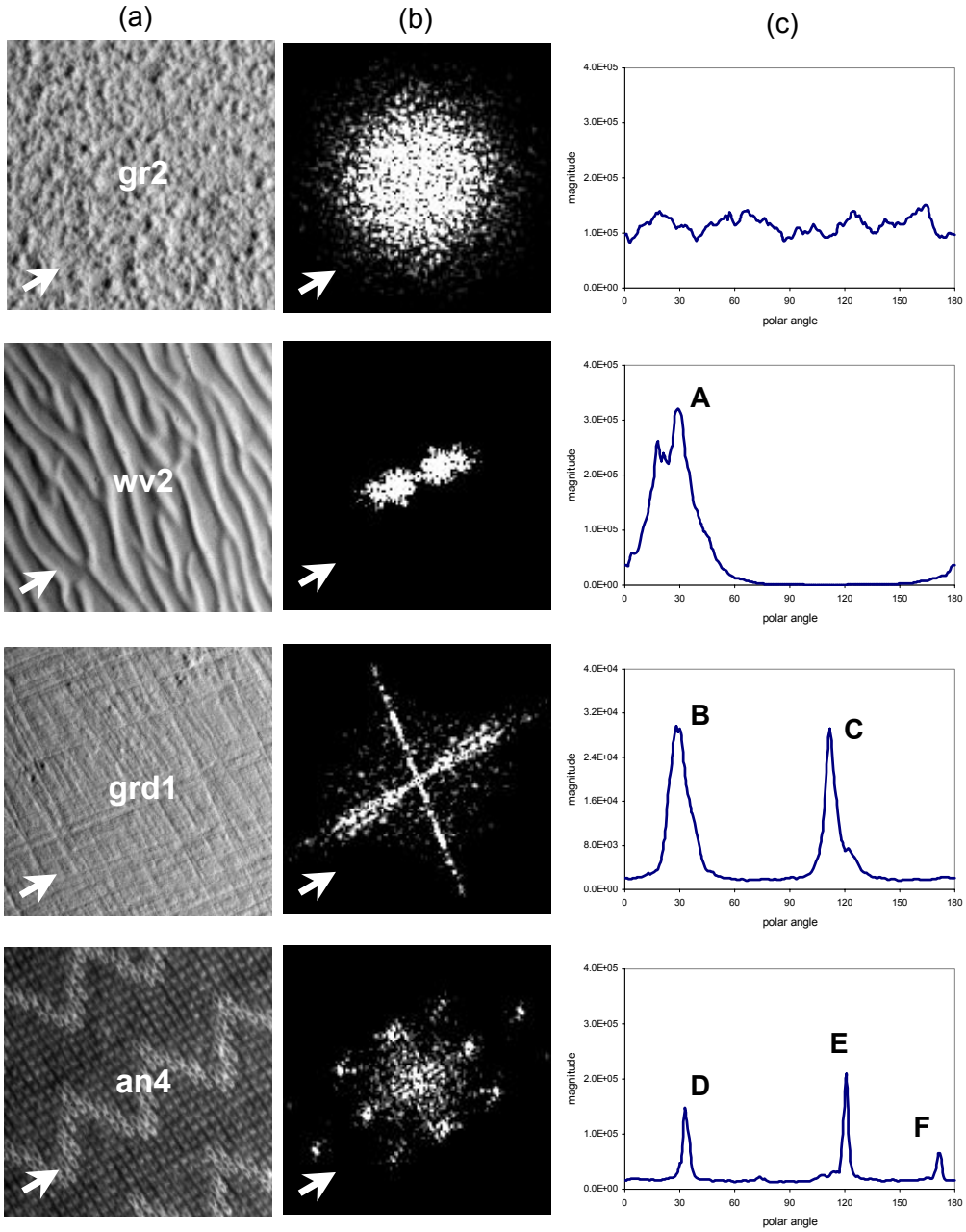

Figure 6. 17 Polar spectrums of four selective real textures (gr2, wv2, grd1 and an4) on gradient spectra $M(\omega, \theta)$ at a surface rotation of $\varphi = 30°$. (a). surface at constant tilt angle $\tau = 0°$; (b) gradient spectra; (c) polar spectrum.

6.4.5 Polar Spectrum at Different Surface Orientations

Note that while both gradient spectra $M(\omega,\theta)$ and its polar spectrum do not theoretically contain any directional artefacts such as a directional filtering effect,

they are, rotationally sensitive. That is, if the surface is rotated by an angle φ then a new gradient spectra $M_\varphi(\omega,\theta)$ and a new polar spectrum $\Pi_\varphi(\theta)$ will result (see *Figure 6. 18*), such that in theory:

$$\Pi_\varphi(\theta) = \Pi(\theta+\varphi) \qquad (6.16)$$

This implies that a rotated texture's polar spectrum $\Pi_\varphi(\theta)$ is equivalent to a translation of its polar spectrum $\Pi(\theta)$ by the same amount φ along the orientation axis. For comparison images taken under surface rotation are shown individually and all captured images are at a constant illuminant tilt angle τ = 0° (90° and 180° illuminant tilt angle images are also captured for the photometric stereo process but are not shown here). Comparison of the images at $\varphi = 0°$ and $\varphi = 90°$ shows that they are not simple rotations of each other. In the image corresponding to $\varphi = 0°$ the vertical lines of the texture are clearly presented. While in the image corresponding to $\varphi = 90°$ the texture has been attenuated and the lines which should be horizontal are no longer visible.

On the other hand, this is not surprising. *Figure 6. 19* illustrates the relationship between $\Pi_\varphi(\theta)$ and $\Pi(\theta + \varphi)$. By depicting the polar spectrums of the rotated *"wv2"* surface, this shows that a rotated texture's polar spectrum is an approximate translation of the unrotated texture's polar spectrum, and that the degree of each translation approximates to the corresponding rotation of the surface.

6.4.6 Estimation of Surface Orientation via Polar Spectrum

Obviously since the polar spectrum is rotationally sensitive, we cannot directly use polar spectra for surface rotation invariant classification. We have to estimate the surface orientation angle first for each test texture and then compare the test texture's polar spectrum to the training textures' polar spectra. This is done by translating each by the estimated surface orientation angle.

In the section, we will estimate the surface orientation angle of the polar spectrum by using the simple sum of squared difference metric. The estimation process will be presented in the next section. We also discuss surface orientation estimation obtained from gradient spectra and gradient space.

- ***Estimation of surface orientation***

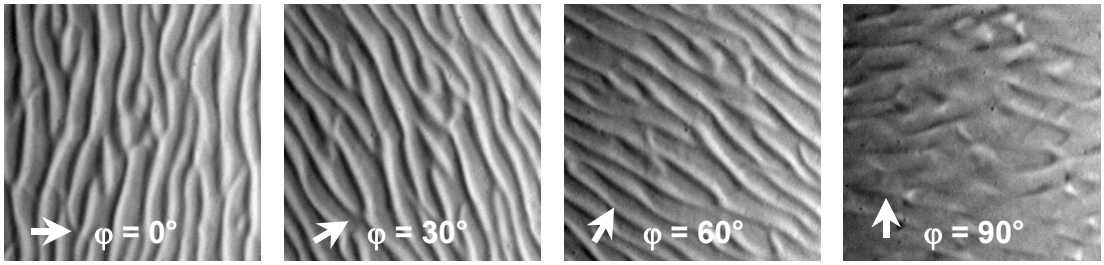

(a) surface

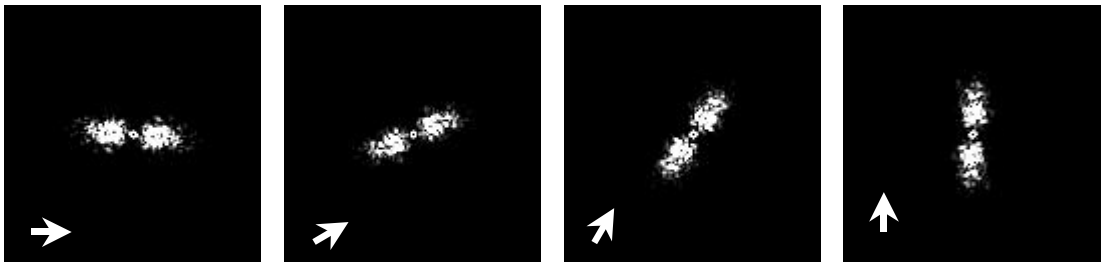

(b) gradient spectra

Figure 6. 18 Textures "wv2" on gradient spectra M(ω, θ) at different surface rotations of φ = 0°, 30°, 60° and 90° (the white arrows indicate the surface orientations). (a) surface at constant tilt angle τ = 0°; (b) gradient spectra.

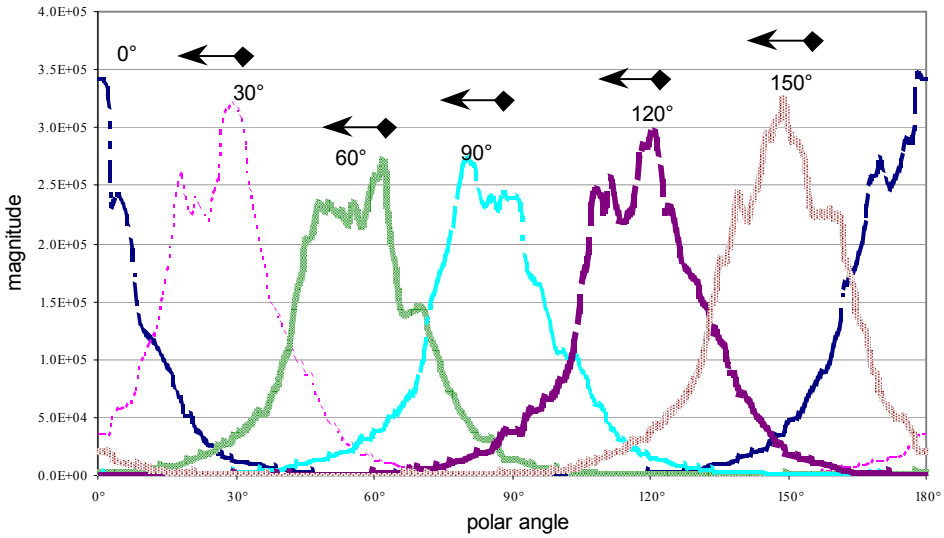

Figure 6. 19 Polar spectrums of real textures "wv2" at surface rotations of φ = 0°, 30°, 60°, 90°, 120° and 150°.

Figure 6. 19 shows polar spectra of real textures *"wv2"* at surface rotations of φ = *0°, 30°, 60°, 90°, 120°* and *150°*, some examples of corresponding gradient spectra $M(\omega, \theta)$ are shown in *Figure 6. 18.* As the polar spectrum provides a measurement of texture directionality. It can be used to estimate its orientation. From *Figure 6. 19*, we note that a rotated texture's polar spectrum is approximately a translation of the non-rotated texture's polar spectrum. Thus we must compare polar spectrums over a range of angular displacements (φ_{test} = 0°, 1°, 2°, ….180°) in order to determine the degree of correspondence and the relative angle of two surfaces. We use the sum of squared difference metric function *SSD* to measure the distance between two polar spectrums:

$$SSD(\varphi_{est}) = \min\left\{ \sum_{\theta=0°}^{180°} [\,\Pi_{rotated}(\theta + \varphi_{est}) - \Pi_{unrotated}(\theta)\,]^2 \right\} \qquad (6.17)$$

where φ_{test} = 0°, 1°, 2°, ….180°. When the cost function of $SSD(\varphi_{test})$ is minimised the angular displacement φ_{test} in the polar spectrum will be the relative angle of these two surfaces.

- ***Estimation results from directional and isotropic textures***

Table 6. 2 shows the estimated angles of surface orientation for real and directional texture "*wv2*" obtained from polar spectra. Four sample images are constructed from the images of the textures rotated individually in *Table 6. 2 (a)*. We note that the results of estimated angles in *Table 6. 2 (b)* shows good performance for this directional texture "*wv2*", while the maximum error in the angle is *2°*.

On the other hand, *Table 6. 3* gives the estimated angles of surface orientation for the real isotropic texture "*gr2*" obtained from polar spectra. We can see that the estimation that took place with the surface orientation angle $\varphi = 90°$ has failed, and the error in the angle increased to *82°*.

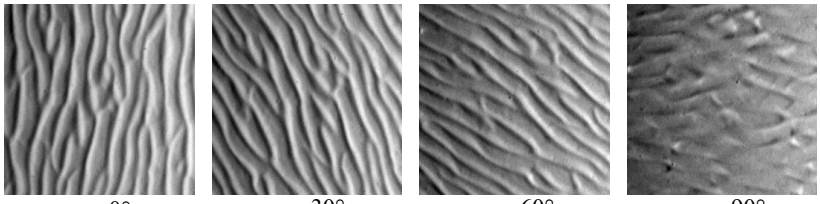

(a)

Original surface rotation angles φ	30°	60°	90°	120°	150°	180°
Estimated angles obtained from polar spectrums	30°	60°	90°	122°	152°	179°
Error	***0°***	***0°***	***0°***	***+2°***	***+2°***	***-1°***

(b)

Table 6. 2 The estimated angles of surface orientation for the real directional texture "wv2" obtained from polar spectra. (a) some rotated surface samples at orientation angle of $\varphi = 0°, 30°, 60°$ and $90°$, while the tilt angle τ is kept constant at 0°; (b) estimation error.

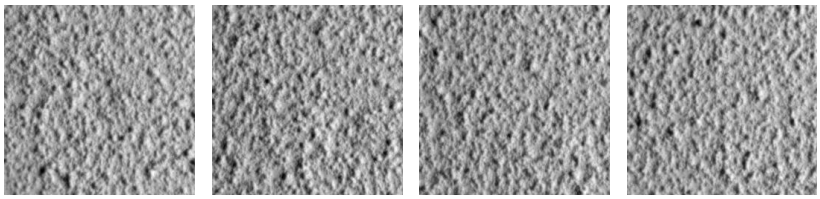

φ = 0° φ = 30° φ = 60° φ = 90°

(a)

Original surface rotation angles φ	30°	60°	90°	120°	150°	180°
Estimated angles obtained from polar spectrum	30°	60°	8°	121°	151°	181°
Error	***0°***	***0°***	***-82°***	***+1°***	***+1°***	***+1°***

(b)

Table 6. 3 The estimated angles of surface orientation for the real isotropic texture "gr2" obtained from polar spectra. (a) some rotated surface samples at orientation angle of φ = 0°, 30°, 60° and 90°, while the tilt angle τ is kept constant at 0°; (b) estimation error.

Regarding the isotropic texture, it would be difficult to achieve better accuracy than the directional texture, because there are no obvious peaks within the polar spectrum. In this case, translating the polar spectrum $\Pi(\theta)$ may not give the correct estimation. This means that we cannot estimate the direction of an isotropic texture from the polar spectrum $\Pi(\theta)$.

- ***Comparison with those estimated from gradient spectra and gradient space***

Figure 6. 20 shows the estimates of the surface orientation angle for four synthetic textures (*rock, sand, ogil and malv*) obtained from polar spectrum $\Pi(\theta)$, gradient spectra $M(\omega, \theta)$ and gradient space $G(x, y)$. Regarding the four different textures, the estimated orientation angle obtained by the polar spectrum $\Pi(\theta)$ has the highest accuracy. In this case, most of the error angles are under $2°$ apart from one at an angle of $8°$. Those obtained by the gradient space $G(x, y)$ have the worst estimation results. While the resulting estimation angle obtained by the 2D gradient spectra $M(\omega, \theta)$ can be thought of as reasonable.

Comparing results for the different textures, the performance of the estimation on the isotropic ones (*rock* and *malv*) is worse than that for the directional ones. We also note that the estimation processing failed for the isotropic texture *rock* and *malv* in the gradient space *G(x, y)*. This is because the distribution of the gradient space for those textures does not relate well to the surface orientation and leads to the failure of the surface rotation at an angle of about *0°*. As previously mentioned, our estimation results based on the frequency domain methods (gradient spectra and polar spectrum) are much better than those obtained with the spatial domain method (gradient space).

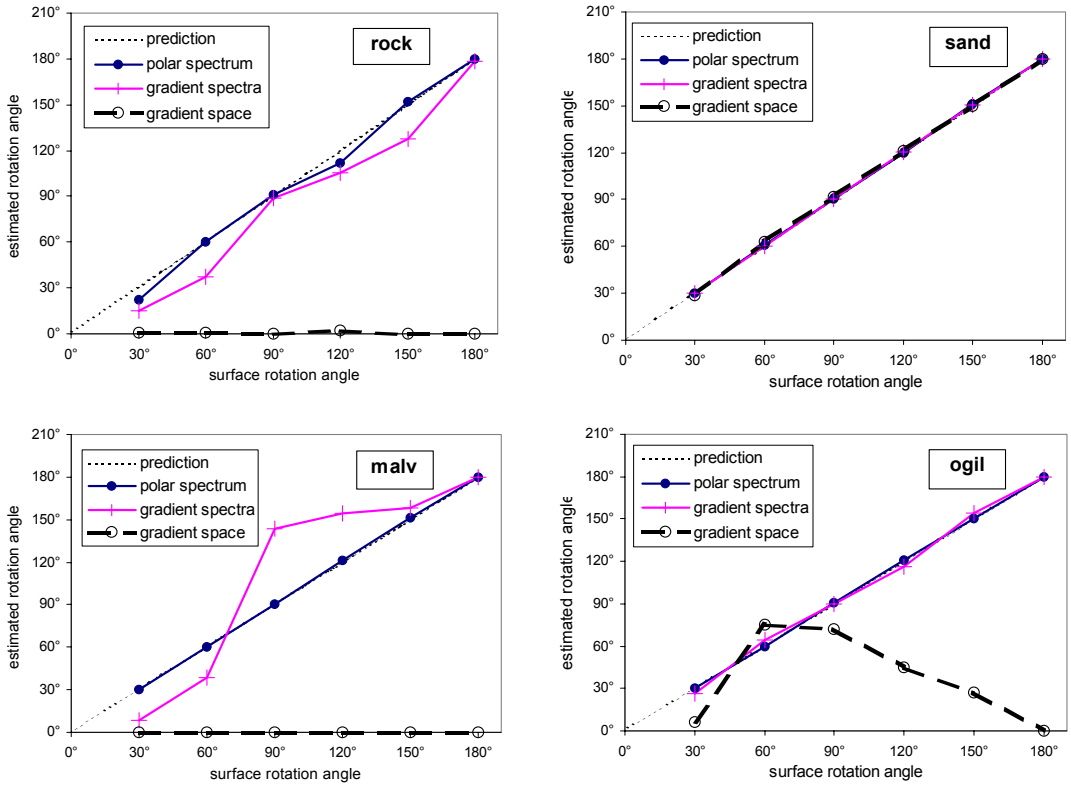

Figure 6. 20 Comparing the estimations of the surface orientation angle for four synthetic textures (rock, sand, ogil and malv) obtained from polar spectrum Π(θ), gradient spectra M(ω, θ) and gradient space G(x, y).

6.4.7 Summary

In the section, the polar spectrum technique was introduced. It enables us to reduce the dimension of feature space from 2D gradient spectra *M(ω, θ)* to a 1D polar

spectrum $\Pi(\theta)$, while maintaining the majority of useful characteristics. In addition, it also avoids the heavy computation resulting from comparing the gradient spectra $M(\omega, \theta)$ of a test texture with those of the training textures over a complete range of rotations.

Noises due to the discrete Cartesian nature of $M(\omega, \theta)$ were investigated and reduced using interpolation and a low frequency integration limit. Next, two of the main properties of the polar spectrum were investigated:

- the polar spectrum as a function of texture directionality, and
- the polar spectrum as a function of surface orientation.

Regarding these two important aspects, we confirm that a rotated texture's polar spectrum is an approximate translation of the non-rotated texture's polar spectrum and that the degree of each translation approximates to the corresponding rotation of the surface. This property of the polar spectrum allows us to estimate the surface orientation or rotation angle by comparing the polar spectrums over a range of angular displacements using the sum of the squared difference function. Finally, we discuss a comparative study on the estimation of surface orientation angles obtained from polar spectra $\Pi(\theta)$, gradient spectra $M(\omega, \theta)$ and gradient space $G(x, y)$. The results of estimation based on the polar spectrum $\Pi(\theta)$ gives the best accuracy.

In the next section, we will develop classifier using features obtained from the polar spectrum and illustrate how it works.

6.5. Classifier

In this section we will illustrate how the classifier works based on the goodness-of-fit measurement and also consider the corresponding estimated surface orientation obtained by this method.

In *Figure 6. 21*, we illustrate the goodness-of-fit measurement of the test texture's polar spectrum (*wv2* at $\varphi = 60°$) and compare it to four training textures' polar spectra obtained at the surface orientation angle $\varphi = 0°$. Consequently, the sum of squared difference (SSD) metric between the test texture *wv2* ($\varphi = 60°$) and four training textures ($\varphi = 0°$), and their corresponding estimated surface orientation angles are listed in *Table 6. 4*. We note that the minimal value of SSD *(1.14e+11)* is only achieved between the polar spectrum of the test texture *wv2* and its training polar spectrum. Moreover the estimated surface orientation angle φ_{test} *(60°)* is exactly equal to the angular displacement between the test polar spectrum and the training one for texture *wv2*. While on the other hand, the estimated surface orientation angle φ_{test} between the test texture *wv2* and the other two directional training texture (*an4* and *grd1*) is also found to be *57°* and *55°* respectively. This is because all of them have a peak of distribution at a polar angle of approximately *0°*. This illustrates that SSD evaluation can be effective.

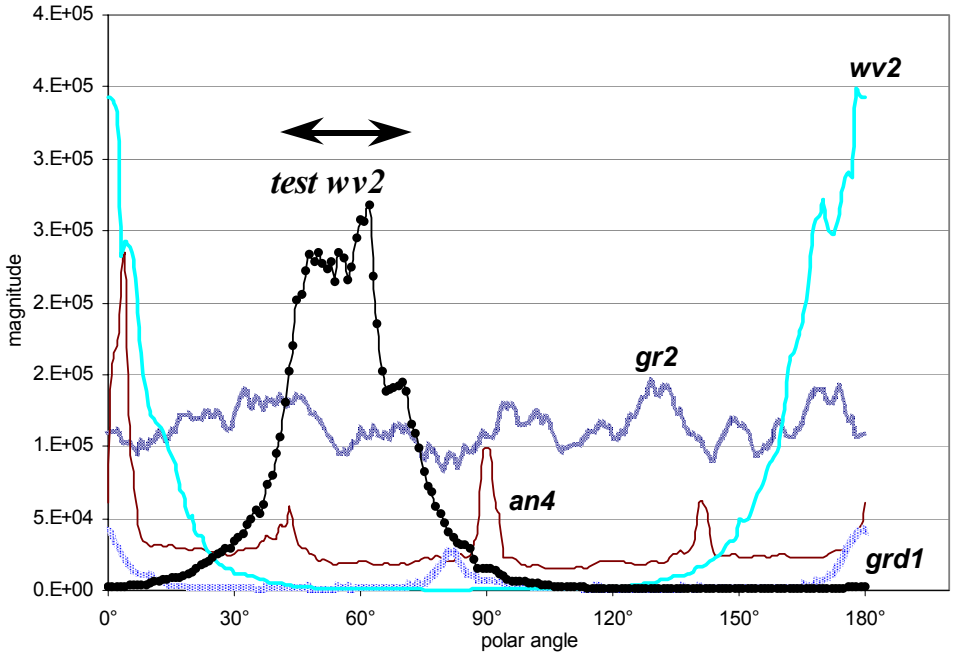

Figure 6. 21 Goodness-of-fit measurement for testing a texture's polar spectrum (wv2 at $\varphi = 60°$) against four training textures' polar spectra obtained at the surface orientation angle $\varphi = 0°$

Training textures (φ=0°)		***an4***	***gr2***	***grd1***	***wv2***
Testing texture wv2 (φ=60°)	SSD	*8.17e+11*	*1.74e+12*	*1.15e+12*	*1.14e+11*
	Estimated angle φ_{test}	*57°*	*23°*	*55°*	*60°*

Table 6. 4 Sum of squared difference (SSD) values between the test texture wv2 (φ = 60°) and four training textures (φ = 0°), together with their corresponding estimated surface orientation angles.

6.6. Summary of the Complete Algorithm

6.6.1 Surface Rotation Invariant Classification Scheme Using Photometric Stereo (Surface Information)

Now it is time to illustrate the complete surface rotation invariant classification scheme in *Figure 6. 22*. The process is as follows:

1. A photometric image set of the texture to be classified is captured by a digital camera which is fixed above the 3D rotated surface texture sample (i.e. three images are taken at illuminant tilt angles of *0°*, *90°* and *180°* respectively).
2. The photometric stereo algorithm uses this image set to estimate the surface partial derivatives *p(x,y)* and *q(x,y)*. This enables us to use surface relief characteristics rather than the image intensity characteristics so that the classifier is to be robust to surface rotation.
3. However, the surface partial derivative *p(x,y)* and *q(x,y)* are not surface rotation invariant features and they are vectors containing directional artifacts as well. Therefore, they are Fourier transformed into $P(\omega, \theta)$ and $Q(\omega, \theta)$, and combined to provide the corresponding gradient spectra $M(\omega, \theta)$ which are free of directional artifacts.
4. Gradient spectra $M(\omega, \theta)$ are processed to provide polar spectra $\Pi(\theta)$. This compresses the data from 2D to 1D while maintaining the major directional characteristics. It also avoids the heavy computations involved in comparing the gradient spectra $M(\omega, \theta)$ of a test texture with those of the training texture over a

complete range of rotations.

5. The polar spectrum is compared with the polar spectra obtained from training images over a range of angular displacements (φ_{test}) using a sum of squared differences metric. The comparison results in the corresponding surface orientation angle since a rotated texture's polar spectrum is an approximate translation of the non-rotated texture's polar spectrum.
6. The total sum of squared difference metric calculated from step *5* and the best combination provides a classification decision based on the goodness-of-fit measurement and an estimate of the relative orientation of the test texture.

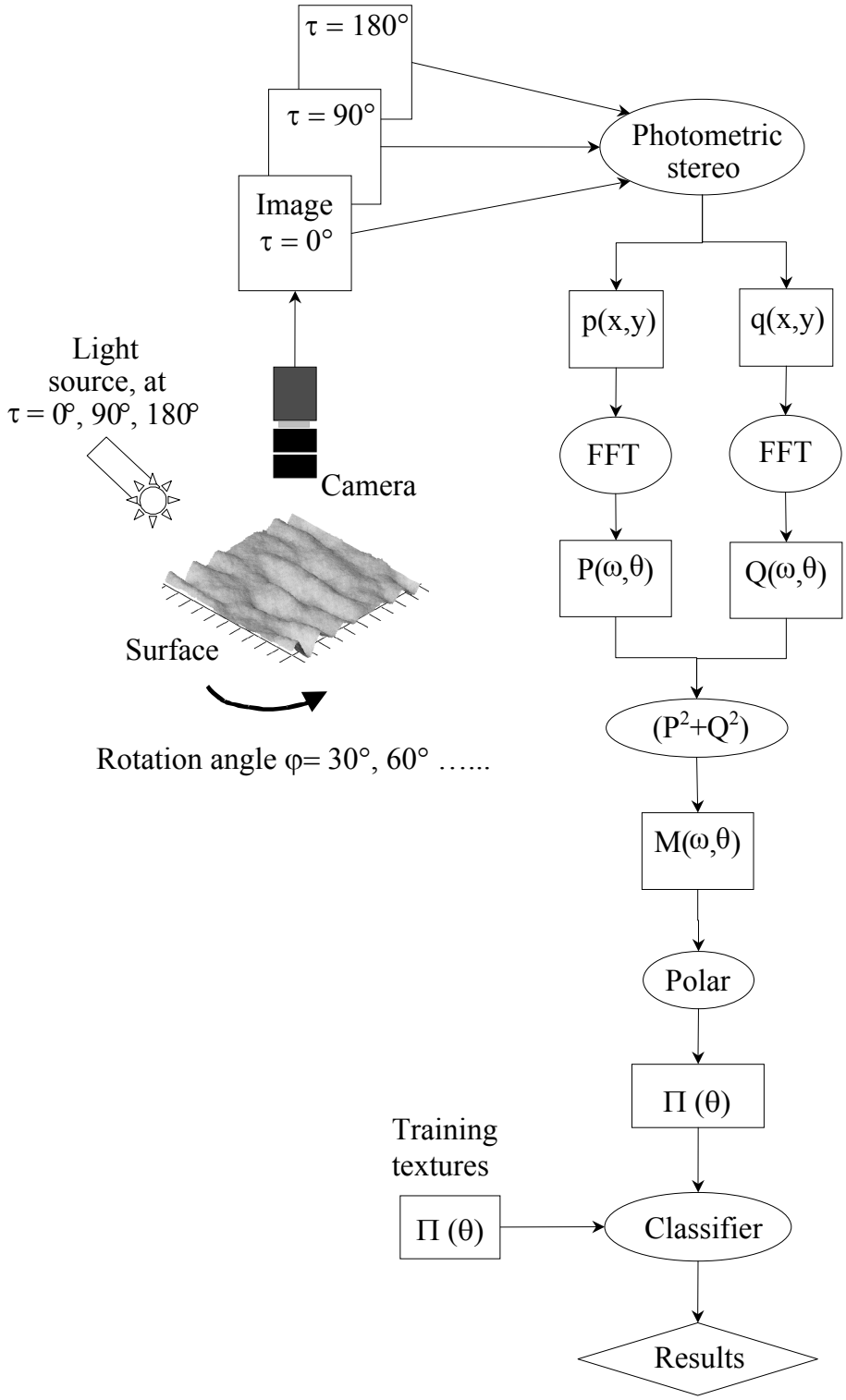

Figure 6. 22 The complete surface rotation invariant classification scheme

6.6.2 Texture Classification Scheme Using Image Information Only

In order to give the comparison of performance of *3D* surface rotation invariant classification using surface information (presented in *Figure 6. 22*) and image information respectively, we therefore present a classification scheme which only uses image information rather than surface information. The image-based texture classification for 3D surface is illustrated in *Figure 6. 23*.

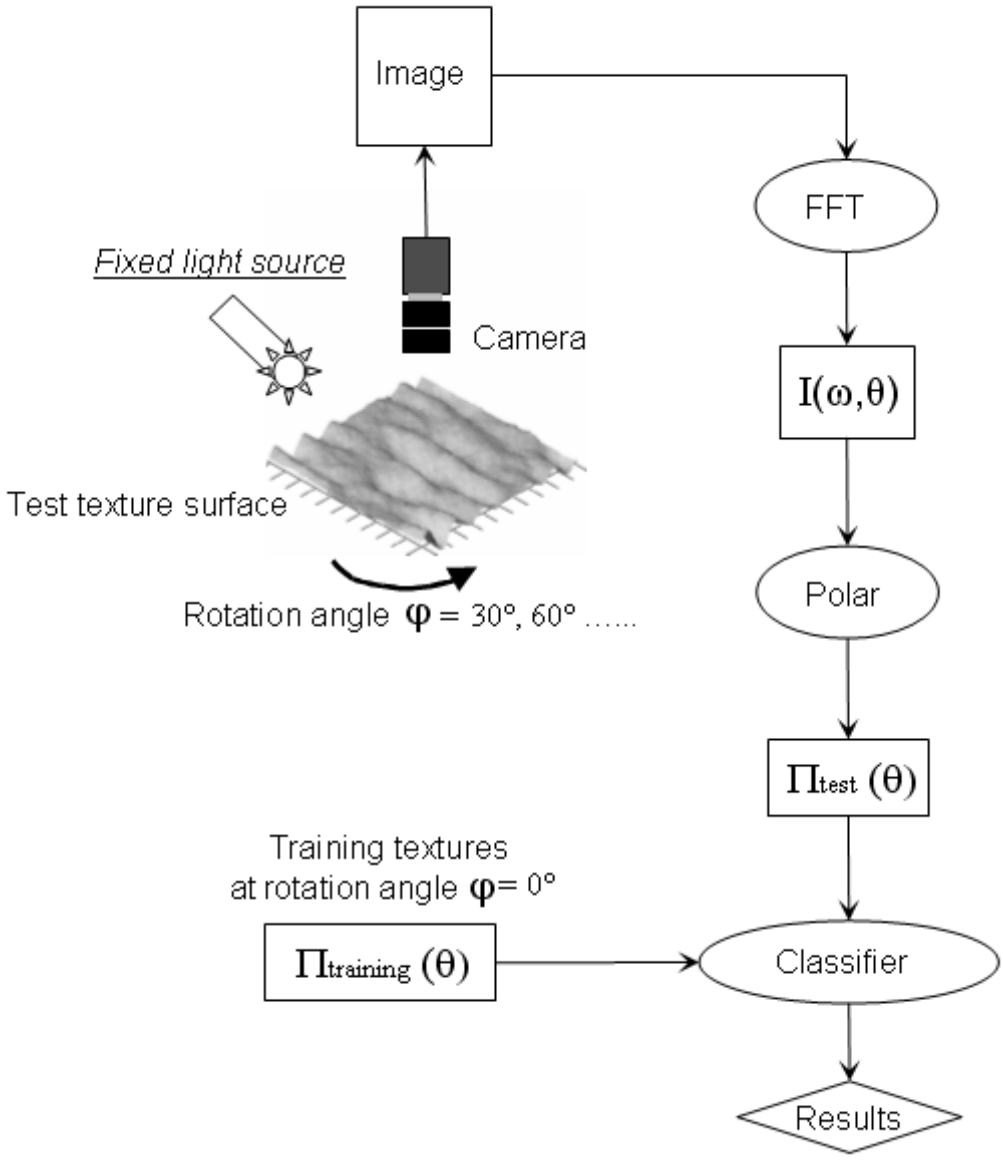

Figure 6. 23 The image-based texture classification for 3D surface

The process is as follows:

1. An image of the texture to be classified is captured by a digital camera which is fixed above the 3D rotated surface texture sample, while the illuminant tilt angle is fixed to *0°* during the whole experiment. Note that, for this image-based texture classification scheme, we only use a single image as the test set. On the other hand, for surface-based texture classification scheme, we use three input images to obtain the surface information by photometric stereo.
2. The captured single image is Fourier transformed into $I(\omega, \theta)$.
3. $I(\omega, \theta)$ is therefore processed to provide polar spectrum $\Pi_{test}(\theta)$.
4. The polar spectrum $\Pi_{test}(\theta)$ is compared with the polar spectra $\Pi_{training}(\theta)$ obtained from training images over a range of angular displacements (φ_{test}) using a sum of squared differences metric.
5. The total sum of squared difference metric calculated from step *4* and the best combination provides a classification decision based on the goodness-of-fit measurement.

CHAPTER 7

Experiment and Results

7.1. Introduction and Aims of the Experiment

In chapter *6*, we proposed a novel texture classification scheme that is surface-rotation invariant rather than image-rotation invariant. In this chapter, in order to test the efficiency of the proposed classification scheme for rotation invariant texture analysis, we design and carry out the experimental work on four synthetic textures and thirty real textures.

Regarding the test data set used in the experiment, we note that currently existing and publicly available texture databases are not suitable for our task. In terms of our surface rotation invariant texture classification scheme, the texture database should provide a set of surface rotations rather than image rotations, along with the registered photometric stereo image data. Our developing photometric texture database is not only concerned with the real surface rotation, but also with the different and controlled illuminant conditions. We provide a detailed description of our new photometric texture database contents and measurement procedure. This method gives us enough information about varied images of different kinds of surfaces directly obtained from the surface properties (e.g. surface partial derivative fields). In addition, the database has already been made public and may be used by interested researchers. Our photometric texture database can be accessed and downloaded online from:

http://www.cee.hw.ac.uk/texturelab/database/

In this database, images are captured and stored individually while surfaces are rotated and illuminated in varied conditions. In addition, the related settings of the experimental apparatus will be discussed. Thereafter, the experimental processing of photometric stereo is carried out on those images in order to obtain surface partial derivative fields by isolating the albedo information, which will give us the representation of gradient space either in the spatial domain or in the frequency domain. Then, rotation invariant features in polar spectra may be obtained in a straightforward manner. Finally, the classification results on both synthetic textures and real textures will be presented.

7.2. A Photometric Texture Database

7.2.1. Introduction

In order to test the efficiency of the classification scheme proposed in chapter *6*, our texture database should provide:

1) *real surface rotation* rather than image rotation, where most of currently existing texture databases only support image rotation; and
2) *registered photometric stereo data sets* so that we may employ surface properties obtained by photometric stereo in our surface-based classifier.

Therefore, we developed two categories of 3D surface photometric texture databases:

- *Synthetic texture data set*, and
- *Real texture data set*.

where both sets provide a varying range of images of 3D surface texture, captured at different surface rotations and under different controlled illumination conditions so that photometric stereo techniques may be used.

7.2.2. Comparison with Other Existing Texture Databases

There are many texture databases available to the public so far. So-called ***Brodatz*** textures [Brodatz66] are probably the most widely used image data in the texture analysis literature. Other well known data sets are ***CUReT*** (Columbia-Utrecht Reflectance and Texture Database, Columbia University) [Dana97] [Dana99a], ***VisTex*** (Vision Texture Database, MIT) , ***MeasTex*** (Texture database for the MEASurement of TEXture classification algorithms, the University of Queensland) [Ohanian92], ***OUTex*** framework (University of Oulu, Finland) [Ojala96], and ***PhoTex*** (Texture Lab, Heriot-Watt University) [McGunnigle01], etc.

- ***Brodatz Texture Database***

The "*Brodatz* texture database" is derived from the Brodatz album [Brodatz66]. It has a relatively large number of classes (112 classes), and a small number of examples for each class. Although the *Brodatz* texture database has become the standard for evaluating texture algorithms, with hundreds of studies having been applied to small sets of its images, it is not suitable for use by our classification scheme.

Our experiment requires that the photometric stereo algorithms are able to run on textures taken under different and controlled lighting and perspective. Since the *Brodatz* texture database is based on image rotated textures [Leung92] [Greenspan94] [Haley96] [Porter97] [Fountain98] [Ojala00] *et al,* the original *Brodatz* texture database is not suitable for our experiments as it can not provide photometric stereo image sets for each texture classes and it does not provide true surface rotation.

- ***VisTex***

To assist in the development of more robust computer vision algorithms and their comparison on a common set of data, the *VisTex* collection has been assembled and maintained by the Vision and Modelling Group at the MIT Media Lab. The most difference between the *VisTex* database and other texture databases is that it does not

conform to *rigid frontal plane perspectives* and *studio lighting conditions*. Their lighting conditions include daylight, artificial-florescent and artificial-incandescent. Moreover, some of the lighting conditions are imprecise. For example, descriptions are given as *"daylight, direct and from right"*. With regard to perspective, the angle between film an object plane, there are two settings: frontal-plain and oblique. Apart from these differences, *VisTex* also provides some examples of many non-traditional textures (such as texture scenes and sequences of temporal textures).

Therefore, considering the limitations of the *VisTex* database with unknown illumination directions, we can not use them with our texture classification scheme, because we have to recover the surface properties from several images with the known and controlled light conditions using photometric stereo.

- ***MeasTex***

MeasTex is about the MEASurement of TEXture classification algorithms, an image database and quantitative measurement framework for image texture analysis algorithms. It is not only a texture database of homogeneous texture images, but also a frame work for the quantitative measurement of texture algorithms targeted on a number of texture testing suites, and an implementation of some major well-known texture classification paradigms. The comparative study of four texture classification algorithms evaluated in the database is presented by Ohanian and Dubes [Ohanian92].

Although a number of texture sets in *MeasTex* have been compiled by other texture databases such as the *Brodatz* texture database and the *VisTex* database, most of their natural textures are 2D texture rather than 3D texture. The natural texture images are obtained from 35mm camera film, thereafter each photograph is scanned at 256dpi and stored in the database. In these cases, we do not know what the exact illumination direction is when the real texture is captured. Therefore this database is not suitable for our 3D surface classification scheme.

Another point to note about in the images of *MeasTex* is that they use direct sunlight as the lighting source in most cases, although they have made note of where the sunlight is exactly coming from. Unfortunately, our simple solution for photometric stereo cannot use these images, since the path of the sun across the sky is very nearly planar [Woodham80]. The same problem also appears in the *VisTex* database.

- ***OUTex***

OUTex stands for University of Oulu Texture database, and it is a framework for the empirical evaluation of texture classification and segmentation algorithms. At this time, the collection of *319* surface textures are captured by well defined variations to a given reference in terms of illumination directions, surface rotations and spatial resolutions. Hence given three different simulated illumination directions, six spatial resolution *(100, 120, 300,360, 500 and 600 dpi)* and nine rotation angles *(0°, 5°, 10°, 15°, 30°, 45°, 60°, 75° and 90°), 162 (3 × 6 × 9)* images are captured from each texture sample, in both *24-bit* RGB and *8-bit* grey scale. Ojala and Pietikäinen [Ojala96] [Ojala98] give a comparative study of texture measures with classification based on successfully using *OUTex* database.

Compared with other texture databases such as *Brodatz*, *VisTex* and *MeasTex*, *OUTex* is comprise of a wide range of 3D texture images (*162* images for each texture) taken under different illumination directions and surface orientations which potentially can be used as input images for our surface rotation invariant texture classification scheme. However, the *OUTex* database cannot used to provide registered photometric stereo data. For example, although texture images of 3D surfaces are taken under three different illumination directions in the space, all of the three involving illumination directions are lying on the same plane (coplanar or collinear), shown in *Figure 7. 1*. In the other words, all of these three illumination conditions only vary in the change of slant angle *(σ)*, the tilt angle *(τ)* is constant. Therefore we can not correctly resolve the surface partial derivatives *p(x,y)* and *q(x,y)* from these images using photometric stereo, as the inverse of the lighting matrix in the photometric stereo solution does not exist when the three illumination vectors lie in the same plane [Woodham80] [Horn89] [Horn96] [Davies90].

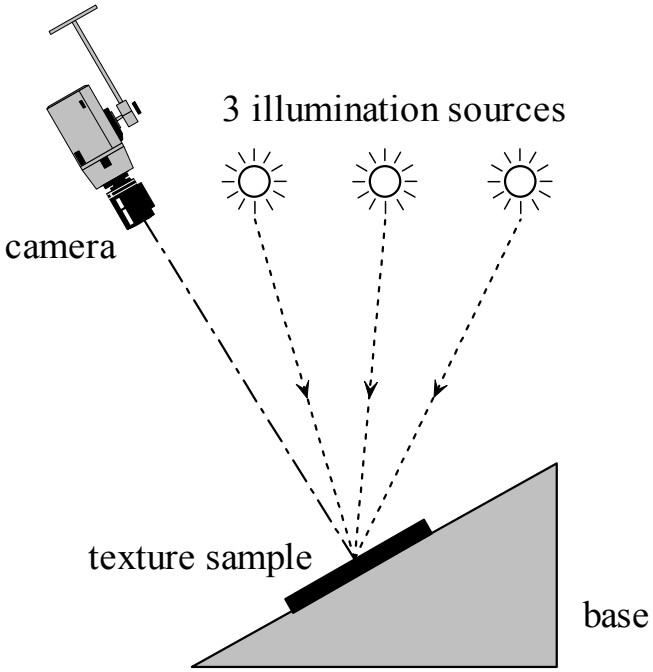

Figure 7. 1 Relative positions of texture sample, illuminant and camera, used in OUTex database.

- ***CUReT***

Characterising the appearance of real-world surfaces is important for many computer vision algorithms. ***CUReT*** (Columbia-Utrecht Reflectance and Texture Database) developed at Columbia University and Utrecht University has collaborated in an extensive investigation of the visual appearance of real-world surfaces [Dana97] [Dana99a]. It comprises three texture databases:

1) ***BRDF database*** (bi-directional reflectance distribution function [Nayar91] [Wolff94]) with reflectance measurements for *61* different samples, each observed with over *205* different combinations of viewing and illumination directions,
2) ***BRDF parameter database*** with estimated parameters for two recent BRDF models: the Oren-Nayar model [Nayar95] [Oren95] for surfaces with isotropic roughness and the Koenderink *et al* model [Koenderink96] for both anisotropic and isotropic surfaces, and
3) ***BTF*** (bi-directional texture function) database. *61* real-world surfaces are measured using new texture representation called BTF. BTF describes the appearance of a textured surface as a function of the illumination and viewing

directions. Also the BTF measurement database is the first comprehensive investigation of texture appearance as a function of viewing and illumination directions [Dana99a].

They note that the appearance of real world texture is a function of both orientation of the 3D sample and the directions of viewer and illuminant. Their database combines the foreshortening effect of the texture and the associated changes in its corresponding illumination directions. For 3D textures, the BFT must also capture more complicated effects such as local shading, interreflections, and masking of surface elements. The difficulty in finding appropriate data sets for characterising BRDF and BTF of 3D texture has been resolved by the construction of *CUReT*. The set of images for each texture sample is obtained over a wide range of viewing and illumination directions.

The substantial interest in the *CUReT* database is evident in the numerous works using the database. It has been used by Dana and Nayar [Dana98] to confirm models for observed intensity distribution as a function of illumination and viewing angles. Dana and Nayar [Dana99b] describe a correlation model for 3D surface texture and suggest how this might be used to provide a 3D surface texture feature, the measured correlation length as a function of viewing direction. They do not however, use this for texture classification purposes. Suen and Healey [Suen98] [Suen00] study the properties of the dimensionality surface via analysing the Bi-directional Texture Function (BTF) using the *CUReT* database. A multi-band correlation model is used to describe image texture as a function of viewing and illumination angles. They also do not use this database for texture classification. Mäenpää and Ojala [Mäenpää00] perform an experiment using the *CUReT* database to demonstrate the robustness of texture classification in terms of changing tilt angle τ only by using local binary patterns (LBP). However, they do not involve the surface rotation as well.

Finally, we have to note that, for all measurements of a selected texture sample, the light source remains fixed. However as the camera is mounted on a tripod, with its optical axis parallel to the floor of the lab, it can be positioned to any one of seven

different locations in a plane during measurements. For each camera position and a given light source direction, the texture sample is rotated. The relative positions of texture sample, illuminant and camera used in *CUReT* database are shown in *Figure 7. 2*. The measurement setup for *CUReT* database is not suitable for photometric stereo, as for a given texture sample at a certain orientation we need to capture the different images by fixing the position of camera and moving the light source, not by fixing the light source and moving camera.

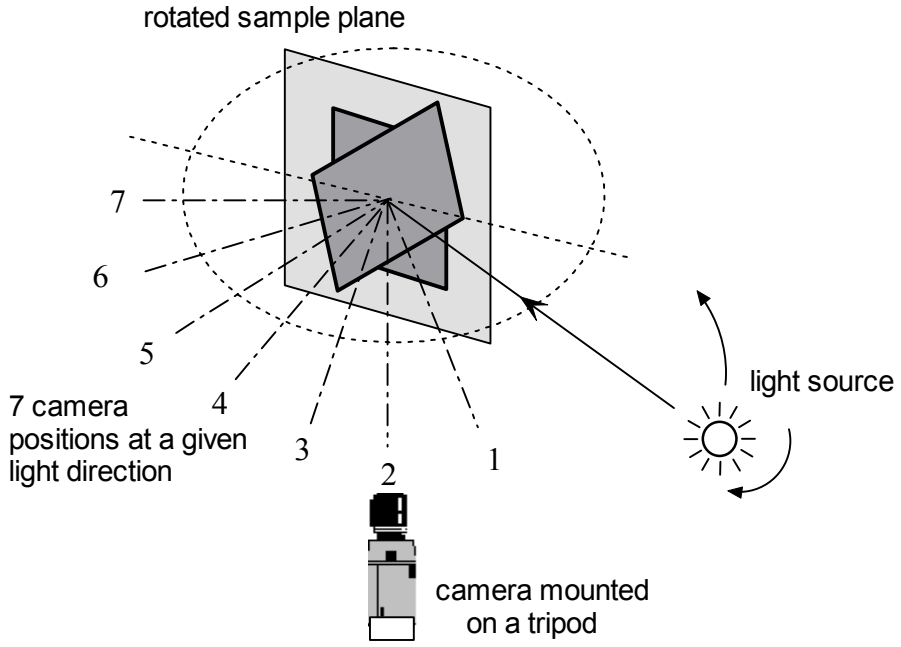

Figure 7. 2 Relative positions of texture sample, illuminant and camera, used in CUReT database.

- ***PhoTex Database***

PhoTex database [McGunnigle01] is a texture database of rough surface. It holds images of rough surfaces that have been illuminated from various directions. Images that allow the user to calibrated the image transfer function, and measure the noise in the process are also held in the database. The main variables in the database are azimuth and zenith of the illumination. In few cases, the surface sample is also rotated. This database therefore mainly focuses on the changes of illumination condition rather than the surface rotation. In fact, although it is a photometric texture

database that is mostly close to our requirement, it does not provide full surface rotation samples.

- ***Comparative study***

Table 7. 1 summarises the properties of the texture databases that have been discussed above. It can be seen that there is no existing texture database which provides registered photometric stereo data sets.

texture database	image rotation	surface rotation	controlled illumination	registered photometric stereo
Brodatz	√	×	×	×
VisTex	√	×	√[1]	×
MeasTex	√	×	×	×
OUTex	√	√	√	×
CUReT	√	√	√	×
PhoTex	×	×	√	√

Table 7. 1 Comparative study of existing texture databases.

7.2.3. Developing Our Photometric Texture Database

The texture due to surface roughness has complex dependencies on viewing and illumination directions. These dependencies can not be studied using those texture databases that include few images of each sample. Our texture database covers a diverse collection of rough surfaces and captures the variation of image texture with changing illumination direction. It is intended to provide photometric surface data for texture analysis (e.g. texture classification and segmentation, and 3D rough surface modelling, etc), while our task is mainly concerned with surface rotation invariant

[1] Some of them are unknown.

texture classification. There is a varied range of images of rough surfaces within the database, and the major variables are the surface orientation and the tilt angle of illumination. These provide enough information to estimate surface properties using photometric stereo. Also, we capture our images under much more constrained and controlled conditions, when compared with other texture databases available on the internet.

7.2.4. Set Up Photometric Texture Database

The first step of experimental procedure is to obtain the texture data set from the 3D surface texture. The data set consists of images captured at different rotations and illuminated from different directions. A photometric image set of each texture to be classified is captured, as shown in *Figure 7. 3*, i.e. eight images are taken at illuminant tilt angles of *0°, 45°, 90°, 135°, 180°, 225°, 270°, and 315°*. Although only three of them are needed to estimate surface partial derivatives using the basic photometric stereo technique, others are needed for further investigation. The position and orientation of the surface sample will not be varied during the capture of these eight images. Each 3D texture surface is then rotated into *7* positions (surface orientation angles $\varphi = 0°, 30°, 60°, 90°, 120°, 150°$ *and* $180°$). The original texture image size in the digital camera (a Vosskuhler CCD 1300LN) is set to 1280×1024 pixels. Note that the slant angle (σ) is kept as a constant of $50°$ during the whole experimental procedure. Thereafter, the final images are obtained by reducing them to a size of 512×512 pixels. Finally a database of *30* real textures with *1680* images *(30 textures × 7 rotations × 8 illumination directions)* and *4* synthetic textures with *224* images *(4 textures × 7 rotations × 8 illumination directions)* is constructed for our experiment.

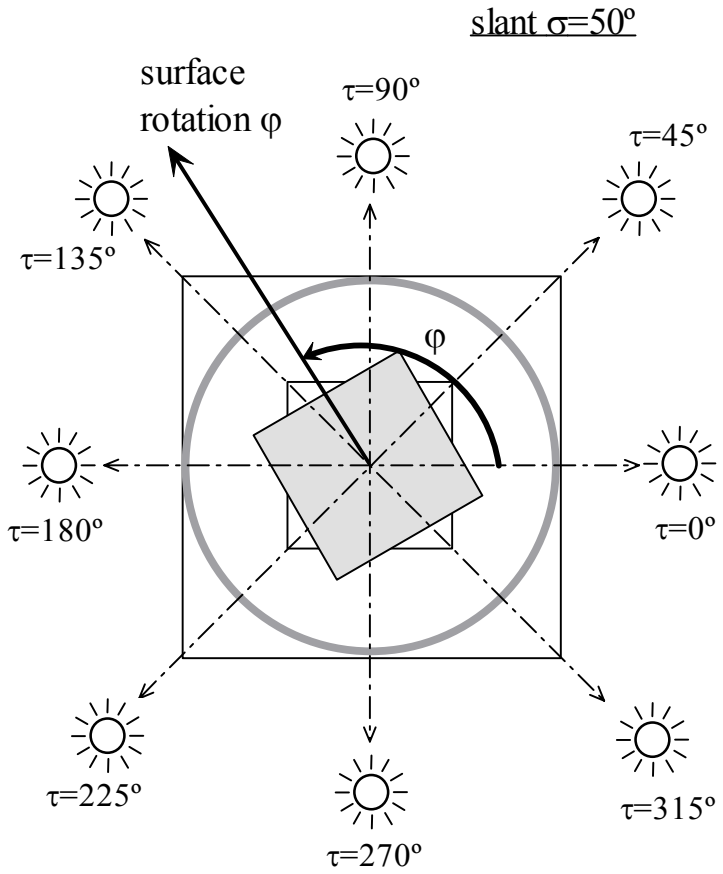

Figure 7. 3 Geometry for capture of photometric image set in our experiments.

7.2.5. Texture Samples

- ***Synthetic texture data set***

We refer to the synthetic textures introduced in chapter 3. Although there are only four textures in this data set, the experimental texture set contained patterns with different degrees of regularity as well as non-regular directional patterns. The montage samples of the synthetic images (*rock, sand, ogil malv*) at different surface orientations are shown in *Figure 7. 4*.

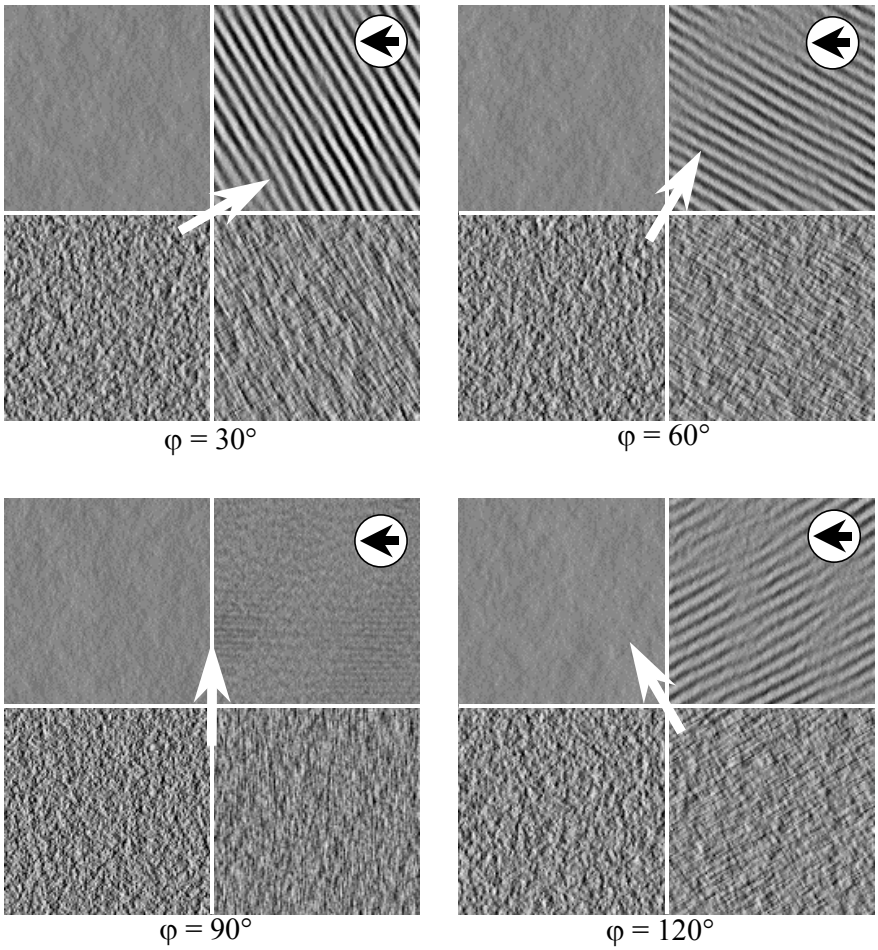

Figure 7. 4 Four synthetic textures at four surface rotations (φ = 30°, 60°, 90°, and 120°) with constant illumination (slant σ = 50°). Surfaces are generated synthetically, rotated as indicated by white arrows in the centre, rendered using Lambert's law at an illuminant tilt of τ=0° as indicated black arrows in white circles and combined into montage format for display purposes. (rock on left top, sand on right top, malv on left bottom and ogil on right bottom).

- ***Real texture data set***

There is a great diversity of textures for a real world scene (micro-textures and macro-textures), and consequently of texture classification problems. For example, textures can be as diverse as landmarks, forests and oceans viewed from space, different kinds of textiles, clothes, rock, patterns of photographs on a flat surface, any homogenous region that can be seen as an image [Graham70]. On the other hand, we are interested in texture features such as directionality, periodicity, randomness, roughness, regularity, coarseness, albedo distribution, contrast and complexity,

which are hypothesised to be important for human perception an attention [Tamura78]. This real texture data set is focused on the use of collective visual properties or vision textures, shown in *Figure 7. 5*.

The samples are chosen from the wide range of physical surfaces, including isotropic surfaces *(gr2),* directional surfaces *(tl5),* bi-directional surfaces *(tl4),* multi-directional surfaces *(tl2),* specula surfaces *(wps2),* heavy-shadowed surfaces *(rkb1),* surfaces with small height variations *(grd1),* surfaces with large height variations *(bn1),* and so on. The materials include textile, corduroy, terry, bean, wallpaper, plaster, rock, noodle, wood, concrete, styrofoam, etc.

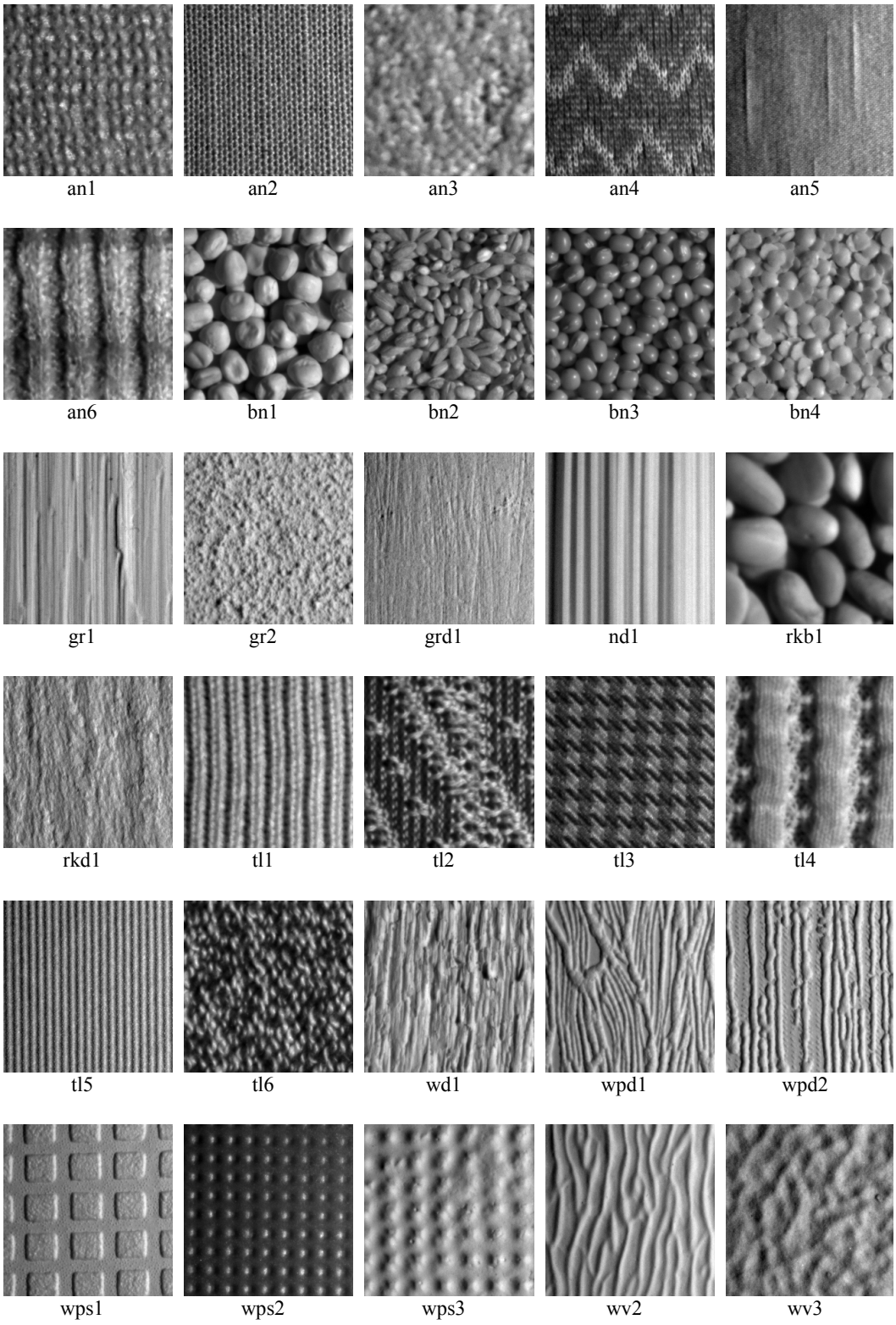

Figure 7. 5 30 real texture samples at surface rotations $\varphi = 0°$ under the illuminant condition of slant $\sigma = 50°$ and tilt of $\tau = 0°$. (image size 256 × 256)

7.3. Settings of the Experimental Apparatus

Experimental apparatus was constructed for the acquisition of images under controlled lighting conditions. All of the imaging facilities were placed in a dark room, and an overview of the layout of the system is shown in *Figure 7. 6* and *Figure 7. 7*, followed by a detailed discussion of significant design aspects.

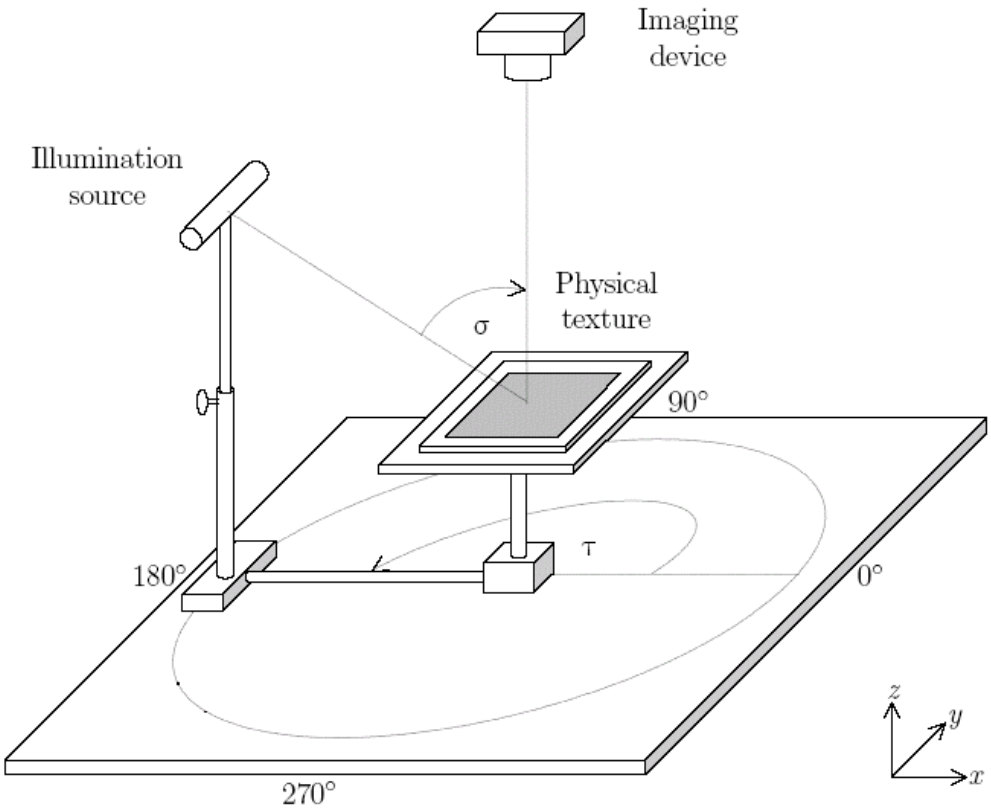

Figure 7. 6 . Laboratory apparatus to collect photometric stereo image data.

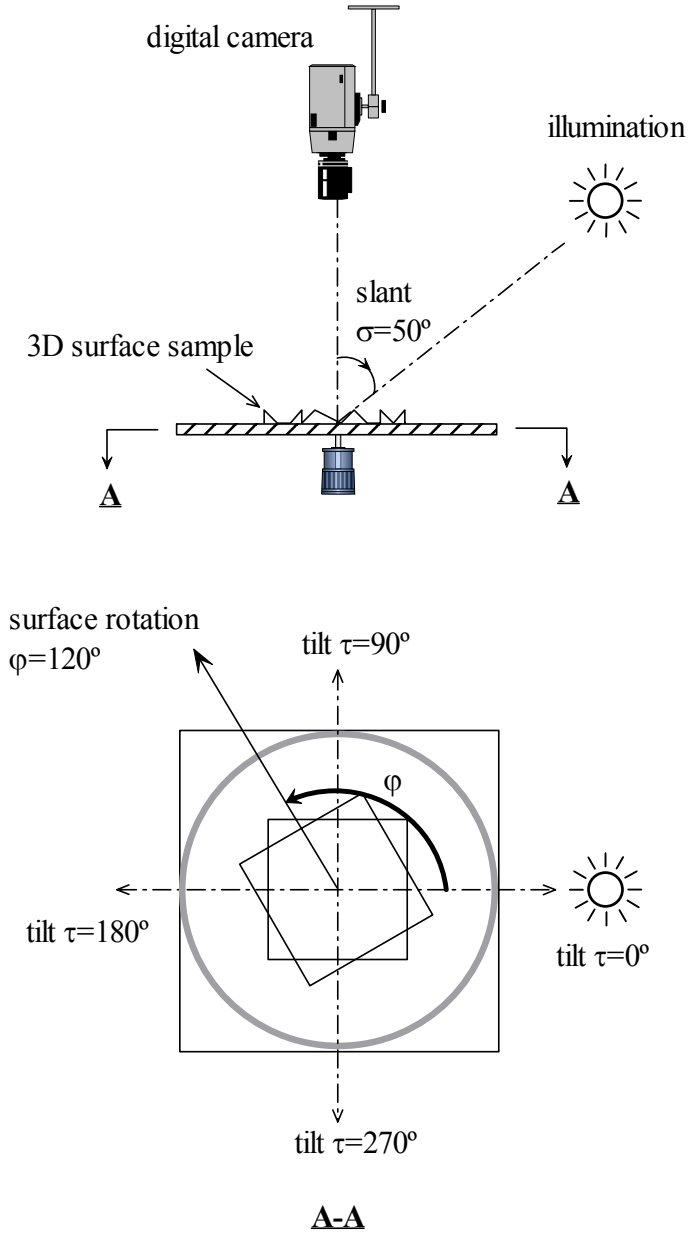

Figure 7. 7 Geometry of the surface capturing systerm

We mount the CCD camera directly overhead the testing sample and put the 3D surface texture sample on a rotated plane. Apart from the rotation variance, our system can cope with changes in illumination conditions (i.e. changes of tilt angle *(τ)* and slant angle *(σ)*). The image is captured by an overhead digital camera and illuminated by a light source with slant angle *(σ)* and tilt angle *(τ)*. The multiple images required for photometric stereo can be obtained by explicitly moving a single light source arm. The illumination direction (σ and τ) can be adjusted manually. In

our experiment, the slant angle (σ) is kept as a constant of $50°$ during the whole experimental procedure.

- ***Digital Camera***

The digital camera used in our experiments is a CCD-1300LN made by VDS Vosskühler (*http://www.vdsvossk.de*). It is used with a Matrox PC-SIG framestore with a resolution of *1280(height) × 1024(width)* effective pixels. Pixel size is $6.7\mu m \times 6.7\mu m$. The RS-644 digital output supplies images data with *12-bit* precision in uncompressed grey-level TIFF format.

The camera aperture is fixed at one setting for all data capture. This helps to keep the linear relationship between pixels and radiance, specially in the range between low and high radiance values, as pixel underflow and overflow, i.e. pixels which are clipped into values of *0* or *4095* by digitisation (*12-bit*), contribute significantly to non-linearity.

- ***Light Source***

The single light device is powered by a stabilised DC supply and mounted on a rotated arm which can be moved to the specified tilt and slant angle. Thus selecting the illumination directions over the hemisphere of possible directions can be achieved manually. The light source is a filament tube with a mask, which provides a Gaussian spatial distribution of illumination. The time varying component of the image, photon noise is associated with the quantum nature of light in [Healey94]. In order to assess the stability of the light source (e.g. spatial uniformity and non-time-varying), we measure the light intensity via a digital light meter (*Lux-Meter 0560 in standard DIN 5035*). The *Lux-Meter* was a useful measuring instrument for ensuring that the illumination was kept at a constant *65 Lux* for each texture.

7.4. Experimental Procedure

In this section, we will outline the experiment procedure in four main steps in order to demonstrate our surface rotation invariant texture classification scheme: set up photometric texture database; partitioning the training and testing textures; extracting features and classification.

7.4.1. Partitioning the Training and Test Textures

- ***Using Over-lapping Textures***

For our classification system, the data are partitioned into training and test sets respectively. Training is performed using photometric image sets with the surfaces obtained at a surface rotation angle of $\varphi = 0°$, and the size of training images is set to 512×512 pixels. The test textures are obtained by using separate sample with rotations at $30°$ increments over the range from $30°$ to $180°$. This partition strategy will give us a blind classification scheme.

In order to increase the number of classifications tests, each of the photometric sets was divided into nine smaller over-lapping photometric sets, in which each image has the size of 256×256 pixels, illustrated in *Figure 7. 8*. This gave a total of *4860 (30 textures × 3 photometric stereo images × 6 rotations × 9 subimages)* photometric test samples. *Table 7. 2* summarises the partition strategy of training and test textures.

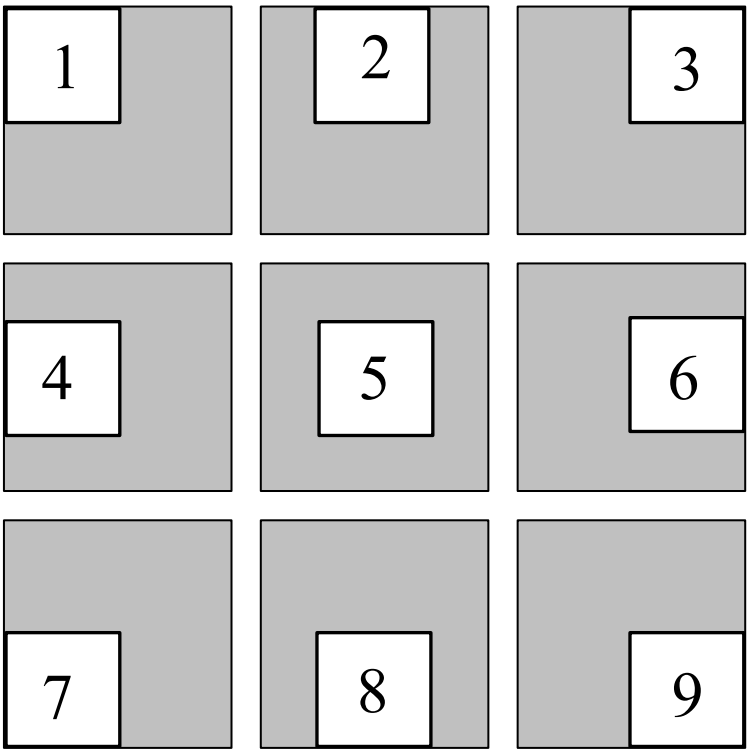

Figure 7. 8 Illustration of positions of the 9 over-lapping test 256×256 images obtained from a single 512×512 image.

		Training textures	Test textures
Surface orientation φ		0°	30°, 60°, 90°, 120°, 150° and 180°
Image size		512 × 512	256 × 256
Number of textures	**Synthetic**	4	
	Real	30	
Number of images	**Synthetic**	4 × 3 = 12	4 × 3 × 6 × 9 = 648
	Real	30 × 3 = 90	30 × 3 × 6 × 9 = 4860
Number of classifications	**Synthetic**	4 × 6 × 9 = 216	
	Real	30 × 6 × 9 = 1620	

Table 7. 2 Summary of partitioning of training and test textures using over-lapping textures.

- ***Using Non-overlapping Textures***

Figure 7. 9 and *Table 7. 3* show the strategy of partitioning of training and test textures using non-overlapping textures.

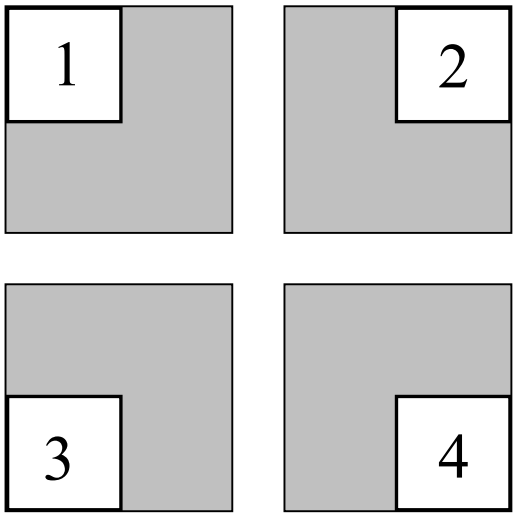

Figure 7. 9 Illustration of positions of the 4 non-overlapping test 256×256 images obtained from a single 512×512 image.

		Training textures	***Test textures***
Surface orientation φ		*0°*	*30°, 60°, 90°, 120°, 150° and 180°*
Image size		*512 × 512*	*256 × 256*
Number of textures	***Synthetic***	*4*	
	Real	*30*	
Number of images	***Synthetic***	*4 × 3 = 12*	*4 × 3 × 6 × 4 = 288*
	Real	*30 × 3 = 90*	*30 × 3 × 6 × 4 = 2160*
Number of classifications	***Synthetic***	*4 × 6 × 4 = 96*	
	Real	*30 × 6 × 4 = 720*	

Table 7. 3 Summary of partitioning of training and test textures using non-overlapping textures.

7.4.2. Extracting Features

1. The photometric algorithm uses this image set to estimate the surface partial derivatives $p(x,y)$ and $q(x,y)$.

2. These are Fourier transformed and processed to provide gradient spectra $M(\omega,\theta)$ and polar spectrum $\Pi(\theta)$. The variance of the coefficients and the spectral leakage introduced by a standard FFT are reduced by using a Welch periodogram [Welch67] coupled with a circular Hann window. The principle of 2-D Welch periodogram is take a series of overlapping, smaller 2-D Hanning windows in the image, the FFT for each of these windows is calculated and finally the results are obtained by averaging across FFT. This reduces the variance of the power estimate by averaging over all the windows, which leads to a general smoothing of the final spectrum.

3. The polar spectrum of the test texture is compared with the polar spectrum obtained from training images over a range of angular displacements φ_{test} using a sum of squared differences metric. The experiments based on synthetic textures and real textures are designed to show that the gradient spectra $M(\omega,\theta)$ functions and their polar spectrums are rotationally sensitive but contain no directional artefacts. That is $M_{\varphi}(\theta) = M(\theta+\varphi)$ and similarly $\Pi_{\varphi}(\theta) = \Pi(\theta+\varphi)$.

7.4.3. Classification

In the classification process, the similarity between the training and test data sets are measured with SSD and the testing sample is assigned to the class. The total sum of squared errors statistic is calculated from polar spectrums and the best combination provides a classification decision and an estimation of the relative orientation of the

test texture. The test polar spectrum must be “rotated” (or rather translated) to find the best-fit. The texture is then assigned to the class for which the lowest sum of square differences occurs at each of these best-fit rotation angles. The classification experiments are performed on both synthetic and real texture data sets, respectively.

In terms of the classification using over-lapping texture images, each of the resulting *1620 (30 textures × 6 rotations × 9 subimages)* polar spectrums is compared with each of the *30* 'training' polar spectrums in the database of real textures; while each of the resulting *216 (4 textures × 6 rotations × 9 subimages)* polar spectrums is compared with each of the *4* “training” polar spectrums in the database of synthetic textures.

On the other hand, in terms of the classification using non-overlapping texture images, each of the resulting *720 (30 textures × 6 rotations × 4 subimages)* polar spectrums is compared with each of the *30* 'training' polar spectrums in the database of real textures; while each of the resulting *96 (4 textures × 6 rotations × 4 subimages)* polar spectrums is compared with each of the *4* “training” polar spectrums in the database of synthetic textures.

7.5. Presentation of Experimental Results

Note that the classification results presented on the following chapters in this thesis are based on the over-lapping textures for both training and test data set unless it is indicated.

7.5.1. Synthetic Textures

- ***Classification Results by Using Over-lapping Synthetic Texture Images***

For our synthetic texture data set, we achieve perfect classification accuracy of *100%*. Some of examples of sum of squared difference (SSD) metrics between the

training textures (at surface orientation $\varphi = 0°$) and test textures (at orientations $\varphi = 30°, 60°, 90°,$ and $120°$) are shown in *Table 7. 4*. We note that, the classification performs well whatever the orientation of the test data. The minimal value of SSD (indicated by the grey colour background in the table) is only achieved between the polar spectrum of the test texture and their OWN training polar spectrum, although the orientation of the test polar spectrum is different from that of training polar spectrum. Hence, our classification scheme is rotation-invariant for these textures.

Training->	*rock_ref0*	*sand_ref0*	*ogil_ref0*	*malv_ref0*
Rotation φ = 30° (testing)				
rock_30	***5.83E-01***	2.99E+05	1.67E+04	1.65E+04
sand_30	5.42E+05	***6.11E+04***	4.51E+05	5.14E+05
ogil_30	1.19E+04	2.42E+05	***7.52E+02***	5.66E+03
malv_30	1.45E+04	2.79E+05	6.81E+03	***3.36E+02***
Rotation φ = 60° (testing)				
rock_60	***5.12E-01***	2.99E+05	1.67E+04	1.65E+04
sand_60	6.09E+05	***1.24E+05***	5.27E+05	5.85E+05
ogil_60	1.10E+04	2.40E+05	***9.38E+02***	5.59E+03
malv_60	1.33E+04	2.81E+05	6.62E+03	***4.54E+02***
Rotation φ = 90° (testing)				
rock_90	***8.35E-02***	2.99E+05	1.66E+04	1.64E+04
sand_90	2.31E+05	***2.50E+04***	1.73E+05	2.16E+05
ogil_90	1.69E+04	2.28E+05	***3.15E+02***	7.11E+03
malv_90	1.69E+04	2.79E+05	7.11E+03	***1.22E+02***
Rotation φ = 120° (testing)				
rock_120	***7.10E-01***	2.99E+05	1.67E+04	1.66E+04
sand_120	5.45E+05	***6.21E+04***	4.53E+05	5.17E+05
ogil_120	1.18E+04	2.42E+05	***7.60E+02***	5.69E+03
malv_120	1.31E+04	2.79E+05	6.58E+03	***4.55E+02***

Table 7. 4 Sum of squared difference metric values between the training textures (at the surface orientation of φ = 30°, 60°, 90°, and 120°) and test textures (at the surface orientation of φ = 0°) for four synthetic textures (rock, sand, ogil and malv).

We note that the minimal values of SSD (indicated by the grey colour background) in *Table 7. 4* are still high apart from texture "*rock*". This is due to consideration of that our training data are rotated surfaces rather than image rotation which involve much more noises.

- ***Effect of Sample Size by Using Non-overlapping Synthetic Texture Images***

In these experiments with synthetic textures good performance (*100%* classification accuracy) was achieved using relatively large samples with a size of *256 × 256* pixels. In order to show the effect of image size against the classification accuracy, the experiment was repeated using test sample sizes of *128 × 128, 64 × 64,* and *32 × 32* pixels. Consequently, all of the smaller samples are cut from the original *512 × 512* images to provide the maximum number of samples without overlapping. Thus for example, in the case of test image size of *32 × 32*, *6144* classifications were performed *(4 textures × 6 rotations × 256 samples per rotation).* The classification results are shown below in *Table 7. 5* and *Figure 7. 10.*

Testing sample size	***256 × 256***	***128 × 128***	***64 × 64***	***32 × 32***
Number of samples per rotation	9	16	64	256
	Overlapped	Non-overlapped		
Number of classification	4×6×9=216	4×6×16=384	4×6×64=1536	4×6×256=6144
Misclassification rate	*0%*	*8%*	*21%*	*32%*

Table 7. 5 Classification results for 4 synthetic textures with the different testing sample size.

Figure 7. 10 Misclassification rate for 4 synthetic textures against the size of the test samples.

As expected, the results show that this approach is sensitive to the test sample size.

- ***Surface-based Texture Classification vs. Image-based Texture Classification***

Firstly, *Table 7. 6* summarises the partitioning of training and test textures used in image-based texture classification scheme (presented in *Figure 6.23*). This gives a total number of *216 (4 textures × 6 rotations × 9 subimages)* classifications. On the other hand, the strategy of partitioning for surface-based texture classification scheme (presented in *Figure 6.22*) can be referred back to *Table 7. 2*.

	Training textures	***Test textures***
Surface orientation φ	*0°*	*30°, 60°, 90°, 120°, 150° and 180°*
Image size	*512 × 512*	*256 × 256*
Number of textures	*4*	
Number of images	*4*	*4 × 6 × 9 = 216*
Number of classifications	*4 × 6 × 9 = 216*	

Table 7. 6 Summary of partitioning of training and test textures used in image-based texture classification scheme for synthetic textures.

Secondly, the classification accuracy for image-based classifier is shown in *Table 7. 7*, compared with those for surface-based classifier. Note that the classification performance of image-based classifier is worse than that of surface-based classifier. In addition, in terms of image-based classification, the isotropic textures *"rock"(81.5%)* and *"malv"(92.6%)* have better classification accuracies than directional textures *"sand"(37.0%)* and *"ogil" (55.6%)*. This can be explained by the fact of that the directional illumination filter effects on the directional *3D* surfaces. Classifier only using image information loses the information about the directionalities of *3D* surfaces.

	rock	*sand*	*malv*	*ogil*
Surface-based	*100%*	*100%*	*100%*	*100%*
Image-based	*81.5%*	*37.0%*	*92.6%*	*55.6%*

Table 7. 7 Classification accuracy for 4 synthetic textures: image-based classifier vs surface-based classifier.

7.5.2. Real Textures

- ***Classification Results by Using Over-lapping Real Texture Images***

An average recognition rate of *76.30%* was obtained for 30 real textures. Classification results for each of the real texture classes are shown in *Figure 7. 11*.

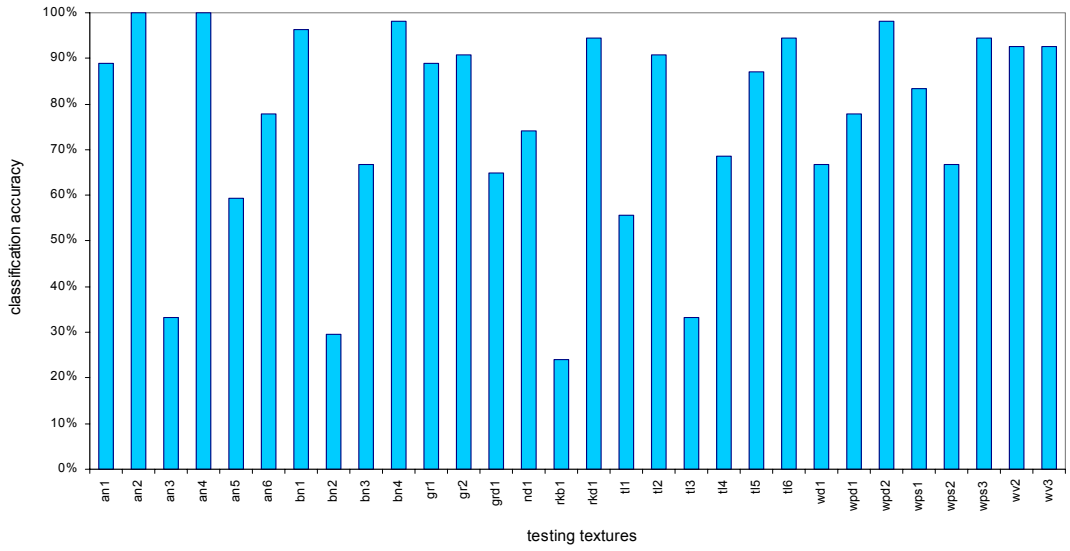

Figure 7. 11 Classification results for 30 real textures by using over-lapping texture images.

Comments on results can be summarised as followings:

1. The misclassifications may well be due to shadows and non-Lambertian surfaces – both of these factors cause the photometric stereo to introduce errors (e.g. a classification accuracy of *24.07%* is obtained with the heavily shadowed texture *"rkb1"*).

2. The results of classification accuracy for each individual texture show that our classification scheme performs better with directional textures than isotropic textures. For example, three of the four worst classification results are caused by isotropic textures (*"rkb1"* with *24.07%, "bn2"* with *29.63%* and *"an3"* with *33.33%*).

- ***Classification Results by Using Non-overlapping Real Texture Images***

Figure 7. 12 shows the classification results for *30* real textures by using non-overlapping images. The strategy of partitioning of non-overlapping images can be referred back to *Figure 7. 9*. In addition, the number of training and test images and the number of classifications has been summarised in *Table 7. 3*.

The overall classification accuracy is *78.5%* by using non-overlapping texture images, which is a little better than that of *76.30%* by using over-lapping texture images (*Figure 7. 11*). However, those two overall classification accuracies for *30* real textures between using non-overlapping images and using over-lapping images are not comparative. The reason of this case is that they share the same training data set (see *Table 7. 2* and *Table 7. 3*), while the test data set using non-overlapping images is only the sub-set of the test data set using over-lapping images. On the other hand, the classification number using non-overlapping is reduced from *54* (*6 rotations × 9 subimages*) to 24 (*6 rotations × 4 subimages*) for each texture class, which also results in that the total number of classifications is reduced from *1620* to *720* (see *Table 7. 2* and *Table 7. 3*). Therefore, we cannot compare those two classifications that have the different test data sets.

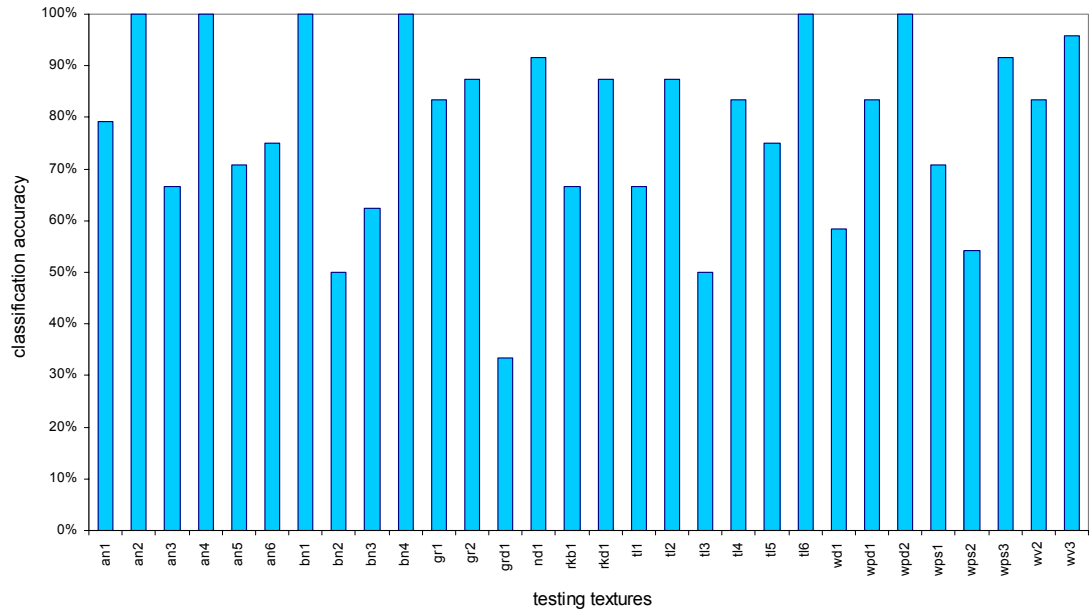

Figure 7. 12 Classification results for 30 real textures by using non-overlapping texture images.

- ***Surface-based Texture Classification vs. Image-based Texture Classification***

Now we carry out the similar comparative studies on real textures in the same way as we do on synthetic textures. *Table 7. 8* summarises the partitioning of training and test textures used in image-based texture classification scheme (presented in *Figure 6.23*). This gives a total number of *1620 (30 textures × 6 rotations × 9 subimages)* classifications.

	Training textures	***Test textures***
Surface orientation φ	*0°*	*30°, 60°, 90°, 120°, 150° and 180°*
Image size	*512 × 512*	*256 × 256*
Number of textures	*30*	
Number of images	*30*	*30 × 6 × 9 = 1620*
Number of classifications	*30 × 6 × 9 = 1620*	

Table 7. 8 Summary of partitioning of training and test textures used in image-based texture classification scheme for real textures.

Figure 7. 13 shows the classification results for *30* real textures between image-based classifier and surface-based classifier. The overall classification accuracy of

29.2% for image-based classifier is much worse than that of *76.3%* for surface-based classifier. It also proofs that *3D* surface rotation is not the same as the *2D* image rotation. Rotation of the physical texture surface under fixed illumination conditions can cause significant changes to its appearance, and cause failure of classifiers designed to copy with image rotation.

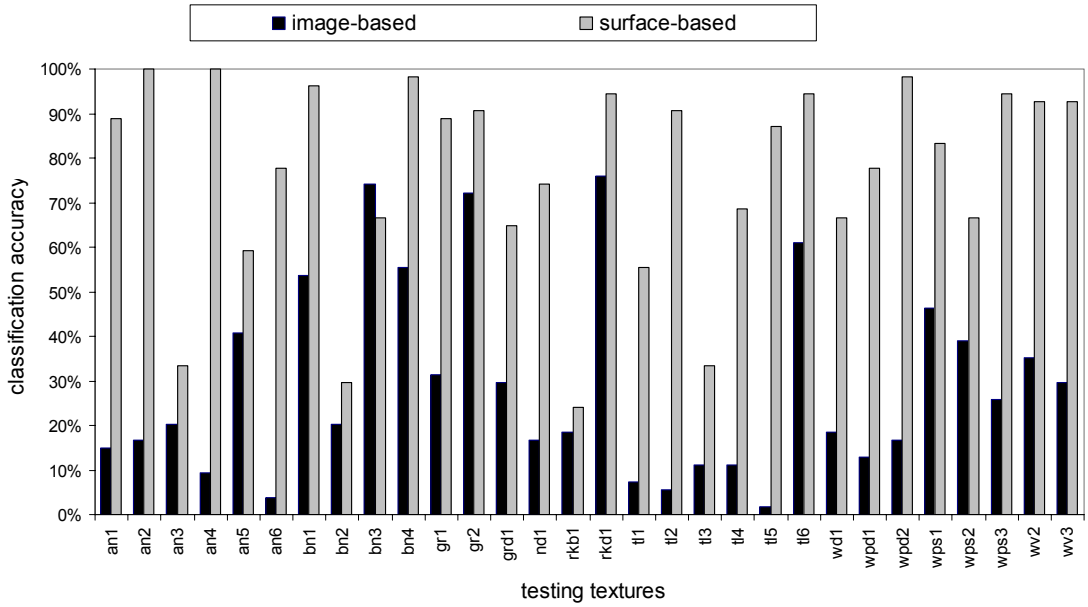

Figure 7. 13 Classification results for 30 real textures: image-based classifier vs surface-based classifier.

7.5.3. Comparative Study on Other State-of-the-art Approaches

In this section, our algorithm is compared to those of Leung and Malik [Leung99], Varma and Zisserman [Varma02a], which are the current state-of-the-art approaches. The tests [Varma02b] on both algorithms are using our photometric texture database.

- ***Leung and Malik's Method***

Leung and Malik [Leung99] make an important innovation in giving an operational definition of a *texton*. The main idea is to construct a vocabulary of prototype tiny surface patches with associated local geometric and photometric properties. They call

those *3D textons*. They make a serious attempt on the problem of classifying textures under varying viewpoint and illumination. Their solution was a *3D texton* which is a cluster centre of filter responses over a stack of images with representative viewpoints and lighting.

- ***Varma and Zisserman's Method***

Varma and Zisserman [Varma02a] present an approach to material classification under unknown viewpoint and illumination. Their texture model is based on the statistical distribution of clustered filter responses. However, unlike previous *3D texton* representations [Leung99], they use rotationally invariant filters and clusters in an extremely low dimensional space. Their approach to the classification problem is to model a texture as a distribution over textons, and learn the textons and texture models from training images. Classification of a novel image then proceeds by mapping the image to a texton distribution and comparing this distribution to the learnt model.

We therefore investigate Varma and Zisserman's method and implementation [Varma02b] along the comparative studies to our algorithms. The overview of their algorithm is as follows:

❖ Learning Phase

1. Take all the training images of a given texture class and filter them using given filter-bank.
2. Vector quantizes all the filter responses, across all texture classes, into textons using the *K-Means* clustering algorithm.
3. To each filter response, associate the texton which lies closest to it in filter response space.
4. The texture model for a given training image then becomes the histogram of texton labelling for that training image.
5. The texture model for a class is the set of models generated by all the training images for that class.

❖ Classification Phase

1. Given a single novel image to classify, filter it using the same filter bank and then label it using the textons that were generated in the learning phase.
2. Construct the histogram of texton labelling for the novel image.
3. Using the χ^2 metric as a distance function, determine the training model closest to the novel image histogram. Report the novel image as belonging to the same texture class as the training model (i.e. use a nearest neighbour classifier).

❖ Implementation Details

1. All *56* (*7* surface rotations by *8* illumination rotations) images per texture were used. *28* were used for training and *28* for testing.
2. All the images were sub-sampled into 256×256 pixels.
3. Also, all the pre and post processing steps described [Varma02a] were implemented. The MR8 filter bank was used.
4. Again, *10* textons were learnt from each texture class to make a total of *300* textons.

❖ Classification Results

All the *840* (*30* textures by *7* surface rotations by *4* illumination rotations) test images were classified correctly.

It is also reported that the classification accuracy of *100%* is achieved by both two algorithms on our photometric texture database [Varma02b]. Compared with our classification accuracy of *76.30%* on the same texture database at this stage, further investigation must be carried out to address this matter. In the next two chapters, we will give details of the misclassifications, and present the new classification schemes which overcome these problems.

7.6. Summary

In this chapter we presented the experimental procedure and results for a surface rotation invariant texture classification scheme. The experiments are performed using four synthetic textures and thirty real textures. For each texture, images at different surface orientations and under controlled illumination conditions are classified. We assume we have three frontal-parallel views of the test and training textures obtained under three different, known illumination conditions. We should also point out that the three-image photometric stereo algorithm used in these experiments assumes that the surfaces are Lambertian and shadow free.

Experiment results are obtained with both synthetic and real textures, where the classifier is trained at one particular rotation angle and tested with samples from other rotation angles. Our results using four synthetic textures show that our classification scheme is able to provide a successful classification rate of *100%*. A average classification accuracy of *76.30%* is obtained when thirty real textures where used. We also, note that, our classification scheme achieves good classification rates using large sample sizes and poorer classification rates using smaller sizes. While the results using real textures are not as high as those published for some image rotation invariant schemes [Cohen91] [Reed93] [Hayley96] [Port97] [Fountain98] [Zhang02a], they are good considering the difficulties involved with the rotation of real 3D surface textures and the large number of different texture classes presented.

In the next two chapters, we will give details of the misclassifications, and explain why they are happening, and present the new classification schemes which overcome these problems.

CHAPTER 8

A New Classification Feature Space and A New Feature Generator

8.1. Introduction

A novel algorithm for rotation invariant texture classification of 3D surfaces using photometric stereo has been proposed in *Chapter 6* and tested in *Chapter 7*. In this chapter, we present improved 3D surface classification strategies to overcome misclassification and achieve higher classification accuracies by introducing a new classification feature space, *radial spectrum*, and a new feature generator, *albedo spectra*.

The structure of this chapter is as follows:

- Both the shortcomings of the classification scheme in *Chapter 6* and the results of misclassification in *Chapter 7* are addressed, and a detailed investigation of the misclassifications is given. We note that there is neither *radial* information nor *albedo* information in our classification scheme described in *Chapter 6*.
- A new classification feature space, *radial spectrum*, is introduced in addition to the polar spectrum.
- In addition, a new feature generator, *albedo spectra*, is presented to provide additional information on surface texture properties.
- In general, the modified surface texture classification scheme is outlined, which combines two main feature spaces:
    1) *polar spectrum* and

2) *radial spectrum*.

We use these feature spaces with two feature generators:

1) *gradient data* and
2) *albedo data*.

- Experimental procedure and results based on our novel photometric stereo texture database are also presented. The comparative study obtained from the different combinations of feature spaces and feature generators is also discussed.
- The final conclusion is drawn.

All test data in this chapter comes from the image set described in *Chapter 7*.

8.2. An Additional Feature Space: Radial Spectrum

In this section, we discuss the misclassification of experimental results described in the previous chapters with the objective of introducing new features to improve the proposed surface rotation invariant texture classification scheme in *Chapter 6*.

8.2.1. Misclassification and Motivation

As we have previously shown in section *7.5.2*, the worst classification performance occurs on the real texture *"rkb1"* and *"bn2"* (*Figure 8. 1a*), with a classification accuracy of *24.07%* and *29.63%* respectively. It is interesting to note that among the testing samples of texture *"rkb1"*, *24* samples out of *54* lead to misclassification of texture *"bn2"*. In another words, nearly *60%* of test samples in the misclassification set (there are *41* test samples in the misclassification set) are misclassified as texture *"bn2"*. Our classification scheme cannot classify these two textures correctly in the majority of the cases.

Figure 8. 1 shows their feature spaces in two ways respectively. We may see that their gradient spectra $M(\omega, \theta)$ are very close in terms of shape and height (the amount of energy in difference at low and high frequency ranges). Their *1D* polar spectra $\Pi(\theta)$, shown in *Figure 8. 1c*, have similar means and furthermore, no obvious peaks. Thus the *SSD* of these two polar spectra is very low.

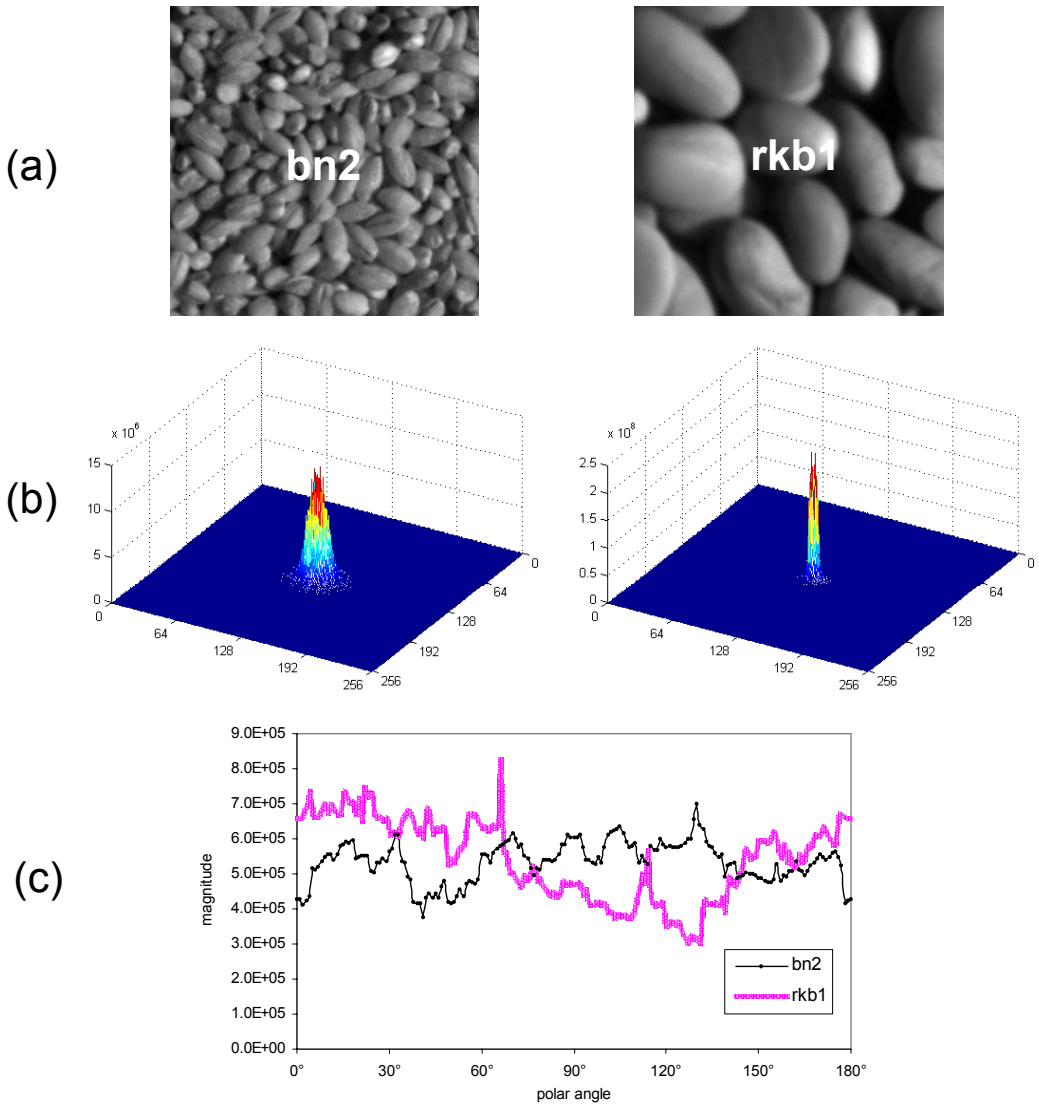

Figure 8. 1 Misclassification between the real texture "bn2" and "rkb1". (a). images of "bn2" and "rkb1"; (b). their gradient spectra $M(\omega, \theta)$; (c). their 1D polar spectrums $\Pi(\theta)$.

Therefore, we may make the conclusion that the polar spectrum $\Pi(\theta)$ cannot discriminate between two isotropic textures of the similar variance. In this case, we need an additional feature.

8.2.2. Definition of Radial Spectrum

- ***Definition***

As we saw in *Figure 8. 1b*, even though the frequency distribution of the gradient spectra $M(\omega, \theta)$ are very similar, there are still differences between them especially in the centre of frequency range. Therefore, we introduce a new feature set: the radial spectrum.

The radial spectrum $\Phi(\omega)$ is calculated by integrating of all of the contributions at each radial frequency ω in the image of the gradient spectra $M(\omega, \theta)$:

$$\Phi(\omega) = \int_0^{2\pi} M(\omega, \theta)\, d\theta \qquad (8.1)$$

We note that this has the advantage that it is *insensitive* to surface rotation in principle. On the other hand, the polar spectrum $\Pi(\theta)$ is *sensitive* to surface rotation, as it sums the magnitudes of all frequencies in one direction θ to produce a measure for the intensity in this direction.

The definition of the radial spectrum is illustrated in *Figure 8. 2* for two of the textures (isotropic texture *"gr2"* and directional texture *"grd1"*). For comparison, we use the same textures for the definition of the polar spectrum. We note that these radial spectra $\Phi(\omega)$ are typical of many textures, having high energy content near the origin and progressively lower values for higher frequencies.

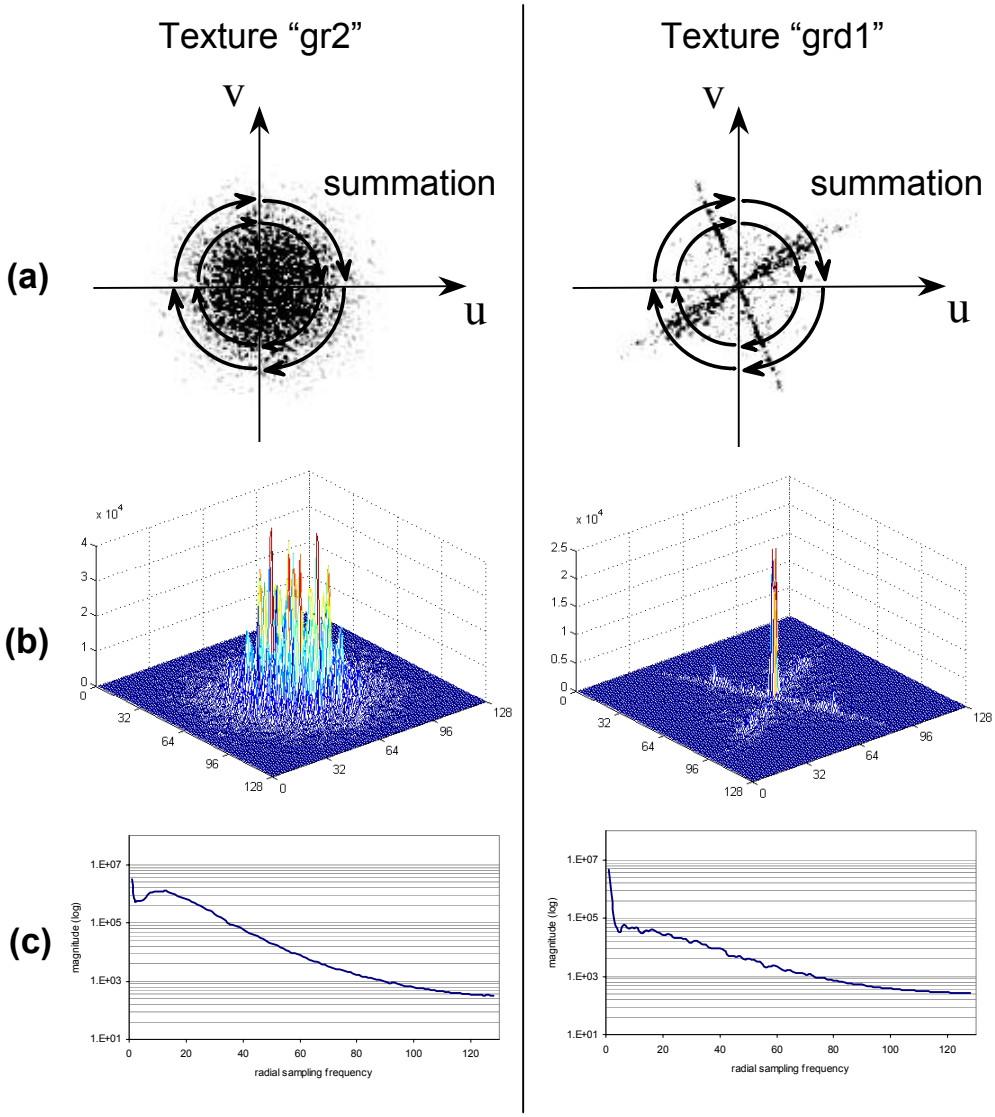

Figure 8. 2 Illustrating the definition of radial spectrum $\Phi(\omega)$ on gradient spectra $M(\omega, \theta)$ using two textures gr2 (left column) and grd1 (right column). (a). gGraphical representation of radial spectra on gradient spectra $M(\omega, \theta)$; (b). $M(\omega, \theta)$; (c). Radial spectra.

- ***Radial spectra examples***

A selection of four real textures *(gr2, wv2, an4* and *grd1)* is shown in *Figure 8. 3*. Their corresponding radial spectra $\Phi(\omega)$ on gradient spectra $M(\omega, \theta)$ at surface rotation of $\varphi = 30°$ are shown in *Figure 8. 4*. These spectra highlight interesting discriminative abilities.

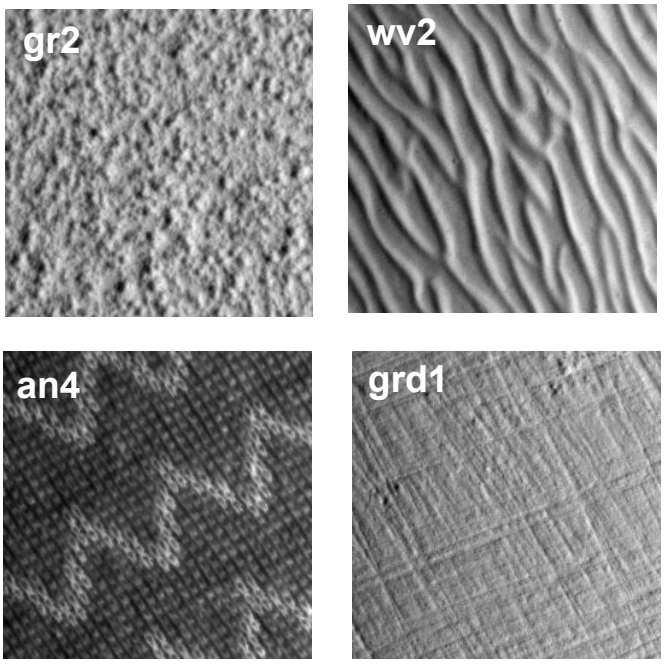

Figure 8. 3 Four real texture samples (gr2, wv2, an4 and grd1) at surface rotation $\varphi = 30°$ with constant illumination tilt angle $\tau = 0°$ and slant angle $\sigma = 50°$.

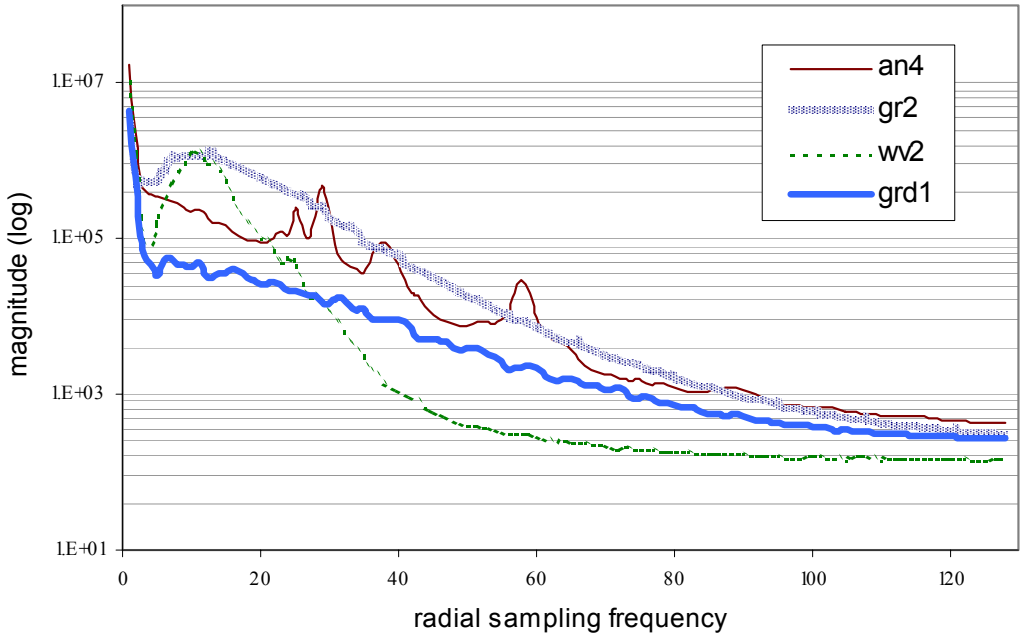

Figure 8. 4 Radial spectra $\Phi(\omega)$ of four selective real textures (gr2, wv2, grd1 and an4) on gradient spectra $M(\omega, \theta)$ at a surface rotation of $\varphi = 30°$.

- ***Expectation of radial spectra of texture "bn2" and "rkb1"***

Regarding the misclassification occurring between textures *"bn2"* and *"rkb1"*, it is interesting to examine the characteristics of their radial spectra *(Figure 8. 5)*. It is obvious that these radial spectra have additional discriminative abilities. Therefore, we expect the classification accuracy for textures *"bn2"* and *"rkb1"* based on the feature space of the radial spectrum $\Phi(\omega)$ to be better than that based on the feature space of the polar spectrum $\Pi(\theta)$ alone.

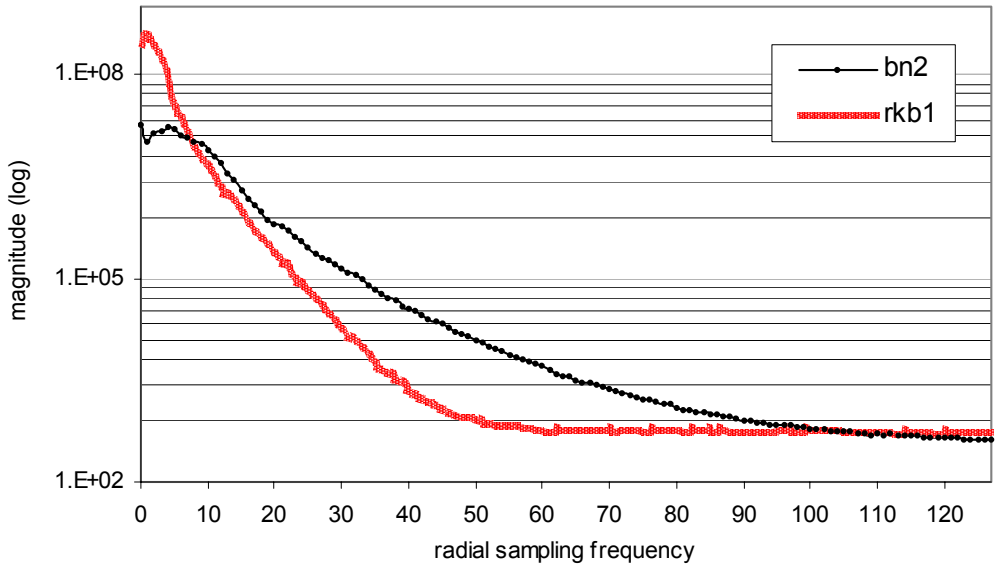

Figure 8. 5 Radial spectra $\Phi(\omega)$ of textures bn2 and rkb1 on gradient spectra $M(\omega, \theta)$ at surface rotation of $\varphi = 0°$.

8.2.3. Examination of Radial Spectrum Insensitivity to Surface Rotation

As the radial spectrum $\Phi(\omega)$ calculates the sum of the magnitude on gradient spectra $M(\omega, \theta)$ in all the directions, the radial spectrum is insensitive to surface rotation. This is shown in *Figure 8. 6*, where the respective radial spectrums $\Phi(\omega)$ of four real textures *(gr2, wv2, grd1 and an4)* at surface rotations of $\varphi = 0°, 30°, 60°, 90°, 120°$ and $150°$ are presented. We note that for each individual texture, there are no obvious

differences amongst the radial spectra $\Phi(\omega)$ calculated from those gradient spectra $M(\omega, \theta)$ whatever the surface orientation is.

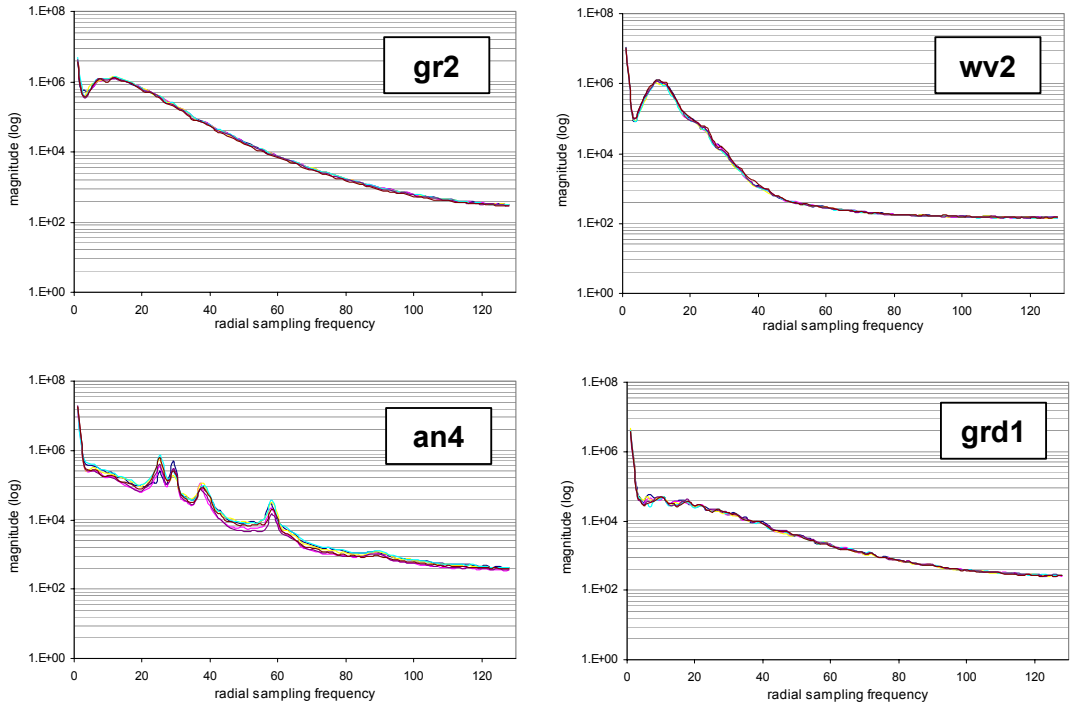

Figure 8. 6 Respective radial spectra $\Phi(\omega)$ of four selective real textures (gr2, wv2, grd1 and an4) on gradient spectra $M(\omega, \theta)$ at surface rotation of $\varphi = 0°, 30°, 60°, 90°, 120°$, and $150°$.

This important property of the radial spectrum allows the comparison of different textures to be performed using a simple sum of squared differences metric and it is not necessary to estimate the surface orientation angle prior to comparison. In other words, comparisons using radial spectra $\Phi(\omega)$ are cheaper computationally than those on polar spectrum $\Pi(\theta)$.

8.2.4. Surface-based Classification Using Radial Spectra Only

- ***Surface-based classification scheme***

The surface-based classification scheme using only the radial spectra $\Phi(\omega)$ on gradient spectra $M(\omega, \theta)$ is summarised in *Figure 8. 7*. This radial spectrum-based

classification scheme is quite similar to the polar spectrum-based one illustrated in *Chapter 6* and *Chapter 7.* As the radial spectrum is rotation insensitive, we do not have to estimate the corresponding rotation angle prior to comparison of the sum of squares difference metric between the classes.

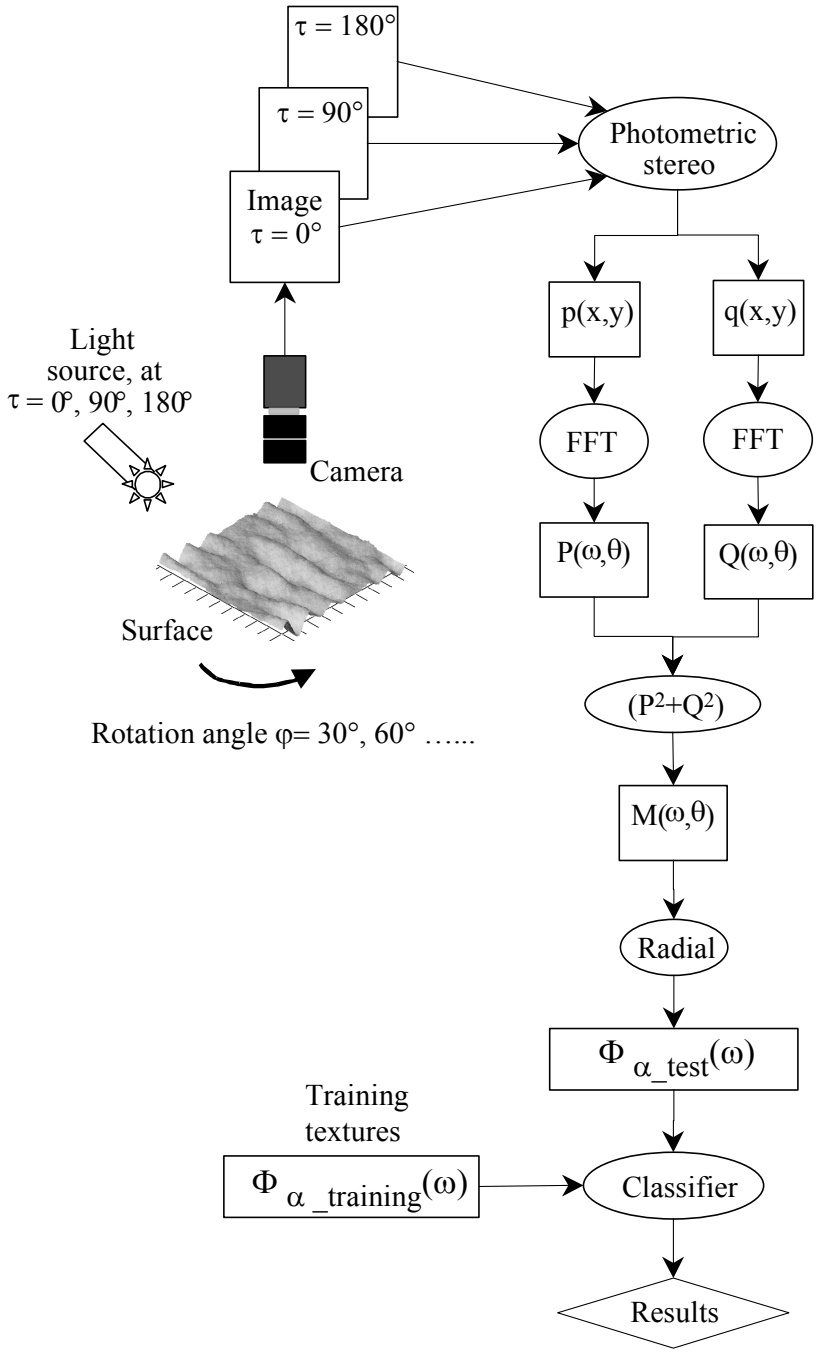

Figure 8. 7 The surface rotation invariant classification scheme using only the feature space of the radial spectrum Φ(ω) on gradient spectra M(ω, θ).

- ***Presentation of classification results***

Classification results for each real texture class are shown in *Figure 8. 8*. In addition, we also show the classification results (polar-spectrum-based) obtained in *Chapter 7* for comparison.

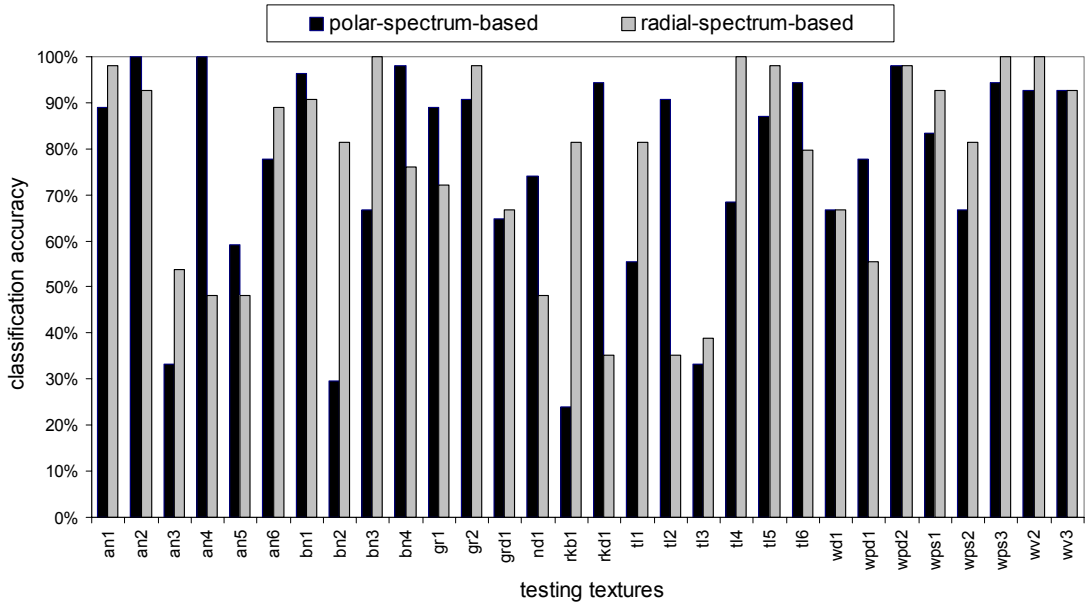

Figure 8. 8 Classification results for 30 real textures for radial spectrum feature space $\Phi(\omega)$ and polar spectrum feature space $\Pi(\theta)$ on gradient spectra $M(\omega, \theta)$.

The radial spectrum classifier achieves an average classification accuracy of *76.7%* for the same thirty real textures as used in the previous experiment in *Chapter 7*. Compared to the average classification accuracy of *76.3%* based on the polar spectrum $\Pi(\theta)$ for the same texture data set, there is little difference between them. However, as we see in *Figure 8. 8*, for some of individual real textures, their correct recognition rate changes dramatically between these two feature spaces.

- ***Discussion of classification results***

It is also interesting to note that as what we have expected, the performance of the "radial spectrum" classifier on texture *"bn2"* and *"rkb1"* is better than that obtained using the "polar spectrum" classifier. For texture *"bn2",* the correct recognition rate increases to *81.48%* from *29.63%*. On the other hand, for texture *"rkb1"* its correct recognition rate increases to *81.48%* from *24.07%.*

Although the classification accuracy of the radial spectrum-based scheme has improved and is better than that of polar spectrum-based scheme (especially for some of the isotropic textures such as *bn2, rkb1, an3,* and *bn3*), some of the directional textures give a worse performance on radial spectrum-based scheme compared to that of polar spectrum-based scheme. Texture *an4, nd1, rkd1* and *wpd1*. The summary of classification accuracy is shown in *Table 8. 1*.

Classification accuracy		Classifier based on gradient spectra $M(\omega, \theta)$	
		Polar-spectrum-based $\Pi(\theta)$	Radial-spectrum-based $\Phi(\omega)$
Overall 30 real textures		**76.30%**	**76.67%**
Isotropic texture samples	*bn2*	29.63%	81.48% ↑
	rkb1	24.07%	81.48% ↑
	an3	33.33%	53.07% ↑
	bn3	66.67%	100.00% ↑
Directional texture samples	*an4*	100.00%	48.15% ↓
	nd1	74.07%	48.15% ↓
	rkd1	94.44%	35.19% ↓
	wpd1	77.78%	55.56% ↓

Table 8. 1 Classification accuracy comparison between the polar spectrum-based scheme and radial spectrum-based scheme on gradient spectra $M(\omega, \theta)$, for 30 real textures.

8.2.5. Image-based Classification Using Radial Spectra Only

In the section, we introduce an image-based classification scheme using radial spectra only (see *Figure 8. 9*), as the comparison to the surface-based classification scheme. This classification is done in a similar way in which we present the image-based classification scheme using polar spectra in Chapter *6*.

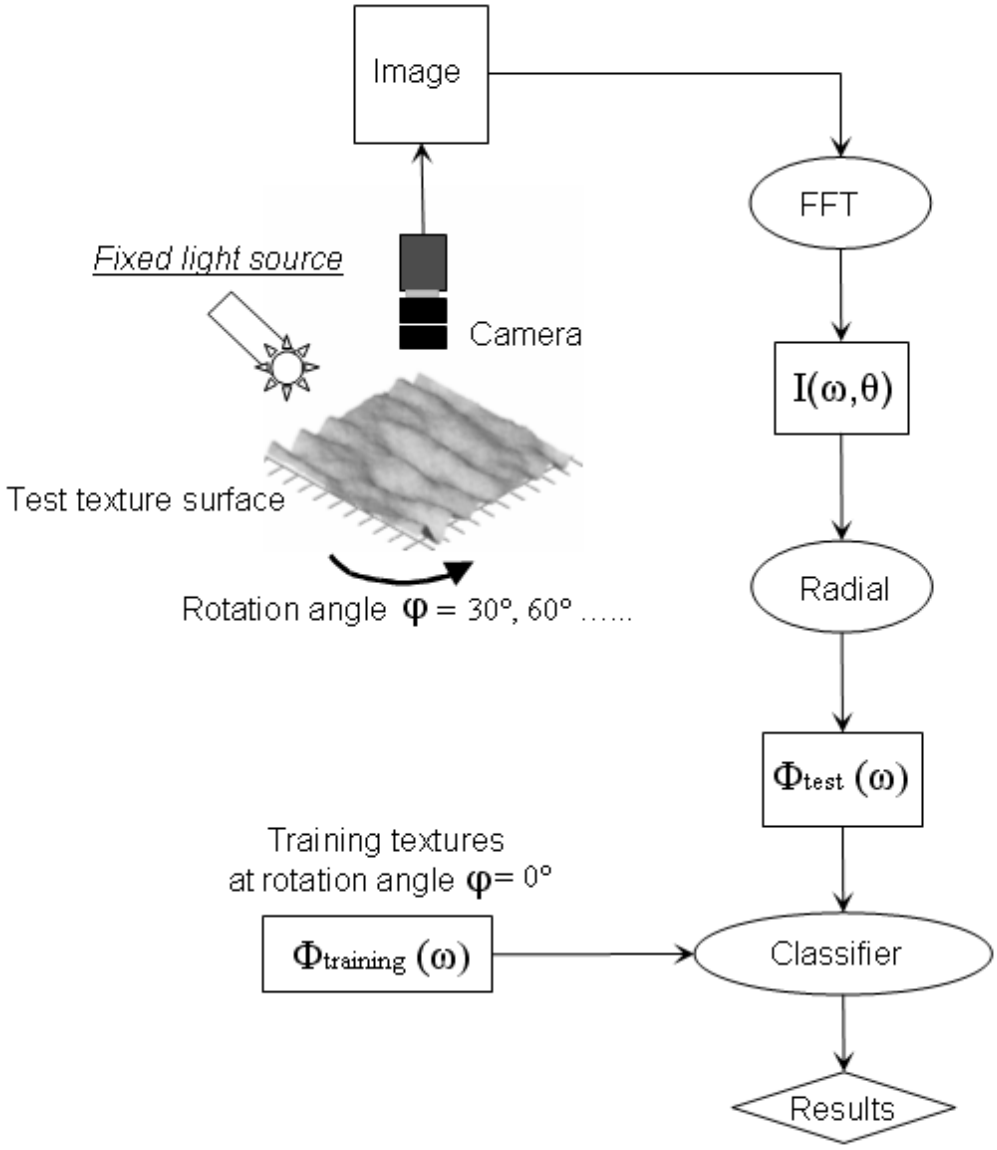

Figure 8. 9 Image-based texture classification scheme using radial spectra only.

The image-based classifier using radial spectrum only achieves an average classification accuracy of *35.3%* (*Figure 8. 10*). Compared to the average classification accuracy of *76.7%* based on the surface information for the same texture data set, it can be understood that this scheme is not surface invariant texture classification scheme. It also proofs that *3D* surface rotation is not the same as *2D* image rotation, while considering the effect of illumination conditions.

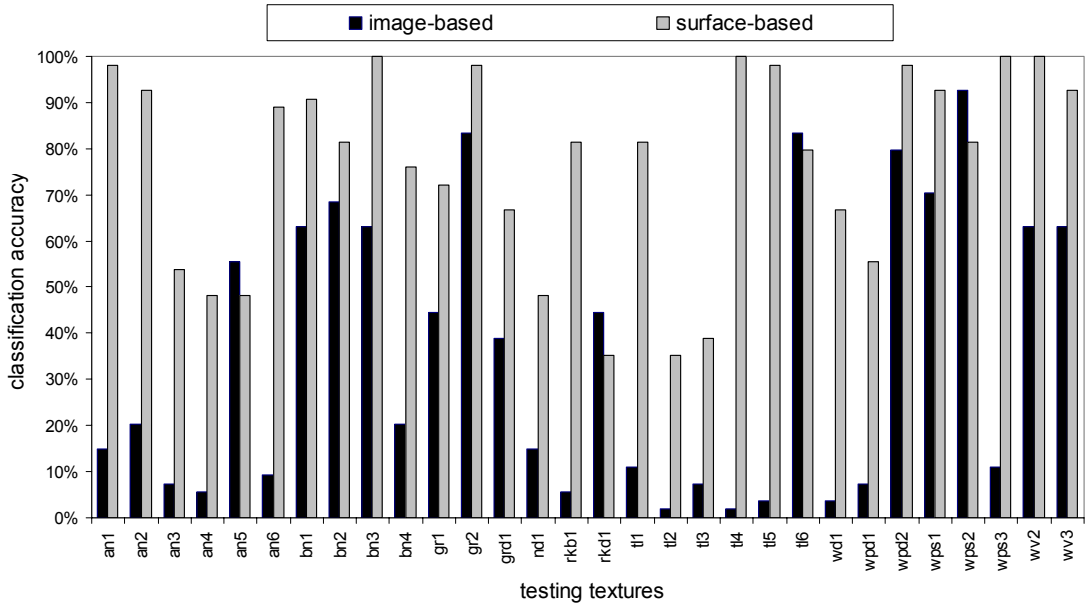

Figure 8. 10 Image-based and surface-based classification results for 30 real textures for radial spectrum feature space $\Phi(\omega)$.

8.3. New Feature Generator: Albedo Spectra

8.3.1. Misclassification and Motivation

Looking back to the classification results in *section 7.5.2*, we note that the texture *"tl3"* classification accuracy of *33.33%* gave the poorest performance. Through deeper investigation, we find that:

- there are *13* samples of *"tl3"* misclassified as *"an2"*;
- there are *23* samples of *"tl3"* misclassified as *"tl5"*,

among *54* test samples. It is easier to understand why the misclassifications take place among textures *"tl3", "an2"* and *"tl5"*. In *Figure 8. 11*, gradient spectra $M(\omega, \theta)$ of real textures *"tl3", "an2"* and *"tl5"* and their polar spectra $\Pi(\theta)$ are shown together. We note that after translating the polar spectrum of texture *"tl3"*, the dominant peaks of all three polar spectra are lying close together except for three small peaks of the polar spectrum of texture *"an2"*. This explains the misclassifications, as the values of the cost function are very close to each other.

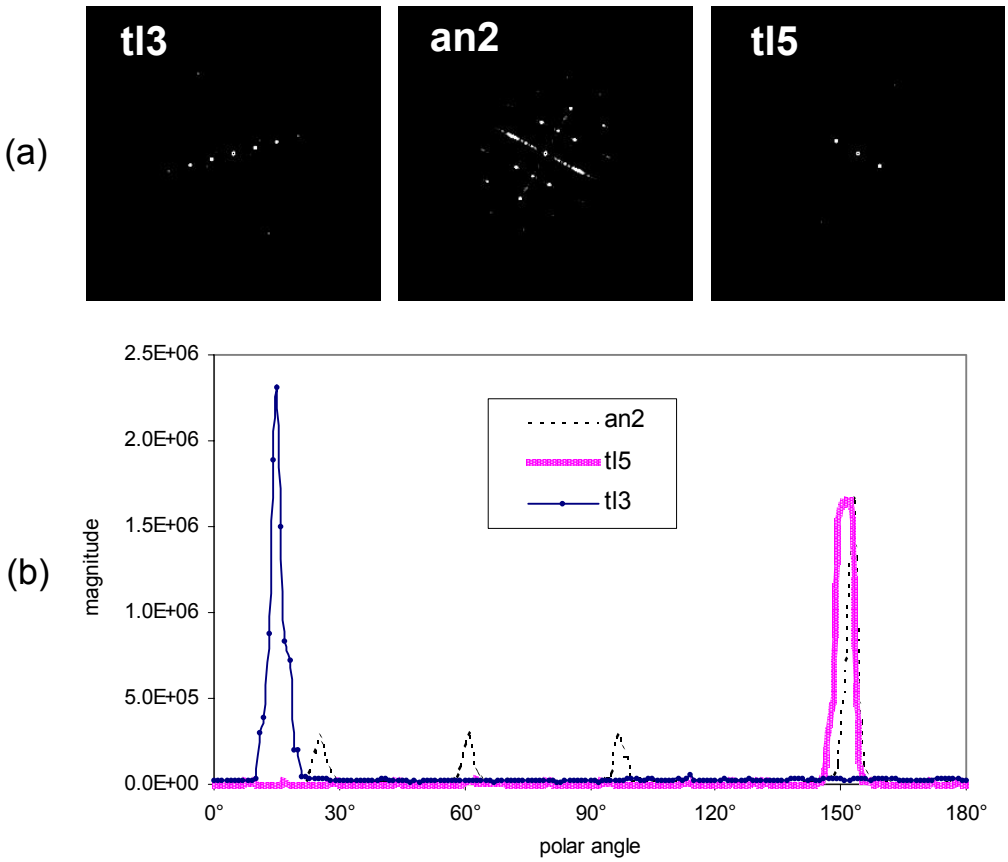

Figure 8. 11 Misclassification which occurred with real texture "tl3". (a). gradient spectra M(ω, θ) of real textures "tl3", "an2" and "tl5" respectively; (b). their 1D polar spectrums Π(θ) integrated together.

Examining the original surface images of these three textures in *Figure 8. 12* shows that there are significantly different texture patterns appearing in their surface images. On the other hand their relief images, on which our classifier really depends, are similar to each other. However, these patterns remain in the albedo image and our current classifier discards this information.

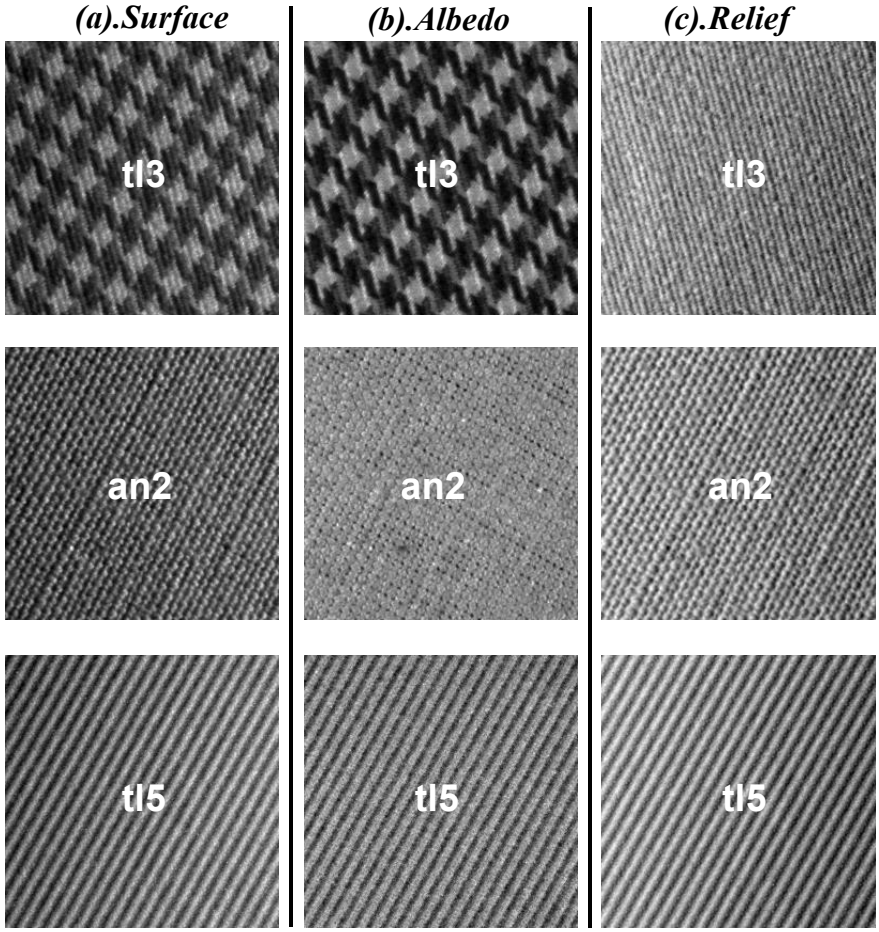

Figure 8. 12 Surface images, albedo images and relief images for real texture "tl3", "an2" and "tl5" respectively.

The conclusion drawn for the investigation of misclassification of texture *"tl3"* is that the albedo information is also important for classification, and cannot be ignored.

8.3.2. New Feature Generator: Albedo

- ***Obtaining albedo images***

From the experiments described in chapter 7, we have already obtained the surface partial derivatives $p(x, y)$ and $q(x, y)$. They can be used at each (x, y) to solve for the albedo data $\rho(x, y)$ [McGunigle98] [Kay95] [Woodham80]. Thus albedo data $\rho(x, y)$ can be easily obtained as below:

$$\rho(x,y) = \frac{i(x,y)}{\left(\frac{-p(x,y)\cos\tau\sin\sigma - q(x,y)\sin\tau\sin\sigma + \cos\sigma}{\sqrt{p^2(x,y) + q^2(x,y) + 1}} \right)} \tag{8. 2}$$

where: $\rho(x, y)$ is the albedo of the surface;

σ, τ are the illuminant's slant and tilt angles;

$p(x, y)$ and $q(x, y)$ are surface partial derivatives; and

$i(x, y)$ is image intensity.

- ***Albedo spectra in the frequency domain***

As both the polar spectrum and radial spectrum features are calculated in the frequency domain, the albedo data must be Fourier transformed. The albedo function $\rho(x,y)$ does not suffer from the same directional artefacts as the partial derivatives and may therefore be directly transformed and used:

$$A(\omega,\theta) = \Re[\rho(x,y)] \tag{8. 3}$$

where $A(\omega, \theta)$ is the albedo spectra in the frequency domain.

- ***Polar spectra and radial spectra derived from albedo spectra***

The polar spectrum $\Pi_\beta(\theta)$ and radial spectrum $\Phi_\beta(\omega)$ of the albedo data $\rho(x,y)$ are defined below:

(1). $$\Pi_\beta(\theta) = \int_0^\infty A(\omega,\theta)\, d\omega \tag{8. 4}$$

(2). $$\Phi_\beta(\omega) = \int_0^{2\pi} A(\omega,\theta)\, d\theta \tag{8. 5}$$

where ω is radial frequency in polar co-ordination,

θ is the polar frequency angle in polar co-ordination,

$A(\omega, \theta)$ is the albedo spectra in the frequency domain,

$\Pi_\beta(\theta)$ is the albedo-based polar spectrum, and

$\Phi_\beta(\omega)$ is the albedo-based radial spectrum.

Note that, in order to discriminate between the polar spectra and radial spectra based on gradient spectra $M(\omega, \theta)$ and albedo spectra $A(\omega, \theta)$, we re-define the polar spectrum on gradient data as $\Pi_\alpha(\theta)$, and the radial spectrum on gradient data as $\Phi_\alpha(\omega)$. This is summarised in *Table 8. 2*.

	Gradient spectra $M(\omega, \theta)$	Albedo spectra $A(\omega, \theta)$
Polar spectrum	$\Pi_\alpha(\theta)$	$\Pi_\beta(\theta)$
Radial spectrum	$\Phi_\alpha(\omega)$	$\Phi_\beta(\omega)$

Table 8. 2 Definition of the polar spectrum and radial spectrum on both gradient spectra and albedo spectra.

Recalling the misclassifications that occurred between textures *"tl3", "an2"* and *"tl5"*, we expect that the albedo data should be better than surface relief data in the classifier. *Figure 8. 13* where albedo spectra $A(\omega, \theta)$ plus corresponding polar spectrum $\Pi_\beta(\theta)$ and radial spectrum $\Phi_\beta(\omega)$ for real textures *"tl3", "an2"* and *"tl5"* are shown respectively, confirms this expectation. We note that both the polar spectra $\Pi_\beta(\theta)$ and the radial spectra $\Phi_\beta(\omega)$ calculated on albedo data have a discriminative ability compared with those obtained from gradient spectra $M(\omega, \theta)$.

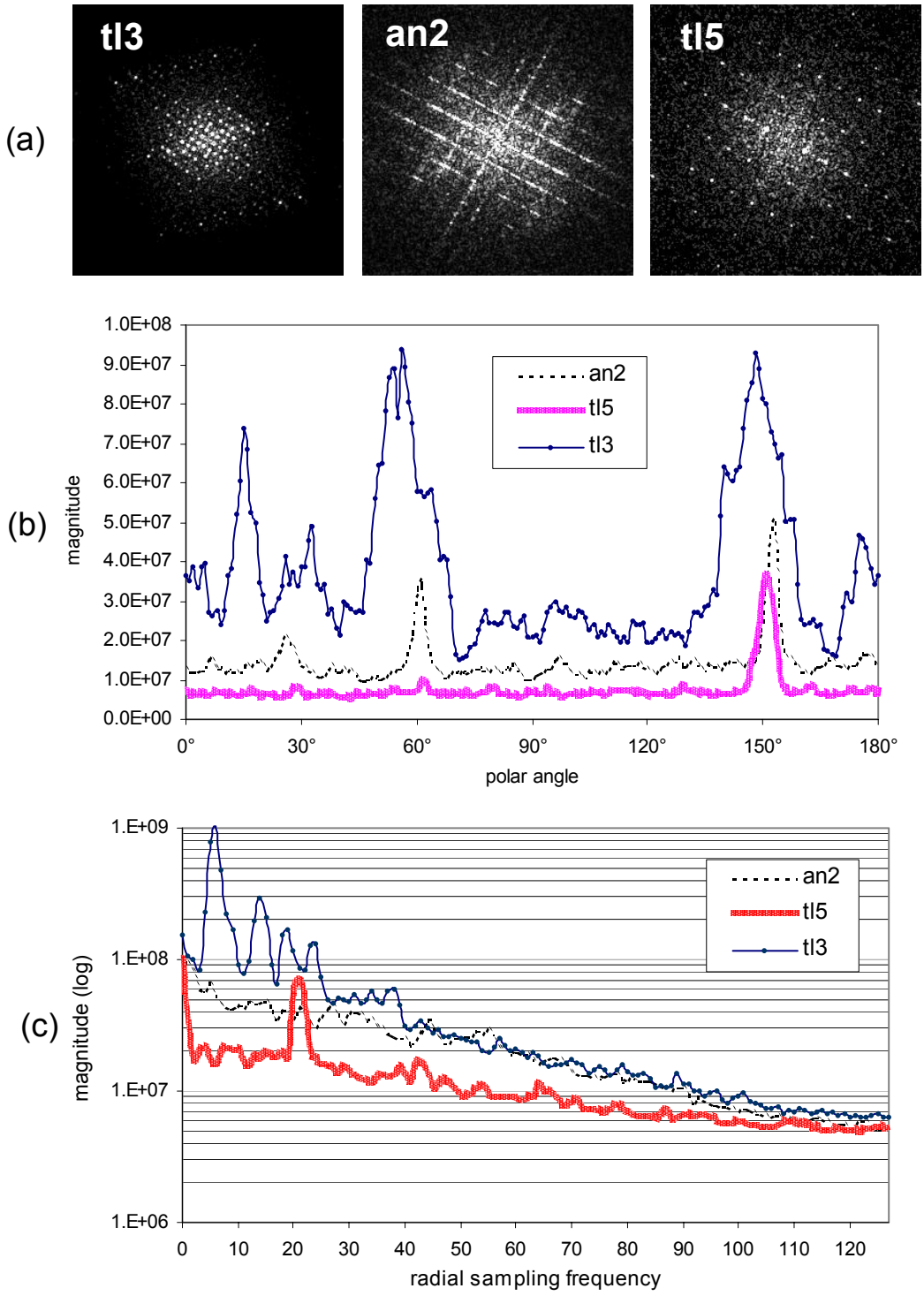

Figure 8. 13 Albedo spectra plus the corresponging polar spectrum and radial spectrum for real texture "tl3", "an2" and "tl5" respectively. (a). albedo spectra $A(\omega, \theta)$. (b). polar spectrum $\Pi_\beta(\theta)$. (c). radial spectrum $\Phi_\beta(\omega)$.

8.3.3. Feature Characteristics on Albedo

We use the four textures *(gr2, wv2, grd1* and *an4)* to illustrate the feature characteristics of albedo data (three are the same as those used in chapter *6*). Firstly, their albedo images and albedo spectra $A(\omega, \theta)$ in the frequency domain at surface orientation angle of $\varphi = 30°$ are shown in *Figure 8. 14*. Secondly their corresponding polar spectra $\Pi_\beta(\theta)$ on albedo spectra $A(\omega, \theta)$ are shown in *Figure 8. 15*. Finally their polar spectra $\Pi_\beta(\theta)$ on albedo spectra $A(\omega, \theta)$ are shown in *Figure 8. 16*.

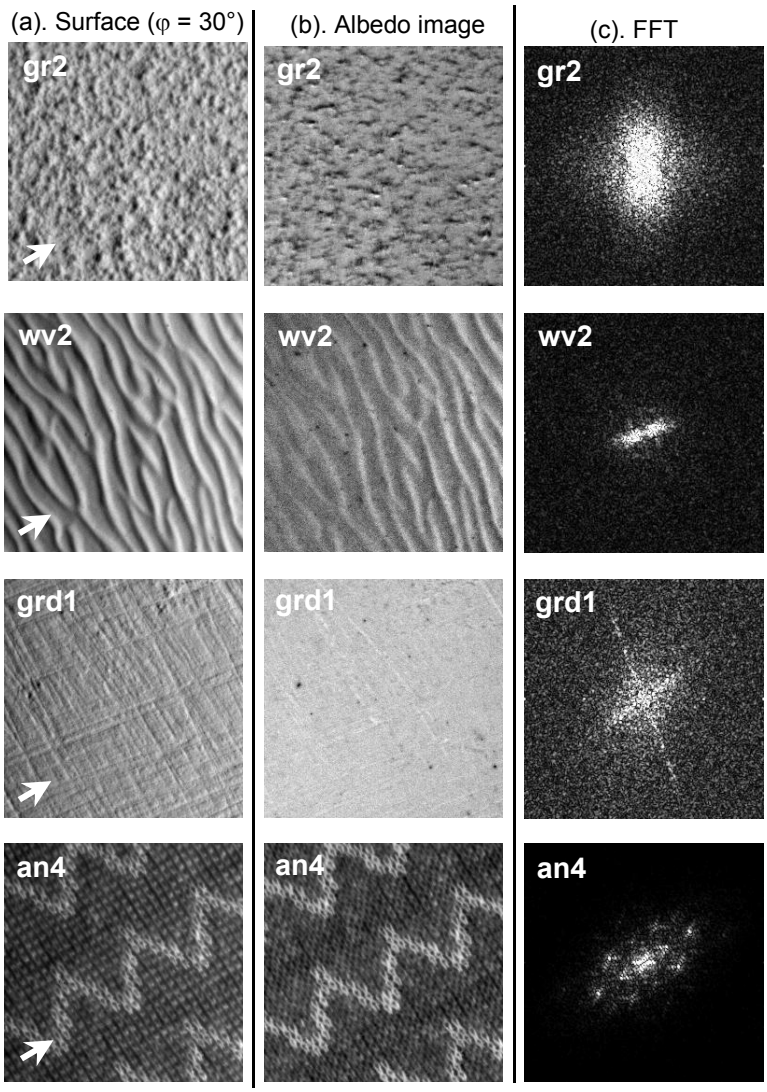

Figure 8. 14 Albedo spectra $A(\omega, \theta)$ for four real textures (gr2, wv2, grd1 and an4). (a). surface at orientation angle of $\varphi = 30°$. (b). their corresponding albedo image p(x,y) obtained by using photometric stereo. (c). their corresponding albedo spectra $A(\omega, \theta)$ in the frequency domain.

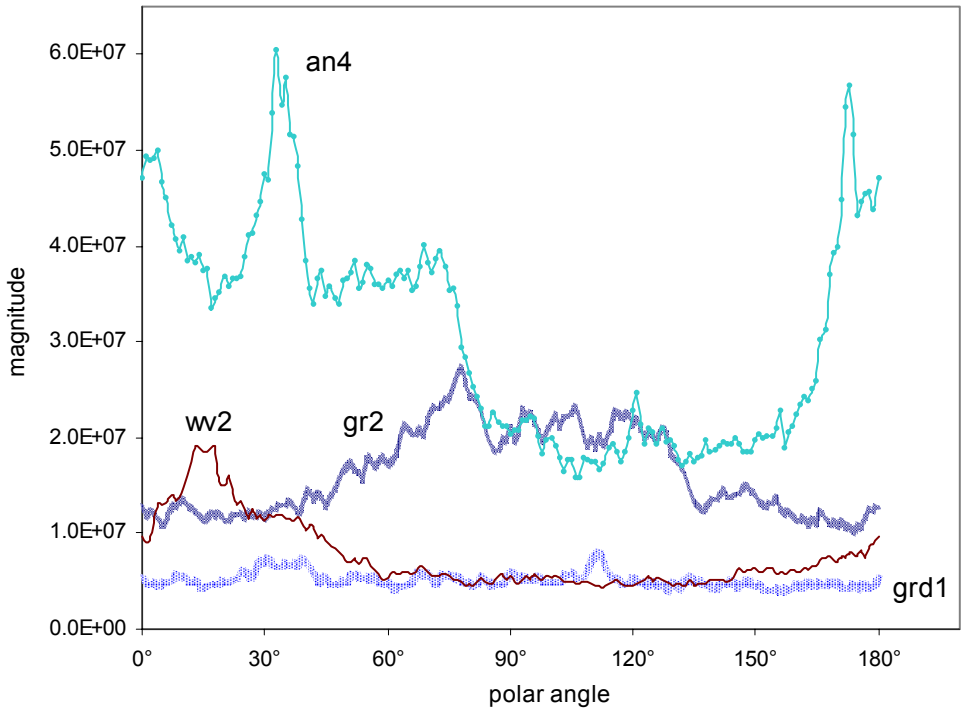

Figure 8. 15 Polar spectrum $\Pi_\beta(\theta)$ on albedo spectra $A(\omega, \theta)$ for four real textrues (gr2, wv2, grd1 and an4) at orientation angle of $\varphi = 30°$.

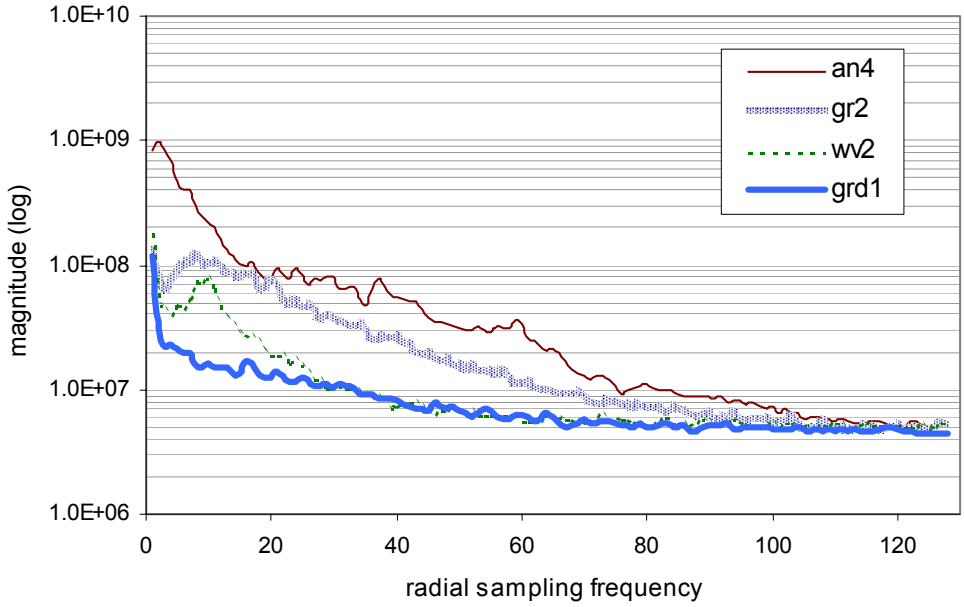

Figure 8. 16 Radial spectrum $\Phi_\beta(\omega)$ on albedo spectra $A(\omega, \theta)$ for four real textrues (gr2, wv2, grd1 and an4) at orientation angle of $\varphi = 30°$.

8.3.4. Albedo Feature Sensitivity to Surface Rotation

Figure 8. 17 shows the albedo images $\rho(x, y)$ at a surface orientation angles of φ = *30°, 60°, 90°* and *120°* of four textures *(gr2, wv2, grd1 and an4)*, obtained by using photometric stereo. Their corresponding albedo spectra $A(\omega, \theta)$ are shown in *Figure 8. 18*.

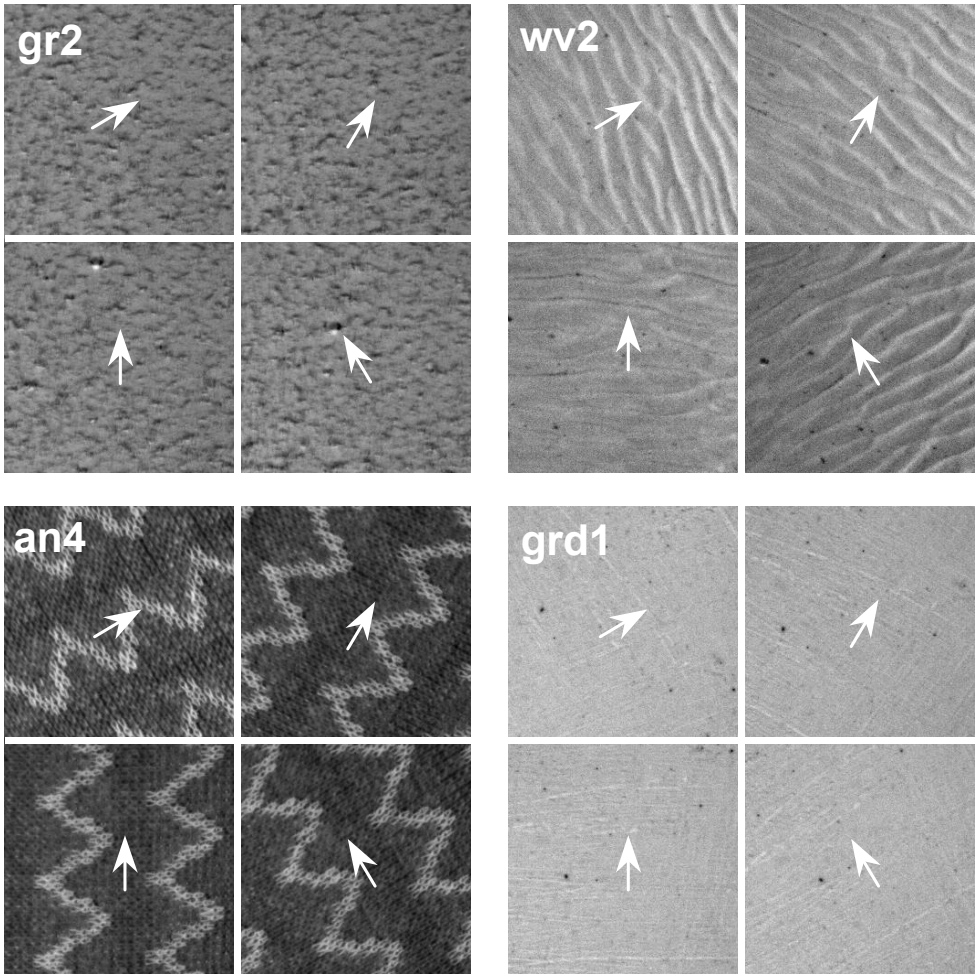

Figure 8. 17 Albedo image $\rho(x,y)$ at surface orientation angles of φ = 30°, 60°, 90° and 120° for four real textures (gr2, wv2, grd1 and an4). For the purpose of display, they are shown in a montage format where the white arrows indicate the surface rotation directions.

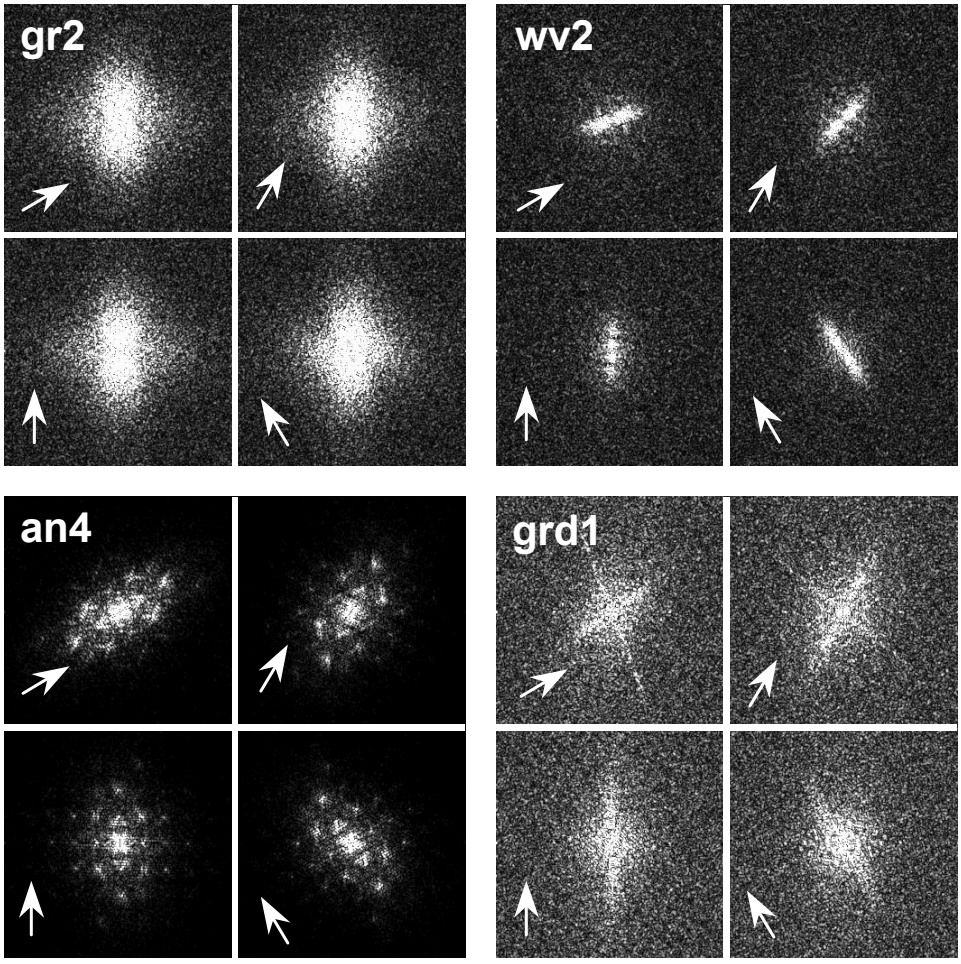

Figure 8. 18 Albedo spectra A(ω, θ) at surface orientation angles of φ = 30°, 60°, 90° and 120° for four textures (gr2, wv2, grd1 and an4). For the purpose of display, all four albedo spectra at different surface orientations are displayed in a montage format for each individual texture (the white arrow indicates the surface rotation direcetion).

From these figures, it is clear that albedo data are sensitive to surface rotation in the same manner as gradient spectra $M(\omega, \theta)$ shown before. Therefore, the rotation invariant texture classification scheme previously discussed, using both polar spectra and radial spectra, can be applied.

8.3.5. Developing New Classifiers

- ***Developing three classifiers based on albedo data***

A modified surface rotation invariant texture classification scheme based on albedo data is summarised in *Figure 8. 19*.

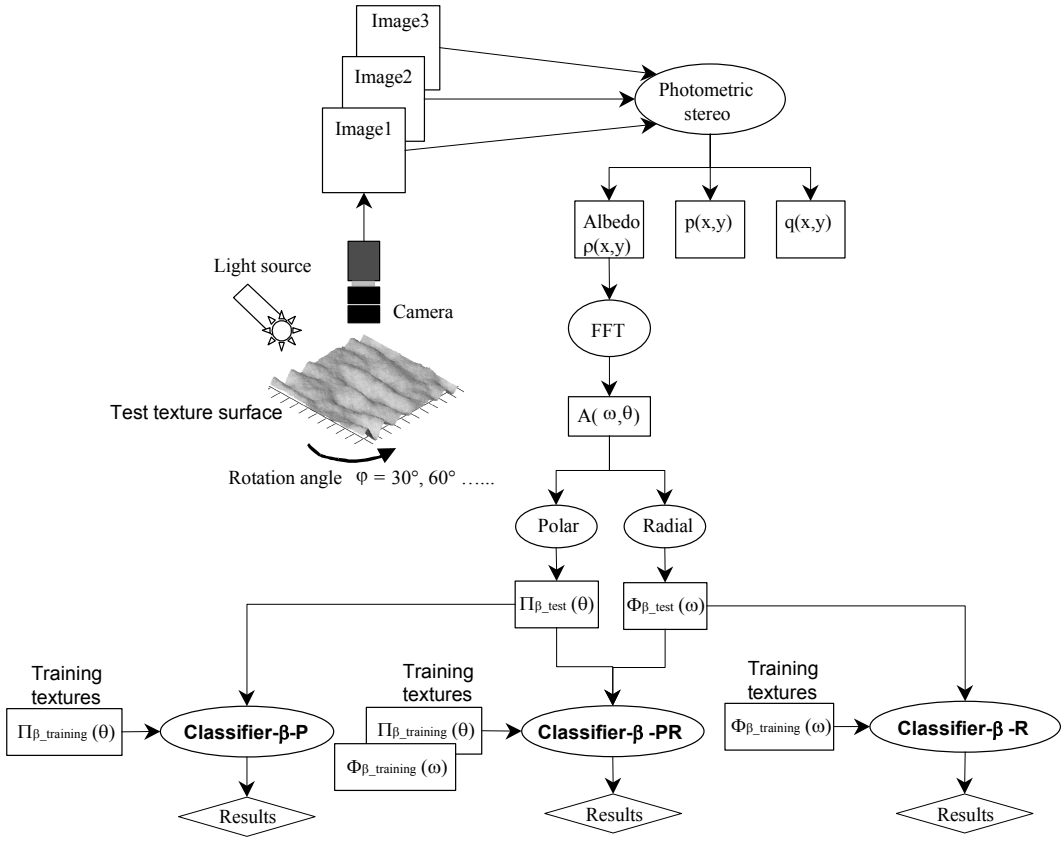

Figure 8. 19 Surface rotation invariant texture classification scheme based on albedo data only. Classifier-β-P is based on the polar spectrum $\Pi_\beta(\theta)$ only; Classifier-β-R is based on the radial spectrum $\Phi_\beta(\omega)$ only; and Classifier-β-PR is based on the combination of the polar spectrum $\Pi_\beta(\theta)$ and radial spectrum $\Phi_\beta(\omega)$ together.

The process is as follows:

1) albedo data $\rho(x,y)$ of the test texture can be directly estimated by using three-image-based photometric stereo.
2) They are then Fourier transformed to give the albedo spectra $A(\omega,\theta)$ and processed to provide the albedo polar spectrum $\Pi_{\beta\_test}(\theta)$ and albedo radial spectrum $\Phi_{\beta\_test}(\omega)$.
3) The polar spectrum $\Pi_{\beta\_test}(\theta)$ of the test texture is compared with the polar spectra $\Pi_{\beta\_training}(\theta)$ obtained from training images using a sum of squared differences metric. As before the task is to minimise the difference metric with

regard to surface orientations. This also provides an estimate of the orientation angle $\varphi_{estimate}$ of the test texture.

4) The radial spectrum $\Phi_{\beta\_test}(\omega)$ is compared with the radial spectra $\Phi_{\beta\_training}(\omega)$ obtained from training images. (This also uses a sum of squared differences metric but it does not need to be calculated over a range of angular displacements, as radial spectra are insensitive to surface orientation.)
5) The total sum of squared errors statistic is calculated from step *3* and *4* and the lowest score provides the classification decision. There are three different kinds of classifier thus allowing a for comparative study.

I. **Classifier-β-P** uses only the albedo polar spectrum $\Pi_{\beta}(\theta)$, and its classification cost function is:

$$SSD_{\beta\_polar} = \sum_{\theta=0°}^{180°} [\, \Pi_{\beta\_test}(\theta + \varphi_{estimate}) - \Pi_{\beta\_training}(\theta) \,]^2 \qquad (8.\ 6)$$

where $\Pi_{\beta\_test}(\theta)$ is the polar spectrum of the albedo spectra $A(\omega,\theta)$ obtained from the *test* texture data set; $\Pi_{\beta\_training}(\theta)$ is the polar spectrum of the albedo spectra obtained from the *training* texture data set; while $\varphi_{estimate}$ is the estimated surface orientation angle; and the resolution of θ is at step *1°* from *0°* to *180°*.

II. **Classifier-β-R** is based on the radial spectrum $\Phi_{\beta}(\omega)$ only and its classification cost function is:

$$SSD_{\beta\_radial} = \sum_{\omega=1}^{R} [\, \Phi_{\beta\_test}(\omega) - \Phi_{\beta\_training}(\omega) \,]^2 \qquad (8.\ 7)$$

where $\Phi_{\beta\_test}(\omega)$ is the radial spectrum of the albedo spectra $A(\omega,\theta)$ obtained from the *test* texture data set; $\Phi_{\beta\_training}(\omega)$ is the radial spectrum of the albedo spectra obtained from the *training* texture data set; and R is the high frequency range radius of a circle centred at the origin. For $N \times N$ albedo spectra $A(\omega,\theta)$, R is typically chosen as $N/2$.

III. **Classifier-β-PR** is based on a combination of the polar spectrum $\Pi_{\beta}(\theta)$ and the radial spectrum $\Phi_{\beta}(\omega)$.

$$SSD_{\beta\_polar\&radial} = (SSD^{*}_{\beta\_polar}) + (SSD^{*}_{\beta\_radial}) \quad (8.\ 8)$$

where $SSD^{*}_{\beta\_polar}$ is the normalised cost function value of SSD_{β_polar} obtained from *Classifier-β-P*; $SSD^{*}_{\beta\_radial;}$ is the normalised cost function value of SSD_{β_radial} obtained from *Classifier-β-R*. We note that the original SSD_{β_polar} and SSD_{β_radial} come from different kinds of feature spaces: polar spectrum and radial spectrum respectively. We have to normalise their values in each feature vector within all of the considered texture classes prior to using the *classifier-β-PR*.

- ***Developing a new classifier based on gradient data for comparison***

In a similar manner to the way in which we developed three albedo based classifiers *(Classifier-β-P, Classifier-β-R and Classifier-β-PR)*, we may define our two exiting classifiers based on gradient data as *Classifier-α-P* (where the feature space comes from the polar spectrum) and *Classifier-α-R* (where the feature space comes from the radial spectrum). In addition, we can extend and develop a new classifier (*Classifier-α-PR)* which combines the polar spectrum and radial spectrum features obtained from gradient data. Note that α indicates that the feature space in a classifier comes from gradient data. On the other hand, β denotes that the feature space in a classifier comes from albedo data. *Figure 8. 20* summarises all three classifiers *(Classifier-α-P, Classifier-α-R and Classifier-α-PR)*.

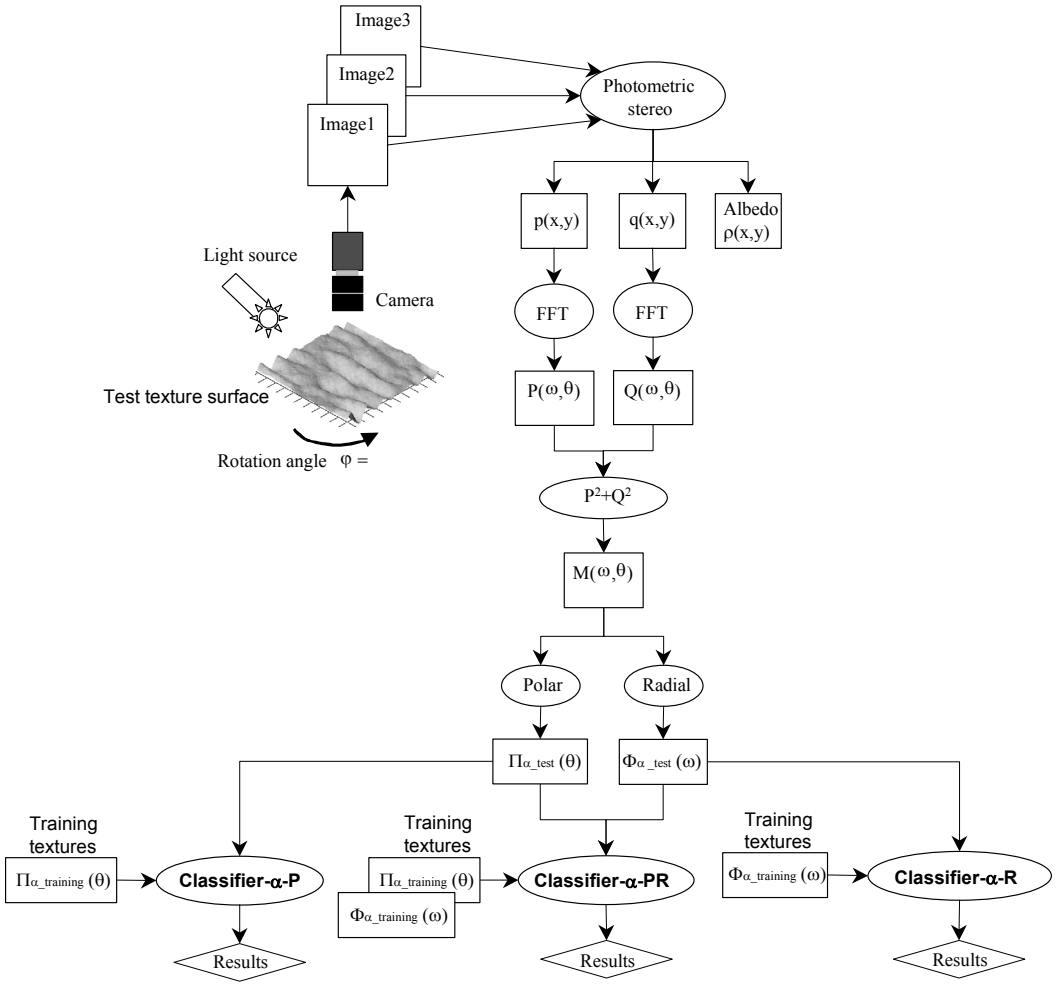

Figure 8. 20 Surface rotation invariant texture classification scheme based on gradient data only. Classifier-α-P is based on the polar spectrum $\Pi_\alpha(\theta)$ only; Classifier-α-R is based on the radial spectrum $\Phi_\alpha(\omega)$ only; and Classifier-α-PR is based on a combination of the polar spectrum $\Pi_\alpha(\theta)$ and the radial spectrum $\Phi_\alpha(\omega)$.

The notation of all the designed classifiers in terms of polar spectra and radial spectra on both gradient spectra and albedo spectra is shown in *Table 8. 3*.

Classifier [Feature space]	***Polar spectrum $\Pi(\theta)$***	***Radial spectrum $\Phi(\omega)$***	***Polar spectrum $\Pi(\theta)$ & Radial spectrum $\Phi(\omega)$***
Gradient spectra $M(\omega, \theta)$	Classifier-α-P [$\Pi_\alpha(\theta)$]	Classifier-α-R [$\Phi_\alpha(\omega)$]	Classifier-α-PR [$\Pi_\alpha(\theta)$ & $\Phi_\alpha(\omega)$]
Albedo spectra $A(\omega, \theta)$	Classifier-β-P [$\Pi_\beta(\theta)$]	Classifier-β-R [$\Phi_\beta(\omega)$]	Classifier-β-PR [$\Pi_\beta(\theta)$ & $\Phi_\beta(\omega)$]

Table 8. 3 Notation of classifiers' design in terms of the polar spectrum and the radial spectrum on both gradient spectra and albedo spectra.

8.3.6. Classification Results on Albedo Data Only

In this section, we will present and discuss the classification results using albedo data only. A comparative study of the classification results for gradient data and albedo data will be given in the next section.

Figure 8. 21 shows classification results for the three albedo-based classifiers derived from *30* real textures. In addition, the overall classification accuracy for the classifiers *(Classifier-β-P, Classifier-β-R and Classifier-β-PR)* is presented in *Table 8. 4*. The *Classifier-β-P* uses only the polar spectrum $\Pi_\beta(\theta)$ to achieve an overall classification accuracy of *67.28%* and the *Classifier-β-R* using only the radial spectrum $\Phi_\beta(\omega)$ improves this figure to *71.05%*. The *Classifier-β-PR* combining the polar spectrum $\Pi_\beta(\theta)$ and radial spectrum $\Phi_\beta(\omega)$ actually pushes the classification rate up to *76.54%*.

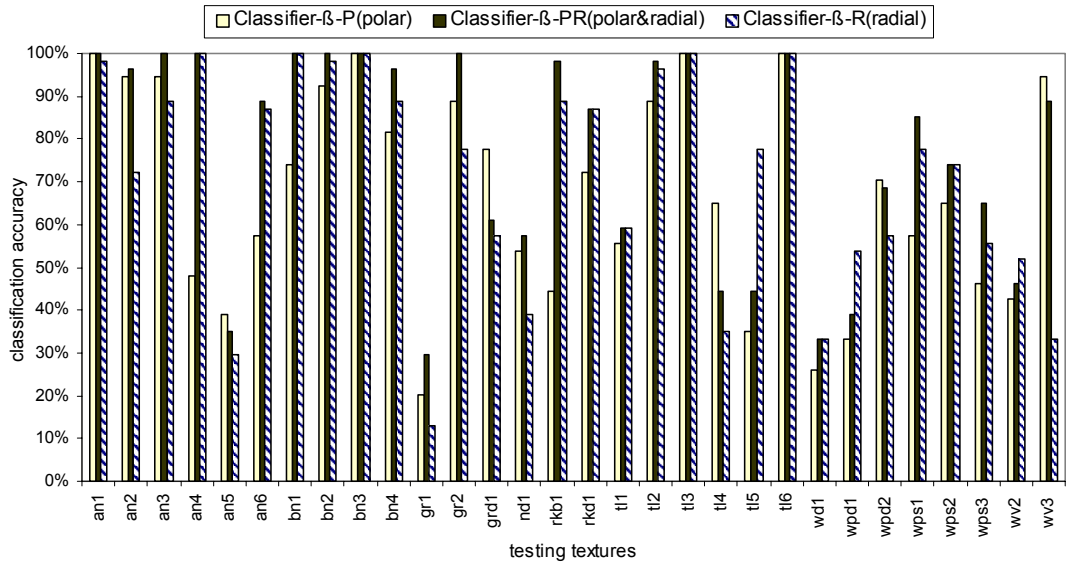

Figure 8. 21 Classification results for 30 real textures based on albedo data only. Note that Classifier-β-P is based on the polar spectrum $\Pi_\beta(\theta)$ only; Classifier-β-R is based on the radial spectrum $\Phi_\beta(\omega)$ only; and Classifier-β-PR is based on a combination of the polar spectrum $\Pi_\beta(\theta)$ and the radial spectrum $\Phi_\beta(\omega)$.

	Polar spectrum $\Pi(\theta)$	***Radial spectrum $\Phi(\omega)$***	***Polar spectrum $\Pi(\theta)$ & Radial spectrum $\Phi(\omega)$***
Classifier [Feature space]	Classifier-β-P [$\Pi_\beta(\theta)$]	Classifier-β-R [$\Phi_\beta(\omega)$]	Classifier-β-PR [$\Pi_\beta(\theta)$ & $\Phi_\beta(\omega)$]
Overall Classification accuracy	67.28%	71.05%	76.54%

Table 8. 4 Overall classification accuracy for all 30 real textures in three different classifiers (Classifier-β-P, Classifier-β-R and Classifier-β-PR).

We can also see that adding extra feature space, either on the polar spectrum $\Pi_\beta(\theta)$ or on the radial spectrum $\Phi_\beta(\omega)$, improves the overall performance of the classifier on the *30* real textures. In most cases, for each individual texture we note that the classification accuracy obtained from *Classifier-β-PR* is better than those of *Classifier-β-P* and *Classifier-β-R*, apart from a few textures such as *"an5", "grd1", "tl4", "tl5"*.

8.3.7. Comparative Study of Classification Results Between Gradient Data and Albedo Data

We have introduced the new feature generator of albedo data in addition to our existing feature generator of gradient data shown in *Chapter 6*. The classification results from the albedo data have been given and analysed. Now we will discuss the comparative study of classification results for gradient data and albedo data.

- ***The importance of albedo data***

A summary of classification accuracy for texture *"tl3"* is given in *Table 8. 5*. It shows very clear that the successful classification rates obtained from the feature generators of albedo spectra $A(\omega, \theta)$ are *100%* and are much improved compared to those (from *33.33%* to *38.89%*) obtained from the gradient spectrum $M(\omega, \theta)$, whether the feature space is based on the polar spectrum $\Pi(\theta)$, the radial spectrum $\Phi(\omega)$, or the combination of the polar spectrum $\Pi(\theta)$ and the radial spectrum $\Phi(\omega)$.

	Gradient spectra $M(\omega, \theta)$	***Albedo spectra*** $A(\omega, \theta)$
Polar spectrum $\Pi(\theta)$	33.33%	100% ↑
Radial spectrum $\Phi(\omega)$	38.89%	100% ↑
Polar spectrum $\Pi(\theta)$ ***& Radial spectrum*** $\Phi(\omega)$	33.33%	100% ↑

Table 8. 5 Classification accuracy for texture "tl3" for gradient feature space $M(\omega, \theta)$ and albedo feature space $A(\omega, \theta)$.

We may draw the conclusion that albedo can be an important feature in our classification schemes.

- ***Classification results only based on gradient data for all 30 real textures***

Before we consider the comparative study on the classification results for gradient data and albedo data, we firstly extend our existing surface rotation invariant texture classification scheme on gradient data to a full range of classifiers *(Classifier-α-P, Classifier-α-R and Classifier-α-PR in Figure 8. 20)* in the same manner as was we have done with the albedo data *(Classifier-β-P, Classifier-β-R and Classifier-β-PR in Figure 8. 19)*.

The classification results for *30* real textures based on gradient data are shown in *Figure 8. 22* and *Table 8. 6*.

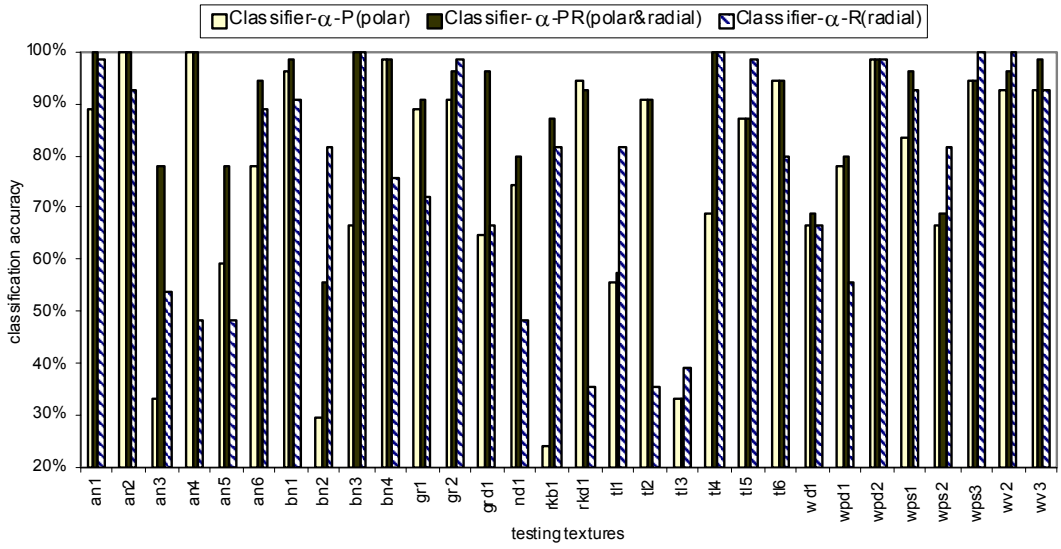

Figure 8. 22 Classification results for 30 real textures based on gradient data only. Note that Classifier-α-P is based on the polar spectrum $\Pi_\alpha(\theta)$ only; Classifier-α-R is based on the radial spectrum $\Phi_\alpha(\omega)$ only; and Classifier-α-PR is based on a combination of the polar spectrum $\Pi_\alpha(\theta)$ and the radial spectrum $\Phi_\alpha(\omega)$.

Classifier	Classifier based on gradient spectra $M(\omega, \theta)$		
	Classifier-α-P [$\Pi_\alpha(\theta)$]	*Classifier-α-R* [$\Phi_\alpha(\omega)$]	*Classifier-α-PR* [$\Pi_\alpha(\theta)$ & $\Phi_\alpha(\omega)$]
Overall 30 real textures	**76.30%**	**76.67%**	**86.91%** ↑↑

Table 8. 6 Comparison of classification accuracy for three different classifiers (Classifier-α-P, Classifier-α-R and Classifier-α-PR) on gradient spectra $M(\omega, \theta)$, for 30 real textures and some selected texture samples.

- ***Comparative study of classification results between gradient data and albedo data***

Now it is time to give the comparative study of classification results for the gradient data and albedo data. In *Figure 8. 23*, we only give the results for two of the classifiers *(Classifier-α-PR and Classifier-β-PR)* based on gradient data and albedo data respectively. On the other hand, *Table 8. 7* provides the comparative classification results for all the six classifiers *(Classifier-α-P, Classifier-α-R, Classifier-α-PR, Classifier-β-P, Classifier-β-R and Classifier-β-PR)*.

We note:

1) That the classification accuracy based on gradient spectra $M(\omega, \theta)$ is better than that obtained from albedo spectra $A(\omega, \theta)$, whether the feature space used is the polar spectrum $\Pi(\theta)$, radial spectrum $\Phi(\omega)$ or their combination.
2) The classification results derived from the combination of feature spaces (the polar spectrum $\Pi(\theta)$ and the radial spectrum $\Phi(\omega)$) are better than those derived from the individual feature spaces alone.
3) We may integrate the feature generators of gradient spectra $M(\omega, \theta)$ and albedo spectra $A(\omega, \theta)$ together to provide more discriminative ability.

	Polar spectrum $\Pi(\theta)$	***Radial spectrum $\Phi(\omega)$***	***Polar spectrum $\Pi(\theta)$ & Radial spectrum $\Phi(\omega)$***
Gradient spectra $M(\omega, \theta)$	76.30% [Classifier-α-P]	76.67% [Classifier-α-R]	86.91% [Classifier-α-PR]
Albedo spectra $A(\omega, \theta)$	67.28% [Classifier-β-P]	71.05% [Classifier-β-R]	76.54% [Classifier-β-PR]

Table 8. 7 A full comparative study of overall classification results for 30 real textures for gradient data features and albedo data features.

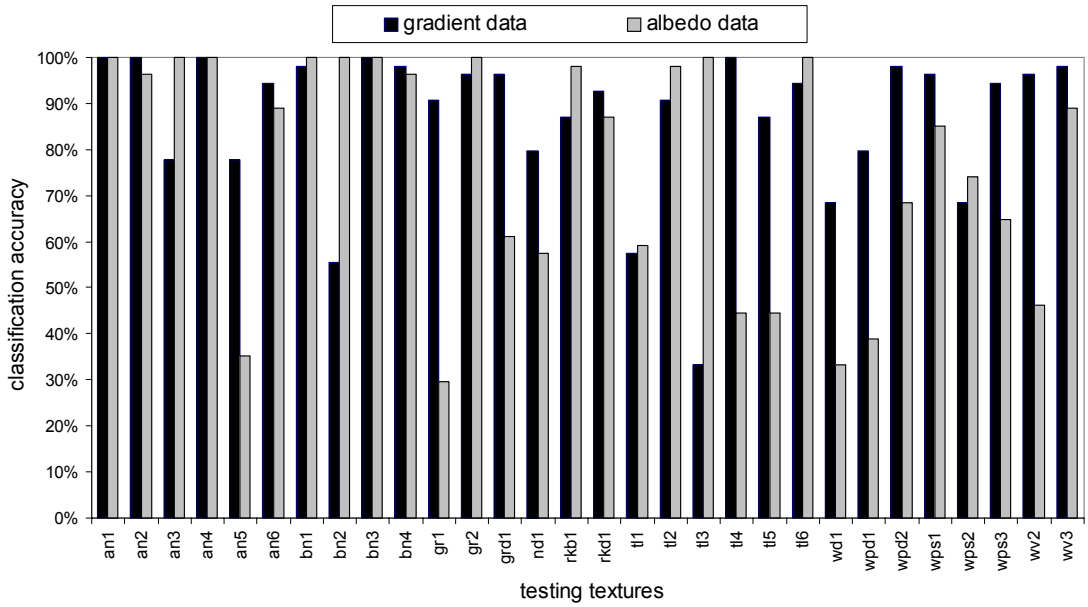

Figure 8. 23 Comparison of classification results for 30 real textures for Classifier-α-PR (obtained from gradient data with the combination of the polar spectrum and the radial spectrum) and Classifier-β-PR (obtained from albedo data with the combination of the polar spectrum and the radial spectrum).

8.4. An Improved Surface Rotation Invariant Classification Scheme by Combining Feature Spaces and Feature Generators

8.4.1. Summary of Classification Scheme

We have already noted that radial spectra can provide very useful features for classification, and albedo information can be important as a feature generator. Therefore, we integrate those two feature space (*polar spectra* and *radial spectra*) and two feature generators (*gradient data* and *albedo data*) in our improved surface rotation invariant classification scheme, illustrated in *Figure 8. 24*.

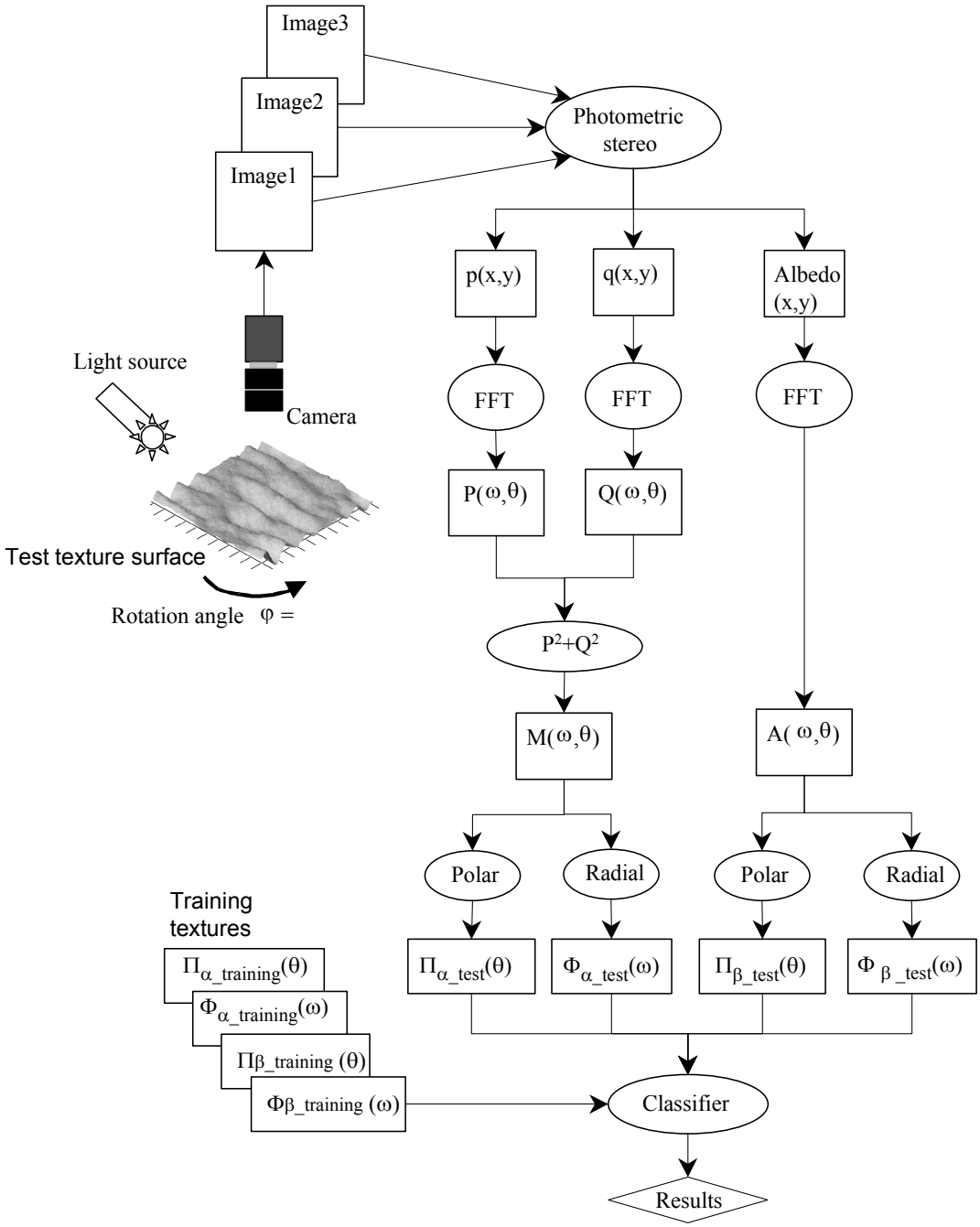

Figure 8. 24 An improved surface rotation invariant texture classification scheme based on both gradient data M(ω, θ) and albedo data A(ω, θ). Note that feature spaces are polar spectra Π(θ) and radial spectra Φ(ω).

The summary of the process is as follows:

1) Gradient data *M(ω, θ)* and albedo data *A(ω, θ)* for each test surface at certain orientation angle is estimated by using photometric stereo algorithm.

2) Gradient data $M(\omega, \theta)$ then provides the gradient polar spectrum $\Pi_{\alpha\_test}(\theta)$ and the gradient radial spectrum $\Phi_{\alpha\_test}(\omega)$. Albedo data $A(\omega, \theta)$ then provides the albedo polar spectrum $\Pi_{\beta\_test}(\theta)$ and the albedo radial spectrum $\Phi_{\beta\_test}(\omega)$.
3) Both the gradient polar spectrum $\Pi_{\alpha\_test}(\theta)$ and albedo polar spectrum $\Pi_{\beta\_test}(\theta)$ of the test texture is compared with the polar spectrum obtained from the training image to produce the difference metric in the same way as described before. At the same stage, the surface orientation of the test texture can also be estimated.
4) While both the gradient radial spectrum $\Phi_{\alpha\_test}(\omega)$ and the albedo radial spectrum $\Phi_{\beta\_test}(\omega)$ are compared with the radial spectrum obtained from the training textures, the difference metric is also calculated.
5) The total sum of squared errors statistic is calculated from steps *3* and *4*, and the best matching provides a classification decision.

8.4.2. Classification Results

In order to compare the classification results, we show our new improved classification results with other two classifiers' results (*Classifier-α-PR* and *Classifier-β-PR* presented in *Figure 8. 23* and *Table 8. 7*) together. *Figure 8. 25* shows the comparative classification results per texture for these three versions of the classifier by using polar and radial spectra. The "*albedo*" classifier used only the albedo radial and polar spectra to achieve a classification accuracy of *76.54%*, using gradient data only ("*gradient*") improved this figure to *86.91%*, while combining gradient and albedo data pushed the classification rate up to *90.56%* (*"gradient & albedo"*). It also shows that integration of the feature generators of gradient and albedo together provides more discriminative ability and comprehensive information for the classifier.

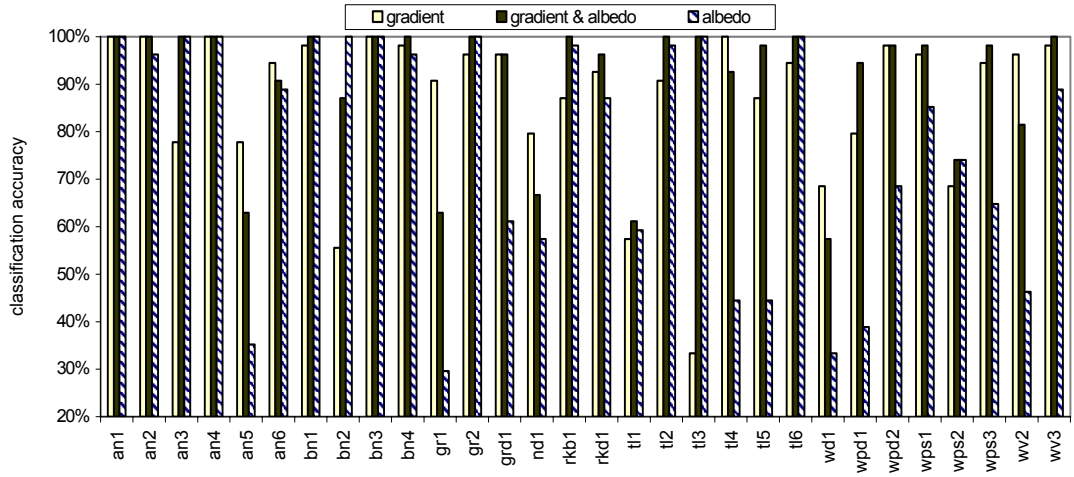

Figure 8. 25 Classification results for 30 real textures between our new improved classifier ("gradient & albedo"), and Classifier-α-PR (based on "gradient" data) and Classifier-β-PR (based on "albedo" data).

8.5. Summary

In this chapter, we introduce a new classification feature space, *radial spectrum* in addition to *polar spectrum* and a new feature generator, *albedo spectra* in addition to *gradient spectra* in order to provide additional information on surface texture properties. Furthermore, the comparative classification results show that the integration of more feature spaces and more feature generators provides more discriminative ability for the classifier, finally our new improved classification scheme achieves the best result with the classification accuracy of *90.56%* for all *30* real textures.

CHAPTER 9

Classification Scheme Using Modified Photometric Stereo and 2D Spectra Comparison

9.1. Introduction

In *Chapter 8*, even we combine more feature spaces and more feature generators, we note that the classification results are not quite as high as those published for some image rotation invariant schemes [Cohen91] [Reed93] [Hayley96] [Port97] [Fountain98] [Zhang02a] [Varma02], as they are good considering the difficulties involved in rotation of real surface textures and the large number of different texture classes presented. In order to justify the cost and problems caused by photometric stereo imaging, such as shadow presented on textures, we present a modified photometric stereo strategy using more images.

Furthermore, one reason of misclassification is that the classification algorithm stops too soon. We only compare *1D* spectra features (*polar* and *radial*) so far, these *1D* spectra are integrals of the original *2D* spectra (*gradient* or *albedo*). Two textures with different *2D* spectra may well have the same *1D* spectra. Therefore a final verification step should be included where the *2D* spectra are compared. This *2D* comparison would not be costly because the rotation angles are already known from their *1D* polar spectra. We finally present the classification scheme using *2D* spectra together with the classification results.

9.2. Photometric Stereo Using More Images

9.2.1. Introduction

All the classifiers presented in this thesis use data obtained from photometric stereo. Their performance therefore depends on the accuracy with which the surface properties are obtained. The method is prone to difficulty sometimes where the parts of the surface are shadowed.

In this section, we will propose an additional strategy for the photometric stereo technique by using more images to estimate surface properties, including both gradient data and albedo data, where we take into account of the effect of shadow. The main advantage of the new method is that surface properties can be estimated more accurately. More images are obtained using further illumination sources, such that more information can be obtained. The improved experimental results obtained from this new strategy are also presented, while comparing to those from our existing simple three image-based photometric stereo strategy, denoted by *PS3*.

9.2.2. The Problem of Shadows in PS3

So far, we have assumed that there are no shadows in the images. But it is clear from our database that this is a poor assumption. In this section, we will show that how much shadows affect our classification scheme.

In the circumstance that we have no control in capturing images of real textures with regard to its physical surface and illumination, we have to simulate a surface both with and without shadow on synthetic textures only. Therefore we only test the performance of the classification scheme in simulated experiments. *Figure 9. 1* shows the classification results for four synthetic textures *(rock, sand, malv and ogil)* for different slant angle σ settings, in terms of those without shadow and with

simulated shadow. We note that while increasing the slant angle of σ, the classification accuracy for the textures with shadow decreases from *100%* to *95.83%*. On the other hand, whatever the slant angle σ is, the classification accuracy for the textures without the effect of shadow is constant at *100%*.

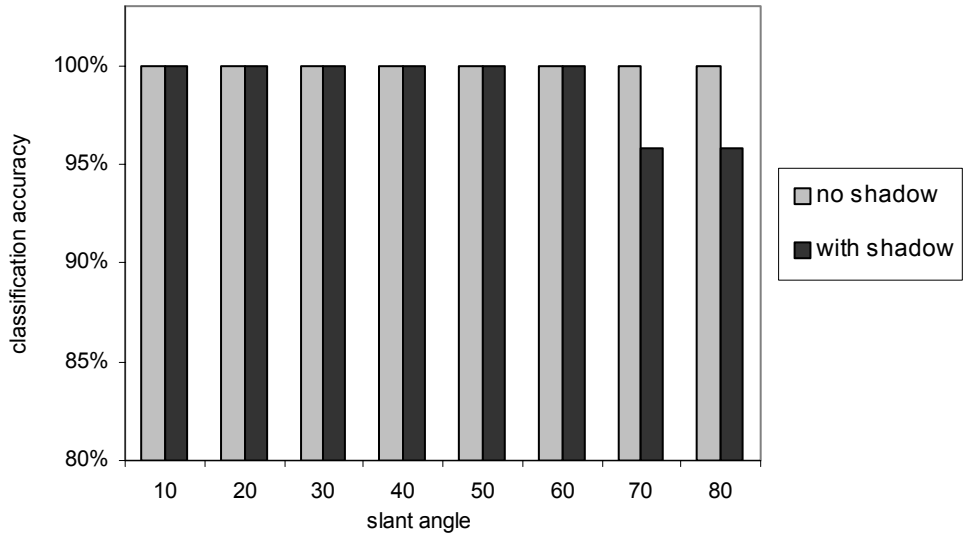

Figure 9. 1 Classification results for four synthetic textures for different slant angle σ settings, in terms of those without shadow and with simulated shadow.

Moreover, it is interesting to see that all of the misclassification only occurred on the directional texture of *"sand"*. *Figure 9. 2* displays images of the texture *"sand"* with a constant illumination tilt angle of $\tau=0°$ as indicated by black arrows in white circles, while the slant angle is varied ($\sigma=30°$, $\sigma=50°$ and $\sigma=70°$ respectively), and the texture is simulated with and without shadow. We may see the texture of *"sand"* with shadow results in very unnatural looking images as they have bright spots and dark regions which indicate the effect of shadow.

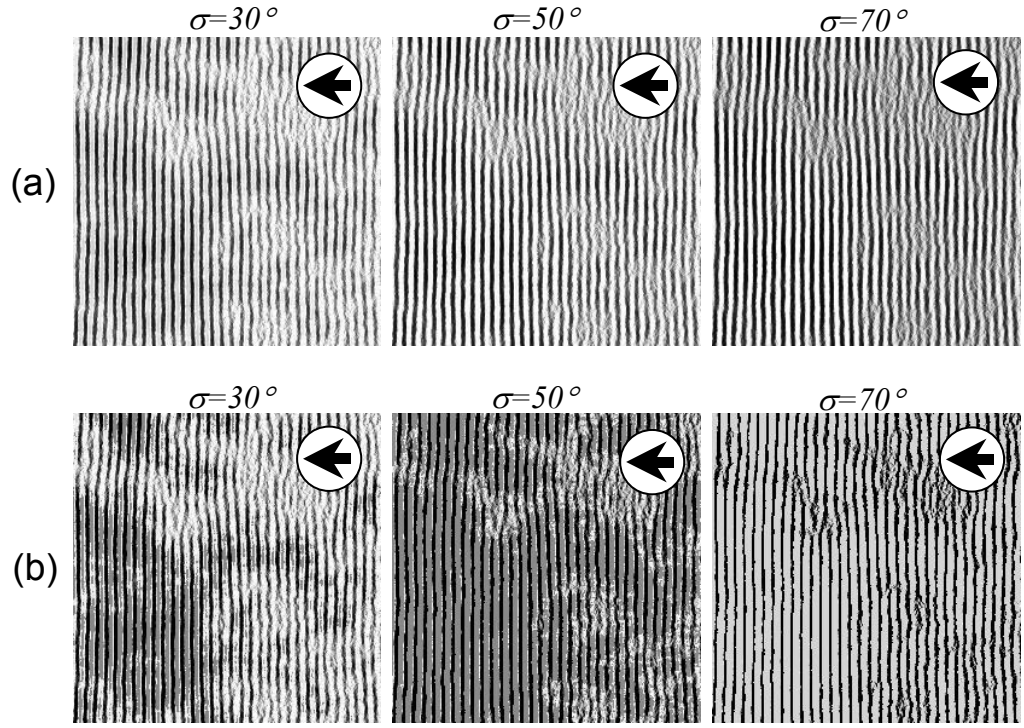

Figure 9. 2 Images of the texture "sand" with a constant illumination tilt angle of τ=0° as indicated by black arrows in white circles, with the slant angles of σ=30°, σ=50° and σ=70° respectively. (a). simulated textures without shadow. (b). simulated textures with shadow.

Things are clearer in the *Figure 9. 3*, where shadow count against slant angle σ for *"sand"* with simulated shadow effect is shown. The shadow area is becoming bigger and bigger as the slant angle σ increases. It is the dominant effect of shadow that makes our classifier using photometric stereo fail. In other words, a photometric stereo image set (three images) contains quite a lot of pixels with shadow information which also violates to the assumptions of our simple photometric stereo algorithm *(PS3)* based on three input images. This motivates us to improve our existing photometric stereo technique in order to remove or reduce the effect of shadows and achieve better performance in the latter stage of classification.

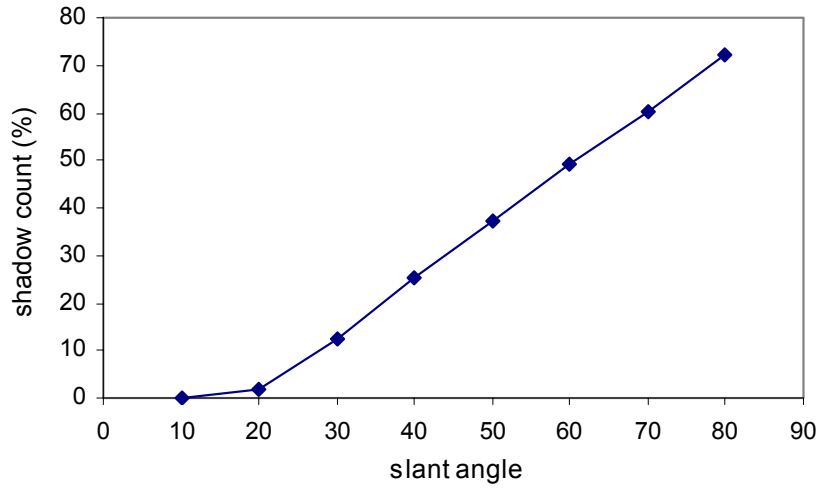

Figure 9. 3 Shadow count against slant angle for texture of "sand" with simulated shadow effect.

9.2.3. Existing Photometric Stereo Techniques (PS3) Obtained from Different Light Sets

So far our current photometric stereo technique *(PS3)* is based on three images taken under the illumination conditions with a constant slant angle σ, with the tile angles of $\tau=0°$, $\tau=90°$ and $\tau=180°$. We may extend this photometric stereo image set into different versions which use different combinations of three input images taken from different illumination directions. *Figure 9. 4* illustrates four different sets of photometric stereo images; each of them has three input images which come from three different illumination conditions with tilt angles of $\tau=0°$, $\tau=90°$, $\tau=180°$ and $\tau=270°$ (as indicated by black arrows in white circles), while the slant angle σ is constant.

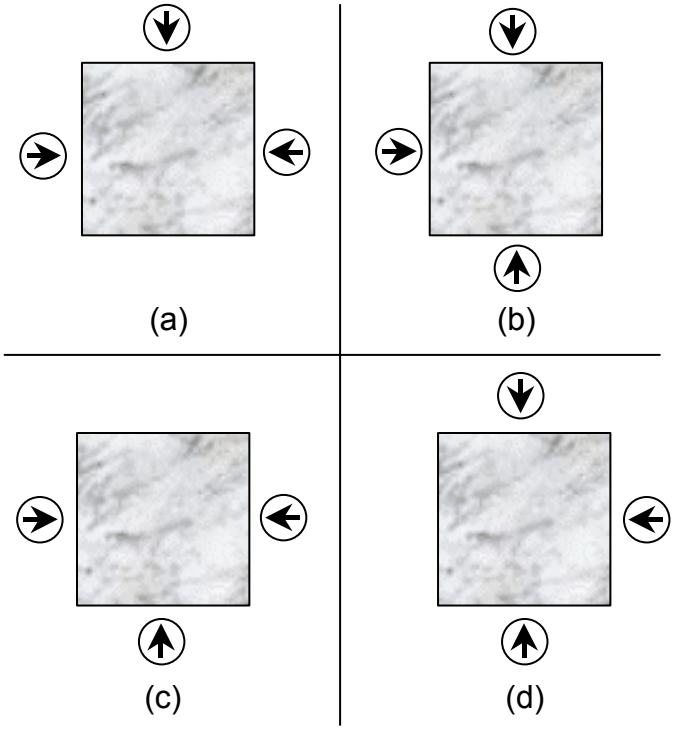

Figure 9. 4 Illustration of four different sets of images, each of them has three input images which come from three different illumination conditions with tilt angels of τ=0°, τ=90°, τ=180° and τ=270° (as indicated by black arrows in white circles), while the slant angle σ is constant.

It is interesting to generate the corresponding polar spectra in order to see how robust our features are. For example, *Figure 9. 5* shows the polar spectra $\Pi_\alpha(\theta)$ for the texture *"sand"* with simulated shadow, obtained from the four different sets of photometric stereo images shown in *Figure 9. 4*. The three input images come from combinations of the illumination conditions as follows:

a) τ=0°, 90° and 180° (PS3a);

b) τ=90°, 180° and 270° (PS3b);

c) τ=180°, 270° and 0° (PS3c); and

d) τ=270°, 0° and 90° (PS3d).

Each polar spectrum contains those surfaces with different orientation angles of φ=0°, 30°, 60°, 90°, 120° and 150°.

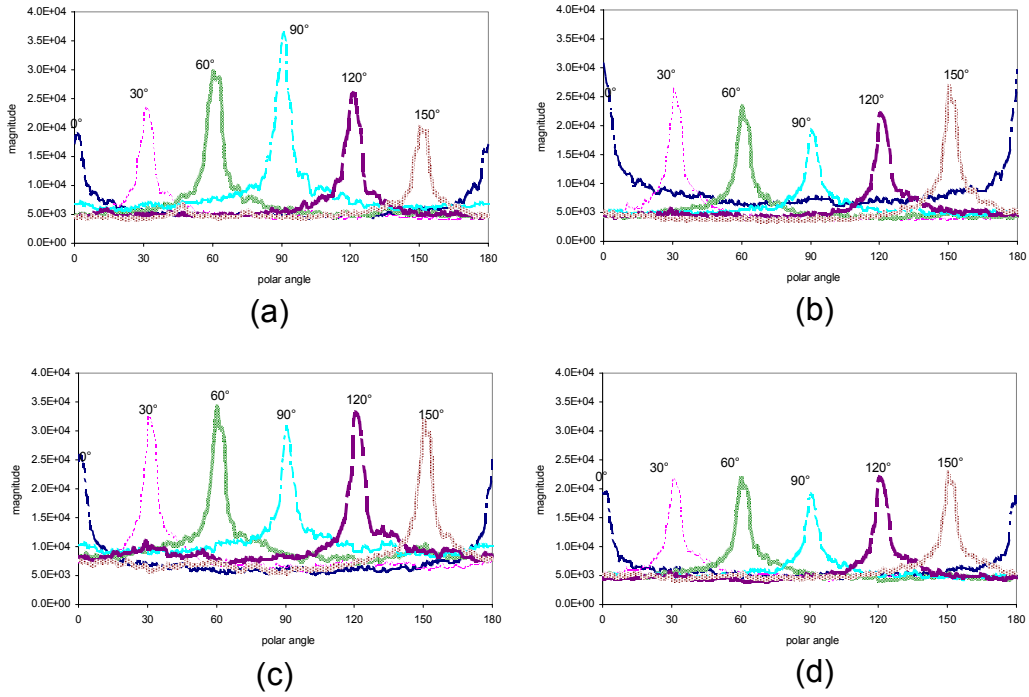

Figure 9. 5 Polar spectra $\Pi_\alpha(\theta)$ for the texture "sand" with simulated shadow, obtained from four different sets of photometric stereo images. While their respective three input images come from the illumination conditions of (a). τ=0°, 90° and 180°; (b). τ=90°, 180° and 270°; (c). τ=180°, 270° and 0°; (d). τ=270°, 0° and 90°. (each polar spectrum contains those surfaces with different orientation angels of φ=0°, 30°, 60°, 90°, 120° and 150°)

It is obvious that the polar spectra vary with the selection of photometric stereo algorithm versions *(PS3a, PS3b, PS3c and PS3d)*. In addition, for each algorithm version, the individual polar spectrum corresponding to the surface orientation is not robust to surface rotations. For example, we may see that the magnitude of the peak in the polar spectrum at the same surface orientation such as φ=90° is either accentuated or attenuated in the different versions of *"PS3"*. On the other hand, for one version of *"PS3"*, all of the magnitudes of the peaks at different surface orientations are at different levels due to the artefacts of surface rotation and the effect of shadow.

9.2.4. A New Strategy of Photometric Stereo by Using Four Light Sources (PS4)

As discussed before, we note that the more images we use in photometric stereo, the more information we obtain about the surface. In our new strategy of photometric stereo, we approach the problem of detecting and removing the effect of shadow for the estimation of surface properties by acquiring a set of images of the same surface illuminated from different at least four different directions. Our strategy is to treat the shadows as outliers which can be removed.

- ***Method to remove shadow and specular component***

There are two well-known problems with traditional photometric stereo:

1. There will be some points that will be in *shadow* for one or more of the images; That is, there will not always be three non-zero values to use in solving photometric equation;
2. Surfaces are not truly Lambertian and can have a *specular* component. That is, the reflectance model may be a very bad one for the reflected radiance.

The computer vision literature has many approaches to deal with aspects of these problems (e.g. [Tagare91]). Rushmeier *et al.* [Rushmeier97] present a photometric stereo system to remove the shadow and specular component, using five light sources. In their system, all pixel values with low intensity values must be eliminated from the photometric stereo calculation, and more than three images will be required as inputs. On the other hand, by excluding very high pixel values in the input images, specular effects can be eliminated from the calculation too. Taking into account the above factors, a system is designed to use five light positions that gives five image values from which the high and low values can be discarded and the surface normal can be calculated from the remaining three values.

Drbohalv *et al.* [Drbohalv98] [Drbohalv02] also present a method for detecting shadows and specularities by acquiring a set of images of a scene illuminated from different directions. The method exploits the basic properties of Lambertian surfaces and treats shadows and specularities as outliers. They also note that when there exist

three images *in which* the brightness value of a given pixel behaves Lambertian, it is enough to predict the brightness of this pixel in *any* image taken under *arbitrary* illumination. In their method, they firstly detect and remove both shadows and specularities and replace their brightness by values corresponding to the Lambertian model of reflectance.

- ***Our PS4 method***

With respect to the textures in our database and system design, we do not consider the specular component. In this section, we therefore propose a PS4 method (photometric stereo method using four light sources) to remove the effect of shadows. It is a simplified Rushmeier's method [Rushmeier97].

Our model from surface to image formation employs the Lambertian model of the surface reflectance, which we assume to be valid with the exception of points in shadow. In other words, we consider only the brightness values of pixels which are not shadowed. While shadow results outliers with respect to the Lambertian model, it also conveys no information about reflectance properties. In a shadowed region, the reflectance information is lost.

When an image of the surface illuminated from a certain direction contains a shadowed region, the necessary way to estimate surface reflectance properties for that specific region is to get another image illuminated by one of four different light sources as shown in *Figure 9. 6*. By increasing the number of images of a surface illuminated from different lighting directions, we will increase the chance that each pixel in the image plane behaves according to the Lambertian model in three of the images.

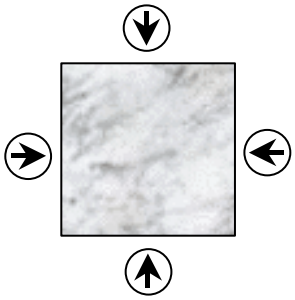

Figure 9. 6 Illustration of a new photometric stereo image set based on four input images (PS4), which comes from four different illumination conditions with tilt angels of τ=0°, τ=90°, τ=180° and τ=270° (as indicated by black arrows in white circles), while the slant angle σ is constant.

The scheme of this new algorithm of photometric stereo may take the following form:

---

for each image pixel ***x (x=0;x<n;x++)***
{
    select three image pixels x_i , x_j *and* x_k *among four input image pixels* i_1, i_2 , i_3 *and* i_4;
        {
        where x_i , x_j *and* x_k *are the three brightest pixels.*
        }
    do
    {
    estimating surface derivatives and albedo using selected three pixels of x_i , x_j *and* x_k *from a selective photometric stereo set with three images of* I_i , I_j *and* I_k ;
    }
}
end

To achieve this, we

1) first need to able to distinguish pixel with the most shadow from the pixels in each of the four input images based on a pixel by pixel basis. In this case, the darkest pixel is considered to be a shadowed one and the brightest three pixels are used as a set of photometric stereo data for that specific pixel location. In other words, we assume that the outlier pixel is a shadowed one.

2) and secondly we have to resolve the surface properties at the corresponding pixel. Shadowed pixels in each set of photometric stereo images can be highlighted in this process with the hope that there are still enough image pixels which are not in shadow. So that we can exclude the shadowed pixel from consideration and recover the surface partial derivatives and albedo using the other three pixels.

The problem of discriminating between less-shadowed pixels and the most-shadowed pixels is crucial. Obviously, if we use less images to estimate the surface properties, the resulting surface properties may be far away from reality. Therefore we use at least four images taken from four different illumination directions to estimate surface partial derivatives and albedo.

In general, our solution to the confounding problems of shadow is to derive images which are shadow free or with minimal shadow: that is to process images such that the shadows are removed whilst retaining all other salient information within the image. Therefore we need a sequence of images, captured with a stationary camera over a period of time, such that the illumination in the scene changes considerably, specifically the position of the shadows.

9.2.5. Improved Experimental Results

In this section we test some of the following aspects by using our improved photometric stereo technique *"PS4"*. Some successful and improved results obtained on *"PS4"* are also presented and compared against those on *"PS3"*.

- ***Detecting shadow area***

At the same time when we estimate surface partial derivatives and albedo data by using the improved photometric stereo algorithm *"PS4"* which uses four images taken under four different illumination directions, we may also detect the shadowed area in the image plane and produce a shadow image. *Figure 9. 7* shows a

successfully detected shadow image for one of the real texture *"rkb1"* which is in our photometric texture database produced by *"PS4"* (the white area indicates the shadows integrated from all four input images). We note that this all-in-one shadow image is valid for all of four input images wherever the illumination direction comes from (tilt angle of $\tau=0°$, $\tau=90°$, $\tau=180°$ and $\tau=270°$).

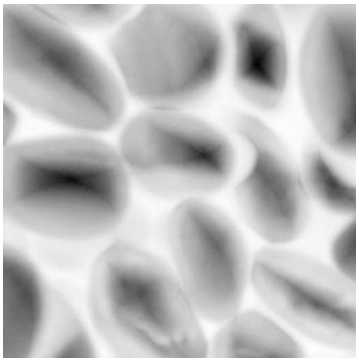

Figure 9. 7 Detected shadow image for real texture "rkb1" using four photometric stereo images "PS4" (the white area indicates the shadow regions integrated from all four input images).

- ***Estimation of surface relief and albedo image***

The pair of images shown in *Figure 9. 8* are recovered surface relief images obtained using *"PS3"* and *"PS4"* for the real texture *"rkb1"*. Their corresponding recovered surface albedo images are presented in *Figure 9. 9*. We may note that the resulting image obtained using *"PS4"* is better that that obtained using *"PS3"* and provides more detailed information about either the surface relief or albedo. There are some obvious improvements in the images of *"PS4"*. For example, looking at the region *B1*, a better recovered surface relief is apparent in the image for *"PS4"*, and clarifies the darker region in the image for *"PS3"* which is due to the effect of shadow. With regard to the albedo image, the region *B2* obtained using *"PS4"* reveals more correct albedo information than that obtained using *"PS3"*.

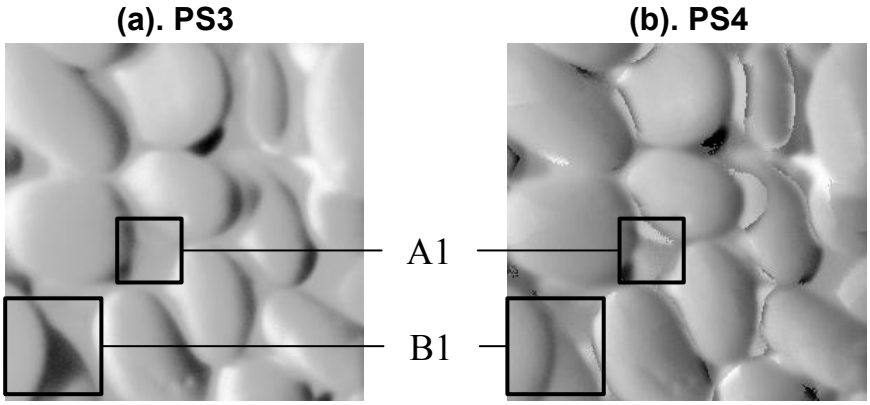

*Figure 9. 8 Recovered surface **relief** images obtained from "PS3" and "PS4" for real texture "rkb1".*

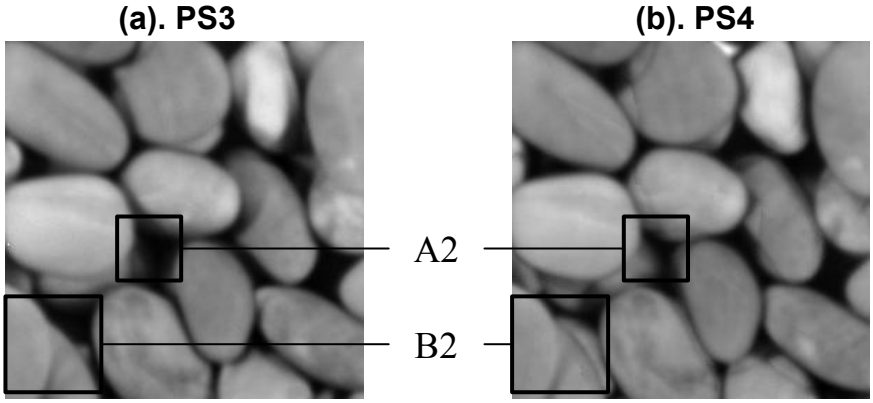

*Figure 9. 9 Recovered surface **albedo** images obtained from "PS3" and "PS4" for real texture "rkb1".*

- ***Polar spectra to be robust to surface rotation***

Figure 9. 10 shows the polar spectrum $\Pi_\alpha(\theta)$ of gradient spectra $M(\omega, \theta)$ for the synthetic texture *"sand"* with simulated shadow at surface rotations of $\varphi = 0°, 30°, 60°, 90°, 120°$ and $150°$, which are obtained using *"PS4"*. We may note that the magnitude and shape of these polar spectra, whatever the surface orientations are, are robust to surface rotation, compared to those results obtained from *"PS3"* shown in *Figure 9. 5*.

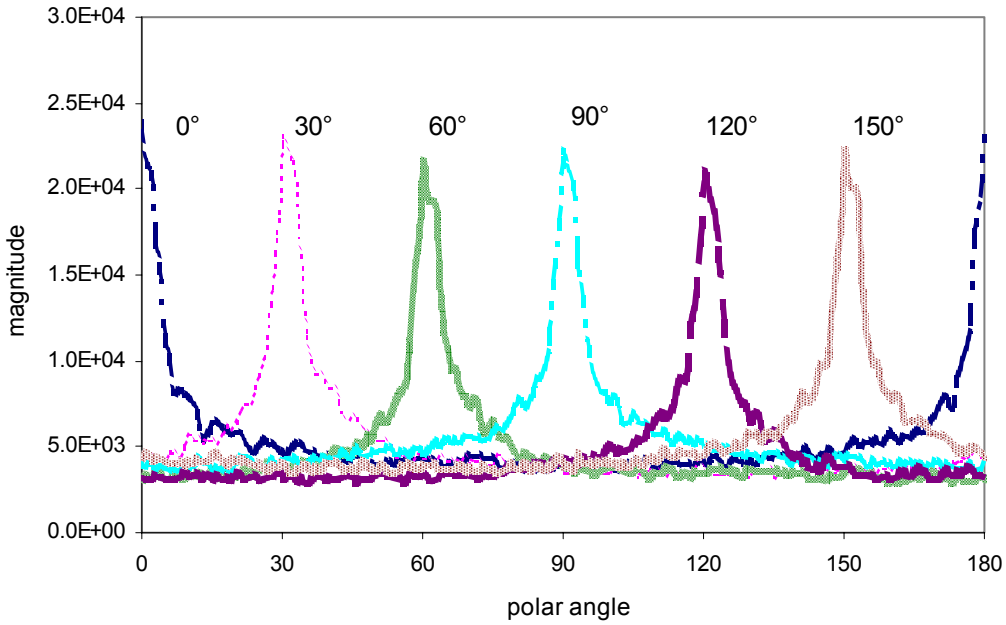

Figure 9. 10 Polar spectra $\Pi_\alpha(\theta)$ of gradient spectra $M(\omega, \theta)$ for synthetic texture "sand" with simulated shadow at surface rotations of $\varphi = 0°, 30°, 60°, 90°, 120°$ and 150°, which are obtained by using "PS4" (τ=0°, 90°, 180° and 270°).

In general, the technique of *"PS4"* presented in this section is better than *"PS3"* by using one more input photometric stereo image, and we will incorporate it into our new improved surface rotation invariant classification scheme which is summarised in next section.

- ***Classification results (PS3 vs. PS4)***

Figure 9. 11 shows the classification results for *30* real textures between *PS3* and *PS4* method. A classification accuracy of *90.56%* (Section *8.4.2*) is achieved by *PS3* method. On the other hand, a classification accuracy of *95.93%* is achieved by *PS4* method, where the shadow artefacts are removed by introducing one more image for each photometric stereo data set. In general, *PS4* method has better performance than *PS3*. More images, more information about surfaces.

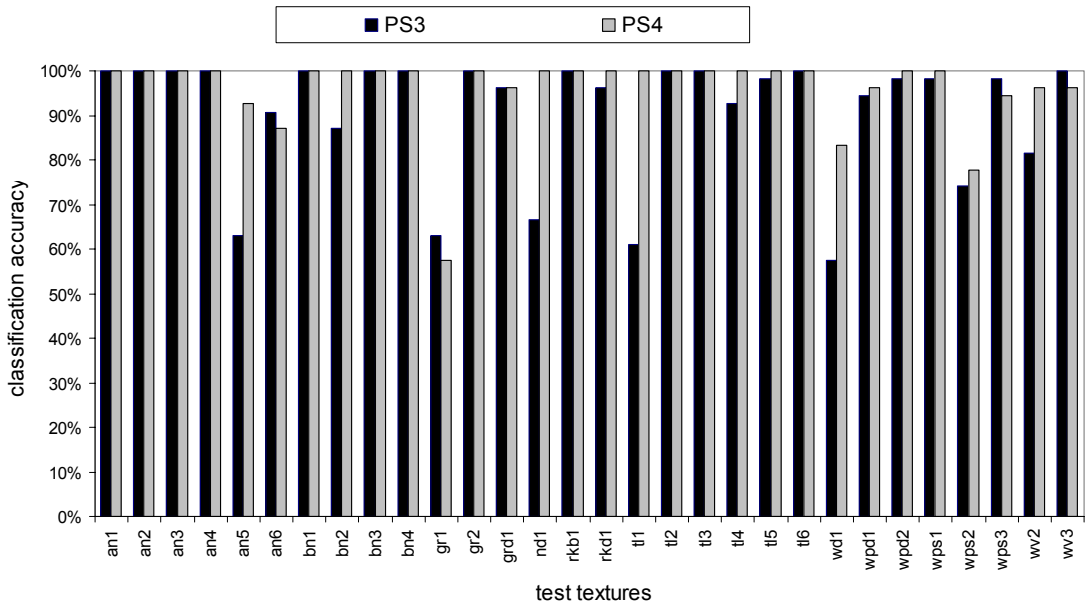

Figure 9. 11 Classification results for 30 real textures between PS3 and PS4 .

9.3. Classification Scheme Using 2D Spectra Comparison

Comparing to the classification algorithms based on polar and radial spectra of 2D gradient spectra *M* and albedo spectra *A*, which are presented in Chapter *6*, *7* and *8*, we propose a new classification scheme directly using *2D* spectra themselves.

After investigation of image-based classifier against surface-based classifier in Chapter *6*, *7* and *8*, we note that for *3D* surface rotation invariant texture classification, we have to use surface information obtained by photometric stereo instead of only using image information in order to make the classification scheme robust to surface rotation.

9.3.1. Classification Scheme

As discussed before, one reason of misclassification presented previous chapters is that the classification algorithm stops too soon. We only compare *1D* spectra features

(*polar* and *radial*) so far, these *1D* spectra are integrals of the original *2D* spectra (*gradient* or *albedo*). Two textures with different *2D* spectra may well have the same *1D* spectra. Therefore a final verification step should be included where the *2D* spectra are compared. This *2D* comparison would not be costly because the rotation angles are already known from their *1D* polar spectra. *Figure 9. 12* presents the classification scheme using modified photometric stereo *(PS4)* and together with *2D* spectra comparison.

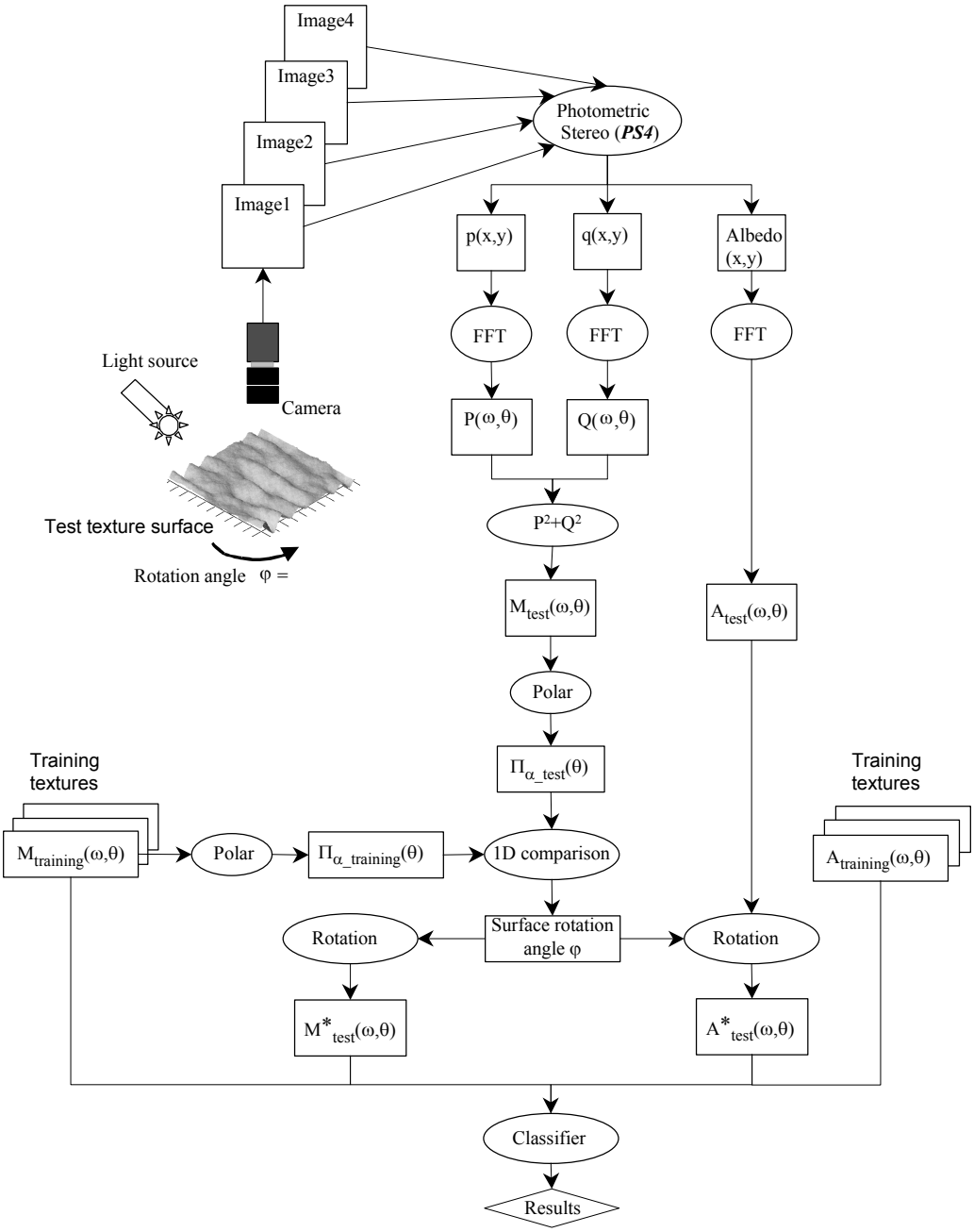

Figure 9. 12 Surface rotation invariant texture classification scheme using modified photometric stereo (PS4) and 2D spectra comparison.

The classification scheme can be summarised as follows:

1. Surface gradient spectra $M_{test}(\omega,\theta)$ and albedo spectra $A_{test}(\omega,\theta)$ of test textures can be estimated using modified photometric stereo *(PS4,* discussed in last section*),* where each photometric stereo image set contains four images taken at illuminant tilt angles (τ) of $0°$, $90°$, $180°$ and $270°$ respectively.
2. *2D* Gradient spectra $M_{test}(\omega,\theta)$ of test textures are processed to provide *1D* polar spectra $\Pi_{\alpha\_test}(\theta)$. In the same way, *2D* gradient spectra $M_{training}(\omega,\theta)$ of training textures are processed to provide *1D* polar spectra $\Pi_{\alpha\_training}(\theta)$.
3. The *1D* polar spectrum $\Pi_{\alpha\_test}(\theta)$ of test texture is then compared with the *1D* polar spectra $\Pi_{\alpha\_training}(\theta)$ obtained from training textures in order to estimate surface orientation angle φ. This step can be done by calculating *SSD* values presented in section *6.4.6*.
4. The *2D* Gradient spectrum $M_{test}(\omega,\theta)$ of test texture is therefore rotated by estimated surface orientation angle φ to provide the *2D* rotated gradient spectra version $M^*_{test}(\omega,\theta)$. At the same time, the *2D* albedo spectrum $A_{test}(\omega,\theta)$ of test texture is also rotated by angle φ to provide the *2D* rotated albedo spectra version $A^*_{test}(\omega,\theta)$. This step results in that both the *2D* gradient spectra and *2D* albedo spectra between test and training textures have the same surface orientations.
5. The total sum of squared errors statistic is calculated by *2D* spectra comparison and the lowest score provides the classification decision.

9.3.2. Classification Results

Figure 9. 13 shows the classification results per texture for two versions of the classifiers using *2D* spectra comparison and *1D* spectra comparison. The classification accuracy of *95.93%* (based on *PS4* method, referred Section *9.2.5*) is achieved by using *1D* spectra only. A better performance with classification accuracy

of *99.07%* is improved by comparison of *2D* spectra. Note that both classifiers use *PS4* photometric stereo method. In general, considering the fact of that we perform the classification on real surface rotation rather than synthetic surface rotation, our classification accuracy does not reach *100%*. On the other hand, we ignore the specular-reflection and inter-reflection in fact existing on the real surfaces, which result in misclassification occurred.

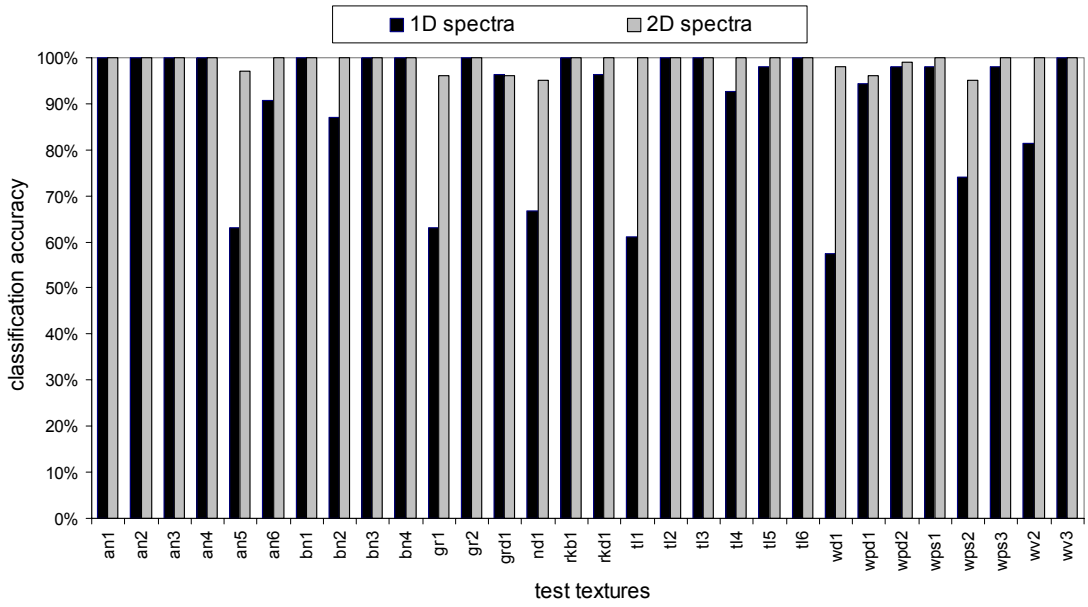

Figure 9. 13 Classification results for 30 real textures between 2D spectra comparison classifier and 2D spectra comparison classifier. (Note that both of them use PS4 photometric stereo method).

We note that the classification scheme presented in *Figure 9. 12* is successful and achieves the best classification results for our real texture database. The results also shows that the combination of *1D* spectra and *2D* spectra makes the classifier to be robust to surface rotation. Furthermore, the estimated surface orientations calculated from *1D* polar spectra keep the classification scheme in less computation, since we don't have to perform the heavy-computational *2D* image rotation of gradient spectra in very possible orientation angle of test surface texture in order to match with *2D* gradient spectra of training textures.

9.3.3. Comparing with Varma and Zisserman's Method

Table 9. 1 summarises the comparative studies between our method (*PS4*) and Varma and Zisserman's Method.

	Our Method (PS4)	**Varma and Zisserman's Methods**
Classification Accuracy	*99.07%*	*100%*
Number of Classes	*30*	*30*
Number of Classifications	*1620*	*840*
Number of images per texture class for training	*4*	*28*
Number of images per texture class for test	*54*	*28*
Computational Cost	*Heavy (2D spectrum rotation)*	*Medium (histogram of texton labelling)*
Robustness to surface rotation	*Excellent (with surface orientation estimation)*	*Good (no estimation of surface orientation)*
Ease of deployment	*Need 4 images / texture for both test and training to estimate feature space*	*1 image / texture for test, however need 28 images per texture for training*
Suitability for applications	*Controlled illumination conditions*	*Unknown illumination directions*

Table 9. 1 Comparative study between our method (PS4) and Varma and Zisserman's method.

9.4. Summary

In this chapter, the problem of shadowing using three-image photometric stereo *(PS3)* is considered. We therefore develop a four-image photometric stereo *(PS4)* to provide more accurate *3D* surface texture properties and to reduce shadow artefacts. With regarding to the classification design, we combine the *1D* spectra and *2D* spectra feature sets to achieve a better classification accuracy of *99.07%*. It uses both *2D* gradient spectra data and *2D* albedo spectra data. In order to make the classifier to be robust to surface rotation, the surface orientation angles are estimated by *1D* polar spectra in the first step. Therefore the classification decision depends on the comparison of *2D* spectra data.

CHAPTER 10

Summary and Conclusion

10.1. Summary

The objective of this thesis is the development of the classifiers that are capable of discriminating between surface textures on the basis of their visual appearance, yet which are robust to the changes of surface orientation.

Many texture classification schemes have been presented that are invariant to image rotation. All of these algorithms deal with the rotation of image texture. However, in this thesis it is argued that this is an insufficient model for many applications. Rotation of a rough surface is not equivalent to the rotation of the image. It follows that rotation invariant algorithms will not be robust to surface rotation and the conventional image rotation invariant algorithms may fail under certain conditions. An example phenomenon is illustrated in *Chapter 1*. This is the motivation for this thesis in which we develop a surface rotation invariant texture classification scheme.

Chapter 2 surveys texture feature measurements and rotation invariant texture classification. Before we discuss the texture features, some definitions of texture, surface relief and albedo are given. We note that most of rotation invariant feature methods are based on image rotation rather than physical surface rotation. Furthermore, there are few methods in which the effect of changing illumination conditions are taken into account.

The formation of the image from the surface is considered in *Chapter 3*. Firstly, a review of related work on reflection and illumination modelling is given. Afterwards, a simple Lambertian illumination model is selected, and it is proven to describe diffuse reflection well. Secondly, we present Kube and Pentland's model, a linear Lambertian model, which assumes fixed illumination and viewing geometry and expresses observed intensity as a linear function of surface partial derivatives. Furthermore, the formation of Kube and Pentland's model in the frequency domain enables the directional effect of illumination to be more easily understood, and its directional filter is also investigated. One of important conclusions is that image variance is not a surface rotation invariant feature for directional surfaces. In addition, the non-linear effects neglected by the Kube and Pentland's model are considered. Their effect on surface amplitude variance, frequency doubling and intensity clipping is investigated through the use of simulation. This confirms Kube and Pentland's s linear model must be used on the basis that surface height variance is low and that the slant angle does not approach *0* degrees. Finally, we briefly introduce four models of rough synthetic surfaces, which are used in this thesis for the purpose of simulation.

We demonstrate in *Chapters 1* and *3* that the rotation of a directional surface is not equivalent to the rotation of its image. We therefore classify the surface texture using the properties of the surfaces rather than those of images so that an intrinsic characteristic of a surface has to be recovered prior to the classification. Photometric stereo is presented in *Chapter 4*, which enables us to estimate surface orientation and surface albedo using several images of the same surface obtained under different illumination directions. It has no smoothness assumption, only requires additional lighting and can be easily implemented at a reasonable computational cost. Furthermore, the surface orientation captured by photometric stereo in *Chapter 4* is mapped and examined in the spatial gradient space domain by means of moment analysis in *Chapter 5*. However the estimation process on non-directional texture surfaces provided poor results, because a gradient space image is *n-fold* symmetric where there are multiple possible sets of principal axes. We will discuss how to remove directional artefacts in the frequency domain in *Chapter 6*.

Having recovered the surface orientation using photometric stereo, the second part of this thesis addresses the design of the classification scheme, which is robust to surface rotation.

Chapter 6 describes the first stage of the design of the classifiers. This Chapter begins by introducing photometric stereo in the frequency domain. Because the surface partial derivatives are not surface rotation invariant features, we combine them in the frequency domain. The resulting gradient spectrum function is therefore free of directional artefacts. Secondly, the results from using both synthetic and real textures are used to show one important property of gradient spectrum: a rotation of the surface produces a corresponding rotation of its gradient spectrum. Thirdly, since comparing the gradient spectra of a test texture with those of the training classes over a complete range of rotations is computationally prohibitive, we extract a *1D* feature space, the polar spectrum, from its *2D* gradient spectrum to retain the directionality information. The results also show that a rotated texture's polar spectrum is equivalent to a translation of its polar spectrum. In other words, the surface orientation can be estimated from the polar spectra. Finally the complete classification scheme is described in *Chapter 6*.

In *Chapter 7*, we present the experimental procedure and classification results for the scheme described in *Chapter 6*. Since currently existing and publicly available texture databases are not suitable for our task, we develop a photometric stereo texture database, which includes *4* synthetic textures and *30* real textures with various surface rotations and illumination conditions. The average classification accuracy of *100%* is obtained while using *4* synthetic textures, on the other hand, the accuracy of *76.30%* is achieved using *30* real textures. After fully investigating the misclassifications we introduce a new classification feature space: the radial spectrum; and a new feature generator: albedo spectra. The comparative classification results show that this provides more discriminative ability. Our new classification scheme achieves better results with a classification accuracy of *90.56%* for *30* real textures.

The problem of shadowing using three-image photometric stereo is considered in *Chapter 9*. We develop a four-image system to provide more accurate estimation of *3D* surface texture properties. Furthermore, one reason of misclassification is that we only compare *1D* spectra features (*polar* and *radial*). These *1D* spectra are integrals of the original *2D* spectra (*gradient* or *albedo*). Two textures with different *2D* spectra may well have the same *1D* spectra. Therefore a final verification step is included where the *2D* spectra are compared. This *2D* comparison is not costly because the rotation angles are already known from their *1D* polar spectra. Finally, we achieve the classification accuracy of *99.07%*.

While our results using real surface textures are even higher than those published for some image rotation invariant schemes [Cohen91] [Reed93] [Hayley96] [Port97] [Fountain98] [Zhang02a], they are good considering the difficulties involved with the rotation of real 3D surface textures and the large number of different texture classes presented. However, our algorithm is still not perfect at the classification accuracy of *99.07%*. Comparing to Varma and Zisserman's method [Varma02a] [Varma02b], which is achieved to a classification accuracy of *100%* by using our photometric texture database, we note that they use more images than ours as training set (*28* images per texture class). On the other hand, we only use *4* images per texture class. In addition, the surface orientation can be estimated at the same time of the classification, while Varma and Zisserman's method does not do it. The limitation of our algorithm is that we need controlled illumination conditions, and computational cost is heavy by considering the rotation of 2D spectrum.

10.2. Future Work

This work investigates a rotation invariant classification of *3D* surface texture using photometric stereo. Surface gradient and albedo information can be recovered by using registered photometric image set where the illumination directions are known. However in many cases of real world, the illumination directions of images for *3D*

surface are unknown, therefore the position of illumination source has to be estimated or precision calibration of the illumination is required before applying registered photometric stereo. This will lead to investigation of non-calibrated photometric stereo.

In this thesis, we only change the tilt angle of illumination direction in order to achieve the different illumination conditions. While changing the slant angle of illumination direction can produce the same situation however, it will result in the effect of self or cast-shadowing introduced. It is worthwhile to investigation of how our classification algorithm is robust to illumination tilt and illumination slant angles.

One of the assumptions about *3D* surface textures in this thesis is that there is no inter-reflection. However, the inter-reflection has to be considered in real world. Nayar has raised this problem and investigated the possibility of shape recovery from inter-reflections [Nayar91b]. This matter should be investigated on photometric stereo, too.

10.3. Conclusion

This thesis has used theory, simulation and laboratory experiment, to investigate the rotation invariant texture classification for *3D* surface using photometric stereo.

We have presented a new surface rotation invariant texture classification scheme that uses photometric stereo. It combines polar and radial spectra of gradient and albedo data. We have shown that the image rotation is not equivalent to the rotation of rough surface. We have therefore presented theory and experimental results that show that our basic feature spaces of polar and radial spectra of gradient and albedo data are free of directional artefacts and that they may be used as discriminate features in surface rotation invariant classification.

Results using our texture database show that combining the gradient and albedo data improves the classification performance. The best classification rate of *99.07%* is achieved by using the combination of *1D* and *2D* features.

Some possible applications applying to our technique are detection of machined surface defects in industry, classification of satellite images in order to landmark the terrain, recovery topography and albedo of rough surface with fingerprint, recovery of imprints from clay tablets in archaeology and texture mapping on *3D* rough surface.

Reference

Alapati85 N. K. Alapati and A. C. Sanderson, “Texture classification using multi-resolution rotation-invariant operators”, Proc. of SPIE, Vol.5, pp.27-38, 1985.

Angelopoulou99 Elli Angelopoulou, and James P. Williams, "Photometric Surface Analysis in a Triluminal Environment." Proceedings of IEEE International Conference on Computer Vision (ICCV) 1999.

Awcock95 G. J. Awcock and R. Thomas, “Applied Image Processing”, Macmillan Press Ltd, ISBN 0-333-58242-X, 1995.

Belhumeur99 P. N. Belhumeur, D. J. Kriegman, and A. L. Yuille. The bas-relief ambiguity. International Journal of Computer Vision, 35(1):33--44, 1999.

Blinn77 J. F. Blinn, “Models of light reflection for computer synthesized picture”, Computer Graphics, Vol.11, No.2, pp.192-198,1977.

Bovik87 A. C. Bovik, M. Clark and W.S. Geisler, "Computational texture analysis using localised spatial filtering", Proceedings of IEEE Computer Society workshop on Computer Vision, Miami Beach, pp.201-206, 1987.

Bovik90 A. C. Bovik, M. Clarke and W. S. Geisler, “Multichannel texture analysis using localised spatial filters”, IEEE Transactions on Pattern Analysis and Machine Intelligence, Vol.12, pp.55-73, 1990.

Box76 G. E. P. Box and G. M. Jenkins "Time series analysis forecasting and control", Holden-Day, San Francisco, 1976.

Brodatz66 P. Brodatz66, “Textures: A Photographic Album for Artists and Designers”, Dover, New York, 1966.

Castleman96 K. R. Castleman, "Digital Image Processing", Englewood Cliffs, NJ, 1996.

Chantler94a M. J. Chantler, “The effect of illuminant direction on texture classification”, Ph.D. Thesis, Department of Computing and Electrical Engineering, Heriot-Watt University, Edinburgh, 1994.

Chantler94b M. J. Chantler, “Why illuminant direction is fundamental to texture analysis”, IEE Proc. on Visual Image and Signal Processing, Vol.142, No.4, pp.199-206, 1994.

Chellappa92 R. Chellappa, R. L. Kayshap and B. S. Manjanuth, “Model-base texture Segmentation and Classification”, in “Handbook of pattern recognition and vision”, Editor: C.H. Chen and L.F. Pau and P.S.P. Wang, Chapter 2.2, pp.277-310,World Scientific, 1993.

Chen93 C. H. Chen, L. F. Pau, and P. S. P. Wang, “Handbook of pattern recognition & computer vision”, ISBN 981-02-1136-8, World Scientific Publishing Co. Pte. Ltd, 1993.

Chen95 Y. Q. Chen, M. S. Nixon and D. W. Thomas, “Statistical geometrical features for texture classification”, Pattern Recognition, Vol.28, No.4, pp.537-552, 1995.

Cho93 C. Cho & H. Minanitani, “ A new photometric method using 3 point light sources”, IEICE Trans. Inf. & Syst. V.E76-D, No.8, pp.898-904, August 1993.

Coggins82 J. M. Coggins, “A framework for texture analysis based on spatial filtering”, Ph.D. Thesis, Computer Science Department, Michigan State University, East Lansing, MI, 1982.

Cohen91 F. S. Cohen, Z. Fan and M. A. S. Patel, “Classification of rotated and scaled textured images using Gaussian Markov field models”, IEEE Transactions on Pattern Analysis and Machine Intelligence, Vol.13, pp.192-202, 1991.

Coleman82 E. N. Coleman and R. Jain, “Obtaining 3-dimensional shape of textured and specular surfaces using four-source photometry”, Computer Vision, Graphics, and Image Processing, Vol.18, pp.309-328, 1982.

Conners80 R.W. Conners & C.A. Harlow, "A theoretical comparison of texture algorithms", IEEE Transactions on Pattern Analysis and Machine Intelligence Vol.2, pp.204-222, 1980.

Cook82 R. L. Cook and K. E. Torrance, “A reflectance model for computer graphics”, Computer Graphics, Vol.3, No.3, pp.307-16, 1982.

Cross83 G. R. Cross and A. K. Jain, “Markov Random Field Texture Models”, IEEE Transactions on Pattern Analysis and Machine Intelligence, Vol.5, pp.25-39, 1983.

Dana97 K. J. Dana, B. Van Ginneken, S. K. Nayar and J. J. Koenderink, “Reflectance and texture of real-world surfaces”, IEEE Conference on Computer Vision and Pattern Recognition (CVPR), pp.151-157, 1997.

Dana98 K. J. Dana and S. K. Nayar, “Histogram model for 3D textures”, Proc. IEEE Conf. Computer Vision and Pattern Recognition, pp.618-624, 1998.

Dana99a K.J. Dana, S.K. Nayar, “Correlation model for 3D textures”, IEEE International Conference on Computer Vision, pp.1060-1067, Corfu, Greece, Sep 1999.

Dana99b K.J. Dana, B. van Ginneken, S.K. Nayar and J.J. Koenderink, “Reflectance and texture of real world surfaces”, ACM Transactions on Graphics, Vol.18, No.1, pp.1-34, January 1999.

Davies90 E. R. Davies, “Machine vision: theory, algorithms, practicalities”, ISBN 0-12-206090-3, Academic Press Inc, 1990.

Davis81 L. S. Davis, "Polarograms : a new tool for image texture analysis", Pattern Recognition, Vol.13, No.3, pp.219-223, 1981.

Davis81b L. S. Davis, M. Clearman & J. K. Aggarwal, "An empirical evaluation of generalised cooccurrence matrices", IEEE Transactions on Pattern Analysis and Machine Intelligence Vol.3, pp.214-221, 1981.

Davis83 L. S. Davis, L. Janos, and S. M. Dunn, “Efficient recovery of shape from texture”, IEEE Trans. on Pattern Analysis and Machine Intelligence, Vol. PAMI-5, No.5, pp.485-492, 1983.

Drbohav98 Ondrej Drbohlav and Ales Leonardis, “Detecting shadows and specularities by moving light”, Proceeding of Computer Vision Winter Workshop, Ljubljana, Slovenia, pp.60-74, 1998.

Drbohav02 Ondrej Drbohlav and Radim Sara, “Specularities reduce ambiguity of uncalibrated photometric stereo”, Proceedings of the 7th European Conference on Computer Vision, Copenhagen, Denmark, 2002.

Dubes89 R. C. Dubes and A. K. Jain, “Random field models in image analysis”, J. Appl. Stat. Vol.16, pp.131-164, 1989.

DuBuf90 J. M. H. du Buf, M. Kardan and M. Spann, "Texture feature performance for image segmentation", Pattern Recognition, Vol.23, No.3/4, pp.291-309, 1990.

Dyer80 C. R. Dyer, T. H. Hong and A. Rosenfeld, “Texture classification using gray level cooccurrence based on edge maxima”, IEEE Transactions on System, Man and Cybernetics, Vol.10, pp.158-163, 1980.

Forsyth01 D. A. Forsyth, “Shape from texture and integrability”, Proceedings of IEEE International Conference on Computer Vision, Vancouver, BC, Canada, Vol.2, pp.447-452, 2001.

Fountain98 S. Fountain, K. Tan and K. Baker, “A comparative study of rotation invariant classification and retrieval of texture images”, Proceedings of British Machine Vision Conference, Vol.1, pp.266-275, 1998.

Fu82 K. S. Fu, “Syntactic pattern recognition and applications”, Prentice-Hall, New Jersey, 1982.

Galloway75 M. Galloway, “Texture analysis using gray level run lengths”, Computer Graphics and Image Processing, Vol.4, No.2, pp172-199, 1975.

Garding95 J. Garding, “Surface orientation and curvature from differential texture distortion”, International Conference on Computer Vision, pp.733-739, 1999.

Graham70 H. Graham, “Colour, pattern and texture”, Studio Vista, 1970.

Green93 D. Greenhill and E.R. Davies, "Texture analysis using neural networks and mode filters", Proceedings of British Machine Vision Conference, Surrey, Guildford, pp509-518, 1993.

Greenspans94 H. Greenspans, S. Belongic, and R. Goodman, “Rotation invariant texture recognition using a steerable pyramid”, Proceedings of ICPR94, pp.162-167, 1994

Haralick73 R. Haralick, K. Shanmugam, and I. Dinstein, “Texture features for image classification”, IEEE Transactions on System, Man and Cybernetics, Vol.3, pp.610-621, 1973.

Haralick79 R. M. Haralick, “Statistical and structural approaches to texture”, Proceedings of the IEEE, Vol.67, No.5, pp.786-804, 1979.

Hayley96 G. M. Hayley and B. S. Manjunath, “Rotation-invariant texture classification using modified Gabor filters”, IEEE International Conference on Image Processing, Vol.1, pp.262-265, 1996

He91 X. He, K. Torrance, F. Sillon and D. Greenberg, “A comprehensive physical model for light reflection”, Computer Graphics, Vol.25, No.4, August 1991.

Healey94 G. Healey and r. Kondepudy, “Radiometric CCD camera calibration and noise estimation”, IEEE Transactions on Pattern Analysis and Machine Intelligence, Vol.16, No.3, pp267-276, 1994.

Hong80 T. H. Hong, C. R. Dyer, and A. Rosenfeld, “Texture primitive extraction using an edge-based approach”, IEEE Transactions on System, Man and Cybernetics, Vol.10, pp.659-675, 1980.

Horn75 B. K. Horn, “Obtaining shape from shading information”, The Psychology of Computer Vision, P. H. Winston ed., New York, 1975.

Horn79 B. K. P. Horn and R. W. Sjoberg, “Calculating the reflectance map”, Applied Optics, Vol.18, No.11, pp.1770-1779, June 1979.

Horn86 Berthold K. P. Horn, “Robot vision”, McGraw-Hill Book Company, The MIT Press, 1986

Horn89 Berthold K. P. Horn and Michael J. Brooks, “Shape from shading”, Cambridge, MA, The MIT Press, 1989.

Hu62 M. Hu, “Visual pattern recognition by moment invariants”, IRE Trans. Information Theory, Vol.8, pp.179-187, 1962.

Huang90 J. Huang and D. L. Turcotte, “Fractal image analysis: application to the topography of oregon and synthetic images”, J. Opt. Sco. Am. A, Vol.7, pp.1124-1130, 1990.

Ikeuchi81 K. Ikeuchi, “Determining surface orientations of specular surfaces by using the photometric stereo method”, IEEE Transactions on Pattern Analysis and Machine Intelligence, Vol.3. pp.661-669, 1981

Iwahori95 Y. Iwahori, R. Woodham and A. Bagheri, “Principal components analysis and neural network implementation of photometric stereo”, IEEE Transaction, pp.117-125, 1995.

Jacobson82 L. Jacobson and H. Wechsler, “A paradigm for invariant object recognition of brightness”, Pattern Recognition Letters, Vol.1, No.1, pp.61-68, 1982.

Jain91 A. K. Jain and F. Farrokhnia, “Unsupervised texture segmentation using Gabor filters”, Pattern Recognition, Vol.24, pp.1167-1186, 1991.

Jain92 A. K. Jain and S. Bhattacharjee, “Text segmentation using Gabor filter for automatic document processing”, Machine Vision and Applications, Vol.5, No.3, pp169-184, 1992.

Jain96 A. K. Jain and K. Karu, “Learning texture discrimination masks”, IEEE Transactions on Pattern Analysis and Machine Intelligence, Vol.18, pp.195-205, 1996.

Jau90 Jack Y. Jau and Roland T. Chin, “Shape from texture using the Wigner distribution”, Computer Vision, Graphics, and Image Processing, Vol.52, pp248-263. 1990.

Kaizer55 H. Kaizer, “A quantification of textures on aerial photographs”, Technical Note 121, AD 69484, Boston University Research Labboratory.

Karu96 K. Karu, A. K. Jain, and R. M. Bolle, “is there any texture in the image?”, Pattern Recognition, Vol.29, No.9, pp.1437-1446, 1996.

Kashyap86 R. L. Kashyap and A. Khotanzad, "A model-based method for rotation invariant texture classification", IEEE Transactions on Pattern Analysis and Machine Intelligence Vol.8, No.7, pp.472-481, 1986.

Kaugeras80 O. D. Faugeras and W. K. Pratt, “Decorrelation methods of texture feature extraction”, IEEE Transactions on Pattern Analysis and Machine Intelligence, Vol.2. pp.323-332, 1980.

Kay95 Greg Kay and Terry Caelli, “Estimating the parameters of an illumination model using photometric stereo”, Graphical Models and Image Processing, Vol.57, No.5, pp.365-388, 1995.

Keller89 J. M. Keller and S. Chen, "Texture description and segmentation through fractal geometry", Computer Vision, Graphics, and Image Processing, Vol.45, pp.150-166, 1989.

Khotanzad87 A. Khotanzad and R. L. Kashyap, "Feature Selection for Texture Recognition Based on Image Synthesis", IEEE Transactions on System, Man and Cybernetics Vol.17, pp.1087-1095, 1987.

Koenderink96 J. J. Koenderink, A. J. van Doorn and M. Stavridi, “Bidirectional reflectance distribution function expressed in terms of surface scattering modes”, The Fourth European Conference on Computer Vision, Vol.2, pp.28-39, 1996.

Kube88 P. Kube, and A. Pentland, “On the imaging of fractal surfaces”, IEEE Transactions Pattern Analysis and Machine Intelligence, Vol.10, No.5, pp704-707, 1988.

Law80 K. I. Laws, "Textured image segmentation", Ph.D. thesis, Dept. Electrical Engineering, University of Southern California, January 1980.

Lee92 K. M. Lee and C. C. J. Kuo, “Shape reconstruction from photometric stereo”, Journal of Optical Society of America: A, Vol.10, No.5, 1993.

Leung92 M. M. Leung and A. M. Peterson, “Scale and rotation invariant texture classification”, Proc. 26th Asilomar Conference on Signals, Systems and Computers (Pacific Grove, CA), 1992.

Leung97 T. Leung and J. Malik, “On perpendicular texture: why do we see more flowers in the distance?”, IEEE Conference on Computer Vision and Pattern Recognition, pp.807-813, 1997.

Leung99 T. Leung and J. Malik, “Recogniszing surfaces using three-dimensional textons”, IEEE International Conference on Computer Vision, Corfu, Greece, Sep 1999.

Mäenpää00 T. Mäenpää, T. Ojala, M. Pietikäinen and M. Soriano, “Robust texture classification by subsets of Local Binary Patterns”, Proc. 15th International Conference on Pattern Recognition, 2000.

Malik97 J. Malik and R. Rosenholtz, “Computing local surface orientation and shape from texture for curved surfaces”, International Journal of Computer Vision, Vol.23, No.2, pp.149-168, 1997.

Mandelbrot83 B. B. Mandelbrot, "The fractal geometry of nature", W.H. Freeman, New York, 1983.

Mao92 J. Mao and A. K. Jain, “Texture classification and segmentation using multiresolution simultaneous autoregressive models”, Pattern Recognition, Vol.25, No.2, pp.173-188, 1992

Marple87 S. L. Marple, “Digital spectral analysis with applications”, Prentice Hall, 1987.

Matheron75 G. Matheron, “Random sets and integral geometry”, Wiley, New York, 1975.

McCormick74 B. H. McCormick and S. N. Jayaramamurthy, “Time series model for texture synthesis”, International Journal of Computer and Information Sciences, Vol.3. pp.329-343, 1974.

McGunnigle00 G. McGunnigle and M. J. Chantler, “Rough surface classification using point statistics from photometric stereo”, Pattern Recognition Letters, Vol.21, pp.593-604, 2000.

McGunnigle97 G. McGunningle, M. J. Chantler, "A model-based technique for the classification of textured surfaces with illuminant direction invariance", Proceedings of British Machine Vision Conference, pp.470- 479, Essex, October 1997.

McGunnigle98 G. McGunnigle, “The classification of textured surfaces under varying illuminant direction”, Ph.D. Thesis, Department of Computing and Electrical Engineering, Heriot-Watt University, Edinburgh, 1998.

McGunnigle99a G. McGunnigle, M. J. Chantler, “Rotation insensitive classification of rough surfaces”, IEE Proceedings on Vision, Image and Signal Processing, Vol. 146, No. 6, pp.345-352, December 1999.

McGunnigle01 G. McGunnigle, “The M1 Texture Database”, Research Memorandum, Department of Computer Science, Heriot-Watt University, RM/01/1, July, 2001.

Nayar90 S.K. Nayar, K. Ikeuchi, T. Kanade."Determining Shape and Reflectance of Hybrid Surfaces by Photometric Sampling", IEEE Transactions on Robotics and Automation, Vol.6, No.4, pp.418-431, 1990.

Nayar91 S. K. Nayar, K. Ikeuchi and T. Kanade, “Surface reflection: physical and geometrical perspectives”, IEEE Transactions on Pattern Analysis and Machine Intelligence, Vol.13, No.7, pp.611-634, 1991.

Nayar91b S. K. Nayar, K. Ikeuchi, and T. Kanade. “Shape from interreflections”, Int. J. Comp. Vision, Vol.6, No.3, pp173-195, 1991.

Nayar95 S. K. Nayar and M. Oren, “Visual appearance of matte surfaces”, Science, Vol.267, pp.1153-1156, Feb, 1995.

Ohanian92 Philippe P. Ohanian and Richard C. Dubes, “Performance evaluation for four classes of textural features", Pattern Recognition, Vol.25, No.8, pp.819-833, 1992.

Ojala00 T. Ojala, M. Pietikäinen and T. Mäenpää, “Gray scale and rotation invariant texture classification with local binary patterns”, Sixth European Conference on Computer Vision, pp.404-420, Dublin, Ireland, 2000.

Ojala96 T. Ojala, M. Pietikäinen and D. Harwood, “A comparative study of texture measures with classification based on feature distributions”, Pattern Recognition Vol.29, pp.51-59, 1996.

Ojala98 T. Ojala, M. Pietikäinen, “Nonparametric multichannel texture description with simple spatial operators”, Proceedings of 14th International Conference on Pattern Recognition, pp.1052-1056, 1998.

Oren95 M. Oren and S. K. Nayar, “Generalization of the Lambertian model and implications for machine vision”, International Journal of Computer Vision, Vol.14, pp.227-251, 1995.

Peli90 T. Peli, "Multiscale fractal theory and object characterisation", Journal Optical Society of America A, Vol.7, No.6, pp.1101-1112, 1990.

Pentland84 A. A. Pentland, “Fractal-based description of natural scenes”, IEEE Transactions on Pattern Analysis and Machine Intelligence, Vol.6, pp.661-764, 1984.

Pentland94 A. Pentland, R. W. Picard, and S. Sclaroff, “Photobook: Tools for content-base manipulation of image database”, In Proc. SPIE Conf. on Storage and Retrieval of Image and video Databases II, pp.34-47, 1994.

Phong75 B. T. Phong, “Illumination for computed generated pictures”, Communications of the ACM, Vol.18, No.6, pp.311-317, June 1975.

Picard96 R. W. Picard, “A society of models for video and image libraries”, Technical Report, No.360, MIT Media Lab, Cambridge, MA, 1996.

Pietikainen00 M. Pietikainen, T. Ojala and Z. Xu, “Rotation-invariant texture classification using feature distributions”, Pattern Recognition, Vol.33, pp.43-52, 2000.

Pietikainen82 M. Pietikainen, A. Rosenfeld and L.S. Davis, "Texture classification using averages of local pattern matches", Proceedings of IEEE Computer. Society Conference on Pattern Recognition and Image Processing, 1982.

Porter97 R. Porter and N. Canagarajah, “Robust rotaion invariant texture classification: wavelet, Gabor and GMRF based schemes”, IEE Proc. Vision Image Signal Process. Vol.144, No.3, 1997.

Pratt78 W. K. Pratt, O. D. Faugeras and A. Gagalowicz, “Visual discrimination of stochastic texture fields”, IEEE Transactions on System, Man and Cybernetics, Vol.8, pp796-804, 1978.

Press92 W. H. Press, S. A. Teukolsky, W. T. Vetterling and B. P. Flannery, “Numerical recipes in C”, second edition, Cambridge university press, 1992.

Randen99 Trygve Randen and John Hakon Husoy, “Filtering for texture classification: a comparative study”, IEEE Transactions on Pattern Analysis and Machine Intelligence, Vol.21, No.4, pp.291-310, 1999.

Reed90 T. R. Reed and H. Wechsler, “Segmentation of textured images and gestalt organisation using spatial/spatial-frequency representations”, IEEE Transactions on Pattern Analysis and Machine Intelligence, Vol.12, pp.1-12, 1990.

Reed93 T.R. Reed and J.M. Hans du Buf, "A review of recent texture segmentation and feature extraction techniques" Computer Vision, Graphics, and Image Processing: Image Understanding, Vol.57, No.3, pp.359-372, 1993.

Rosenfeld70 A. Rosenfeld and B. S. Lipkin, “Texture synthesis”, In Picture Processing and Psychopictorics, A Rosenfeld and B. S. Lipkin, eds. Academic Press, New York, 1970.

Rushmeier97 Holly Rushmeier, Gabriel Taubin and Andre Gueziec, “Applying shape from lighting variation to bump map capture”, In Eurographics Rendering Techniques’97, pp.35-44, St. Etienne, France, June 1997.

Sarkar97 A. Sarkar, K. M. S. Sharma and R. V. Sonak, “A new approach for subset 2-D AR model identification for describing textures”, IEEE Transactions on Image Process, Vol.6, No.3, pp.407-413, 1997.

Sayles78 R. S. Sayles, T. R. Thomas, “Surface topography as a nonstationary random process”, Nature, Vol.271, No.2, pp.432-434, 1978.

Serra73 J. Serra and A. K. C. Wong, “Mathematical morphology applied to fibre composite materials”, Film Science and Technology, Vol.6, pp.141-158, 1973

Smith99a M. L. Smith, “The analysis of surface texture using photometric stereo acquisition and gradient space domain mapping”, Image and Vision Computing, Vol.17, pp.1000-1019, 1999.

Smith99b M. L. Smith, G. Smith and T. Hill, “Gradient space analysis of surface defects using a photometric stereo derived bump map”, Image and Vision Computing, Vol.17, pp.321-332, 1999.

Solomon92 F. Solomon and K. Ikeuchi, “Extracting the shape and roughness of specular lobe objects using four light photometric stereo”, IEEE Conference on Computer Vision and Pattern Recognition, pp.466-471, 1992.

Stavridi97 M. Stavridi, B, van Ginneken, J. J. Koenderink, “Surface bidirectional reflection distribution function and the texture of bricks and tiles”, Applied Optics, Vol.36, No.16, 1997.

Strand94 J. Strand and T. Taxt, “Local frequency features for texture classification”, Pattern Recognition, Vol.27, No.10, pp.1397-1406, 1994.

Suen00 Pei-hsiu Suen and Glenn Healey, “The analysis and recognition of real-world textures in three dimensions”, IEEE Transactions on Pattern Analysis and Machine Intelligence, Vol.22, No.5, pp491-503, 2000.

Suen98 Pei-hsiu Suen and Glenn Healey, “Analyzing the bidirectional texture function”, IEEE Conference on Computer Vision and Pattern Recognition, pp753-758, 1998.

Tagare90 H. D. Tagare and R. J. P. deFigueiredo, “Simulataeous estimation of shape and reflectance maps from photometric stereo”, IEEE International Conference on Computer Vision, pp.340-343, 1990.

Tagare91 H. D. Tagare, and R. J. P. Defigueiredo, “A theory of photometric stereo fro a class of diffuse non-lambertaian surfaces”, IEEE Transactions on Pattern Analysis and Machine Intelligence, Vol.13, No.2, pp.133-152, February, 1991.

Tamura78 H. Tamura, S. Mori, and T. Yamawaki, “Textural features corresponding to visual perception” IEEE Transactions on Sys., Man and Cyber, Vol. SMC-8, No.6, pp.460-473, 1978.

Tan95 T. N. Tan, “Geometric invariant texture analysis”, Procs. SPIE, Vol.2488, pp475-485, 1995.

Tang98 X. Tang, “Texture information in run-length matrices”, IEEE Transaction on Image Process, Vol.7, No.11, pp.1602-1609, 1998.

Teh86 Ch.-H. Teh and R. T. Chin, “On digital approximation of moment invariants”, Computer Vision, Graphics & Image Processing, Vol.33, pp.318-326, 1986.

Tomita90 F. Tomita and S. Tsuji, “Computer analysis of visual textures”, Kluwer Academic Publishers, Boston, 1990.

Torrance67 K. E. Torrance and E. M. Sparrow, “Theory for off-specular reflection from roughened surfaces”, Optical Society of America, Vol.57, No.9, pp.1105-14, 1967.

Tuceryan90 M. Tuceryan and A. K. Jain, “Texture segmentation using Voronoi polygons”, IEEE Transactions on Pattern Analysis and Machine Intelligence, Vol.12, pp.211-216, 1990.

Tuceryan92 M. Tuceryan, “Moment based texture segmentation”, 11th IAPR International Conference, Vol.III, pp.45-48, 1992

Tuceryan93 M. Tuceryan and A. “Texture Analysis” in “Handbook of pattern recognition and vision”, Editor: C.H. Chen and L.F. Pau and P.S.P. Wang, Chapter 2.1, pp.235-276,World Scientific, 1993.

VanGool85 L. Van Gool, P. Dewaele and A. Oosterlinck, “Texture analysis anno 1983”, Computer Vision, Graphics, and Image Processing Vol.29, pp.336-357, 1985

Varma02 Manik Varma and Andrew Zisserman, “Classifying materials from images: to cluster or not to cluster?”, Proceedings of the 2nd International Workshop on Texture Analysis and Synthesis, in conjunction with ECCV2002, pp.139-144, Copenhagen, Denmark, 2002.

Varma02a Manik Varma and Andrew Zisserman, “Classifying Images of Materials: Achieving Viewpoint and Illumination Independence”, Proceedings of the 7th European Conference on Computer Vision, pp.255-271, Copenhagen, Denmark, 2002.

Varma02b Manik Varma, “Assesing textures classifiers on Jerry Wu’s database”, Research Memorandum, Visual Geometry Group, Department of Engineering Science, University of Oxford., August, 2002.

Wang98 L. Wang and G. Healey, “Using Zernike moments for the illumination and geometry invariant classification of multispectral texture”, IEEE Transactions on Image Process, Vol.7. No.2, pp.196-203, 1998.

Ward92 G. Ward, “Measuring and modeling anisotropic reflection”, SIGGRAPH 1992.

Wechsler80 H. Wechsler, “Texture analysis - A survey”, Signal Processing,Vol.2, pp.271-282, 1980.

Welch67 P. D. Welch, “The use of fast Fourier transform for the estimation of power spectra: a method based on time averaging over short, modified periodograms”, IEEE Transactions on Audio and Electroacoustics, Vol.15, No.2, pp.70-73, 1967.

Wolff94 L. B. Wolff, “A diffuse reflectance model for smooth dielectrics”, Journal of the Optical Society of America A – Special Issue on Physics Based Machine Vision, Vol.11, pp2956-2968, November, 1994.

Wolff96 L. B. Wolff, “Generalizing Lambert’s law for smooth surfaces”, The Fourth European Conference on Computer Vision, Vol.2, pp.642-651, 1996

Wolff98 L. B. Wolff, S. K. Nayar and M. Oren, “Improved diffuse reflection models for computer vision”, International Journal of Computer Vision, Vol.30, No.1, pp.55-71, 1998.

Woodham80 R. Woodham, “Photometric method for determining surface orientation from multiple images”, Optical Engineering, Vol.19, No.1, pp.139-144, 1980.

Wu96 W. R. Wu and S. C. Wei, “Rotation and gray-scale transform-invariant texture classification using spiral resampling, subband decomposition, and hidden Markov model”, IEEE Transactions on Image Processing, Vol.5, No.10, 1996.

You93 J. You and H. A. Cohen, “Classification and segmentation of scaled textured images using ‘tuned’ masks”. Pattern Recognition, Vol.26, pp.245-258, 1993.

Zhang02a Jianguo Zhang and Tieniu Tan, “Brief review of invariant texture analysis methods”, Pattern Recognition, Vol.3, pp.735-747, 2002.